Lawrence Berkeley National Laboratory
Recent Work

Title
FACTORS CONTRIBUTING TO THE BREAKDOWN OF SODIUM BETA ALUMINA

Permalink
https://escholarship.org/uc/item/5sh7p2cx

Author
Buechele, A.C.

Publication Date
1982-05-01

eScholarship.org Powered by the California Digital Library
University of California

LBL-13951

Lawrence Berkeley Laboratory
UNIVERSITY OF CALIFORNIA

Materials & Molecular Research Division

RECEIVED
LAWRENCE
BERKELEY LABORATORY
JUN 15 1982
LIBRARY AND
DOCUMENTS SECTION

FACTORS CONTRIBUTING TO THE BREAKDOWN OF SODIUM BETA ALUMINA

Andrew C. Buechele
(Ph.D. thesis)

May 1982

TWO-WEEK LOAN COPY
This is a Library Circulating Copy which may be borrowed for two weeks.
For a personal retention copy, call
Tech. Info. Division, Ext. 6782.

Prepared for the U.S. Department of Energy under Contract DE-AC03-76SF00098

LBL-13951

DISCLAIMER

This document was prepared as an account of work sponsored by the United States Government. While this document is believed to contain correct information, neither the United States Government nor any agency thereof, nor the Regents of the University of California, nor any of their employees, makes any warranty, express or implied, or assumes any legal responsibility for the accuracy, completeness, or usefulness of any information, apparatus, product, or process disclosed, or represents that its use would not infringe privately owned rights. Reference herein to any specific commercial product, process, or service by its trade name, trademark, manufacturer, or otherwise, does not necessarily constitute or imply its endorsement, recommendation, or favoring by the United States Government or any agency thereof, or the Regents of the University of California. The views and opinions of authors expressed herein do not necessarily state or reflect those of the United States Government or any agency thereof or the Regents of the University of California.

LBL-13951

FACTORS CONTRIBUTING TO THE BREAKDOWN OF SODIUM BETA ALUMINA

Andrew C. Buechele*

Materials and Molecular Research Division
Lawrence Berkeley Laboratory
University of California
Berkeley, California 94720

*Presented to the Faculty of the Graduate School
of Cornell University
in Partial Fulfillment for the Degree of
Doctor of Philosophy

This work was supported by the Assistant Secretary for Conservation and Renewables, Office of Advanced Conservation Technology, Electrochemical Systems Research Division, U.S. Department of Energy, under Contract No. DE-AC03-76SF00098 and from the Electric Power Research Institute under Contract RP 252-3.

This Thesis is Dedicated to

Cathy Babcock

TABLE OF CONTENTS

LIST OF TABLES..... vii

LIST OF FIGURES..... viii

ACKNOWLEDGMENTS..... xvi

ABSTRACT..... xvii

1. THE SODIUM/SULFUR BATTERY..... 1

1.1. Introduction..... 1

1.2. The Electrolyte..... 2

1.3. Relevant Aspects of the Chemistry and Properties of Sodium and Sulfur..... 9

1.4. The Engineering and Design Problems of the Sodium/Sulfur Cell..... 14

1.5. Failure Modes..... 19

2. ASPECTS OF ELECTROLYTE DEGRADATION..... 20

2.1. Physical Characteristics of Degraded Electrolytes..... 20

2.2. Causes of Degradation..... 21

2.2.1. Intrinsic Stability of the Electrolyte..... 21

2.2.2. Electrochemical and Related Effects..... 25

2.2.3. Modifications of the Electromechanical Breakdown Theory. Mode I Versus Mode II Breakdown..... 32

2.2.4. Possible Current Induced Thermal Effects..... 33

2.2.5. Contribution of the Polysulfide Electrode to Breakdown..... 34

2.3. Objectives of this Work..... 35

3. MATERIALS, EQUIPMENT, AND EXPERIMENTAL METHODS..... 36

3.1. Materials and Equipment..... 36

3.2. Characterization of the Ceramatec Material..... 37

3.2.1. Fabrication..... 37

3.2.2. Microstructure..... 37

3.2.3. Surface Features..... 40

3.2.4. Internal Irregularities..... 46

3.2.5. Electrical Properties..... 46

3.3. Silver Decoration..... 46

3.4. Microscopy and Microanalysis..... 49

3.5. A.C. Dispersion Analysis..... 50

4. CHEMICAL COLORATION OF THE BETA ALUMINAS..... 52

4.1. Introduction..... 52

4.2. Experimental..... 52

4.2.1. Single Crystal Experiments..... 53

4.2.2. Polycrystalline Material Experiments..... 61

4.3. Results and Discussion..... 66

4.3.1. Preliminary Analysis..... 66

4.3.2. Penetration of Darkening and Enhancement by Silver Exchange in Single Crystals..... 68

4.3.3. Kinetics of the Advance of the Darkened Layer in Single Crystals..... 71

4.3.4. Other Aspects of Single Crystal Coloration..... 73

4.3.5. Kinetics of the Advance of the Bleached Layer in Single Crystals..... 75

4.3.6. Other Aspects of Single Crystal Bleaching..... 77

4.3.7. Mechanisms of Coloration and Bleaching in Single Crystals..... 87

4.3.8. Photodarkening of Beta" Alumina by UV..... 89

4.3.9. Kinetics of the Advance of the Darkened Layer in Polycrystalline Electrolytes..... 91

4.3.10. Large Grain Behavior During Polycrystalline Electrolyte Coloration..... 99

4.3.11. Sodium Content and Ionic Conductivity in Colored and Bleached Polycrystalline Electrolytes..... 100

4.4. Summary and Conclusions..... 100

5. SODIUM/SODIUM CELL TESTING..... 104

5.1. Introduction..... 104

5.2. Experimental..... 106

5.2.1. Cell Construction..... 106

5.2.2. Cell Cycling Equipment..... 106

5.2.3. Cell Cycling Procedure..... 111

5.2.4. Acoustic Emission Equipment and Techniques..... 111

5.3. Results and Discussion..... 118

5.3.1. Cell Electrical Parameter Behavior During Cycling..... 118

5.3.2. Critical Current Density Determination..... 125

5.4. Summary and Conclusions..... 139

6. FAILURE ANALYSIS OF CYCLED ELECTROLYTES..... 140

6.1. Introduction..... 140

6.2. Examination of Electrolyte Material from Commercial Sodium/Sulfur Batteries..... 140

6.2.1. Sources of Materials and Cycling History..... 140

6.2.2. Preliminary Examination of Cycled Electrolytes..... 143

6.2.3. Surface and Grain Structure..... 144

6.2.4. The Sodium Electrode/Electrolyte Interface..... 149

6.2.5. The Sulfur Electrode/Electrolyte Interface..... 168

6.2.6. Auger Analysis..... 177

6.2.7. Complex Conductivity Measurements on the 23 Ahr cm^{-2} Beta Cell..... 179

6.2.8. X-ray Analysis of Surface Impurities in the SEM..... 184

6.3. Examination of Electrolyte Material from Sodium/Sodium Cells..... 189

6.3.1. Evidence for Grain Size Effects..... 189

6.3.2. Evidence for Mode I Processes..... 195

6.3.3. Impurities..... 204

6.4. Summary and Conclusions..... 207

7. OVERALL SUMMARY AND DISCUSSION..... 209

APPENDIX 1. THE LIKELIHOOD OF FAILURE FROM CURRENT INDUCED THERMAL EFFECTS..... 211

APPENDIX 2. CALCULATION OF THE WEIBULL CURVE FOR CELLS OF DIFFERING AREAS..... 217

BIBLIOGRAPHY..... 222

LIST OF TABLES

Table		Page
3.1	Microstructural data for beta" alumina electrolytes from Ceramatec.....	41
4.1	Single crystal coloration kinetics data.....	74
4.2	Single crystal bleaching and coloration kinetics data.....	79
4.3	Polycrystalline beta" alumina coloration kinetics data.....	96
4.4	Soda content and conductivity data for polycrystalline electrolyte material.....	102
5.1	Current density and Weibull parameter requirements for selected initial failure rates in cell operation.....	133
6.1	Surface impurities found on cycled beta electrolytes by x-ray analysis in the SEM.....	185
A1.1	Comparative properties of sodium and sodium beta" alumina at 350°C.....	216

LIST OF FIGURES

Figure		Page
1.1	Structures of sodium beta alumina and sodium beta" alumina.....	4
1.2	Arrangement of ions in the conduction planes of: A. sodium beta alumina; B. sodium beta" alumina. Regions modified by point defects are enclosed by dashed lines.....	5
1.3	Schematic representation of "Roth defect".....	7
1.4	Sodium-sulfur phase diagram.....	10
1.5	Solubility of oxygen in liquid sodium.....	13
1.6	Schematic cross section of the sodium/sulfur cell.....	15
2.1	Proposed phase diagram of Na_2O-Al_2O_3 system in the region of existence of beta alumina phases. Shaded area represents region of coexistence of beta and beta" phases.....	22
3.1	Low (left) and high (right) magnification views of polished etched electrolyte tube cross sections: A."10 μm" B. "150 μm" C. "300 μm".....	39
3.2	Surface features of "10 μm" beta" alumina tubes: A. inside surface B. outside surface C. cavity, inside surface D. cross section of deep cavity, outside surface E. cross section of "foldover" flaw, outside surface F. adherent agglomerate, inside surface.....	42
3.3	Details of surface and interior microstructures in "10 μm" material. Note curved grains.....	44
3.4	Pullouts from large grain boundaries near surface in "300 μm" material.....	45
3.5	Fracture surfaces of "10 μm" material showing the two types of interior voids.....	47
3.6	Admittance plots for "10 μm" material at 200°C, 275°C, and 350°C.....	48
4.1	Basic steps in coloration and bleaching experiments.....	54

4.2 Single crystal of beta alumina after immersion in molten sodium showing sodium which has infiltrated basal plane cracks. [c] direction is perpendicular to plane of figure..... 55

4.3 Comparison of beta alumina single crystals showing darkening produced by immersion in molten sodium. [c] direction is vertical in plane of figure..... 57

4.4 Schematic cross section showing method of fabrication of single crystal sample with sealed conduction planes..... 59

4.5 Surfaces of immersed polycrystalline electrolyte specimens before (bottom) and after (top) silver ion exchange. Nominal grain size in μm indicated at left of rows on top. Same order on bottom..... 62

4.6 Polished cross sections of silver exchanged colored polycrystalline electrolytes. Days immersed in sodium are indicated adjacent to each specimen..... 63

4.7 Darkening profiles of two "10 μm" electrolyte cross sections in arbitrary units of density..... 65

4.8 Cross section of silver exchanged darkened single crystal viewed in polarized light (top) and unpolarized light (bottom) to show that the layer of darkening polarizes light and that it penetrated the crystal almost isotropically..... 69

4.9 Anisotropy of light transmission by silver exchanged darkened single crystal..... 70

4.10 Darkened layer growth kinetics in beta alumina single crystals..... 72

4.11 Darkened single crystals subjected to various bleaching treatments before silver exchange..... 76

4.12 Bleached layer growth kinetics in beta alumina single crystals..... 78

4.13 Comparison of single crystals heated to 400°C for 24 hours in: A. air and B. high vacuum. Regions identified are: 1) edge of crystal 2) bleached layer 3) darkened crystal..... 81

4.14 Cross sectional view of darkened single crystals subjected to various bleaching treatments before silver exchange..... 82

4.15	Cross section of actual sample with sealed conduction planes after sodium immersion and silver exchange. Darkening has penetrated the crystal through the exposed spinel block side.....	84
4.16	Dual temperature phase bleaching kinetics.....	86
4.17	Photodarkened silver beta" alumina polycrystalline electrolyte. Note lack of coloration where forceps masked specimen.....	90
4.18	Darkening kinetics of polycrystalline electrolytes.....	92
4.19	Polished cross sections of silver exchanged colored polycrystalline electrolytes immersed 16 days.....	93
4.20	Normalized concentration profiles in "10 μm" electrolyte.....	94
4.21	Normalized concentration profiles in "150 μm" electrolyte.....	95
4.22	Admittance plots for polycrystalline electrolyte: A. as received B. after 388 hours immersion in sodium at 350°C C. immersed as in B and then bleached 56 hours at 800°C.....	101
5.1	Cut away view of sodium/sulfur cell showing mode of construction and attachment of acoustic waveguide.....	107
5.2	Block diagram of control amplifier.....	108
5.3	Schematic diagram of control amplifier. Q_1 = 2N3019, Q_2 - Q_4 = 2N3716, *polystyrene.....	109
5.4	Cell with acoustic waveguide and transducer attached, mounted in support bracket ready to be fastened to sodium pot.....	112
5.5	A. Idealized acoustic signal. B. Signal detector response.....	114
5.6	Block diagram of cell environment and cycling system.....	117
5.7	Polarization behavior of cells during rapid triangular current wave ramping.....	119

5.8 Sodium entrance surface of cell 90530 (top) and 91002 (bottom). Optical micrographs (left) show severe darkening of the electrolyte surface (active uncoated surface on cell 91002 has been outlined in black for clarity). Scanning electron micrographs (right) show porous surface texture produced by extended operation of the cell under conditions of severe polarization..... 121

5.9 A segment of the current/voltage versus time curve for cell 00626. The current trace lags the voltage trace by 0.375 min. A and B are small voltage drops associated with crack growth. The large drop at C corresponds to severe crack growth induced by the current pulse marked with an arrow..... 124

5.10 Current density and voltage data superimposed on the acoustic count rate (ACR) for the initial stages of breakdown in cell 00626. Units of vertical axes are specified where the corresponding traces are identified..... 127

5.11 Acoustic emission trace showing: A. first onset of Mode I typified by isolated acoustic events and B. severe onset of Mode I marked by steady acoustic activity. Cell current density (j) is also plotted. (b.l. = background level)..... 131

5.12 Criteria for proof testing..... 135

5.13 Weibull plot for first onset of Mode I degradation as indicated by first increase in acoustic activity..... 136

5.14 Weibull plot for severe onset of Mode I degradation as indicated by start of sustained acoustic activity..... 137

6.1 Beta electrolyte tube as received; removed from sodium/sulfur cell cycled to 332 Ahr cm^{-2} of charge transfer..... 142

6.2 Comparison of beta electrolyte tube segments from four sodium/sulfur cells. Sulfur surfaces are shown..... 145

6.3 Sodium surfaces and polished cross sections of electrolytes shown in figure 6.2..... 146

6.4 A. Surface texture and B. internal grain structure of beta electrolyte tubes..... 147

6.5 Internal grain structure of beta" electrolyte tubes from cycled sodium/sulfur cells..... 148

6.6 Sodium carbonate crystals on sodium surfaces of cycled beta electrolytes..... 150

6.7 Polished, silver decorated cross sections of beta electrolyte tubes. Note white spotty reflections (subsurface fractures due to mode II processes) near sodium surfaces. (332 Ahr cm^{-2} left and 703 Ahr cm^{-2} right)..... 151

6.8 600 KV TEM micrograph of beta electrolyte thick foil. Arrows point to degradation at grain triple junction and along grain boundary..... 154

6.9 600 KV TEM micrograph of beta electrolyte thick foil showing microcracking associated with degradation at grain junction..... 155

6.10 X-ray spectrum from degraded grain junction (dots) compared with spectrum from undegraded region (vertical bars) showing excess sodium and silicon are present in the degraded region..... 156

6.11 Silver decorated polished cross section of beta" electrolyte tube from sodium/sulfur cell cycled to 121 Ahr cm^{-2} of charge transfer over a period of 95 days. A. Sulfur side B. Sodium side..... 157

6.12 Silver decorated polished cross section of beta" electrolyte tube from sodium/sulfur cell cycled to 539 Ahr cm^{-2} charge transfer over a period of 673 days. Note subsurface annular crack..... 158

6.13 Macrocracking (Mode I degradation) originating sodium surface in beta electrolyte and branching to run parallel to surface. Mode II degradation is also in evidence here..... 162

6.14 Mode I crack which has initiated at sodium surface in beta electrolyte and then deflected to run parallel to surface..... 163

6.15 SEM micrograph of Mode I crack in beta electrolyte. Note how crack branched to run parallel to surface..... 164

6.16 Region of enhanced degradation at sodium surface in beta" electrolyte from sodium/sulfur cell cycled to 121 Ahr cm^{-2} of charge transfer. (Polarized illumination)..... 165

6.17 Detail of area shown in Figure 6.16. A. Unpolarized illumination reveals grain structure. B. Partially polarized illumination locates large grain in region of enhanced degradation..... 166

6.18 A. (Unpolarized illumination) Large grains near the sodium surface serve to facilitate B. (polarized illumination) breakdown along their boundaries. Arrows point to same location in both micrographs for reference. Different area from same cell used for Figure 6.16..... 167

6.19 Silver decorated sulfur surface of beta electrolyte showing regular pattern of imprinting from carbon felt. (703 Ahr cm^{-2} charge transfer)..... 169

6.20 Silver decorated sulfur surfaces of cycled beta electrolytes. (703 Ahr cm^{-2} top, 23 Ahr cm^{-2} bottom)..... 170

6.21 Silver decorated polished cross sections of cycled beta electrolytes showing progress of breakdown near sulfur surface..... 171

6.22 Silver decorated polished cross sections of beta" electrolyte first shown in Figure 6.11. Higher magnification reveals details. A. Sulfur surface B. Sodium surface..... 173

6.23 Silver decorated polished cross sections of beta" electrolyte first shown in Figure 6.12 revealing extensive degradation propagating from sulfur surface..... 174

6.24 Probable situation late in discharge cycle at positive electrode/electrolyte interface where carbon fibre contacts electrolyte..... 176

6.25 Auger spectrum from beta electrolyte..... 178

6.26 Silver exchanged beta electrolyte material from 23 Ahr cm^{-2} cell (top) and 703 Ahr cm^{-2} cell (bottom) showing how darkening progresses from partial to full depth..... 180

6.27 Cross section of silver exchanged beta" electrolyte material from 539 Ahr cm^{-2} cell..... 182

6.28 Admittance plots at 200°C for beta electrolyte specimens from 23 Ahr cm^{-2} cell..... 183

6.29 Sodium surface of beta electrolyte from 271 Ahr cm^{-2} cell showing deposited small crystals..... 187

6.30 Close up of a crystal in Figure 6.29 and its x-ray spectrum..... 188

6.31 Silver decorated sodium exit surface of cell 00324, 22 Ahr cm^{-2}, "300 μm" material. Surface of cell had been prepolished and cell was removed from service after the onset of sustained acoustic activity. Note the heavy decoration along the boundaries of the large grains indicating severe degradation in these regions..... 191

6.32 Polished cross section of cell shown in Figure 6.31. Arrow points to mode I crack..... 192

6.33 Silver decorated prepolished surfaces of cell 00624 (exit surface, 30 Ahr cm^{-2}) and of cell 00527 (entrance surface, 44 Ahr cm^{-2}) shown for comparison. Black droplet-like areas on surface are patches of sealing glass which got there accidentally during cell fabrication..... 194

6.34 Schematic representation of mode of current concentration at edge of large grain inclined to electrolyte surface..... 196

6.35 Decorated polished specimens of "300 μm" material: A. immersed in sodium 24 hours at 350°C and baked 1 hour at 800°C B. baked 1 hour at 800°C only..... 197

6.36 Cross section of cell 90425 showing crack approximately parallel to electrolyte tube walls..... 198

6.37 Cell 90521 (10 Ahr cm^{-2}, "300 μm" material) showing crack network visible through transparent large grains of the sodium entrance surface..... 201

6.38 Cross section of cell 90530 (255 Ahr cm^{-2}, "10 μm" material) showing extensive cracking and darkening..... 202

6.39 Silver decorated cross section of cell 90901 and detail of section near adherent patch of sealing glass..... 203

6.40 Section of electrolyte from cell 90427-B broken down at room temperature. Sodium exited through inside surface of tube where extensive spalling is evident..... 205

6.41 Entrance surface of cell 90613 (20 Ahr cm^{-2}, "10 μm" material) and x-ray spectrum from it showing presence of potassium..... 206

A1.1 A. Normal current flow into crack. B. Approximation of current flow into crack. C. Basic geometry for solution of Poisson's equation..... 212

A2.1 Listing of TI 59 program..... 219

ACKNOWLEDGMENTS

The Author expresses his sincere gratitude to all who assisted directly and indirectly in the completion of this thesis, especially:

To my advisor, Lutgard C. De Jonghe, for his constant guidance, helpful discussions, and encouragement.

To my mother for typing the rough draft of this thesis.

To the many members of the staff of LBL who assisted in making effective use of its facilities.

To the usual "too many to mention" friends and associates whose friendship and prayers have continued to sustain and guide me.

This work received support from the Assistant Secretary for Conservation and Renewables, Office of Advanced Conservation Technology, Electrochemical Systems Research Division, U.S. Department of Energy, under Contract DE-AC03-76SF00098 and from the Electric Power Research Institute under Contract RP 252-3.

FACTORS CONTRIBUTING TO THE BREAKDOWN OF SODIUM BETA ALUMINA SOLID ELECTROLYTES

Andrew C. Buechele

Materials and Molecular Research Division
Lawrence Berkeley Laboratory
University of California
Berkeley, California 94720

ABSTRACT

Clarification of the breakdown process occurring during charge transfer in sodium beta alumina solid electrolytes was derived from: 1) studying the effects of molten sodium contact at 350°C on single crystal sodium beta alumina and polycrystalline sodium beta" alumina; 2) determination of critical current density by monitoring acoustic emissions accompanying crack growth in sodium/sodium beta" alumina/sodium cells subjected to linear current ramping at 1 mA cm^{-2} sec^{-1}; 3) failure analysis conducted on cycled electrolytes, some from commercial sodium/sulfur cells, which had been subjected to up to 703 Ahr cm^{-2} of charge transfer.

Gray coloration developing in beta aluminas in contact with molten sodium was found to be a consequence of formation, through reduction by sodium, of oxygen vacancies charge compensated by electrons. Electronic conductivity of the electrolyte increases as a result. No second phase formation was detected. Colored electrolytes from sodium/sulfur cells show evidence of a newly recognized degradation mechanism in which fracture occurs when sodium is reduced and deposited internally under pressure as metal in regions where an electronic conductivity

gradient exists. The new mechanism is herein called mode II to distinguish it from the more familiar mechanism (herein, mode I) based on the enlargement of surface cracks by Poiseuille pressure. Heating colored beta aluminas in air produces reoxidation and bleaching. Kinetics and other properties of the coloration and bleaching processes were determined.

Critical current densities determined here by acoustic emission methods were substantially lower than those reported by other investigators. Critical current density was found to bear an inverse relation to average electrolyte grain size. Evidence of enhanced degradation was frequently found at 00.1 faceted boundaries of very large grains in cycled electrolytes. Evidence was also found in the cycled electrolytes for a slow crack growth mechanism and a progressive mode of degradation advancing from the sulfur electrode interface.

Implications of the findings for the construction and operation of sodium/sulfur battery systems are discussed.

1. THE SODIUM/SULFUR BATTERY

1.1 Introduction

An increased interest in developing high efficiency energy storage systems for use in power utility load leveling applications and for vehicle propulsion is one result of a recognition of the need for efficient energy management. The sodium/sulfur battery was first proposed as a system with promising potential in this area by Kummer and Weber of Ford Motor over ten years ago (Ku 68).

The battery is based on a cell in which sodium and sulfur in their molten state are the reactants. An ionically conducting ceramic membrane of sodium beta alumina separates the reactants, but permits sodium ion transfer so that the reaction can take place when the external circuit is completed. Sodium polysulfides are formed during discharge as chemical energy is converted into electricity. The cell can then be recharged by the application of an external counter electromotive force.

Much work has gone into developing the system from theory to practical application, but many serious obstacles remain to achieving the necessary long term reliability. A recent article in Physics Today, reviewing the status of several high technology energy storage systems for vehicle propulsion, noted that in spite of the high desirability of the sodium/sulfur system, the greater relative difficulty of the problems facing its use makes its application less likely than some competing systems (Wa 80). Some of the requirements of a vehicle propulsion system are different from those of a load leveling system,

but the one requirement in common which has not been realized yet is a low failure rate.

The major problems facing the sodium/sulfur system can be placed in three categories: 1) corrosion problems in the container and its seals, 2) proper functioning of the polysulfide electrode and its associated current collector, and 3) electrolyte degradation processes. Extensive research and testing is underway at General Electric and at Ford Motor in this country and at a number of places worldwide to solve these problems so that production of a practical system can begin. This thesis will focus on certain aspects of the electrolyte degradation problem, but some preliminary discussion on the theory of operation and construction of the sodium/sulfur battery will be necessary as background.

1.2 The Electrolyte

The history of the discovery and determination of the properties of the beta aluminas has been treated in some detail by the author in another thesis (Bu 78, pp. 14-41), and only such items as are relevant to the present work will be repeated or expanded here. Beta alumina was first reported in the literature and named by Rankin (Ra 16) in 1916. Determination of the structure, and even of the composition, was not made until 1936 by Beevers and Ross (Be 36); and recognition and investigation of ionic conduction properties began only in the late 60's, largely upon the observations of Yao and Kummer (Ya 67). There are two phases which are of commercial importance, referred to as sodium beta alumina and sodium beta" alumina. The beta structure is hexagonal and belongs to the space group $P6_3/mmc$ while the beta"

structure is rhombohedral and belongs to the space group $R\bar{3}m$. The structures are closely related as can be seen from their representation in Figure 1.1. In both there are units of four cubic closest packed layers of oxygen atoms, containing the aluminum atoms in a spinel type arrangement, referred to as spinel blocks. These units are interspersed alternately with loosely packed layers of oxygen atoms in which the sodium ions are contained. The sodium ion containing layers in the beta structure are mirror planes, and are referred to as the conduction planes since the rapid movement of the sodium ions is strictly confined to them. There are two conduction planes and two spinel blocks per conventional unit cell in the beta structure; the [c] lattice parameter is 22.6 Å. The conventional unit cell of the beta" structure contains three spinel blocks and three conduction planes, and has a [c] lattice parameter of 33.85 Å. The loosely packed layers in the beta" structure are not mirror planes, and the sodium positions are slightly offset on alternate sides of the plane center resulting in an undulating movement of the ions through the plane.

The ideal arrangement of ions in the conduction planes of beta and beta" alumina, as well as the arrangement in the vicinity of point defects, is illustrated in Figure 1.2. It can be seen that more sodium is present in the ideal structure of beta" than in that of beta. But both compounds normally have high defect concentrations inherent in their actual structures. As a result, beta is sodium rich and beta" is sodium deficient with reference to their ideal structures. The actual structure of beta" still contains a higher percentage of sodium than that of beta. The nature of the defects has been probed with

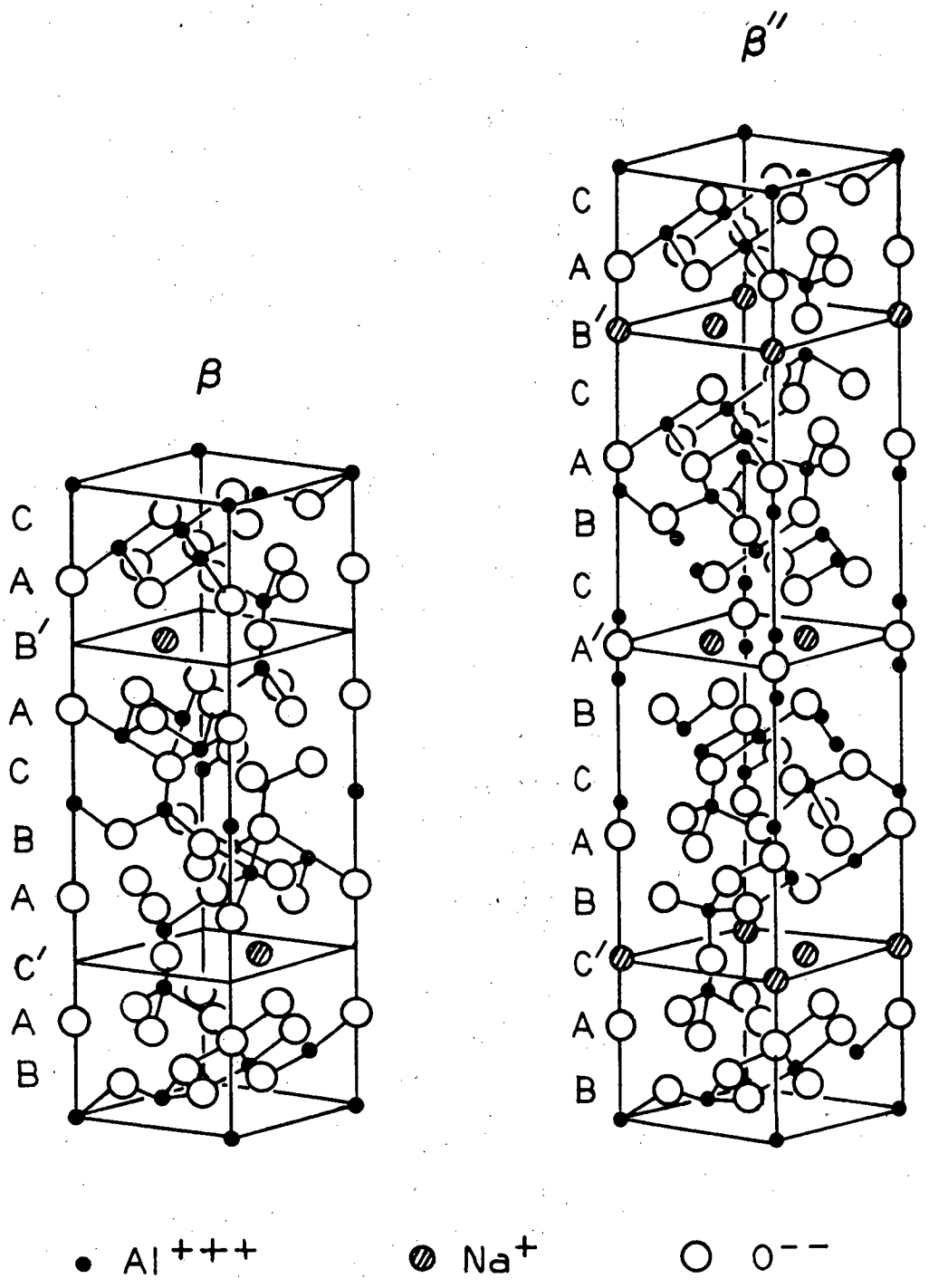

Fig. 1.1 Structures of sodium beta alumina and sodium beta" alumina.

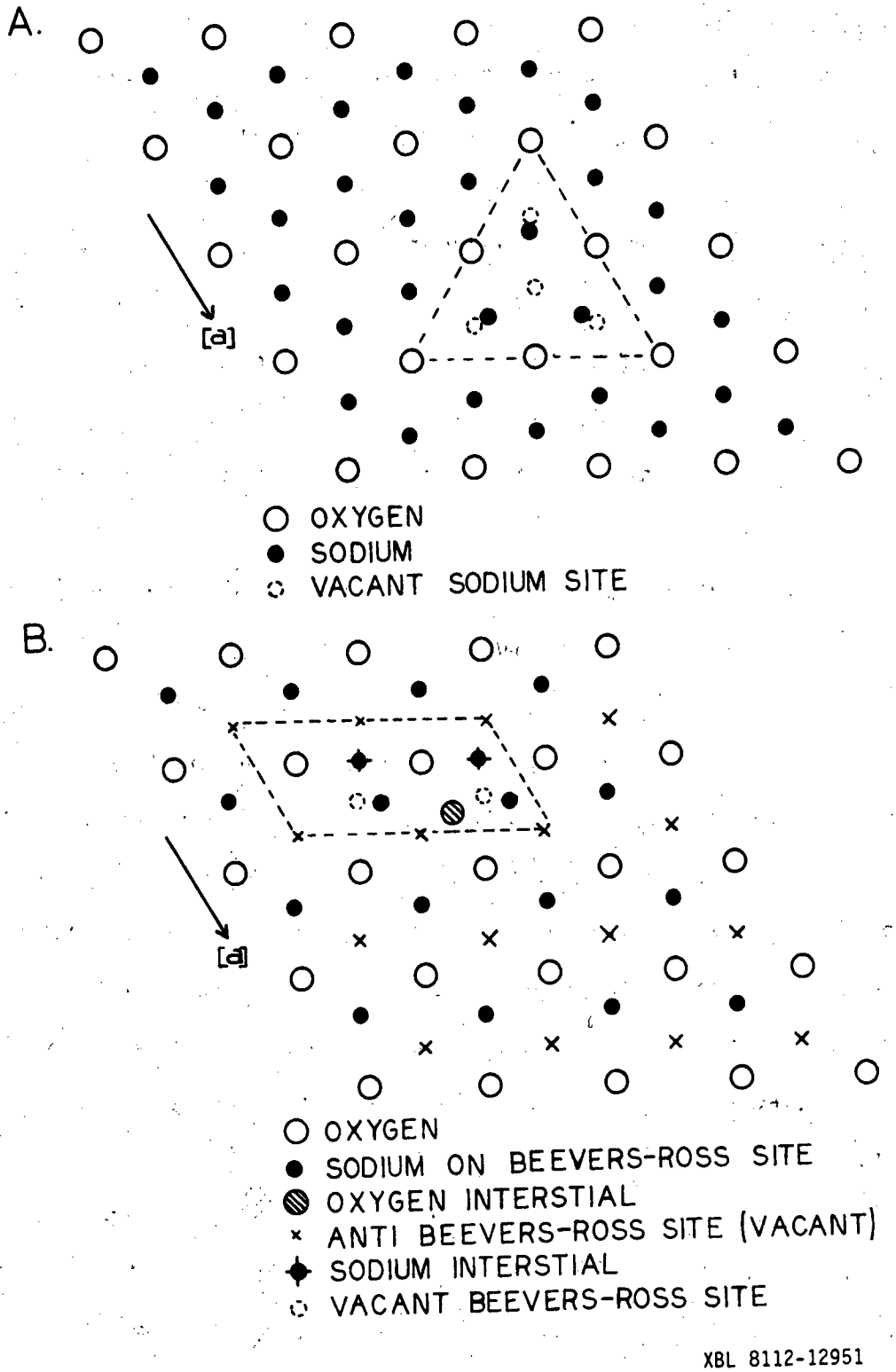

Fig. 1.2 Arrangement of ions in the conduction planes of: A. sodium beta alumina; B. sodium beta" alumina. Regions modified by point defects are enclosed by dashed lines.

neutron diffraction by Roth, et al. (Ro 76), and the following defect configurations have been proposed on the basis of it. In beta alumina an oxygen interstitial in the conduction plane, in the approximate normal sodium position, is coordinated by two aluminum interstitials and two aluminum vacancies, arranged in the two adjacent spinel blocks. Two interstitial sodiums in the conduction plane complete the defect which is indicated schematically in Figure 1.3. The atomic arrangement in the conduction plane has been indicated in Figure 1.2A. In beta" alumina, some of the normal sodium positions are vacant resulting in the displacement of the three adjacent sodium ions about 0.4 Å toward the vacant position. This was indicated in Figure 1.2B. No conduction plane oxygen interstitials appear to be involved in defect formation in the beta" structure.

The conductivity of polycrystalline sodium beta alumina is about 15-20 ohm cm at 350°C and that of polycrystalline beta" alumina is about 3-4 ohm cm at 350°C. Both materials have an activation enthalpy for ion conduction of about 4 kcal $mole^{-1}$. These unusual properties are a consequence both of loose oxygen ion packing in the conduction planes and of the very large concentration of defects in the structure. The rapid conductivity is strictly confined to two dimensions. The close packed structure of spinel blocks effectively prohibits movement of sodium ions in a direction parallel to the [c] axis. This has been demonstrated convincingly in an experiment done by Yao and Kummer (Ya 67) in which they irradiated a single crystal of beta alumina with neutrons converting some of the $^{23}Na^+$ to $^{24}Na^+$. The immediate gamma decay of the $^{24}Na^+$ provides sufficient recoil energy to drive some of them into the spinel blocks. The high mobility of the sodium ions

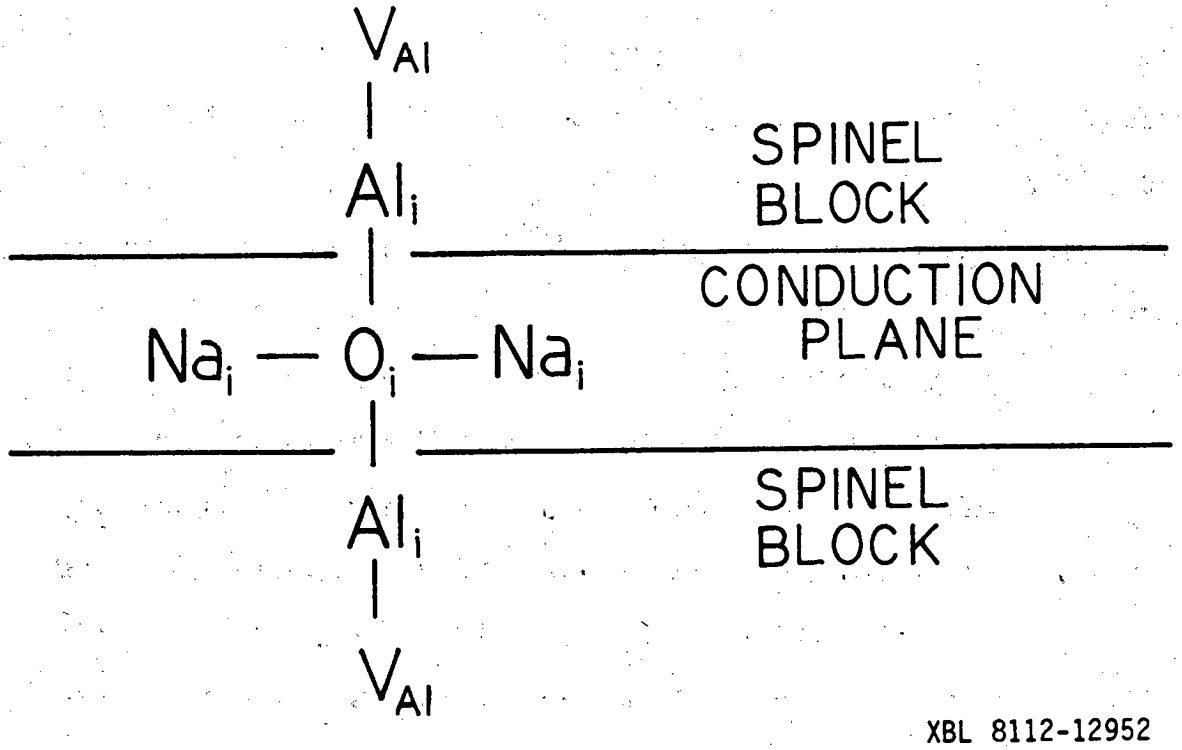

Fig. 1.3 Schematic representation of "Roth defect".

remaining in the conduction planes makes it possible to totally exchange them for $^{23}Na^{+}$ simply by placing the crystal in a melt of a $^{23}Na^{+}$ salt. It is then possible to determine the percentage of ions trapped in the spinel block by measuring the relative radioactivity of the melt and the crystal. It was found that virtually none of the trapped ions could be released from the spinel block until the temperature of the exchange system was raised above 1000°C. Total recovery of trapped ions occurred only after 1/2 hour at 1100°C. Under normal conditions, all sodium ions are mobile and are present only in the conduction planes of the beta aluminas.

This contrasts sharply with the structurally analogous compounds in the Na_2O-Ga_2O_3 system. These have been examined by Foster, et al. (Fo 80), and they exhibit many properties quite similar to those of the beta aluminas including high ionic conductivity. However, 10-15% of the sodium present in these gallates is not readily exchangeable, and is assumed to be located somewhere in the spinel blocks. The lattice parameters of these compounds are about 3 to 4% greater than those of the corresponding beta aluminas, which may account for the greater ease of accommodating sodium in the spinel blocks than in the beta aluminas.

Polycrystalline ceramics of the beta-aluminas having near theoretical density can be readily fabricated by sintering. Beta" alumina requires the presence of an aliovalent ion, usually lithium and/or magnesium, in the spinel block to stabilize the structure and insure the production of a single phase material. Otherwise, either a mixture of beta and beta" or a single phase beta will be produced, depending on the sintering temperature. Conversion of unstabilized beta" to beta occurs above 1400°C. Even in beta alumina, incorporation of magnesium

or lithium leads to a higher percentage of sodium and a higher conductivity in the final product (Ch 76). Sintering of both beta and beta" must be done in an oxidizing atmosphere rich in Na_2O. Otherwise, loss of soda from the material will result in lower conductivity and/or partial conversion to alpha alumina. Melting of the beta aluminas is incongruent and occurs around 1900°C. The mechanical strength of the properly prepared polycrystalline electrolyte is usually around 300 MPa in air and about 200 MPa in liquid sodium at 350°C as measured by Davidge, et al. (Da 79a) in diametral compression fracture of ring specimens. Chemical stability in contact with the components of the sodium/sulfur electrochemical system is acceptable, but perhaps not as good as previously assumed as will be shown subsequently in this thesis.

1.3 Relevant Aspects of the Chemistry and Properties of Sodium and Sulfur.

The abundance of sodium and sulfur is a strong motivating factor for the development of a battery using them as low cost storage electrodes.

A phase diagram of the sodium/sulfur system is shown in Figure 1.4 (Mo 78). Full utilization of the energy available from the couple would require a system which cycled between the extremes of pure sodium and pure sulfur at full charge, and pure Na_2S at full discharge. This is impractical because: a) pure sulfur is essentially an electronic non-conductor and thus power density would vanish at full charge, and b) the melting point of Na_2S is 978°C. A system operating at this temperature would encounter almost insuperable

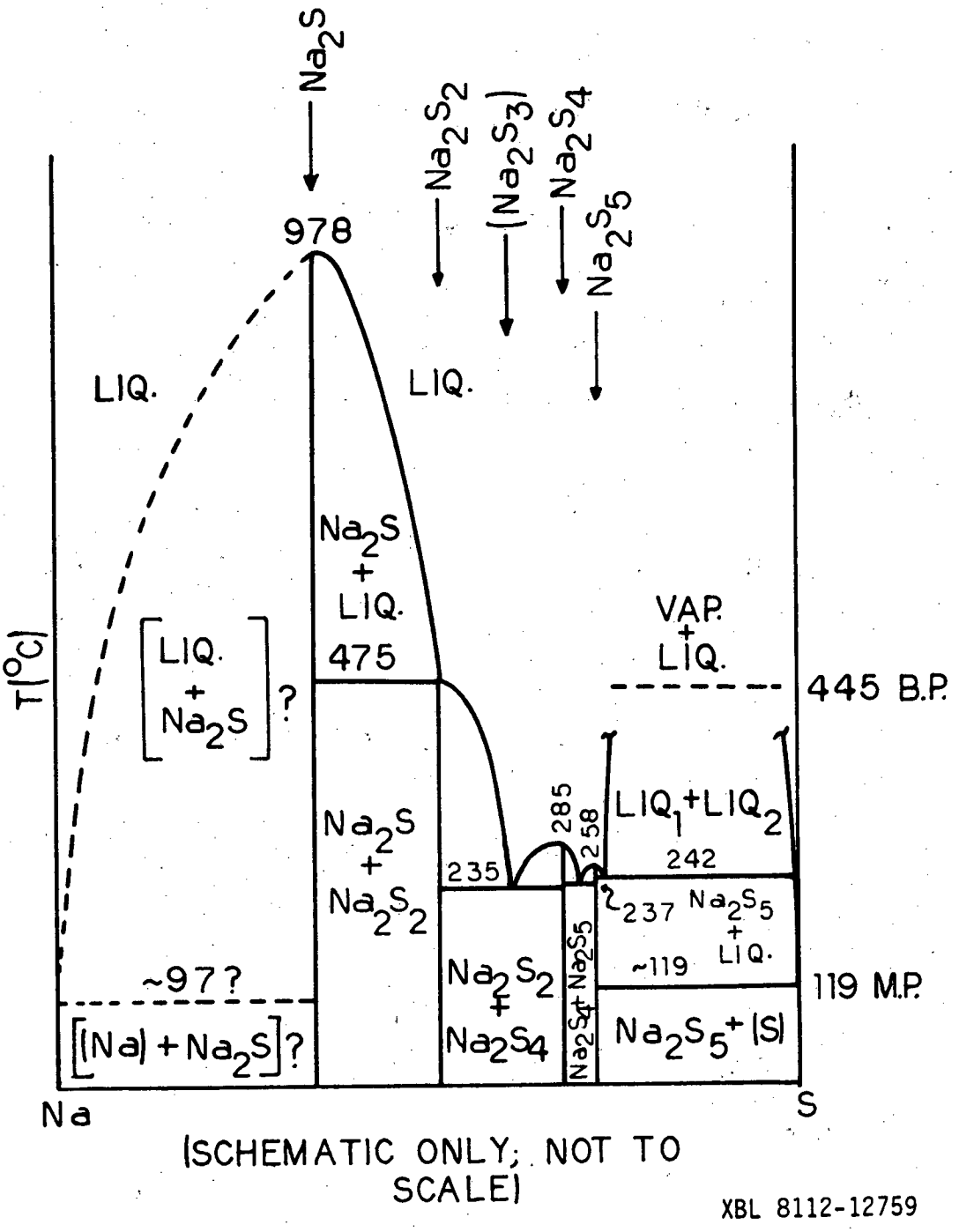

Fig. 1.4 Sodium-sulfur phase diagram.

obstacles to efficient economical construction and operation. Furthermore, as can be seen from the phase diagram, two immiscible liquids are present in the system between the pure sulfur and Na_2S_5 limits of composition. Na_2S_5 is almost totally insoluble in sulfur, and so the sulfur rich phase remains nonconducting through this entire composition range (the so-called two phase region of cell operation). Some compromises with ideal operation have to be made to arrive at a workable system.

If one chooses to operate from the eutectic point between Na_2S_4 and Na_2S_2 (usually referred to as Na_2S_3) to near the pure sulfur, a temperature of 300-350°C will suffice to keep all reactants in the molten state. By operating only between Na_2S_3 and Na_2S_5, one could avoid the problems associated with the production of free sulfur in the cell. This is not usually done because one then sacrifices too much energy density. In practice, the positive electrode reservoir is filled with an electronically conducting matrix of some form of carbon, usually a carbon fibre felt. This serves to facilitate electron extraction and to keep the sulfur dispersed in the positive electrode, so that it can react at a fairly rapid rate even near the fully charged state. By careful design of this positive current collector, experimental cells have been successfully operated well into the two phase region without the formation of layers of free sulfur which do not react readily. Such chemical polarizations have been responsible for progressive decline of the capacity in cells of an older design. If the positive electrode, at 350°C, is discharged much beyond the Na_2S_3 composition, solid Na_2S_2 will be formed, polarizing the cell and possibly cracking the electrolyte.

In the negative electrode the sodium metal is highly reactive, and any cell must be hermetically sealed to prevent rapid and violent oxidation by contact with the atmosphere. Sodium/oxygen chemistry is indirectly important to cell operation as well. The partial pressure of oxygen in equilibrium with liquid sodium and Na_2O at 350°C is on the order of 10^{-60} atm. Nevertheless, as can be seen from Figure 1.5 (after El 65 in which curves are referenced: 1. from Tr 55; 2. from No 58), the solubility of oxygen in sodium is surprisingly high (about 250 ppm by weight) at 350°C. So unless extreme measures are taken, sodium is likely to be partially or completely saturated with oxygen when introduced to the cell; consequently, precipitation of sodium oxide in the negative electrode compartment could occur on discharge.

On the basis of these properties of the sodium/sulfur system, the following points should be noted for future reference in judging battery performance and problems.

1. Polarization is likely to arise as a major problem owing to:
   a) production of nonconducting free sulfur in the positive electrode, over a large portion of the operating cycle.
   b) the possibility of forming solid Na_2S_2 in the positive electrode, if discharge is carried beyond Na_2S_3.
   c) the possibility of forming a nonconducting layer of sodium oxide at the sodium electrode/electrolyte interface.
2. Inhomogeneity in the system may retard the establishment of equilibrium, and lead to unusual local effects which could accelerate cell degradation.

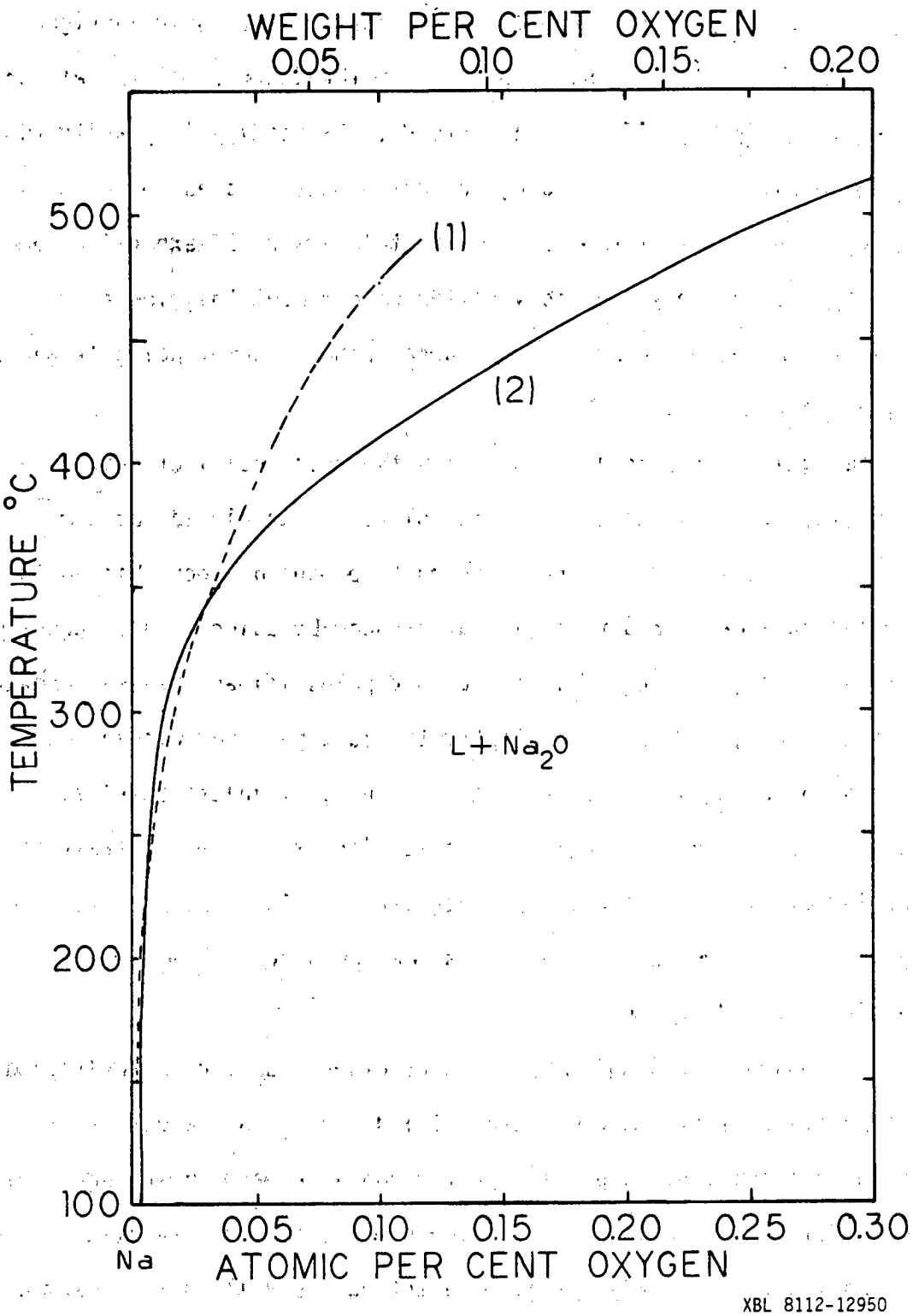

Fig. 1.5 Solubility of oxygen in liquid sodium.

1.4 The Engineering and Design Problems of the Sodium/Sulfur Cell.

A schematic of an actual sodium/sulfur cell is shown in Figure 1.6. In this scheme, the sodium is present in the interior of the electrolyte tube and the sulfur on the outside. The sodium is gravity fed into the tube from a reservoir, generally made of steel or aluminum, located at the top of the cell. A certain amount of expansion space is provided in the sulfur/polysulfide compartment to allow for the volume to be occupied by the increasing proportion of polysulfides as discharge proceeds.

Several design problems exist for the positive electrode. The necessity of a carbon felt current collector has already been mentioned. An electrical connection must be made between this collector and the external circuit. This can be done by using a metal container for the positive electrode. Sulfur and polysulfides are very corrosive at 350°C, and so a resistant metal must be found within the constraint of economical fabrication. Ordinary stainless steel is attacked very severely, but the application of a more resistant metal coating can make its performance acceptable. Chromium plating, properly applied, is one approach that has met both durability and cost requirements (Mi 78, p. L-12).

Corrosion is a problem for reasons other than the destruction of the positive electrode container. Solid corrosion products may build up to an insulating layer between the container and the current collector. Soluble corrosion products may degrade cell performance by contaminating the sulfur/polysulfide electrode as well as the ceramic electrolyte.

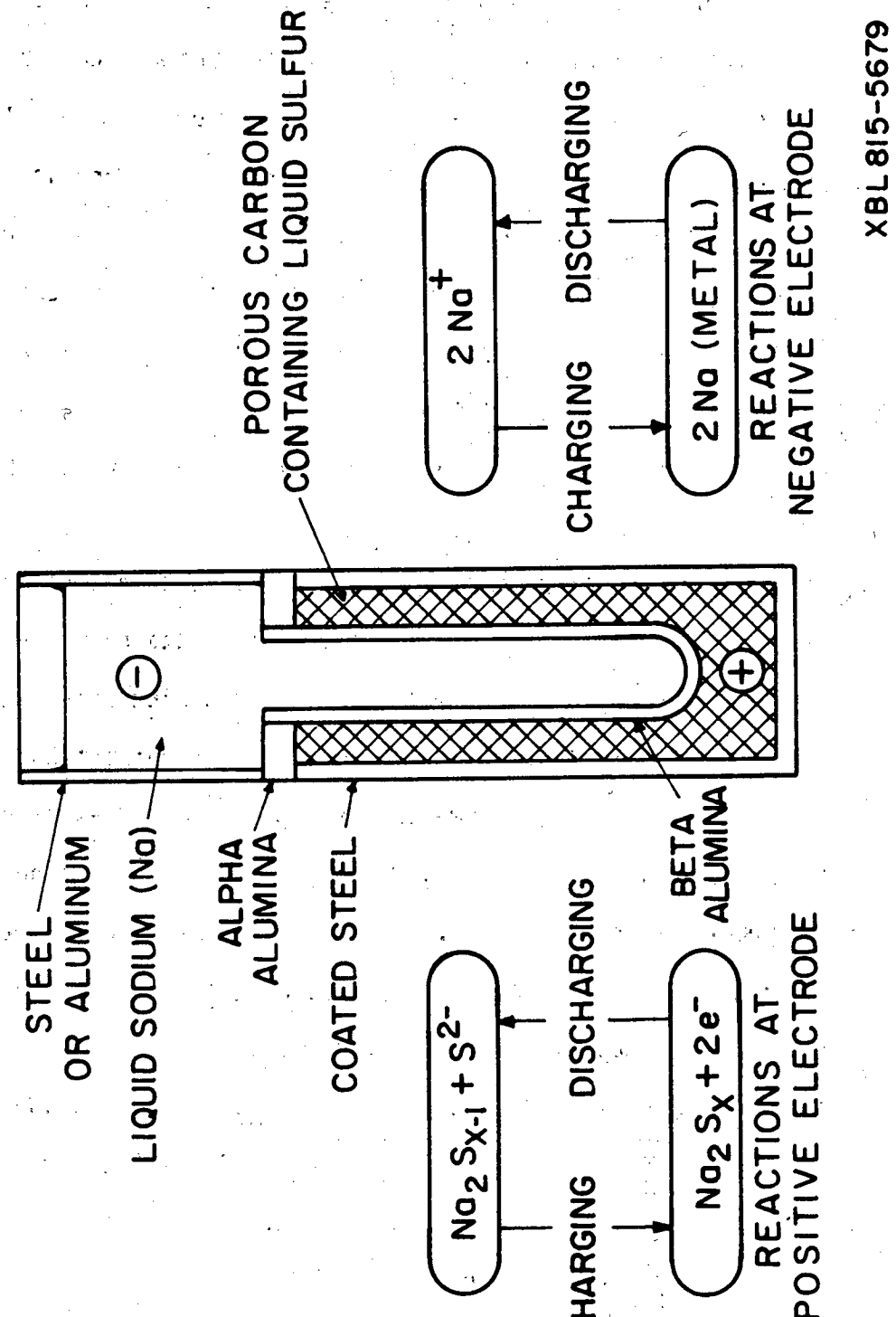

Fig. 1.6 Schematic cross section of the sodium/sulfur cell.

It is possible to reduce the container corrosion problem by designing the cell with the sulfur electrode on the inside of the electrolyte tube. This design is used almost exclusively on cells produced in England by British Rail Corporation. One must still make good electrical contact with the current collector; but, as a much smaller electrode is required for this than for a container, it is economical to use more resistant materials such as molybdenum. Gravity feeding of sodium to the electrolyte surface is more difficult in this design. A capillary feed is usually employed utilizing metal gauze as a sodium wick. The capillary feed, which could also be employed in the sodium-inside design, has the advantage that the cell can be operated in any position.

Some problems are common to all designs. A certain amount of expansion space must be present in the cell at full charge to accommodate the larger volume of the polysulfides formed during discharge. This amounts to some 40% of the volume of the sulfur compartment (Jo 77). Some current collector materials degrade, as a result of the expansion-contraction occurring during the normal cell operating cycle, causing a loss of capacity (Ch 80). Seals must be made between the insulating header and the electrolyte and between the header and the containers. The reliability of these seals is critical, and one of the principal reasons for a tube electrolyte design rather than, say, a flat plate electrolyte design, is the much smaller seals required in the tube design relative to cell capacity. The headers themselves, usually alumina, must be resistant to corrosion, and some types of alumina have been found to be subject to attack by sodium (Mi 78). The minimum operating temperature of the system is about 320°C, because

even though all phases are molten above 285°C, low diffusivity of the sulfur leads to undercharging below 300°C (Iw 80). Insulation must be provided around the cell to conserve the heat required to maintain all reactants in the molten state, and some method of supplying heat for initial startup and for restarts must be provided also. In normal cell operation, heat generated during discharge and recharge by the inherent inefficiency of the cell will keep the system in a molten state, and it may in fact be necessary to provide some means of cooling at certain times in the operating cycle.

The respective wetting characteristics of sulfur and polysulfides are just about the reverse of what is desired. Sulfur preferentially wets the carbon felt, and polysulfides preferentially wet the metal surfaces. This can lead to an effective blocking of the reaction surface of the felt when the cell is in the two phase region of operation. The use of a metallic current collector instead of carbon felt would actually be preferable because of this, but economic practicality excludes those choices which are suitably resistant to corrosion. Several methods of improving the wetability of the felt have been tried experimentally. Adding about 500 ppm of Fe_2S_3 improves wetting of the felt by the polysulfides, and results in an increase in cell capacity, but at the cost of an increase in cell impedance developing during the early stages of cell cycling. Other techniques are also being tested in an attempt to improve the wetting characteristics of the carbon felt. For instance, if the felt is soaked in a solution of aluminum nitrate and then baked at 1000°C, a porous deposit of aluminum oxide remains which acts as a wick improving the wetability of the felt (Fo 77, p. 13-40). It has even been suggested that it might be

worthwhile to introduce a system to circulate the sulfur-polysulfide melt, but it is unlikely that the expense and bulk of such a system would be offset by the improvement in operating efficiency.

When the cell is recharged, the natural tendency is for sulfur to form first on the positive electrode/beta alumina interface. The formation of this layer must be supressed, or the charge process will be inhibited. One way this problem has been handled is by introducing a resistance gradient in the carbon felt. A lower density (and thus higher resistance) felt is used adjacent to the electrolyte surface. x-radiography studies of actual cells, made at various points in repeated operating cycles, have shown that sulfur is not formed in the region filled with the higher resistance felt, even near full charge (Mi 78 pp. C-10, J-19).

This brief survey of design problems and some methods which have been used for their solution is far from exhaustive. But then design problems are of importance in this study only as they relate to the reliability of the beta alumina electrolyte. Characteristics of electrolyte degradation and the models proposed to explain it thus far will be treated in considerable detail in the next chapter. The design considerations covered here suggest that the following factors can be significant in the electrolyte degradation process:

- Contamination of the electrolyte by corrosion products from the containers, seals, or current collector, or by impurities originally present in the reactants.
- Current inhomogeneities in the electrolyte due to the geometry of the current collector or alteration of its geometry through

degradation, or to unfavorable distribution of non-conducting phases (free sulfur, or solid Na_2S_2 or Na_2S).

- Corrosive effects of the reactants or seal materials on the electrolyte.
- Local electrolytic effects arising from inhomogeneities in the sulfur electrode, especially at points of contact between the electrolyte and the carbon current collector.
- Mechanical degradation at the seals due to thermal cycle fatigue, possibly combined with chemical effects.

1.5 Failure Modes.

There are three observed modes of failure in operating sodium/sulfur cells. The first is sudden and catastrophic and is caused by rupture of the electrolyte tube or failure of the seal between the two compartments of the cell. In either case, the cell is short circuited internally and violently destructs. The second is a sudden failure of the cell to accept a charge or to deliver power, usually caused by severe polarization in the sulfur electrode. The third is a gradual increase in cell internal resistance reducing the power capacity and overall efficiency of the cell. In the succeeding chapters of this thesis, degradation modes in the electrolyte will be considered and their contribution to cell failure or decline in performance assessed.

2. ASPECTS OF ELECTROLYTE DEGRADATION

2.1 Physical Characteristics of Degraded Electrolytes.

Examination of electrolyte tubes removed from many cycled sodium/sulfur cells has shown that the electrolyte may undergo a number of changes during cell operation. A diffuse darkening of the electrolyte, slowly propagating into the ceramic from the surface in contact with liquid sodium, is invariably detected in cells after a few days. Frequently, sodium filled dendrites are found in the electrolyte or appear to have initiated and grown from the surface in contact with the sodium. These dendrites sometimes extend through the entire thickness of the electrolyte in cells which have been operated for extended periods of time and/or have failed. In cells which have failed catastrophically, the electrolyte is extensively cracked and even fragmented.

Pitting and pinhole corrosion of the electrolyte surface has been observed in electrolytes from cells cycled extensively. It appears first on the sodium surface of the electrolyte but is eventually found on the sulfur side as well (Iw 80). Local corrosion or imprinting (see Chapter 6) is found where the carbon felt of the current collector in the polysulfide electrode contacts the electrolyte surface.

Finally, it is quite common to observe a gradual increase in the resistivity of the electrolyte during cell operation. An increase in the internal resistance of the cell may be largely or wholly due to polarization phenomena, and therefore is not always an indication of a true increase in electrolyte resistivity. Still, even when polarization is taken into account, there appear to be true increases in the

resistivity of the electrolyte which can probably be attributed to chemical changes occurring in it during cell operation, or to incorporation of detrimental impurities into the electrolyte from the electrodes.

2.2 Causes of Degradation

2.2.1 Intrinsic Stability of the Electrolyte.

An examination of the sodium-aluminum oxide phase diagram (Figure 2.1) in the range where the beta aluminas are found will show that it is reasonable to expect that beta aluminas in contact with molten sodium may show some decomposition into sodium aluminate. Weber noted this possibility but failed to find any evidence for its actual occurrence in beta" alumina electrolytes which had become severely darkened in experimental heat engine service with operating temperatures as high as 900°C (We 74). It is occasionally reported that x-ray diffraction reveals a slight decrease in the [c] lattice parameter in electrolytes which have been in contact with sodium in operating sodium/sulfur cells, but no evidence for second phase formation (Iw 80). It is well documented that cation exchange of Na^+ can readily convert one form of beta alumina into another (Ku 72), and so any exchangeable impurities in the molten electrodes can be expected to readily enter the conduction planes. The differing mobilities and ionic radii of entrant impurities will necessarily affect the lattice parameters and resistivity of the electrolyte (Bo 77). A few impurities, such as lithium and possibly magnesium, may enter either the conduction planes

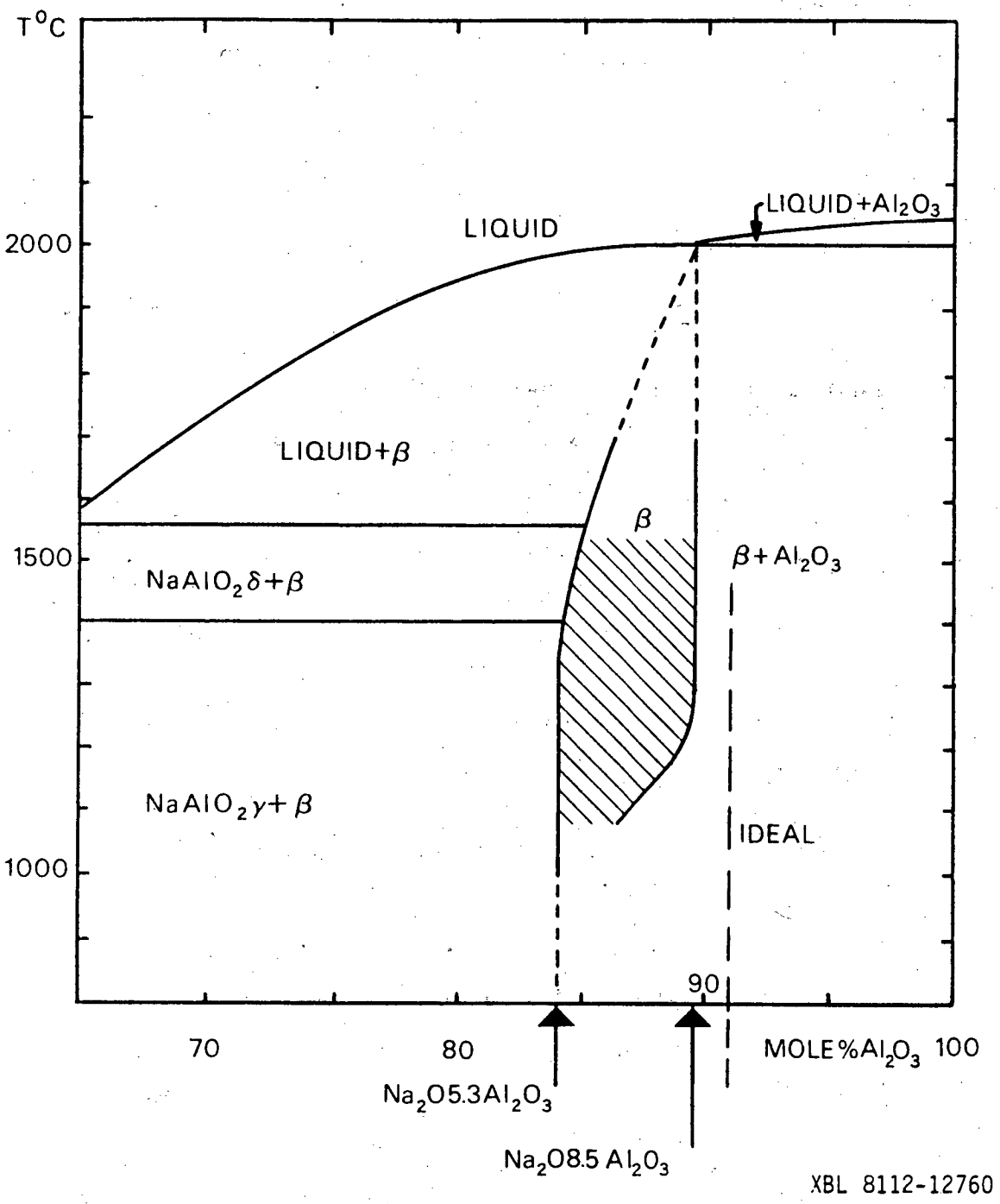

Fig. 2.1 Proposed phase diagram of Na_2O-Al_2O_3 system in the region of existence of beta alumina phases. Shaded area represents region of coexistence of beta and beta" phases.

or the spinel blocks, but most other elements will not enter the spinel blocks at cell operating temperatures.

While no detectable second phases are formed when the beta aluminas are in contact with molten sodium at temperatures up to 900°C or so, it is clear that some change in the electrolyte does take place to produce the darkening which occurs under these conditions. In the absence of evidence for second phase formation, point defects may be suspected as the cause of darkening. It has been reported that an elevated concentration of sodium develops in electrolytes in the region near the electrolyte/sodium interface (Ch 80).

No observable changes have been reported to occur in beta aluminas in simple contact with molten sulfur or polysulfides. Degradation occurring at the polysulfide/electrolyte interface must therefore be explained in other terms. Impurities introduced with the sulfur or by corrosion of the container, or carbon felt interacting with the electrolyte in cell operation, and the effects of contact of the carbon felt with the electrolyte have to be ranked of greatest importance in formulating explanations of degradation.

When an electric field is applied to a beta alumina polycrystalline electrolyte, an ion current will flow in every grain so oriented that there is a component of the local electric field perpendicular to the [c] direction. If a source of ions exists at the positive terminal, and a sink for them at the negative terminal, then the current flow will continue. If these conditions do not apply, that is if ionically blocking conditions exist, then the current will decay as a charge separation occurs at the blocking interface(s). The potential drop associated with the applied field will be opposed by the field in this

charge separated layer. Since the separation of charge at this interface is small, the field strength will be relatively large; and therefore application of modest potentials may be sufficient to cause breakdown.

The existence of a sufficiently strong electric field anywhere in the beta alumina will cause breakdown by one of a number of possible modes. Beta aluminas are wide band gap insulators. Direct electronic breakdown in such materials usually requires fields on the order of 10^9 V m^{-1} to sustain electron avalanche effects or to generate sufficient electromechanical stress to initiate fracture. It is further necessary that the field, E, exist over a region of width, δ, such that δ E >> V_g, where V_g is the electronic bandgap, or no breakdown will occur. This condition would not normally be encountered in cell operation.

It is rare that any insulator fails due to intrinsic electronic avalanche breakdown. It is usually impurity content or local conditions of geometry or composition that facilitate breakdown in applied fields. The electronic bandgap in beta alumina is estimated to lie between 9 and 11 eV (Sh 77), so that direct electron injection or thermal activation of electronic carriers is difficult. But the presence of defects or impurities in the material will create donor or acceptor states in the bandgap, and increase the electronic component of conductivity. If appropriate conditions exist when both ionic and electronic currents are flowing in the electrolyte, electrons may combine with sodium ions internally resulting in the deposition of metallic sodium under pressure in the electrolyte.

Electric fields in the electrolyte and at its surface can be influenced strongly by conditions of local geometry. Interfacial polarization, mutual misorientation of crystal axes between adjacent grains, foreign inclusions at grain boundaries, are a few of the more important geometric effects that may intensify the electric field in the electrolyte leading to discharge and breakdown. The concentration of current associated with such fields may further contribute to degradation through the establishment of extreme local temperature gradients.

2.2.2 Electromechanical and Related Effects

The first analytical approach to the failure of beta alumina ceramic by dendritic penetration was proposed by Armstrong, Dickenson and Turner (Ar 74). In their model, pre-existent cracks or pores in the surface of the ceramic are extended by stress generated by the capillary back pressure of sodium flowing out of the narrow flaw. This will be referred to as mode I failure following De Jonghe, et al. (De 81a). In sodium/sulfur cell operation, sodium is cathodically deposited into cracks at the sodium/electrolyte interface during the recharge cycle of cell operation. Armstrong, et al. offered a very simple analysis in which a typical crack was modeled as a hemispherically capped circular cylinder perpendicular to the electrolyte surface. The conclusion reached was that the crack length would increase exponentially with respect to time; but that relaxation of the stress in the crack, following fracture and crack extension, would moderate the process somewhat, so that immediate penetration of the ceramic would not occur.

Armstrong, et al. offered some experimental support for the dendritic growth mechanism of failure. Sodium/sodium cells constructed with electrolytes having polished, or polished and glass filled surfaces (to reduce initial crack population), were shown to have longer lifetimes than those constructed with as-sintered electrolytes. A large scale analog mechanical model, constructed to electrically simulate penetration of the electrolyte by metal-filled dendrites, showed resistance versus time behavior similar to an actual sodium/sodium cell for a uniform rate of advance of the simulated "dendrites", except at early time. The initial behavior of the actual sodium/sodium cell showed very little resistance change for a time as would be expected if crack growth rate were actually exponential.

Back pressure generated by the flow of a viscous fluid in a confined channel is described in fluid mechanics by the Poiseuille law. It is customary to refer to pressures so generated as Poiseuille pressures.

Further refinements in the analytical treatment of the process of dendritic penetration have been offered by a number of people. The original treatment of Armstrong, et al. was only semiquantitative in character and included no calculation of a degradation threshold or critical current density below which degradation would not be expected to occur. In addition, current focusing, which would occur at the tip of a metal filled crack in the ceramic, was only implicitly included in their preliminary treatment. Richman and Tennenhouse (Ri 75) took a slightly different approach by replacing the circular cylindrical crack geometry with a more realistic flat rectangular one, by considering the role of possible solute fluxes and stress corrosion in

the crack as the major cause of crack growth, and by making an explicit estimate of the current focusing effect at the crack tip. The groundwork was thus laid for a stress-corrosion model of crack enlargement at subcritical tip fracture stress which predicted a critical current density for crack growth. The calculation of this critical current density was possible, and could be reconciled with experimental data (Te 75) through assumptions about electrolyte solubility and suitable choice of adjustable parameters.

However, the choice of adjustable parameters, especially crack width, has been criticized as unrealistic in view of the fact that crack width and Poiseuille pressure within the crack are interdependent quantities (Sh 78). Furthermore, delayed fracture tests done to evaluate the degree to which stress corrosion is operative in the deterioration of the beta aluminas have either indicated no evidence of stress corrosion (Da 79a), or a small effect which can be virtually eliminated by favorable choice of electrolyte composition (Sh 78, Li 79). Shetty, et al. (Sh 78) have pointed out that the delayed fracture tests may not provide valid evidence for discounting the operation of stress corrosion mechanism under conditions of electrolytic cycling, but it can still be said that no convincing evidence has been produced thus far to establish stress corrosion as a significant factor in the electrolytic breakdown of beta aluminas.

A more refined development of the original Armstrong model was made by Shetty, et al. in which crack entension was taken to occur only when the Poiseuille pressure in the crack exceeded the critical (Griffith) fracture strength. From an initial assumption of a linear

increase in pressure from crack opening to crack tip, a self-consistent crack shape profile was calculated by an iterative procedure. The calculated profile was nearly constant in width to about half the depth of the crack, and then the width decreased gradually to form a rounded tip. Applying the critical fracture concept to this crack shape, the authors calculated a critical current density of about 1500 A cm^{-2} for a crack initially 25 μm in length. Previous experimentally observed critical current densities had been reported to be in the neighborhood of 1 A cm^{-2} representing quite a discrepancy.

The treatment of Shetty, et al. was in need of some further refinement. The actual current density distribution around the crack was not calculated, and without such a calculation the effect of current focusing can only be estimated. The actual current density will affect the pressure distribution in the crack, and this will in turn affect the shape, so that all three quantities are interactive. The primary current distribution around the crack can be found, if its geometry is known, by solving Laplace's equation for the system. A further complication enters the calculations because, as pointed out by Brennan (Br 80b, Br 80c), an electrochemical counter potential is generated in sodium under pressure. Thus, there are at least four interdependent quantities that must enter the calculations if one desires to obtain the true, or secondary, current distribution around a crack in the ceramic. A complicated iterative procedure would have to be used to assure attainment of the desired accuracy in solving this problem.

Feldman and De Jonghe (Fe 81) of this group approach the problem by solving Laplace's equation to calculate the primary current distribution around the crack. They choose an elliptical profile for the

crack which seems realistic in view of the crack shape generated by the more approximate treatment of Shetty, et al., and which makes the exact solution of Laplace's equation possible in terms of elementary functions. The dependence of crack opening displacement as a function of current distribution is also included in the analysis. This treatment gives critical current densities which are even larger than those calculated by Shetty, et al. The existence of a pressure gradient induced electrochemical counter-EMF, as suggested by Brennan, would tend to counteract somewhat the effects of current focusing and lead to still larger critical current densities.

Modification of the theories, holding that extension of pre-existent cracks by Poiseuille pressure is solely responsible for degradation of beta alumina solid electrolytes, must clearly be made if the predicted critical current densities are to be reconciled with those actually observed in practice.

Virkar, et al. (Vi 80) proposed that the discrepancy could be reconciled by considering the current concentrations which will develop around unwetted areas or other current blocking conditions. Such concentrations may be one or two orders of magnitude larger than the average current density in the bulk of the electrolyte. Evidence in support of their proposition is cited from experiments done at room temperature in which breakdown was reported to be initiating at the edges of simulated unwetted regions at the sodium exit surface of the electrolyte. However, lack of correspondence between the results of room temperature and high temperature experiments done by Feldman and Buechele (De 80d) brings into question the validity of extrapolating

results from room temperature experiments into the temperature range above the melting point of sodium.

But a more serious objection to the proposal of Virkar et al. can be offered on the basis of calculations done by Feldman, et al. (Fe 81) of the actual size of zones of current enhancement around blocking obstacles. These calculations were made by solving Laplace's equation exactly for blocking flaws or unwetted regions of realistic geometry and dimensions. The calculated sizes of zones of significant current enhancement are much too small to play an important role in growth of any flaws.

Perhaps of greater merit in helping to reconcile the discrepancy between calculated and observed critical current densities is the work of Brennan (Br 80b) which predicts that small changes in the interfacial transfer resistance at the sodium/beta alumina interface produce large changes in critical crack geometry. The prediction is supported in part by the observation that cells in which polarization develops fail prematurely (Br 80a), but a quantitative assessment of the contribution of polarization phenomena to the breakdown process has not yet been made experimentally. The incorporation of impurities from the melt into the ceramic or the deposition of a sodium oxide layer on the ceramic due to oxygen dissolved in the sodium are probably the likely ways that interfacial charge transfer resistance would be increased. Modification of the surface layer of the ceramic by water absorption before cell assembly is also a possible cause; although, in this case the modification would probably cease to have much effect after the crack had propagated beyond the surface of the electrolyte. Other factors certainly contribute to inhomogeneities in the local

current density which make a precise calculation of critical current densities for crack propagation difficult. One of these is the high anisotropy of conductivity in beta alumina itself. In solving Laplace's equation to calculate the primary current distribution around a crack, the assumption is made that one is dealing with an isotropic conductor. As long as the crack is large compared to the average grain size in the electrolyte, this is a reasonable assumption. But even in a long crack, the radius of the tip is usually well under one micrometer, and average grain sizes in high quality electrolytes are rarely less than 1 micrometer. This means that in the region of the crack tip, where the most critical effects of current focusing occur, the actual current distribution is subject to wide variation. Some grain geometries and mutual orientations will be very favorable for feeding current to crack tips, to very small cracks, or to grain boundaries; and others may limit such current flow severely.

The anisotropy certainly must also lead to local variation in the critical stress intensity factor, K_{IC}, so that cracks in some regions may start to grow at much lower relative current densities, until they arrest in regions of high local K_{IC}. It is observed, for instance, that single crystal beta alumina cleaves through its basal planes at a much lower stress than is required to fracture the polycrystalline ceramic. The grain boundaries can also be expected to have widely varying strengths according to the mutual crystal axes orientations of adjacent grains. Impurities or second phases, present at grain boundaries, will further aggravate such variation in strength. These variations may contribute to deflection and branching of the crack network, further complicating the treatment of propagation of breakdown which,

so far, has only been done for a single crack propagating parallel to the current flow. Branching may slow the progress of the crack network by dividing the available current among several crack tips, while deflection of a single crack may accelerate crack progress because one side of the crack will be more effectively fed by the current.

2.2.3 Modifications of the Electromechanical Breakdown Theory. Mode I Versus Mode II Breakdown

Even when all the above factors are taken into account, however, there still seems to remain quite a discrepancy between the calculated and observed critical current densities. This discrepancy led Feldman, et al. (Fe 81) to propose that the critical stress intensity factor, K_{IC}, for mechanical testing, which is employed in the calculations of critical current density, is not the same one which applies in electrolytic degradation. They cite the observation of De Jonghe, et al. (De 79a) that the crack tip radius can be as small as 10 Å, which would lead to a local field at the crack tip of 10^5 V cm^{-1} for a crack length of 10 μm at an average electric field intensity of 10 V cm^{-1} in the bulk of the electrolyte. The high field in the vicinity of the crack tip could lead to a substantial degree of local electron injection which would increase the electronic conductivity of the ceramic in this region. Under these circumstances, sodium may deposit in the ceramic under pressure just ahead of the crack tip. This result of electrolytic cycling may modify the mechanical properties of the ceramic to produce an effective critical stress intensity factor, K_{IC}^{Eff}, which is much lower than the K_{IC} determined by simple mechanical testing.

The proposed modification of the ceramic around the crack tip by electron injection, leads to a local electronic conductivity gradient which may make possible the neutralization of sodium ions and the deposition of sodium metal under pressure within the bulk of the ceramic. The possibility of a similar process occurring as a result of an electronic conductivity gradient induced by chemical modification of the beta alumina through contact with liquid sodium, has already been mentioned. The work done for this thesis has produced substantial evidence for degradation by internal sodium deposition, and has led De Jonghe, et al. (De 81a) to propose that degradation by this mechanism be referred to as mode II degradation. Mode I degradation would be the mechanism described above in which Poiseuille pressure, due to cathodic deposition, propagates individual cracks. Further comment on the nature of mode II behavior will be made in Chapter 6 of this thesis where evidence for its operation will be presented.

2.2.4 Possible Current Induced Thermal Effects

A resistive heating effect will occur in the electrolyte as current flows through it. In operation of the sodium/sulfur cell, part of the heat produced will serve the useful purpose of keeping the reactants in a molten state. But in view of the probable large variations in current density and of severe local anisotropy in the electrolyte already discussed, local I^2R heating should be examined as a possible source of differential thermal expansion which may itself produce cracking and electrolyte failure. The beta aluminas have excellent resistance to thermal shock. Imai (Im 80) reports a critical temperature step for thermal shock failure of about 300°C. His results were

obtained by quenching samples from elevated temperatures in kerosene at 20°C and recording the minimum temperature difference which produced a decline in fracture strength due to cracking. In a rectangular slab or electrolyte 2 mm thick whose surfaces are held at 350°C, simple calculations show that a current density of between 50 and 100 A cm^{-2} would be required to maintain a temperature at the center of the slab which was 300°C above that at the surface. Under normal operating conditions of, say, 0.1 A cm^{-2} average current density, the temperature in the center of such a slab will be only about 0.003°C above that of the surface. A calculation, which is outlined in Appendix 1, was done for a "worst case" situation of current focusing into a crack 20 Å wide and 100 μm long using a simplified geometry in which Poisson's equation could be easily solved. The current density at the tip of such a crack, when the average current density in the electrolyte far from the crack tip is 0.1 A cm^{-2}, would be on the order of 10^4 A cm^{-2}. The calculation predicts a temperature maximum of only a fraction of a degree above the temperature at the crack tip and at a distance of about 0.3 μm from the tip into the electrolyte. This result indicates that it is highly unlikely that current induced thermal stresses will produce failure at normal operating current densities.

2.2.5 Contribution of the Polysulfide Electrode to Breakdown

Extensive work has been done on development and optimization of the polysulfide electrode. These studies can be broadly divided into two categories: those relating to the properties of the polysulfides and their electrochemistry (Ar 75, Cl 73a to e, Gu 72, So 72), and those relating to the design and operation of the polysulfide electrode

(Br 79a to d, Gi 74, Ka 76). No studies have appeared of the effects of the design or operation of the polysulfide electrode on the beta alumina electrolyte, largely because very few effects have been claimed. Those effects which have been reported, imprinting from the carbon felt (Fo 77), minor cracking (Fa 73b), and pinhole pitting and corrosion (Iw 80), have not been considered to be a serious enough threat to acceptable cell lifetimes to warrant any sort of extensive examination and study. But it could simply be that other more serious cell problems have limited cell lifetimes to an extent which has not permitted the sulfur electrode problems to develop sufficiently to need consideration. Clear signs of electrolyte degradation at the polysulfide electrode/electrolyte interface have been observed and studied in the course of the work done for this thesis.

2.3 Objectives of this Work

The following objectives were formulated:

- To examine carefully electrolytes removed from commercially produced and cycled sodium/sulfur cells; and to search for evidence of chemical modification from contact with liquid sodium, for evidence of Mode II breakdown, for evidence of sulfur surface degradation; and to characterize these phenomena.

- To study the chemical modification produced by contact of beta alumina electrolytes with molten sodium.

- To explore the feasibility of using acoustic emission monitoring to determine the critical current density for the onset of mode I more accurately, and to use this method to evaluate the dependence of that critical current density on electrolyte average grain size.

3. MATERIALS AND GENERAL EXPERIMENTAL METHODS

3.1 Materials and Equipment

Polycrystalline electrolytes used in these experiments were in the form of tubes of lithia stabilized sodium beta" alumina manufactured by Ceramatec of Salt Lake City, Utah. The approximate dimensions of the tubes were 200 mm long by 15 mm inside diameter with a wall thickness of about either 1.3 mm or 1.6 mm. The composition of the tubes was specified by the manufacturer as 8.85 wt% Na_2O, 0.75 wt% Li_2O, balance Al_2O_3. Three different microstructures were supplied by special request so that grain size effects could be studied. The tubes were stored under dry argon.

Large single crystals of sodium beta alumina, grown at Union Carbide, Linde Division, San Diego, California, were also used in the experiments. These were stored in an evacuated dessicator and cut up into smaller pieces as required.

Sodium for the experiments was ACS certified grade obtained from Fisher Scientific Company, Santa Clara, California.

Experiments requiring the use of molten sodium were performed in an argon atmosphere, maintained in a VAC HE 43-2 Dri-Lab glove box equipped with a HE-493 Dri-Train to hold the oxygen and water vapor levels in the argon atmosphere around the 1 ppm level. Precision sensors for oxygen and water vapor were not available; but in a standard, practical test 25 watt light bulbs with their glass envelopes removed were maintained in a lighted state for periods of a month or more without burning out, verifying that there were no more than a few ppm of oxygen or water vapor in the glove box. Furthermore, periodic

checks were made with a helium leak detector to insure the integrity of the seals and critical areas of the glove box. In spite of these precautions, the slow formation of sodium oxide around the molten sodium indicated the constant presence of some oxygen or water vapor. Most of this probably entered by diffusing through the neoprene gloves. Therefore it must be assumed that the sodium used in these experiments was saturated with oxygen. This puts the oxygen fugacity in the sodium metal at about 10^{-58} atm at 350°C.

3.2 Characterization of the Ceramatec Material

3.2.1 Fabrication

The fabrication of the lithia stabilized sodium beta" alumina tubes supplied by Ceramatec has been described in the literature (Mi 79). The green tubes are produced from a specially prepared powder of the proper composition by wet bag isostatic pressing at 55 KPSI (380 MPa) on a polished steel mandril. The green tube is then sintered for a few minutes at 1550°C and annealed for 1 to 2 hours at 1475°C. The tube is sealed in a platinum bag during sintering and annealing to prevent soda loss. Full conversion to beta" alumina only takes place during the sintering and annealing operation.

3.2.2 Microstructure

Tubes were supplied by the manufacturer both with a normal fine grain structure and, by special order, with abnormally large grain microstructures produced through high temperature annealing. The fine grain tubes are identical to those supplied to the Ford Motor Co. and

used by them in experimental sodium/sulfur cells. The specially treated large grain tubes were specified by the manufacturer to have average grain sizes of 300 μm, 150 μm, and 10 μm. All were examined carefully before being used to determine relevant microstructural and electrical characteristics. In the course of this examination it was found that the 10 μm average grain size material was essentially identical in microstructure to the fine grain material and both will be referred to hereafter as "10 μm" material.

Figure 3.1 shows cross sections of the various grain size tubes which have been polished and then etched for 15 to 60 seconds in boiling concentrated phosphoric acid. The grains in all of the specimens are platelet shaped with the sectioned surfaces of the grains showing aspect ratios of up to about ten.

It was clear that the "average grain sizes" of 300, 150, and 10 μm quoted by the manufacturer were not representative of the actual average grain sizes of the tubes. Therefore an independent assessment of microstructure was made by drawing several random lines on scanning electron micrographs of each specimen, counting the number of grain boundaries intersected, and dividing the total length of the lines by this number. This is not a rigorous determination of grain size since grain geometry was not taken into account, but is the average grain boundary spacing. The manufacturer's designations of the grain sizes as "300", "150" or "10 μm" will still be used nominally in this work to identify the various microstructures. These designations appear to be approximately correct in reference to the maximum grain dimension observed in the respective materials.

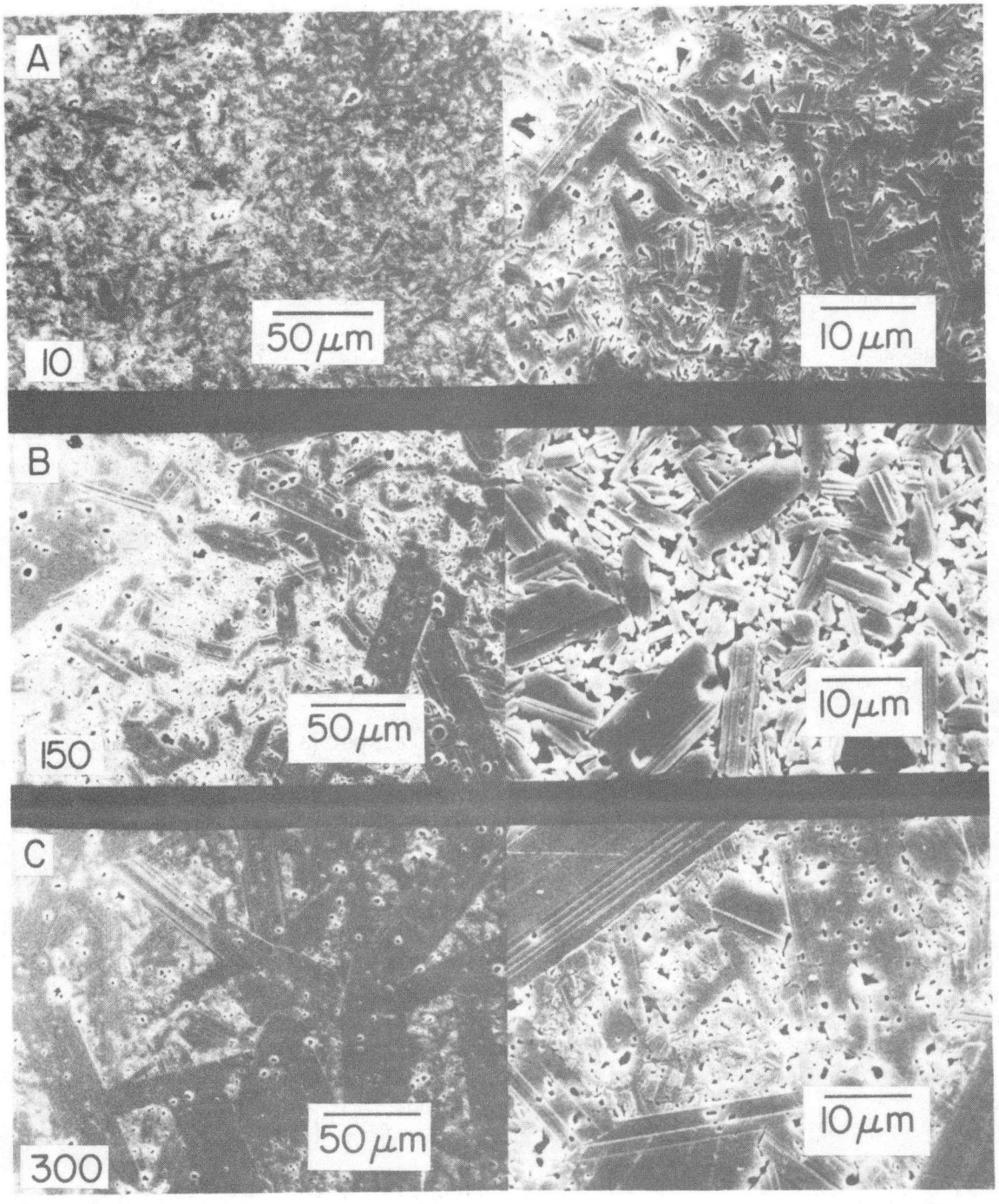

XBB 813-2321

Fig. 3.1 Low (left) and high (right) magnification views of polished etched electrolyte tube cross sections: A. "10 μm" B. "150 μm" C. "300 μm".

All of the microstructures are bimodal in grain size, although this is least evident in the "10 μm" material. The fine grain component of the "300 μm" material is nearly identical to the overall grain structure of the "10 μm" material. The fine grain component of the "150 μm" material is, on the average, larger than that of the "10 μm" material, and more equiaxed. The large grains in the "300 μm" material form a continuous network enclosing isolated regions of fine grain material, in contrast to the opposite situation in the "150 μm" material where the large grains are scattered throughout a continuous matrix of fine grain material. Table 3.1 summarizes the results of the microstructural measurements.

3.2.3 Surface Features

Since it has been postulated that surface features are especially significant in the initiation of breakdown, a special effort was made to find and record such flaws. The following characteristics were noted for their potential importance in the breakdown process. The outer surface of the tubes, especially that of the "10 μm" tubes, was significantly rougher and more highly populated with flaws than the inner surface (Figure 3.2A and B). Surface flaws consisted of: 1) cavities, usually about 3 to 10 μm across at the surface and extending about the same distance below the surface (Figure 3.2C), but occasionally extending much deeper (Figure 3.2D); 2) features appearing in crossection as if the surface had folded over on itself (Figure 3.2E), possibly arising from surface irregularities like the one shown in Figure 3.2F; and 3) curvature of the basal planes in some of the

Table 3.1

Microstructural Data for Beta" Alumina Electrolytes from Ceramatec

Nominal Grain size (μm)	10	150	300
Random line grain boundary spacing (μm)	1.1	5.4	5.2
Large grain fraction (longest dimension > 10 μm)	1%	59%	83%
Average large grain size (μm)	2.4	15.4	20.4
Average fine grain size (μm)	0.94	2.8	1.1
Average longest dimension of largest grain (μm) (measured on the 20 largest grains in a 200 μm square)	14.0	38.2	54.3

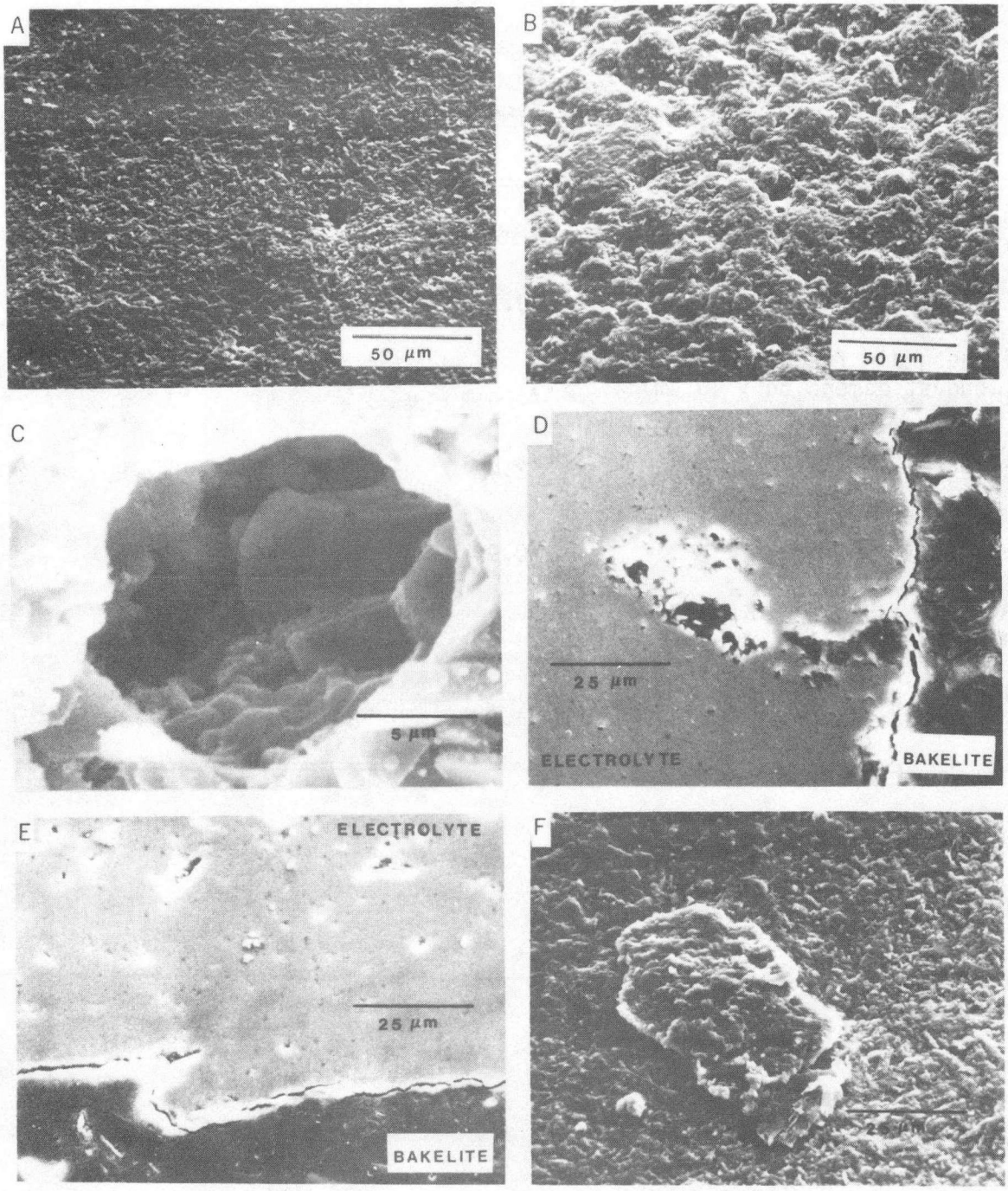

XBB 817-6530

Fig. 3.2 Surface features of "10 μm" beta" alumina tubes: A. inside surface B. outside surface C. cavity, inside surface D. cross section of deep cavity, outside surface E. cross section of "foldover" flaw, outside surface F. adherent agglomerate, inside surface.

grains near the surface (Figure 3.3). Note also that the grains near the surface are more uniformly small sized and equiaxed than those near the center of the tube. The roughness of the outer surface is probably due to the inability of the rubber bag used in the isostatic pressing operation to smooth fully the particle agglomerates that are present in the powder as it is poured into the mold. The "foldover" flaws are likely due to the compaction of especially large agglomerates in the tube surface. The curved grains near the surface may be caused by stresses generated near the surface during sintering. Loss or uptake of soda at the surface during sintering may be responsible for such stresses. A composition gradient over the tube cross section would result, and could account for the difference in microstructure at the surface and in the bulk. The tubes reportedly have a resistivity that is about 25% higher measured radially than measured axially, and the microstructural variation observed here is undoubtedly a contributing factor. It should be added that when polishing large grain size materials for microscopy, pullouts along the boundaries of large grains near the surface were fairly common (Figure 3.4) indicating that areas adjacent to large surface grains might be expected to act as sites of easy crack initiation. Evidence of enhanced breakdown at the boundaries of anomalously large grains near the surface in cycled electrolytes has been found and will be presented later, but the other surface flaws noted here have not been connected to consistent patterns of electrolyte breakdown in this or other studies so far.

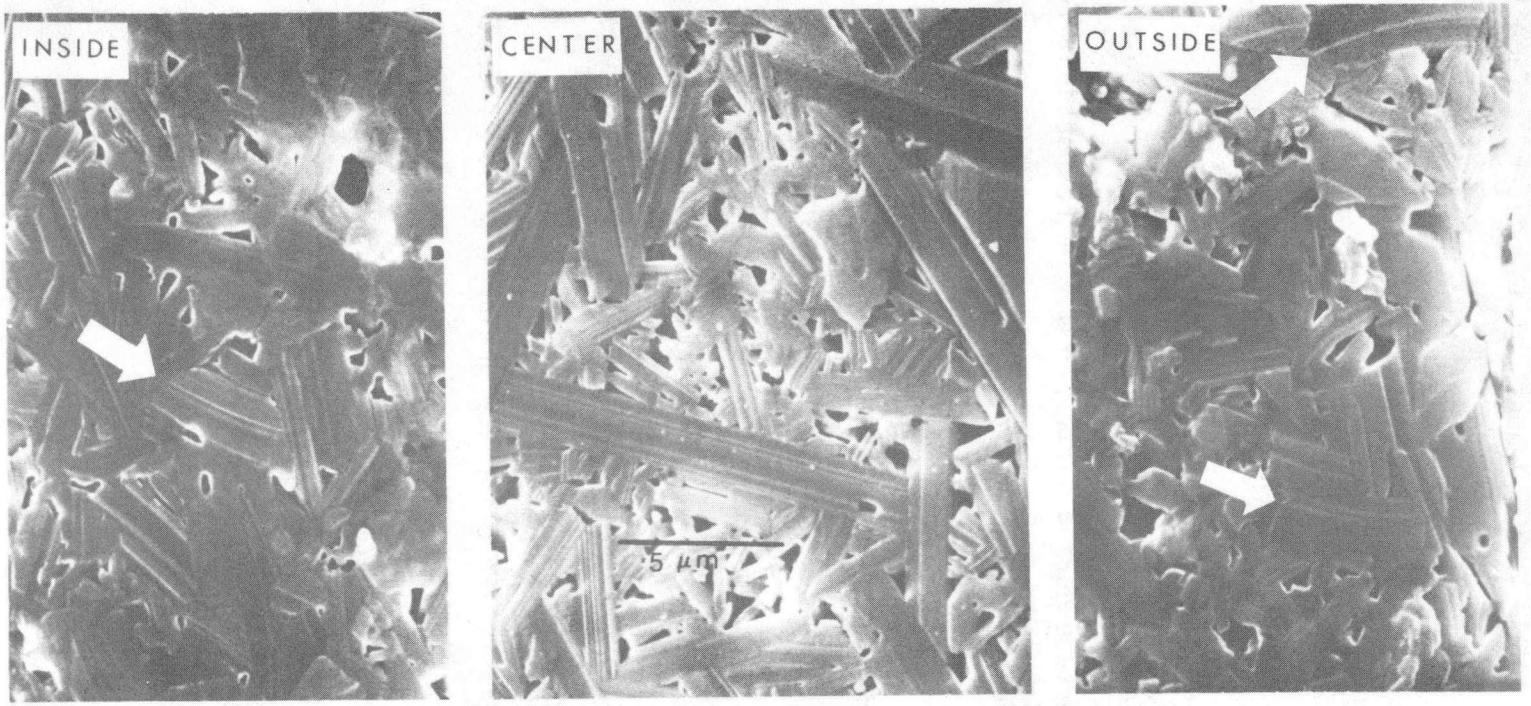

XBB 817-6526

Fig. 3.3 Details of surface and interior microstructures in "10 μm" material. Note curved grains.

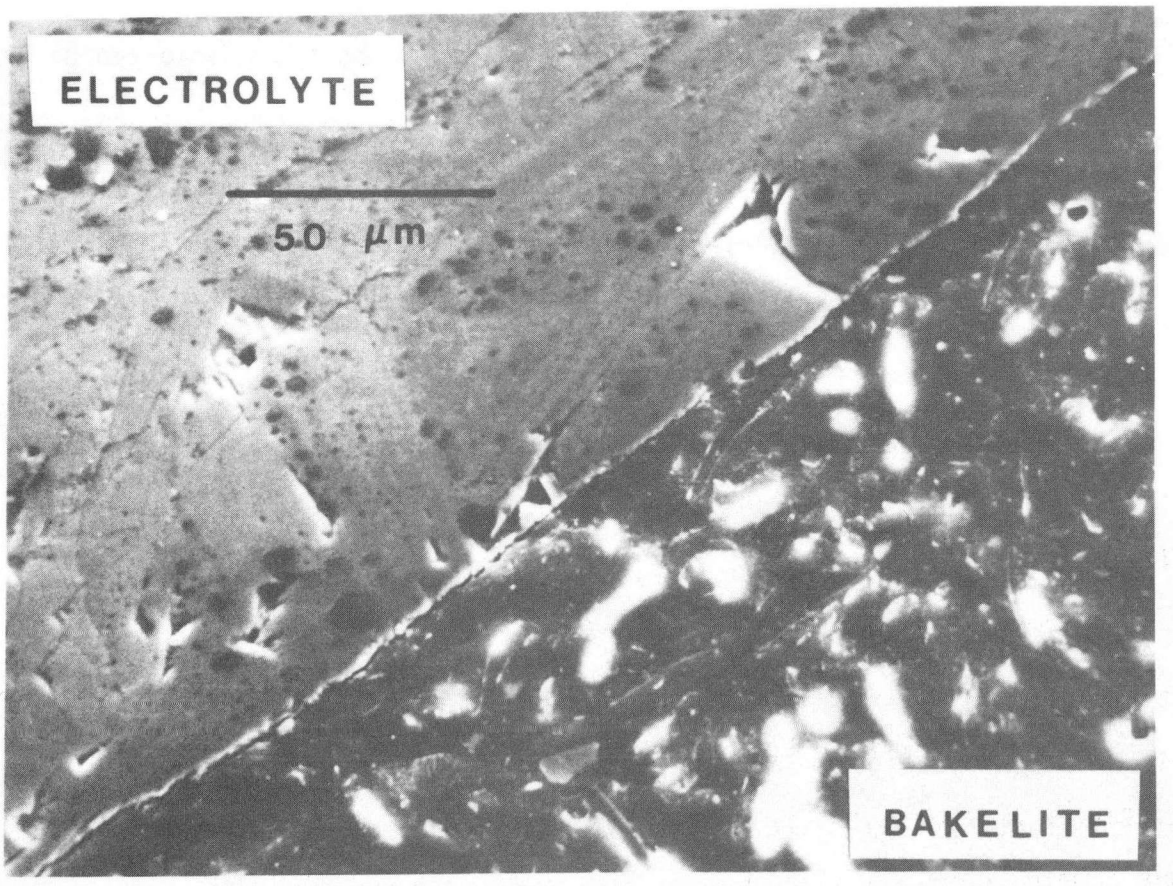

XBB 817-6531

Fig. 3.4 Pullouts from large grain boundaries near surface in "300 μm" material.

3.2.4 Internal Irregularities

In addition to these surface features, two types of interior voids were found: isolated single voids up to about 10 μm across (Figure 3.5A) and patches of small intergranular voids extending over regions about 5 to 50 μm in size (Figure 3.5B).

3.2.5 Electrical Properties

The complex conductivity of one of the tubes was measured by applying blocking gold electrodes to a sample cut from it and by employing a frequency sweep method discussed by the author elsewhere (Bu 78). A microprocessor control was designed to automatically step the frequency through 35 values from 1 hz to 10 Mhz at each of six temperatures from 50°C to 425°C. Figure 3.6 shows the curves generated from these measurements at 200°C, 275°C and 350°C. Here the rightmost intercept of the complex conductivity curve with the conductivity axis gives the D.C. conductivity of the sample. A calculation from the plotted data gives a resistivity value of 4.1 ohm cm at 300°C which compares favorably with the manufacturer's reported value of 4.5 ohm cm at that temperature. The activation energy is 5.14 kcal $mole^{-1}$. On inquiry, the manufacturer said that their measurements had also been done using A.C. techniques, but with sodium nitrite/nitrate eutectic electrodes at 300°C and at 30 khz or some other frequency in the uniform response portion of the dispersion curve.

3.3 Silver Decoration

Small cracks in cycled electrolytes are often impossible to detect without some form of decoration. Some of the cracks are so small as

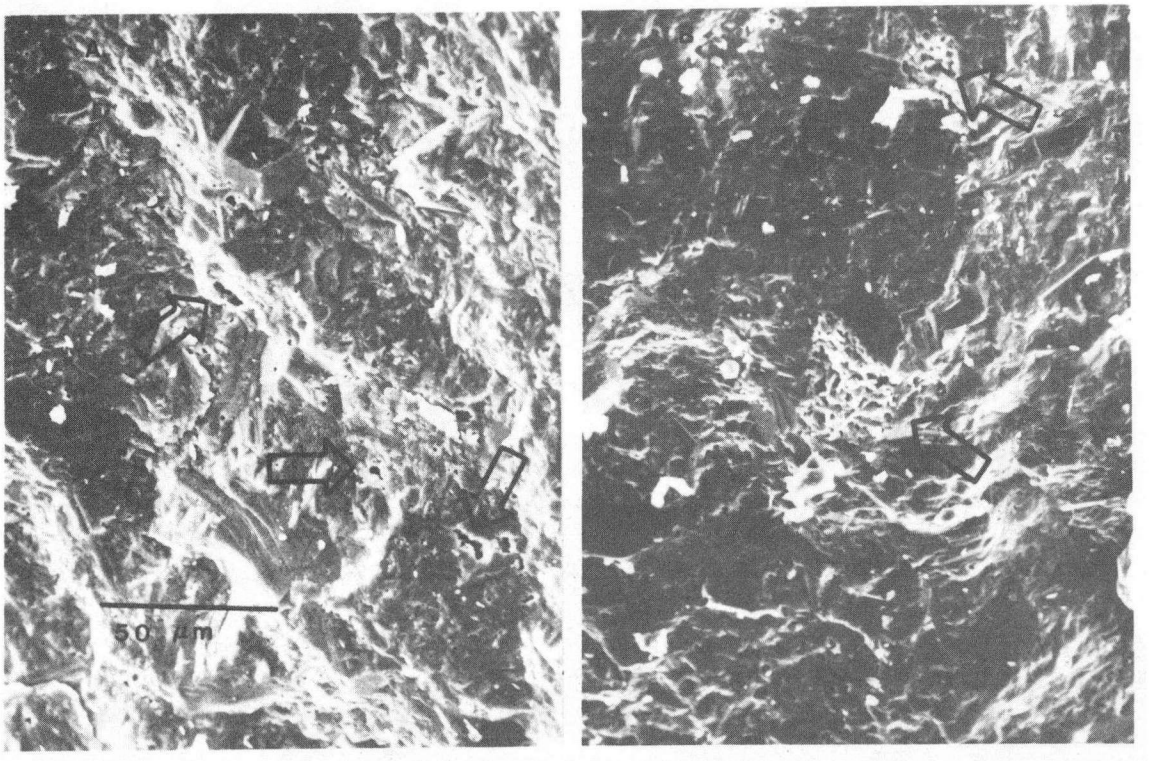

XBB 817-6528

Fig. 3.5 Fracture surfaces of "10 μm" material showing the two types of interior voids.

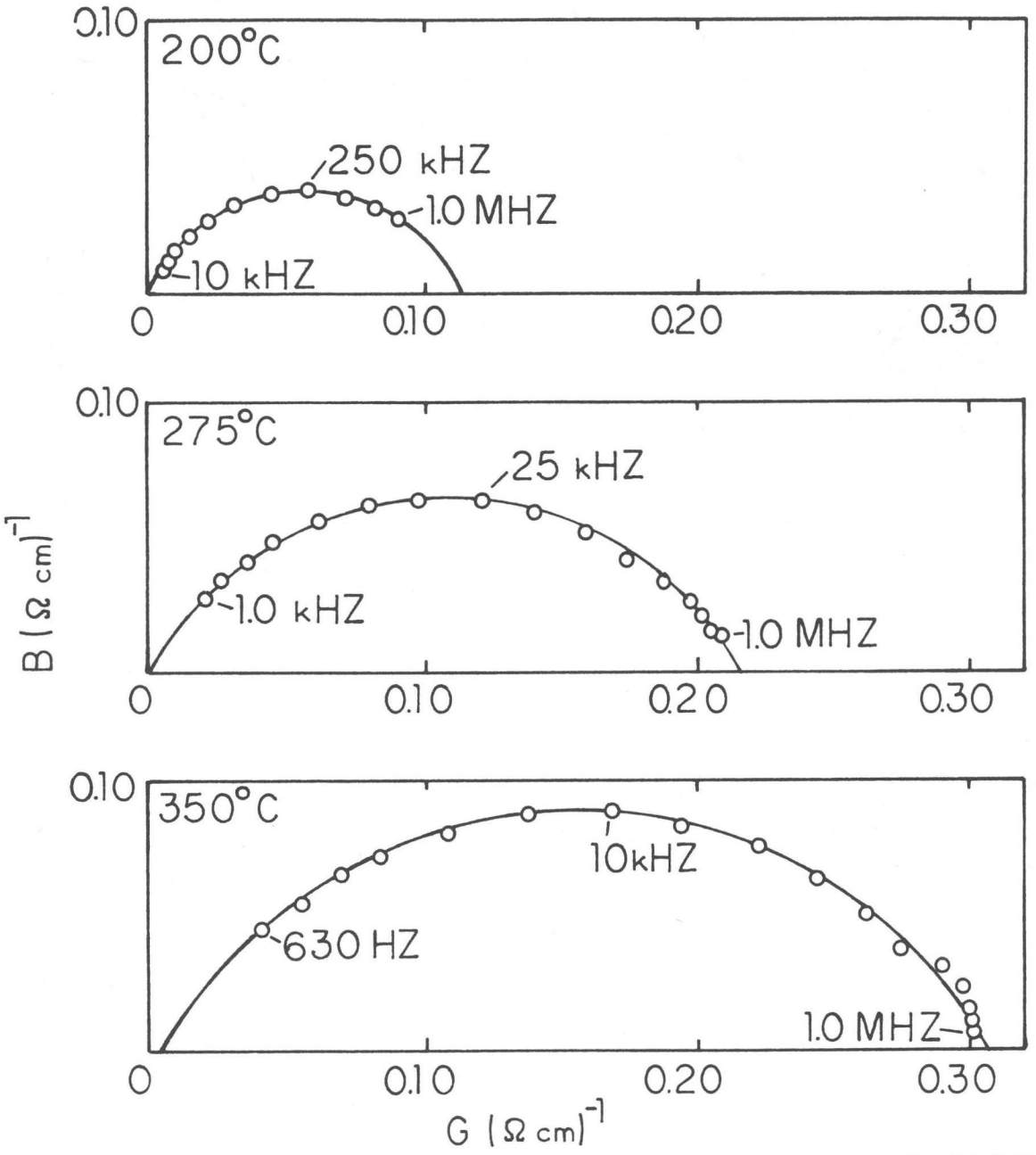

Fig. 3.6 Admittance plots for "10 μm" material at 200°C, 275°C, and 350°C.

to resist penetration by conventional dye penetrants. Complete silver exchange, such as used to examine the effects of sodium immersion, usually obscures rather than reveals the cracks because of the intense darkening which occurs in the electrolytes which have been exposed to sodium. A technique of decoration developed by De Jonghe and Feldman (De 80a) was used in which the samples are immersed for 15 minutes to an hour in a 1 molar aqueous solution of silver nitrate held at about 90°C. The sodium or sodium oxide residue in the cracks is readily replaced by silver, and only a slight enhancement of darkening occurs in the bulk of the electrolyte. Cracks not formed by electrolytic degradation, and surface scratches, contain no sodium residue and do not decorate in this treatment. The decorated cracks are readily observed in the metallographic microscope when viewed in dark field illumination, or through crossed polarizers to reduce surface reflection.

3.4 Microscopy and Microanalysis

Many specimens of electrolyte from sodium/sodium cells made in this lab, and from sodium/sulfur cells manufactured commercially, were prepared for microscopic examination. Low power optical microscopy was used to examine the surface features of the electrolytes. Higher magnification was used on specimens which had been sectioned and polished. Etching and silver decoration/exchange were used as necessary to highlight features of interest.

Other specimens were examined in the AMR scanning electron microscope equipped with an EDAX energy dispersive x-ray analysis unit. Microstructure determination and impurity analysis were generally done in the SEM. Specimens were prepared for microstructural analysis by

sectioning with a diamond saw, and polishing and etching in boiling concentrated phosphoric acid for 5 to 30 seconds. Specimens analyzed for impurity content were simply cut or broken to the proper size.

A few specimens of electrolyte taken from sodium/sulfur cells were examined in a scanning Auger microscope (Physical Industries, Inc., Springfield, New Jersey). The microscope was equipped with a stage which permitted in situ fracturing of specimens. Bars about 3x1 mm and 20 mm long were cut from electrolyte tubes and notched at the desired point of fracture using the diamond saw. The bars were then clamped into the specimen holder, inserted in the microscope stage, and fractured after the system had been pumped down.

Foils were also prepared for transmission electron microscopy by ion thinning samples taken from sodium/sodium cells and from sodium/sulfur cells. Thick (up to 5 μm) regions of these foils were examined using the Hitachi 650 kv electron microscope at the Berkeley Campus of the University of California. Thinner regions (up to 0.2 μm) were examined using 100 kv microscopes: either a Siemens 102 for high resolution work, or a Phillips model 400 scanning transmission electron microscope. The latter instrument could be used easily for very high resolution energy dispersive x-ray analysis, since it had a beam size of about 0.2 μm, and the beam could be directed at any desired portion of the sample. The resulting x-rays were detected and analyzed to determine the elements present. Although the instrument can also be used in the STEM mode, this was not found to be needed here.

3.5 A.C. Dispersion Analysis

Rectangular bar specimens of sodium immersed and of as-prepared

electrolytes were subjected to A.C. dispersion analysis using methods and equipment described in detail by the author elsewhere (Bu 78 pp. 50ff). Some single crystal material was also examined by this method.

One sodium/sodium cell was subjected to A.C. dispersion analysis during D.C. cycling. An A.C. component was superimposed on the D.C. current level using a current control amplifier. This system was then coupled to the gain-phase meter used in the A.C. dispersion measurements. Maximum frequency had to be limited to 10 khz owing to the response of the amplifier and the capacitance and inductance of the relatively long interconnections required.

4. CHEMICAL COLORATION OF THE BETA ALUMINIA

4.1 Introduction

A light gray darkening is produced in sodium beta or beta" alumina by contact with molten sodium. The darkening is a chemical effect, since it appears even in the absence of charge transfer through the electrolyte. Weber (We 74) has noted the coloration, and has shown it to be associated with a factor of 10^2 - 10^3 increase in the electronic conductivity of the ceramic; but no other studies of the properties of darkening have appeared. This lack of interest has probably been due to the assumed unimportance of darkening in comparison to the more widely studied mode I process. The cycled electrolyte failure analysis done for this thesis shows the existence of a slow degradation mechanism in electrolytes taken from sodium/sulfur cells. A gradient in the electronic conductivity of the ceramic plays an important part in this mechanism (De 81a). The effects become evident after prolonged cycling. A clarification of the nature of chemical darkening is therefore necessary to determine its possible role in this slow degradation process. A series of experiments was performed using single crystals of sodium beta alumina, and polycrystalline sodium beta" alumina electrolytes of various microstructures, to promote such clarification.

4.2 Experimental

Experiments requiring the use of molten sodium were carried out in a glovebox, under argon containing less than 5 ppm oxygen. Still, the sodium must be considered as being saturated with oxygen and this places the oxygen fugacity in the sodium at about 10^{-58} atm at 350°C,

the temperature used for most of these experiments. Temperatures were controlled to ± 1°C between 250°C and 450°C.

4.2.1 Single Crystal Experiments

Figure 4.1 follows schematically the basic steps of the coloration and bleaching experiments. Single crystals of sodium beta alumina were prepared for use by subjecting them to a crack healing process. Such single crystals tend to cleave partially or totally through the basal planes in a spontaneous manner after being exposed to air for a period of days. It is believed that this is due to the effects of absorbed moisture. The crystals used in these experiments were stored in an evacuated dessicator, but cleavage cracks still developed. Most of these cracks can be healed by high temperature annealing; and so after cutting the crystals to the desired size, they were annealed for two hours at 1600°C while packed in coarse beta alumina powder of the same soda content to prevent soda loss.

Several of these crystals were then immersed in molten sodium at 300°C and 350°C for periods of time ranging between 30 and 250 hours. Despite the crack healing procedure, it was found that sodium had infiltrated some of the remaining cleavage cracks (Figure 4.2) in all but one case. Since the cracks which were infiltrated had to be very narrow, it would appear that the problem of wetability of beta alumina by molten sodium is less significant than some workers have suggested (Vi 79). The crystals were weighed before and after sodium immersion to detect any weight change that might accompany a possible second phase formation.

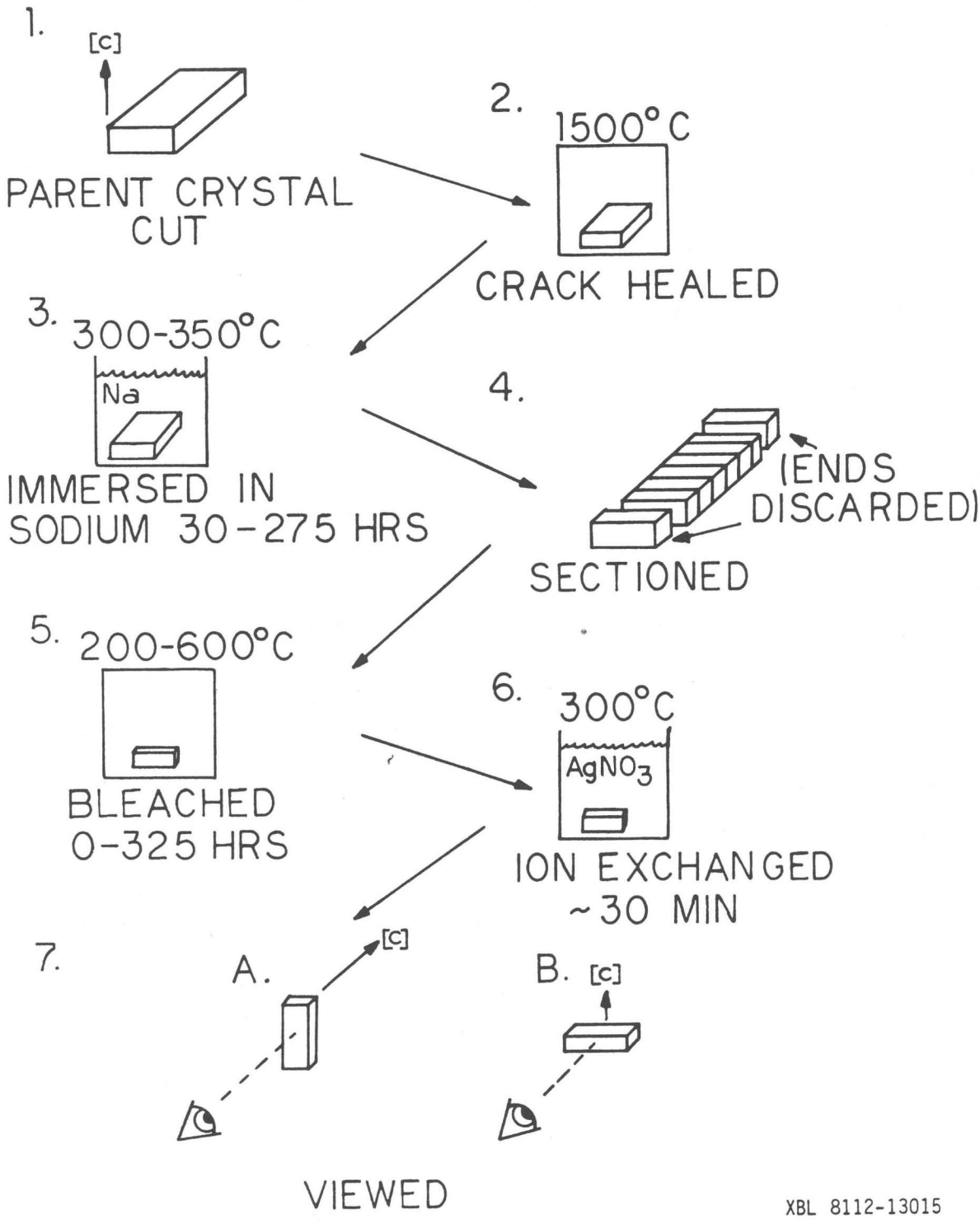

Fig. 4.1 Basic steps in coloration and bleaching experiments.

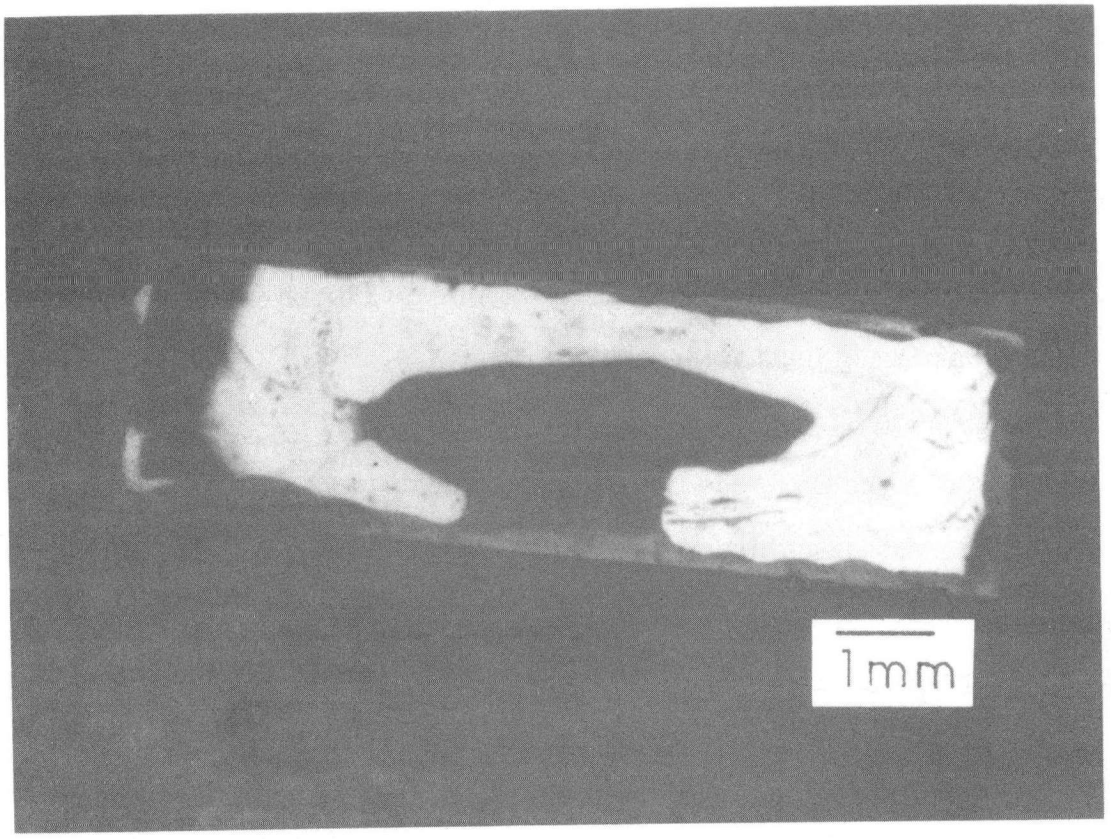

XBB 815-4065

Fig. 4.2 Single crystal of beta alumina after immersion in molten sodium showing sodium which has infiltrated basal plane cracks. [c] direction is perpendicular to plane of figure.

All crystals developed a light grey coloration during sodium immersion. An immersed crystal is compared with a virgin crystal in Figure 4.3 where the darkening is quite apparent. When immersed single crystals are ion exchanged in molten silver nitrate at 325°C, they darken severely. A crystal exchanged without having undergone prior sodium immersion does not darken at all. Measurements of the progress of coloration were assisted by enhancement of darkening through silver ion exchange.

Cross sections through the darkened crystals revealed that the coloration progresses into the crystal in a layer like fashion with a rather sharply defined interface. Kinetics of the darkening were studied by immersing single crystals in sodium for various lengths of time at 300°C and 350° and measuring the thickness of the darkened layer. The cross sections cut from the darkened crystals were rough polished, and micrographed at a suitable magnification; the thickness of the darkened layer was computed from measurement on the micrograph. Other sections from the darkened crystals were heated in air for various lengths of time at temperatures between 250°C and 600°C before silver exchange. This produced bleaching; below 400°C this bleaching also proceeded as a discrete layer from the surface of the crystal. Kinetics of the bleaching process were also studied by measuring the thickness of the bleached layer.

The role of oxygen in the bleaching was investigated by an experiment in which a darkened single crystal and a piece of vanadium foil were sealed together in an evacuated quartz ampoule. The vanadium foil was selectively heated to about 700°C so that it could react with any oxygen remaining. This established an oxygen partial pressure

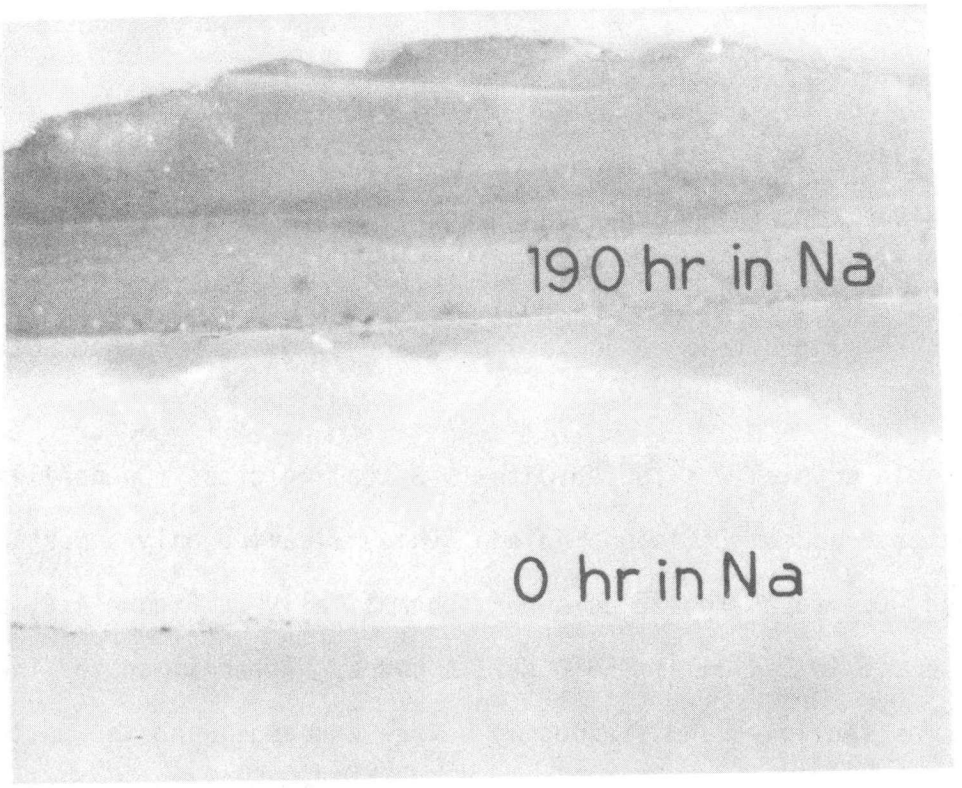

XBB 800-14681

Fig. 4.3 Comparison of beta alumina single crystals showing darkening produced by immersion in molten sodium. [c] direction is vertical in plane of figure.

about about 10^{-37} atm in the ampoule. The ampoule was then heated to 400°C for 24 hours, cooled, and opened; and the crystal then removed and silver exchanged.

To see if low oxygen fugacity alone would cause darkening of beta alumina, several evacuated ampoules were prepared as above, each containing a single crystal and a vanadium foil getter. These ampoules were then heated, each at a different temperature/time combination. Temperatures ranged from 350°C to 800°C, and times ranged from 50 to 350 hours.

A single crystal was coated with IN-3 sealing glass (Owens-Illinois, Electronics Products Division, Toledo, Ohio), leaving only a portion of a cleaved 00.1 face exposed as shown schematically in Figure 4.4, and then immersed in sodium at 350°C for 34 hours. After immersion the crystal was sectioned and stained by silver exchange, and the pattern of coloration was examined. This experiment helped to answer questions about coloration defect diffusion paths and possible coloration anisotropies.

To explore the possible effects of water on the coloration process, a single crystal of sodium beta alumina was placed in a warm 9 molar sulfuric acid for 5 minutes to partially exchange the Na^+ with hydronium ion (H_3O^+). It was then immersed in molten sodium at 350°C for 48 hours along with a crystal, which had not been exchanged, to act as a control.

There was a very rapid initial bleaching to a depth of about 15 μm which developed in all single crystals in about 15 minutes. About one hour would have been required if this layer had bleached at same rate measured in the remainder of the bleaching process. De Jonghe has reported (De 77, pp. 5-42f.) that beta alumina exposed to cool, moist

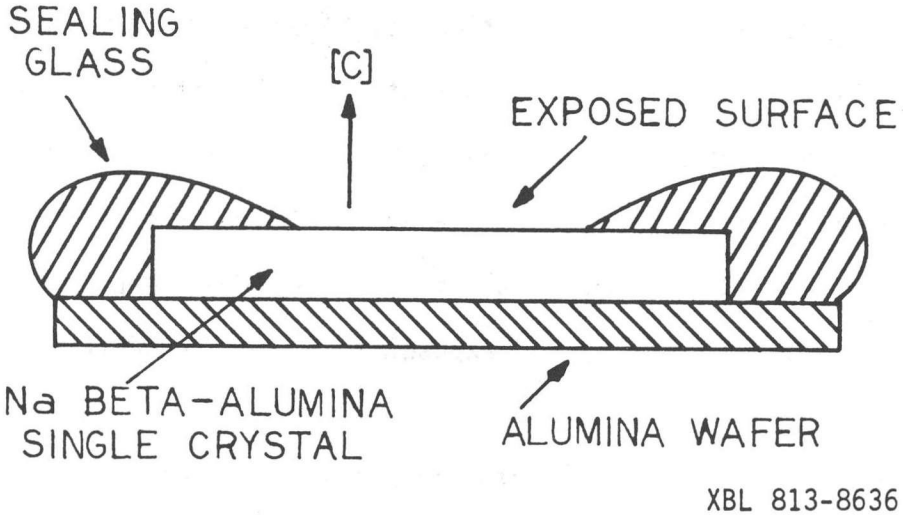

Fig. 4.4 Schematic cross section showing method of fabrication of single crystal sample with sealed conduction planes.

air very rapidly adsorbs a monolayer of water on its surface, and then continues to absorb water into its bulk at a much slower rate. It was thought that this surface monolayer might be diffusing into the crystal during the heating to produce the rapid initial bleaching. To test this theory, two single crystals were exposed to 33% relative humidity at 25°C for 1 hour. One was bleached for 2 hours and the other for 1 hour at 350°C. The former was then silver exchanged and the latter was exposed to the same conditions of temperature and humidity for an additional hour to allow the adsorption of another monolayer of water. This latter crystal was then bleached another hour at 350°C and finally silver exchanged. Since the bleaching time was the same for both crystals, it was reasoned that if the water were responsible for the rapid bleaching, the crystal exposed twice to the humid air should show a greater depth of bleaching.

Because the bleaching rate did not show a steady increase with temperature, but an apparent maximum around 250°C, the following dual temperature phase bleaching experiment was done to clarify the difference between possible oxygen transport mechanisms. Three single crystals were cut from a parent crystal which had been immersed in sodium for 266 hours at 350°C. The first was bleached 96 hours at 350°C. The second was bleached 24 hours at 350°C and then an additional 72 hours at 250°C. The third was bleached 96 hours at 250°C. Then the three crystals were silver exchanged, and the thicknesses of the darkened layers were measured and compared.

Weight changes were recorded in the process of silver ion exchanging uncolored, colored, and bleached single crystals, and used to calculate exchangeable soda content.

Complex A.C. conductivity measurements were made on uncolored colored, and bleached single crystals. These measurements were done to determine approximate ionic conductivity in the conduction planes.

4.2.2 Polycrystalline Material Experiments

Polycrystalline specimens of soidum beta" alumina were also subjected to sodium immersion testing. A large specimen (about 2 grams) of the "10" μm material was immersed in molten sodium at 350°C for 100 hours. It was weighed both before and after immersion, and after bleaching in air for 54 hours at 800°C.

Five sets of polycrystalline tube pieces, each set containing a piece each of the "300", "150", and "10 μm" material were immersed in sodium at 350°C for periods of 1, 2, 4, 8, and 16 days. After being removed, they were washed in methanol to remove the adherent sodium. The surfaces of the samples showed only slight and irregular darkening after immersion, as can be seen in the bottom half of Figure 4.5. The samples were then silver exchanged. They darkened in a graded fashion, as is evident in the top half of Figure 4.5. Darkening increased with increasing time of immersion and with decreasing average grain size. Weight changes during silver exchange were recorded and used to calculate exchangeable sodium contents.

The samples were next sliced and polished in cross section. This revealed a layer of darkening which increased in thickness as time of immersion increased for samples of a given grain size (Figure 4.6). Measurement of the advance of the colored layer in polycrystalline samples was done by making optical micrographs at a suitable magnification of the polished, cut cross sections of the sodium immersed,

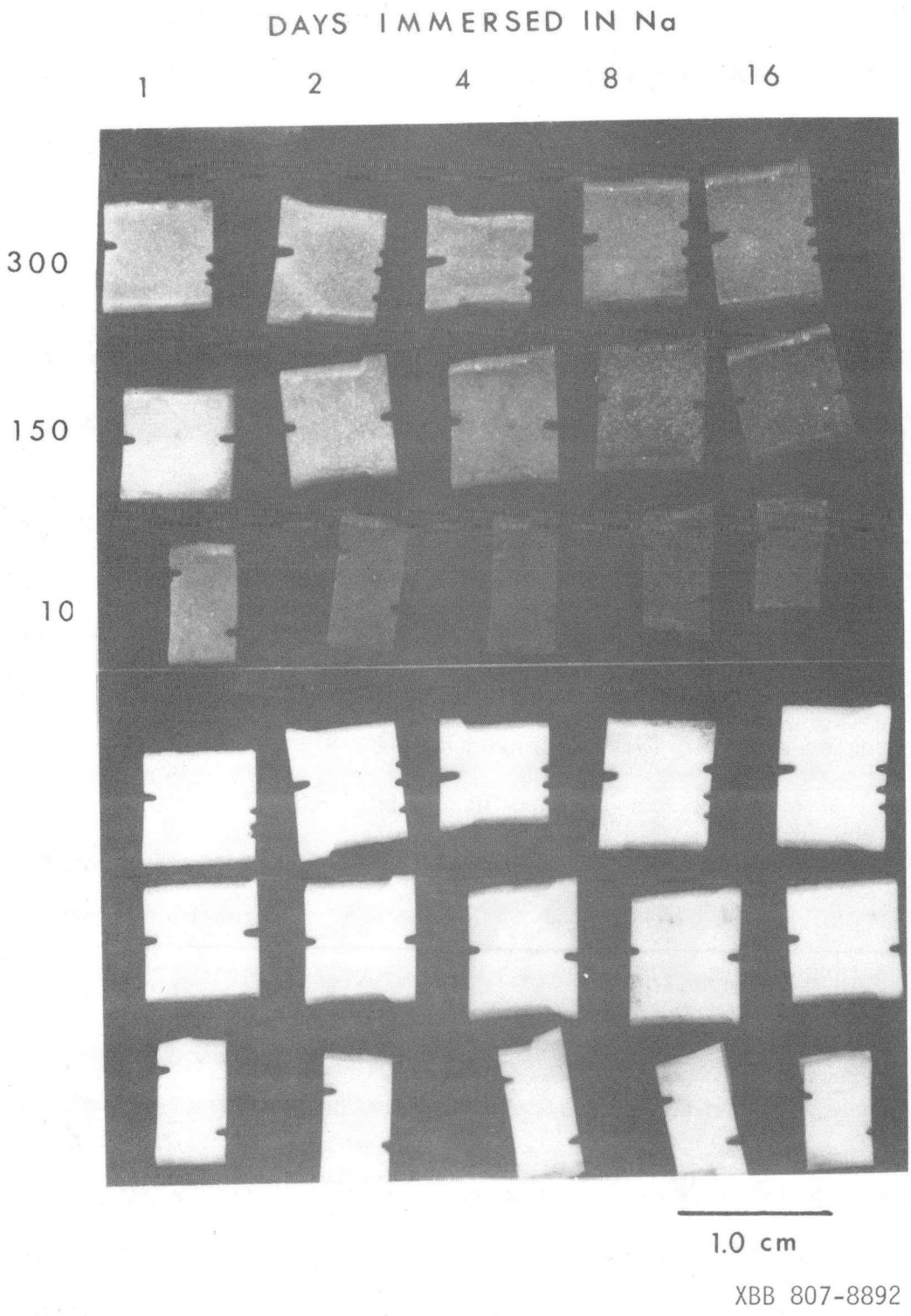

Fig. 4.5 Surfaces of immersed polycrystalline electrolyte specimens before (bottom) and after (top) silver ion exchange. Nominal grain size in μm indicated at left of rows on top. Same order on bottom.

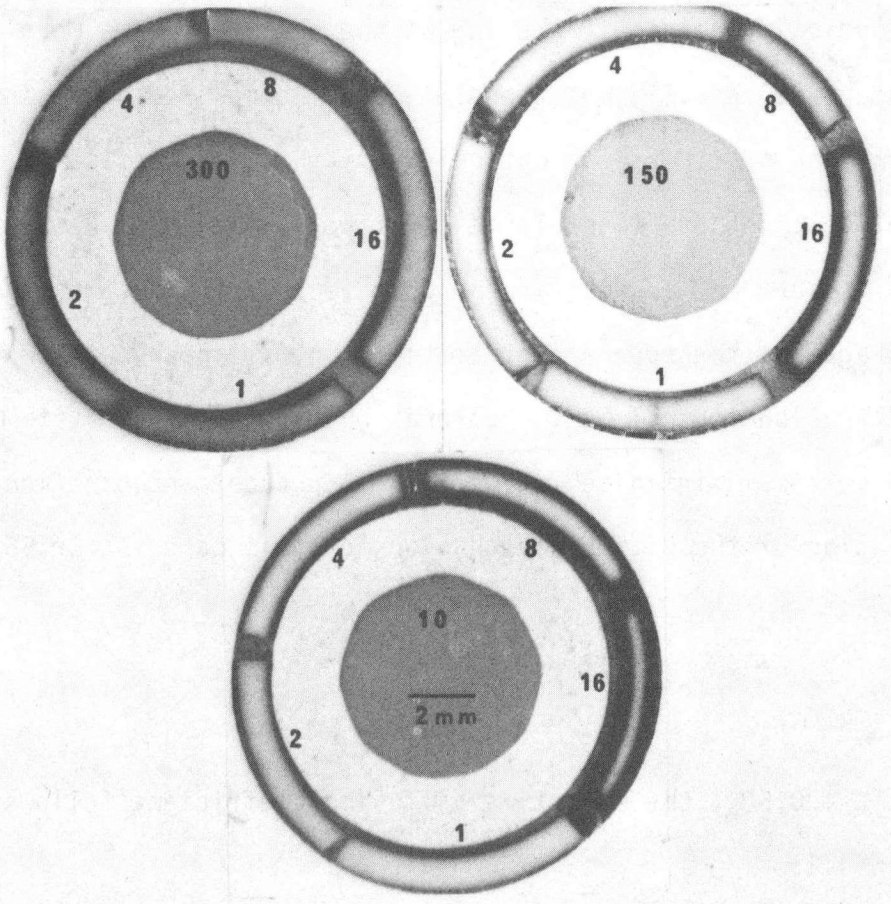

XBB 807-8887

Fig. 4.6 Polished cross sections of silver exchanged colored polycrystalline electrolytes. Days immersed in sodium are indicated adjacent to each specimen.

silver exchanged electrolyte tube segments, and scanning the negatives of these micrographs on an optical microdensitometer to produce plots of the optical density. Darkening at the surface became more intense with time (Figure 4.7), but the plots were normalized by assigning a concentration of 1.0 to the optical density at the surface of the electrolyte. The position of the relative density of 0.5 was then used to measure the advance of the colored layer. This position was plotted against the square root of time, and a linear dependence indicated diffusion control of the coloration process. The system was treated as a semi-infinite medium with a surface concentration C_o. The solution of the diffusion equation for this case is (Cr 56, p. 19):

$$C = C_o(1-\mathrm{erf}(x/2\sqrt{Dt})) \qquad 4.1$$

Letting $C = 0.5C_o$, the effective diffusion coefficient follows from equation 4.1:

$$D = x^2/0.92t \qquad 4.2$$

It was not possible to determine the exact relationship between the concentration of the coloration defect and the optical density of the micrograph. A proportionate relationship should exist, however, allowing reasonably accurate determination of diffusion rates.

Specimens of polycrystalline silver and sodium beta" alumina were partially masked, and placed in a beam of intense ultraviolet light. The silver beta" alumina was produced by ion exchange, and the surface was polished before exposure to insure that effects observed were not

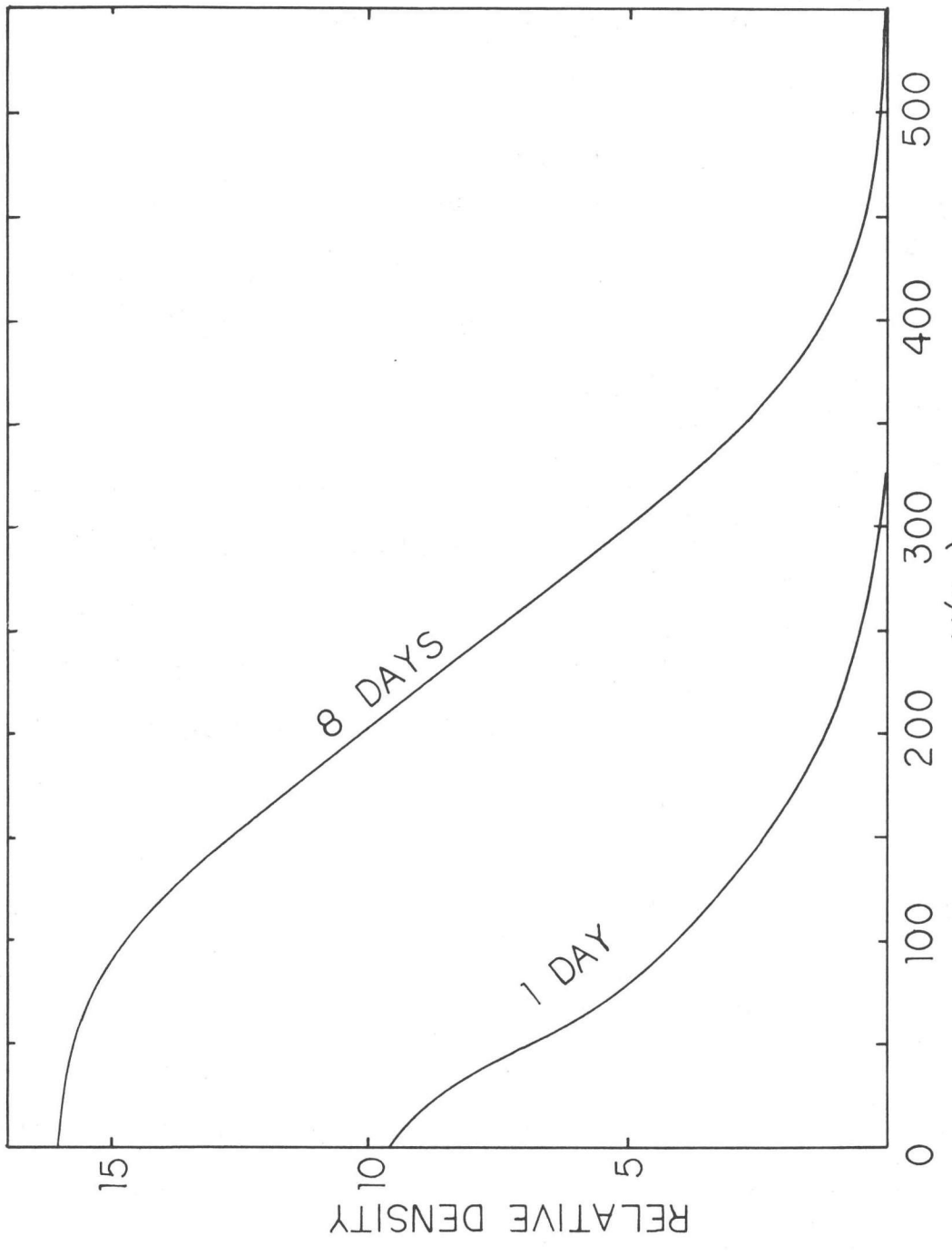

Fig. 4.7 Darkening profiles of two "10 μm" electrolyte cross sections in arbitrary units of density.

due to surface residue of silver nitrate from the ion exchange treatment. Photon energies in the beam ranged up to about 12 eV, so that electron-hole pairs could be created directly in the exposed electrolytes. The experiment was done to seek clarification of the role of free electrons and holes in the coloration process.

The effect of sodium immersion and bleaching on complex conductivity was investigated. A small rectangular bar about 1x1x5 mm was cut from a tube of 10 μm material, and evaporated gold electrodes were applied for the dispersive A.C. conductivity measurements. A precision jet of alumina abrasive from an industrial abrasive blast unit (S.S. White Co., Model F) was used to prepare the surface for electrode application as well as to remove the electrodes before the sample was subjected, first to coloration by immersion, and finally to bleaching. Three pieces cut from the same tube were subjected to silver exchange, one at the outset, one after coloration by immersion, and one after bleaching, in order to monitor the exchangeable sodium content at each stage of the process.

4.3 Results and Discussion

4.3.1 Preliminary Analysis

Extensive examination by transmission electron microscopy of foils made from darkened electrolytes has failed to reveal any feature that can be attributed to the chemical coloration. It is highly likely, therefore, that the coloration results from the creation of point defects rather than from second phase formation.

The results of the weighings done in the course of the coloration and bleaching experiments also failed to provide any evidence of second phase formation.

In single crystals immersed for 100 hours, an average weight gain of 300 ppm was noted, slightly more than the 200 ppm uncertainty in the weighing. The gain was attributed to sodium infiltration because no independent evidence of second phase formation (e.g. increased cleavage tendency, clouding, or disintegration of the crystals) was observed. Second phase formation or sodium metal precipitation would undoubtedly produce severe strains in the single crystals, leading to fracture. Chemically colored crystals examined under the optical microscope in a small, strong transverse light beam showed no evidence of the Tyndall effect which could be expected to be observed if colloidal sodium were present in the crystal.

Exchangeable soda contents, measured in specimens of as-received, colored, and bleached single crystals, all fell within the range of $6.4 \pm 0.3\%$ Na_2O, the high uncertainty being due to the fact that small (25 - 100 mg) specimens had to be used to conserve scarce single crystal material. Within these limits of uncertainty no statistically significant differences were found in the three classes of single crystals. A.C. dispersive conductivity methods also showed that no significant changes in the ionic conductivity were brought about by coloration or bleaching.

Weight changes for the large polycrystalline specimen were within the 20 ppm uncertainty in weighing both after coloration and after bleaching. Neither was there any statistically significant change in exchangeable sodium content or resistivity of the polycrystalline

material after coloration, regardless of the duration of sodium immersion up to 384 hours, or after bleaching.

All of the evidence above favors an interpretation of the darkening in terms of point defects. Therefore, the results of the experiments have been approached from this point of view.

4.3.2 Penetration of Darkening and Enhancement by Silver Exchange in Single Crystals

Penetration of darkening into the crystal is almost isotropic with perhaps slightly deeper penetration along the conduction planes than through the spinel blocks.

Figure 4.8 shows two views of a cross section cut from an immersed and exchanged single crystal; points of deeper penetration are due to basal plane cracks. The upper micrograph in the figure was taken with transmitted polarized light, while the lower was taken with unpolarized light. The darkened portion of the crystal polarizes light strongly. The specimen is completely opaque when viewed parallel to the [c] axis but transparent when viewed perpendicular to it (Figure 4.9). It can be deduced, therefore, that the metallic silver responsible for the blackening is deposited in filaments or platelets, lying in the conduction planes, leaving the spinel blocks clear to transmit light. This also accounts for the polarization of light passing through the darkened part of the crystal, since conduction and optical absorption can occur only along the length of the platelets or filaments but not along the width which is presumably only one silver atom's diameter.

The precipitation of silver in the conduction planes requires that electrons be supplied to the silver ions so that they can be reduced.

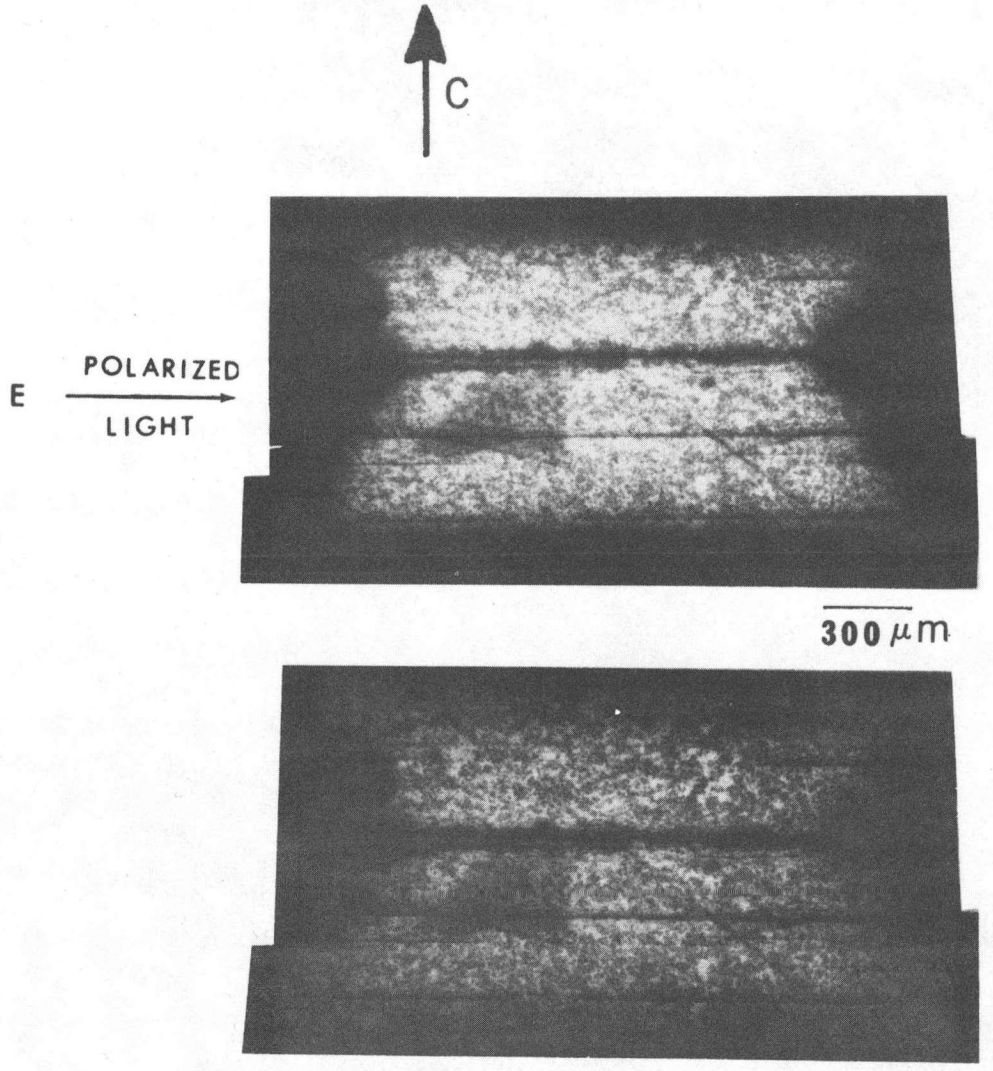

Fig. 4.8 Cross section of silver exchanged darkened single crystal viewed in polarized light (top) and unpolarized light (bottom) to show that the layer of darkening polarizes light and that it penetrated the crystal almost isotropically.

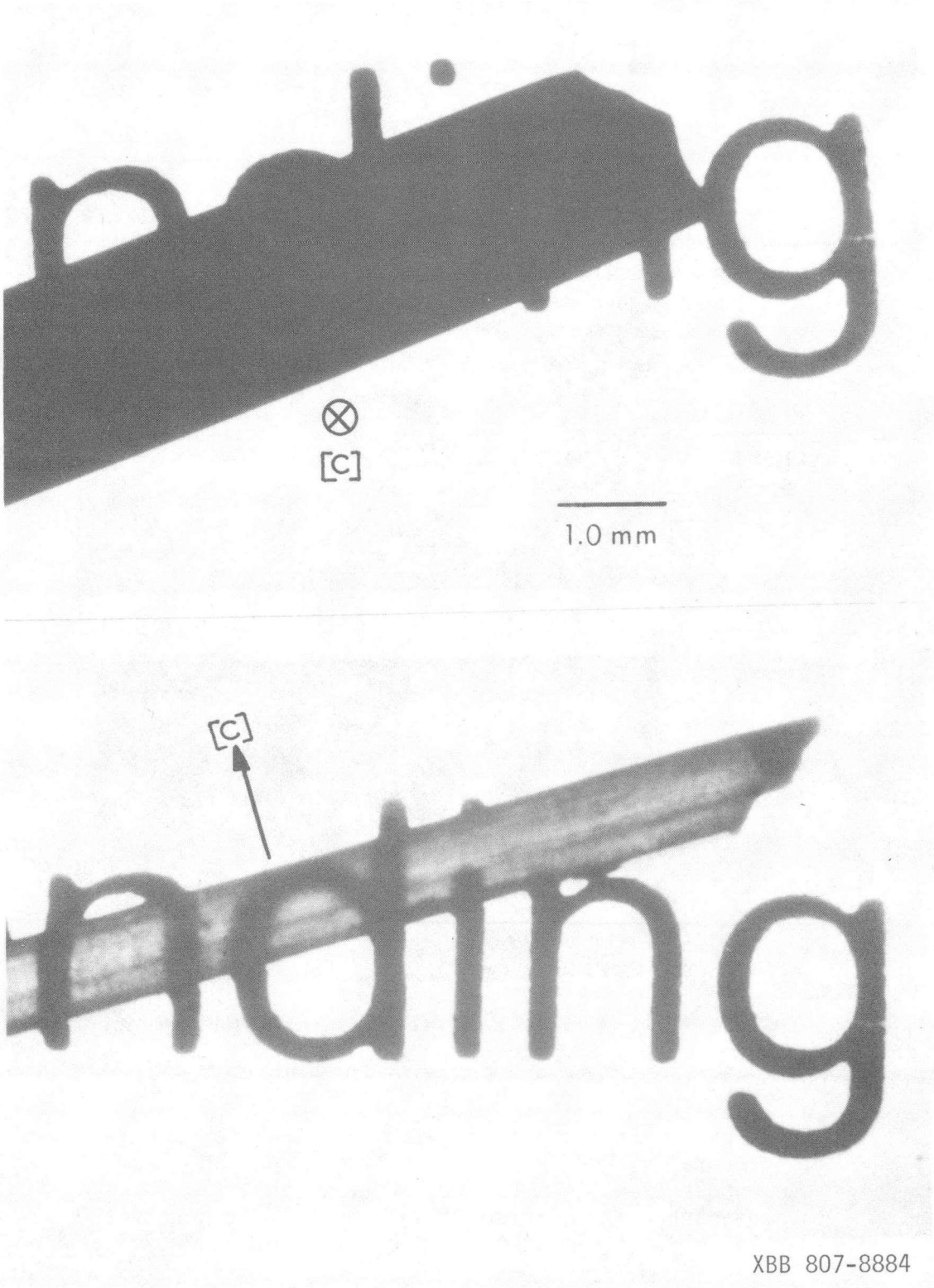

Fig. 4.9 Anisotropy of light transmission by silver exchanged darkened single crystal.

The point defects responsible for the darkening must therefore have this reducing property.

4.3.3 Kinetics of the Advance of the Darkened Layer in Single Crystals

The darkening proceeded more slowly, and appeared to be slightly less dense, at 300°C as compared with 350°C. Figure 4.10 is a plot of the results of the darkened layer growth measurements. A parabolic time dependence was found to apply indicating that the darkening process is under diffusion control. The sharpness of the interface between darkened and undarkened portions of the crystal suggests that the process involves a saturated layer growth such as would occur in tarnishing. In this kind of diffusion process, one cannot obtain the self diffusion constants of the defect components directly from layer progression measurements without a knowledge of a detailed defect reaction, of the fraction of the diffusing species in the reaction product, and of the concentration of the diffusing species at the outer surface of the solid. When these parameters are known, a relationship can be established between the scaling constant, determined from layer thickness measurements, and the self diffusion constants of the various defects involved (cf. Kr 74, pp. 72ff.). The system is described by an equation of form:

$$X_L = (2K_L t)^{1/2} \qquad 4.3$$

where X_L is the layer thickness, K_L is the scaling constant and t is time. In tarnishing a major change in composition occurs in the

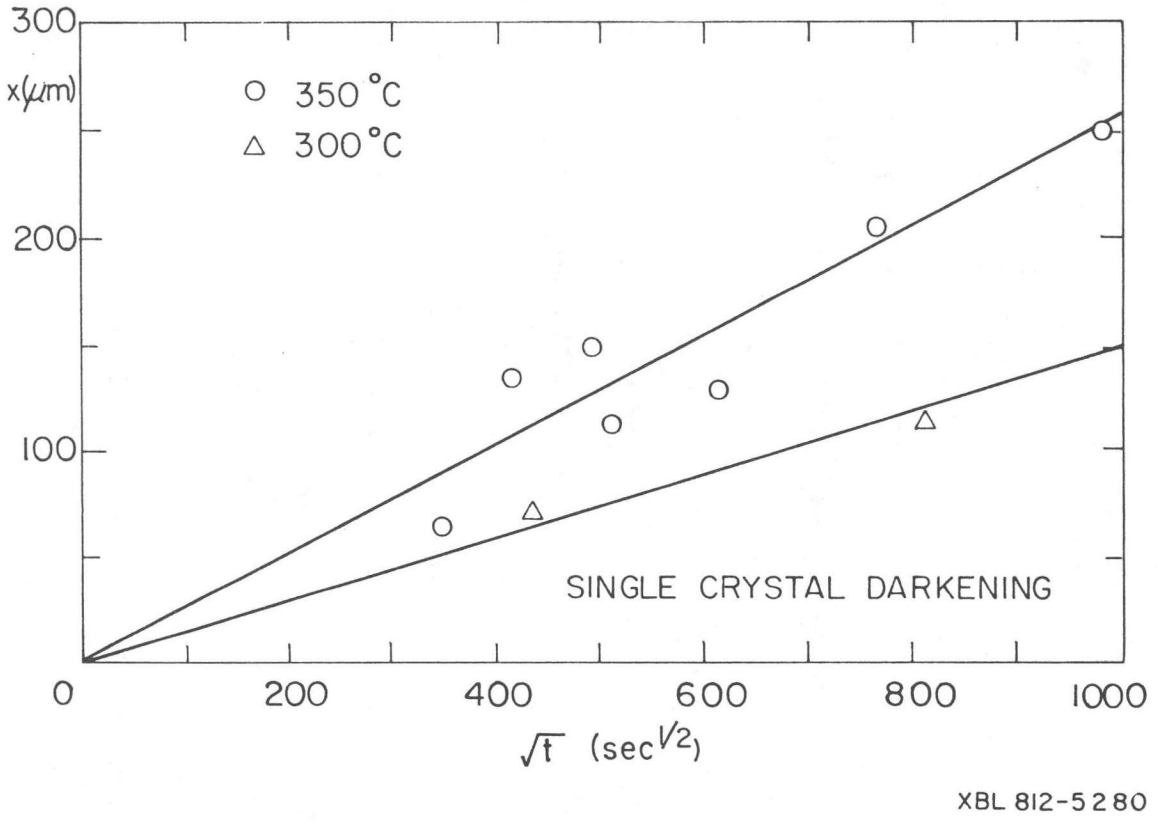

Fig. 4.10 Darkened layer growth kinetics in beta alumina single crystals.

tarnished layer as compared to the substrate. In beta alumina only point defects are involved in the darkening, but the sharpness of the interface indicates a strong concentration dependence for the diffusion constants of the active species. Since the defect reaction is not known in detail, all that can be determined from layer thickness measurements is the scaling constant which is tabulated in Table 4.1. An activation energy has been calculated which is about half that measured for electron transport in the beta aluminas (Wh 71a, We 74) suggesting that electron transport is not the rate determining factor in the progress of darkening. It was mentioned above that sodium ion transport through the spinel blocks has been demonstrated to be effectively nonexistent below 1000°C (Ya 67), and aluminum ion mobility is also expected to be very low. Oxygen transport, therefore, either by oxygen vacancies or hydronium ions, appears to be the prime candidate to explain the progress of darkening. Oxygen vacancies would be created in the reducing conditions of sodium immersion. Hydronium ions would be absorbed from the air as the crystal was being prepared for an experiment.

4.3.4 Other Aspects of Single Crystal Coloration

The role of water in the coloration process was discounted by the results of the experiment in which a partially H_3O^+ exchanged crystal was immersed in sodium along with a crystal which had not been exchanged. The depth of the darkened layer was the same in both specimens indicating that water in low concentration has no effect on the coloration process, contrary to what has been suggested by other workers (Te 80).

Table 4.1. Single Crystal Coloration Kinetics Data

Temperature	K_L
300°C	1.13×10^{-10} cm^2 sec^{-1}
350°C	3.41×10^{-10} cm^2 sec^{-1}

Activation Energy = 15.7 kcal mole^{-1}

All single crystals heated at oxygen partial pressure of 10^{-37} atm were visibly darkened by the procedure, but the darkening did not intensify or even persist when the crystals were silver exchanged. From this result it is concluded that substantial reduction of sodium beta alumina in a gas phase system is probably impossible. This is probably due to kinetic hindrances, since the mean free path of the oxygen is very large at the low pressures involved here.

4.3.5 Kinetics of the Advance of the Bleached Layer in Single Crystals

In Figure 4.11 several single crystals, all cut from the same parent crystal, are shown after bleaching at the temperatures and for the times indicated. They are viewed parallel to the [c] direction. The parent crystal had been immersed in sodium for 73 hours at 350°C. Several things can be noted here. Comparing the 24 hour bleached samples, there is a local maximum in the rate of bleaching at 250°C. At a given temperature (350°C is shown) the bleaching advances inward along the conduction planes as a function of time. The interface between the bleached and unbleached crystal is very sharp up to 350°C and then becomes more diffuse for bleaching done at higher temperatures. The rate of bleaching again increases above 400°C, and at 600°C bleaching was complete in less than 24 hours. The bleached layer is wider at the narrow ends of the crystals in Figure 4.11, but this is an artifact of crystal preparation. The narrow end is part of the surface of the crystal that was exposed to air before sodium

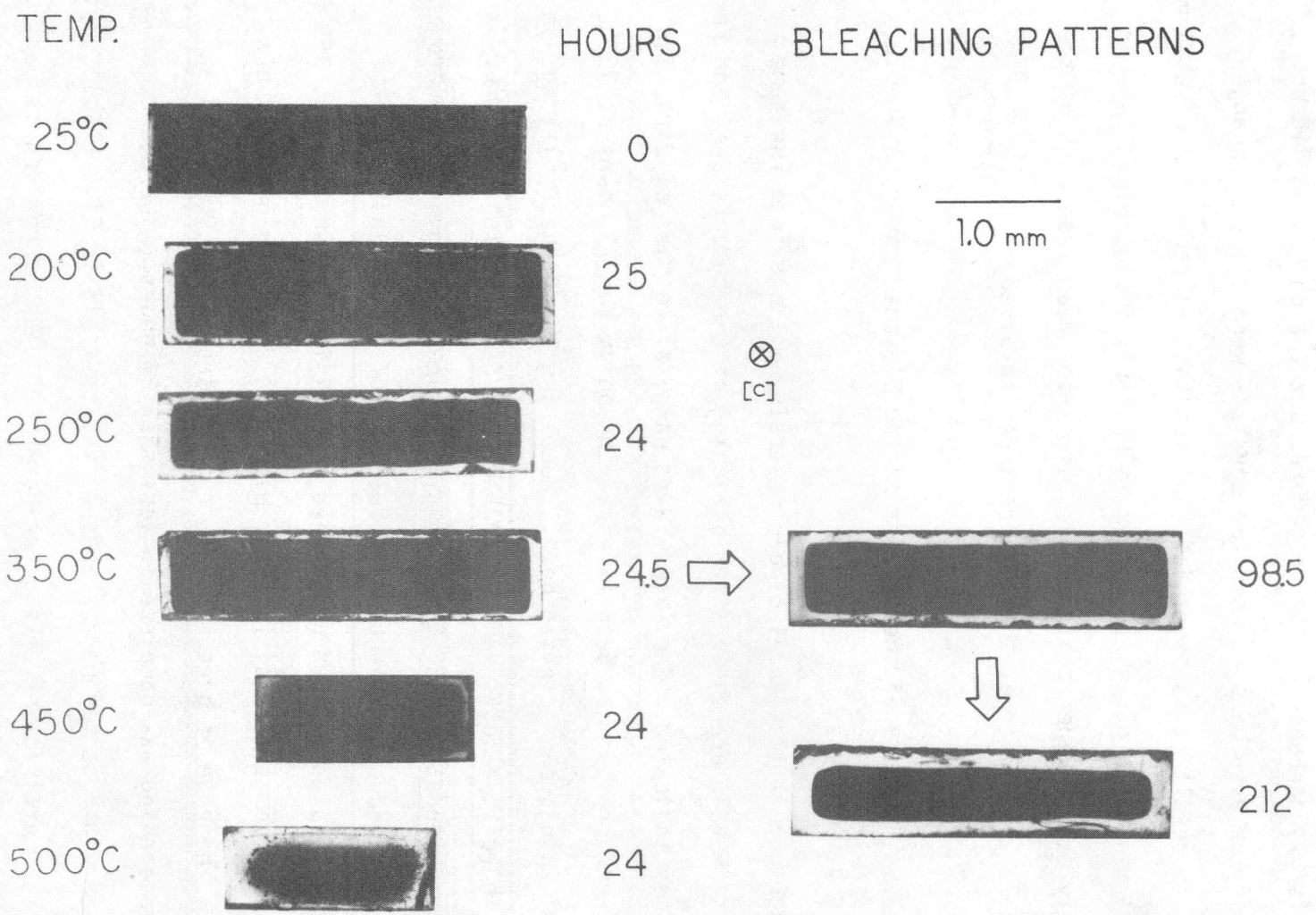

Fig. 4.11 Darkened single crystals subjected to various bleaching treatments before silver exchange.

immersion. The wide surfaces were produced when the parent crystal was sectioned after sodium immersion, and it was these surfaces that were used for measurements of bleaching kinetics to be reported next.

The width of bleached layer was measured for several bleaching times in two sets of crystals: one bleached at 250°C, the other at 350°C. The results are plotted in Figure 4.12. As with the coloration, a parabolic time dependence is shown by the bleaching indicating diffusion control. The values of K_L were calculated from the slopes of the plots and are listed in Table 4.2 where the values of K_L from the coloration are repeated for comparison. The bleaching proceeds much more slowly than the coloration at 350°C, but at 250°C the bleaching is faster than the coloration at 300°C.

4.3.6 Other Aspects of Single Crystal Bleaching

The two plots in Figure 4.12 are corrected since they originally extrapolated back to x = 15 μm at t = 0. The failure to extrapolate to the origin is due to the rapid bleaching effect mentioned above. It was thought that the rapid bleaching in this layer might be due to water absorbed from the air when the parent crystal was being sawed up, but the single crystals exposed to moist air for different periods of time developed bleached layers of the same depth (about 25 μm). Therefore, it can be said that moisture has little or no effect on the bleaching process at the levels it was present here.

The cause of rapid initial bleaching remains unknown. It may be due to minor delamination of the spinel blocks at the edge of the crystal occuring during the sawing process.

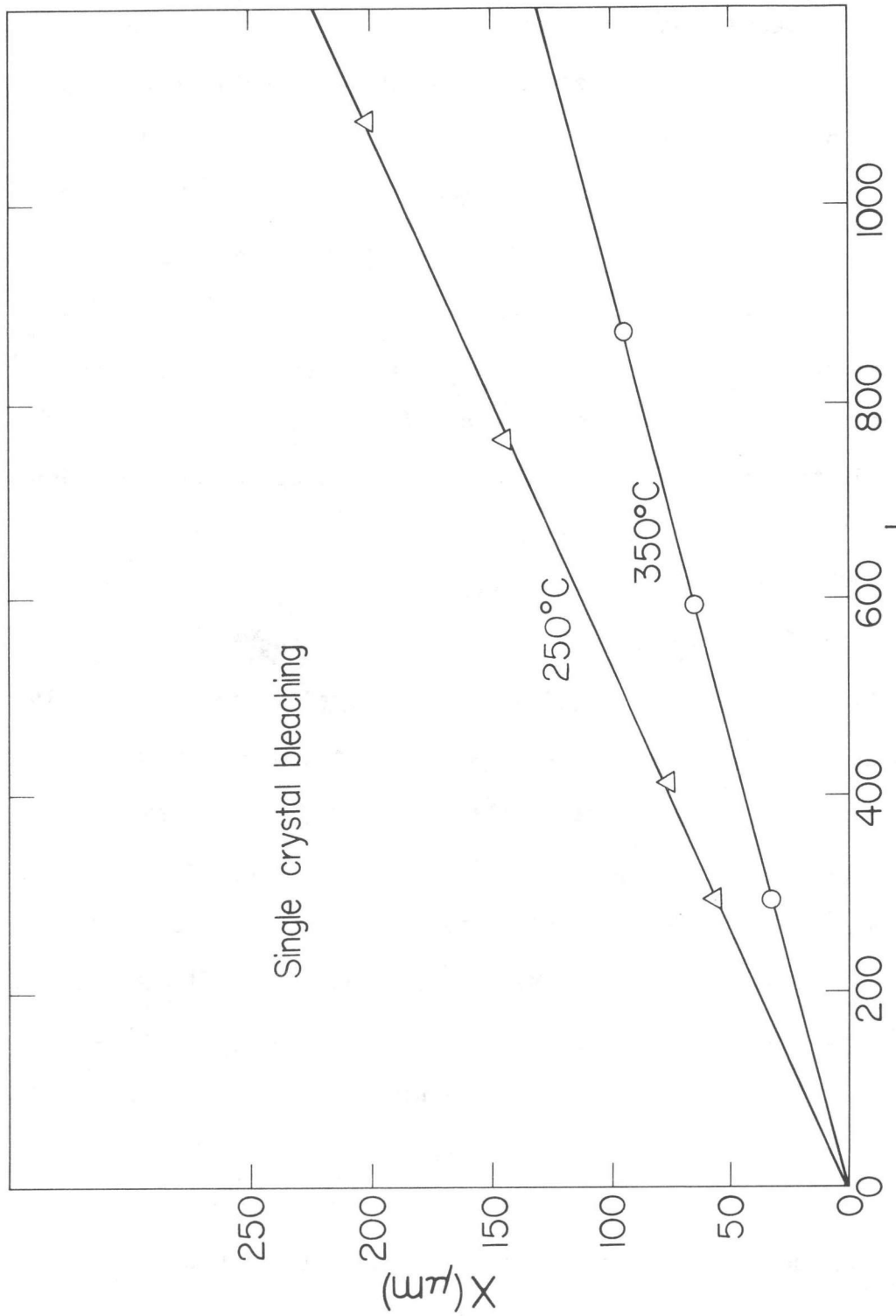

XBL 818-1076

Fig. 4.12 Bleached layer growth kinetics in beta alumina single crystals.

Table 4.2. Single Crystal Bleaching and Coloration Kinetics Data

Temperature	K_L (cm^2sec^{-1})	
	Bleaching	Coloration
250°C	$1.74x10^{-10}$	
300°C		$1.13x10^{-10}$
350°C	$5.90x10^{-11}$	$3.41x10^{-10}$

Figure 4.13 compares the edge of the crystal heated in low oxygen partial pressure with the edge of the one heated in air under the same conditions (24 hours at 400°C). No bleaching has occurred at the exposed edge of the crystal sealed in the ampoule, while, in contrast, the one heated in air has developed a bleached layer about 50 μm wide. The role of oxygen in the bleaching is thus convincingly established.

While coloration occurs in an almost isotropic fashion, bleaching progresses only along the conduction planes. Figure 4.14 shows cross sections of several crystals, the top one unbleached and the rest subjected to the bleaching treatments indicated. It is apparent that no bleached layer develops from the spinel block side of the crystal under any bleaching treatment. Therefore, it can be said that virtually no oxygen can penetrate the outer spinel blocks of the crystal under normal atmospheric bleaching conditions.

Because the spinel blocks in beta alumina are reported to be fairly impervious to transport of any ionic species at the temperature at which darkening was observed, and because of the anisotropy of the bleaching, the first explanation considered for the coloration/bleaching phenomena involved only ionic transport in the conduction planes. It was initially postulated that oxygen ions were removed from the crystal at its conduction plane edges in liquid sodium. The oxygen vacancies created were believed to be compensated by electrons, and electron transport through the spinel block would then be the rate limiting factor in such a case. The electronic short circuit provided by the sodium in contact with the crystal surfaces would permit the compensation required for isotropic darkening. Bleaching done in air could then propagate only through the conduction planes. If the

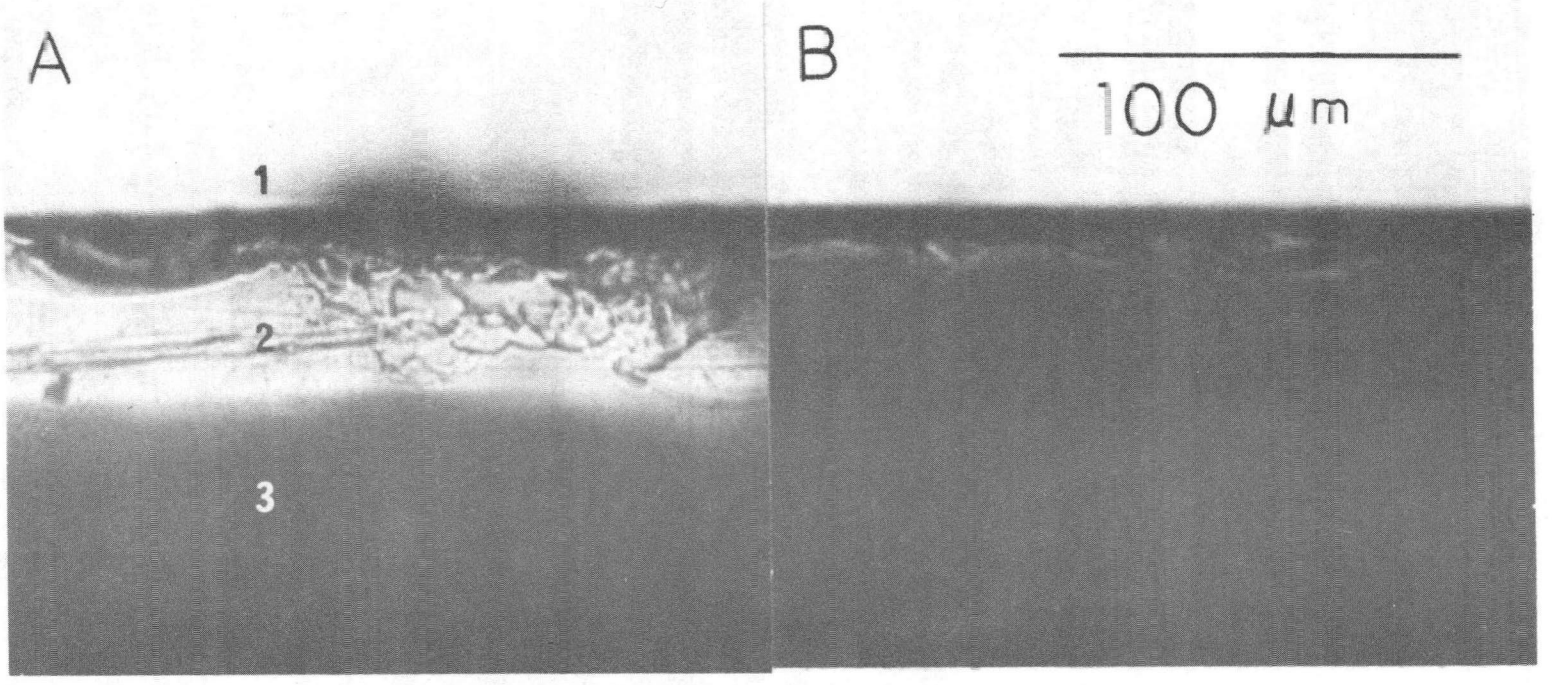

X3B 813-2319

Fig. 4.13 Comparison of single crystals heated to 400°C for 24 hours in: A. air and B. high vacuum. Regions identified are: 1) edge of crystal 2) bleached layer 3) darkened crystal.

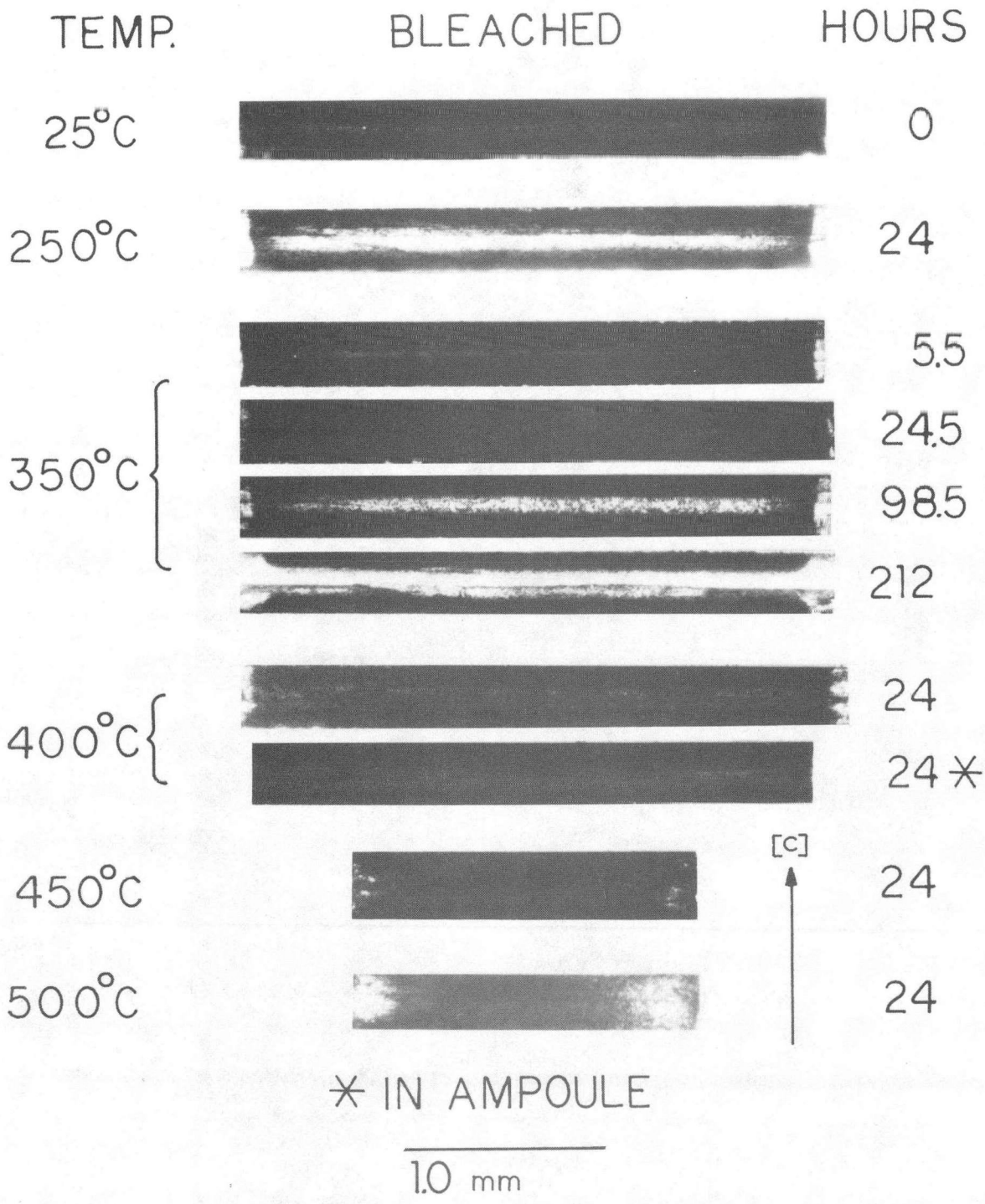

Fig. 4.14 Cross sectional view of darkened single crystals subjected to various bleaching treatments before silver exchange.

explanation was correct, it was reasoned that the crystal could not darken if the conduction plane edges of the crystal were sealed off, even if the other surfaces of the crystal remained in contact with molten sodium.

A single crystal, with all but a portion of its 00.1 face covered, was prepared as described earlier and immersed in sodium for 34 hours at 350°C. After the immersion period, the entire specimen was immersed in molten silver nitrate and then removed, washed, and sectioned. At this point no enhanced darkening was observed anywhere in the sectioned crystal indicating that the assembly had been leak tight and that no modification of the spinel blocks had occurred, during sodium immersion, which would permit them to be penetrated by silver ions. One of the sections with exposed spinel blocks was then reimmersed in silver nitrate, and the area under the exposed surface of the crystal darkened (Figure 4.15) showing that the defect responsible for the darkening can be transported across the spinel blocks, in the [c] direction.

Transport of the coloration defects in the [c] direction is evident in another way in the series of crystals shown in Figure 4.14. The time of immersion in sodium was such that the darkening did not penetrate the crystal entirely, and a narrow clear band is just visible in the center of the unbleached crystal at the top of the figure. In the crystal heated for 24 hours at 400°C in the low oxygen partial pressure ampoule, the coloration has begun to penetrate the central clear band near its middle. After 24 hours at 450°C and 500°C, the darkening penetrated and totally obliterated the central clear band. At high temperatures it is clear that the coloration defects are propagating in the [c] direction.

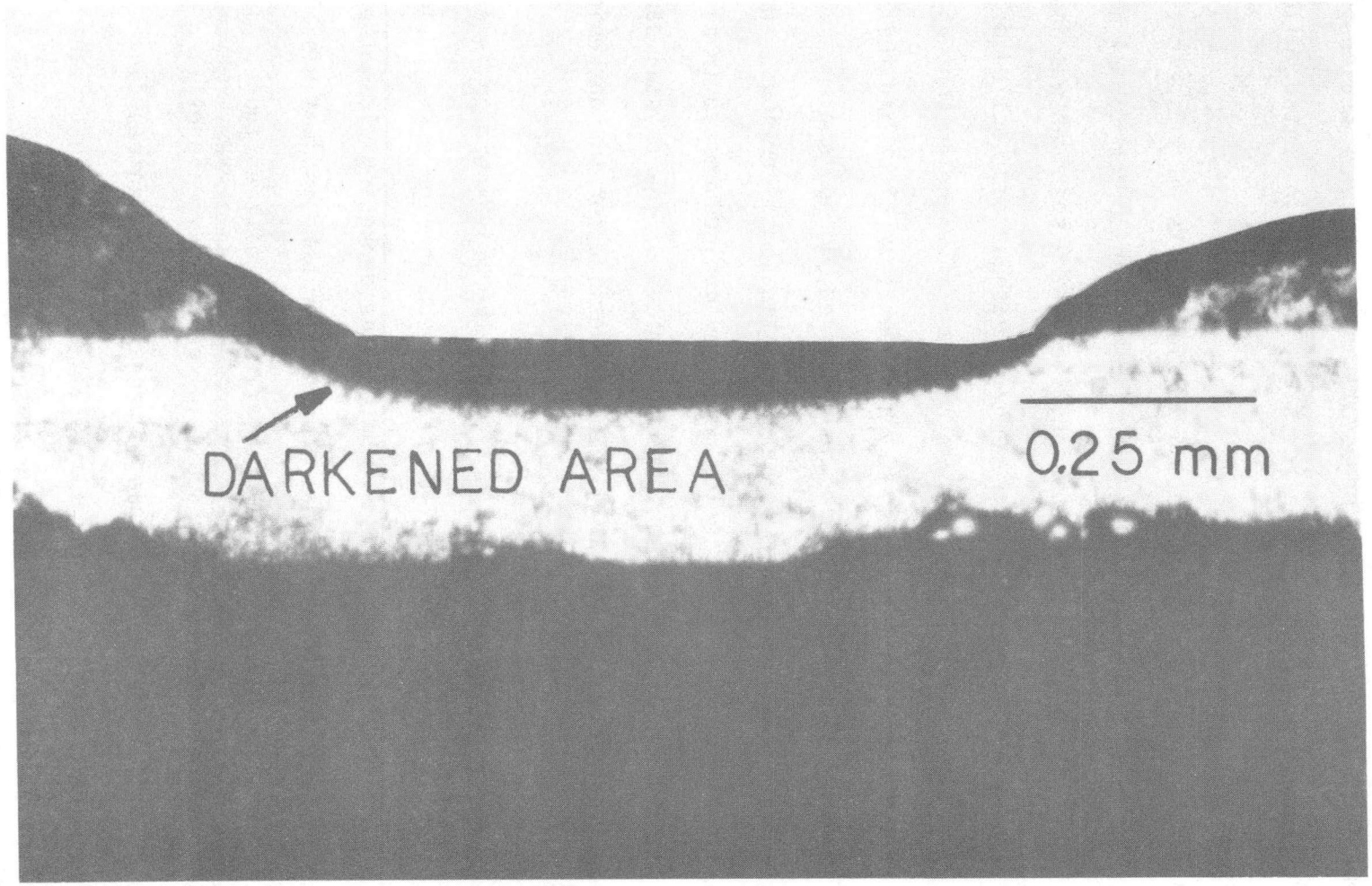

XBB 813-2316

Fig. 4.15 Cross section of actual sample with sealed conduction planes after sodium immersion and silver exchange. Darkening has penetrated the crystal through the exposed spinel block side.

At 250°C, however, a substantial amount of bleaching has occurred in the central clear band widening it considerably. This suggests that a change takes place in the oxygen transport mechanism in the 250-300°C temperature range. It would be consistent with the observed results if relatively rapid oxygen transport in the conduction planes were possible below this transition temperature, and a much slower transport above. There are two possible ways this might come about: a simple, reversible change in the conduction plane oxygen diffusion mechanism, or a reaction or structural change taking place at the transition temperature which permanently alters the conduction plane oxygen mobility. The results of the dual temperature phase bleaching experiment as shown in Figure 4.16 support the existence of a permanent change in the conduction plane oxygen mobility at a transition temperature between 250 and 300°C. The progress of the bleached layer in the sample subjected initially to 350°C for 24 hours is about 13 μm less than would have been expected. The bleached layer produced at 350°C acts as a low mobility barrier for oxygen entering the conduction planes of the crystal.

The behavior of the bleaching evident in Figures 4.11 and 4.14 can now be understood as follows. At 250°C and below, the oxygen moves through the conduction planes to recombine with the oxygen vacancies in the spinel blocks. More complete bleaching develops in the central region of the crystal in this temperature range, because oxygen can enter through the surfaces of the crystal created by sectioning the parent crystal after immersion (see Figure 4.1) and reach this region where the concentration of coloration defects is much less than near the edges. Between 250°C and 300°C an irreversible change takes place

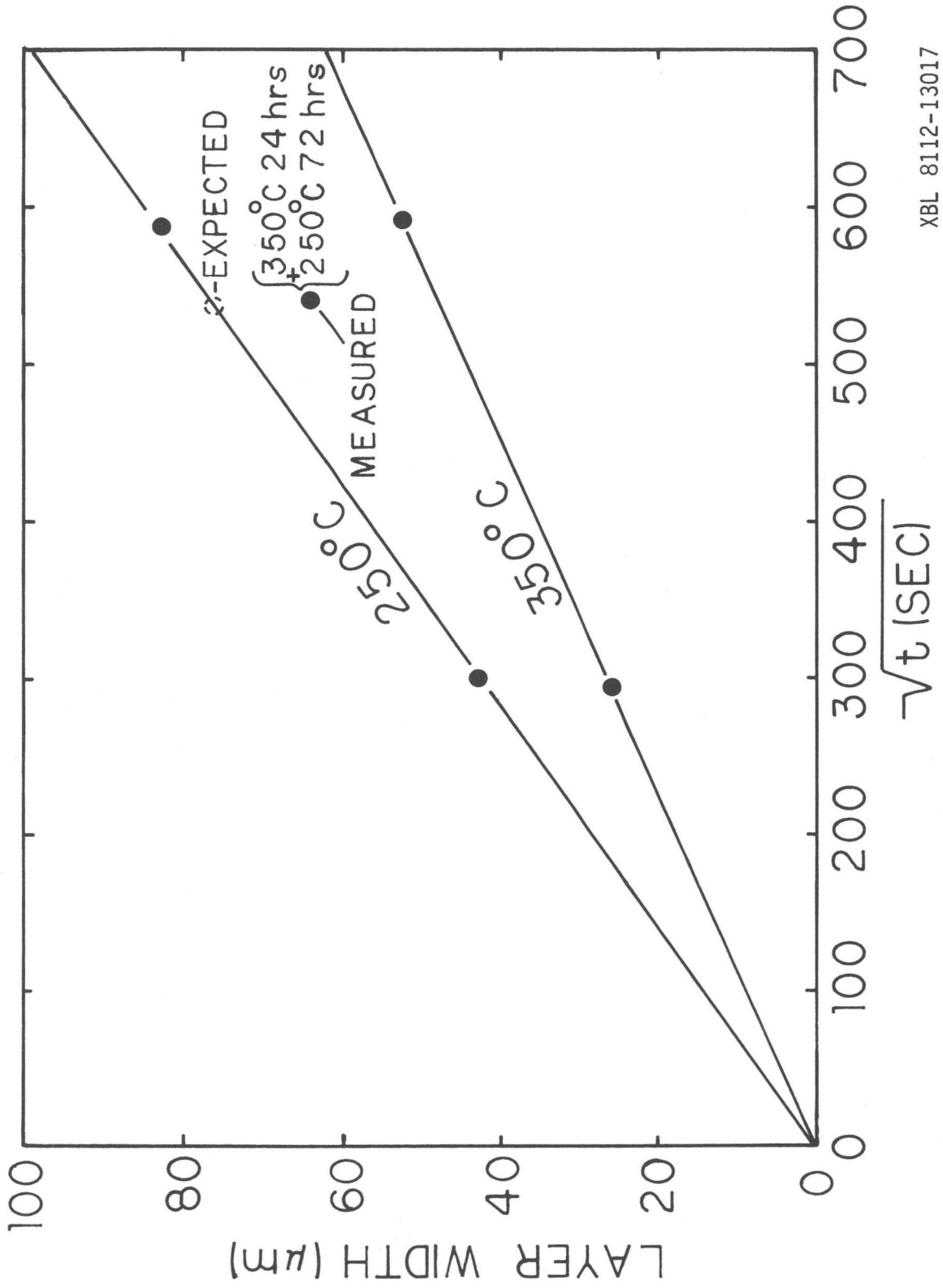

Fig. 4.16 Dual temperature phase bleaching kinetics.

in the bleached region of the crystal which causes the oxygen transport in the conduction planes to drop substantially. At the same time the mobility of the coloration defects in the spinel blocks is also increasing. A gradual transition thus takes place from sharp interface layer bleaching to a diffuse interface bleaching; and at higher temperatures (cf. 500°C in Figure 4.14) an overall reduction is seen in the density of the region remaining darkened, because now the coloration defects are moving out to the interface from the darkened region of the crystal as well as oxygen moving in. The increase in the rates of both processes with temperature results in the overall bleaching rate increasing with temperature again at some point above the transition temperature.

4.3.7 Mechanisms of Coloration and Bleaching in Single Crystals

The results of the coloration and bleaching experiments reported in single crystals lead to the following conclusions concerning the probable mechanisms involved. Coloration of the crystals occurs because oxygen vacancies are created at the surface of the beta alumina crystal when it is immersed in sodium (oxygen fugacity $\sim 10^{-58}$ atm at 350°C). These vacancies then diffuse into the crystal through the spinel blocks. The vacancies have a double positive effective charge and are charge compensated by electrons in a reaction which can basically be written:

$$O_O^X \rightarrow 1/2\ O_2 \uparrow + [V_O^{\cdot\cdot} + 2e'] \qquad 4.4$$

The electrons are believed to remain loosely bound to the vacancy, hence the brackets in expression 4.4, so that the electron/vacancy

complex acts as a shallow donor, increasing the electronic conductivity. This is consistent with the observation of Weber (We 74) that there is an increase of about a factor of 100 to 1000 in the electronic conductivity of polycrystalline beta aluminas which have been darkened by contact with sodium at high temperature. There may be some redistribution of the sodium ions around the electron/vacancy complex accounting for the broad optical absorption producing the gray coloration. The loosely bound electron also makes the defect reducing in its chemical properties which accounts for the precipitation of metallic silver in the colored region during silver ion exchange.

The asymmetry of the bleaching implies a very great difference in the behavior of oxygen transport in the spinel blocks and in the conduction planes. It also implies that there is a very great dependence of diffusion rate on oxygen partial pressure in the spinel blocks. At very low oxygen partial pressures, it appears that oxygen vacancy injection can occur in the spinel blocks from the crystal surfaces; but under oxidizing conditions, the oxygen vacancy concentration in the spinel blocks near the surface of the crystal is so low as to suppress oxygen ion transport in them almost entirely, so that the bleaching layer grows very slowly. The more open structure of the conduction planes should not be as strongly affected by the oxygen partial pressure. The layer like advance of the coloration is consistent with this explanation, because a strong dependence of the vacancy diffusion rate on the oxygen partial pressure would lead to a fairly abrupt change in the vacancy concentration profile. During the bleaching, oxygen enters the crystal primarily through the conduction planes and transfers from there to the spinel blocks where it annihilates the

coloration defects. It is proposed that the conduction plane free interstitial oxygens, and oxygen interstitials associated with the Roth type defects, described in Chapter 1, in beta alumina are crucial to oxygen transport in bleaching. In the "Roth defect" there are two aluminum interstitial-vacancy pairs in the adjacent spinel blocks associated with the oxygen on the midoxygen site in the conduction plane. During coloration as oxygen vacancies are formed in the spinel blocks, and as conduction plane oxygen interstitials are removed from Roth defects, the Al^{3+} interstitial-vacancy pairs recombine. Reentering interstitial oxygens in the conduction plane would then be more mobile until they are trapped again in a Roth defect. During bleaching the aluminum vacancy-interstitial pairs necessary for the formation of Roth defects cannot be reestablished until the threshold temperature, between 250°C and 300°C, is reached, even if sufficient oxygen is present to destroy the coloration defects.

4.3.8 Photodarkening of Beta" Alumina by UV

The role of electronic defects in darkening in silver beta" alumina was demonstrated by holding a silver ion exchanged piece of "10 μm" beta" alumina in a beam of ultraviolet light for about 4 minutes. The central part of the surface in this specimen was masked, and so the clear region under the mask stands out in sharp contrast to the darkened region in Figure 4.17. The surface had been polished before exposure to insure that effects were not simply due to residual silver nitrate on the surface from the ion exchange treatment. The darkening fades noticeably after 8-10 weeks at room temperature. The darkening can be bleached entirely by heating the UV irradiated sample to 400°C

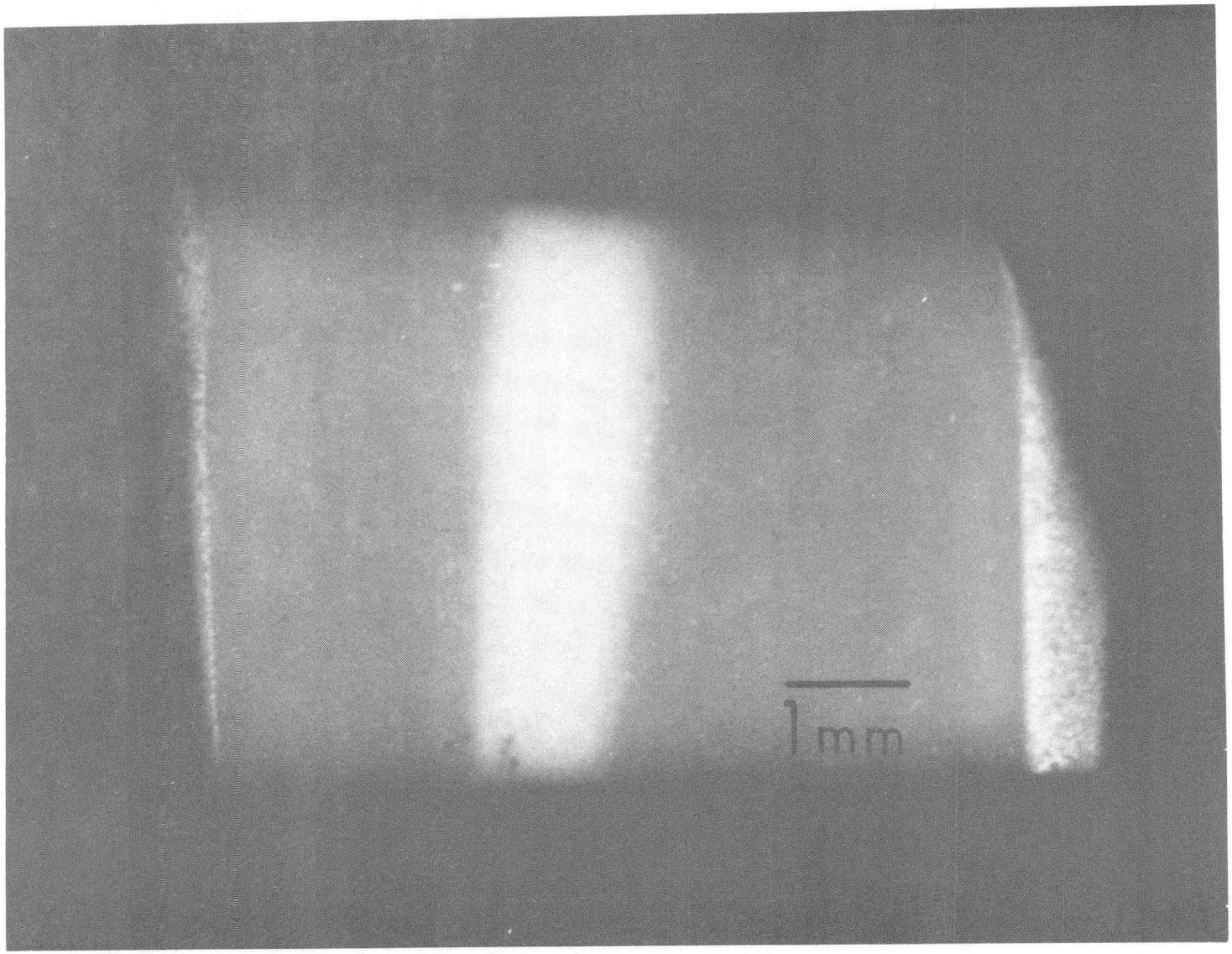

XBB 807-8868

Fig. 4.17 Photodarkened silver beta" alumina polycrystalline electrolyte. Note lack of coloration where forceps masked specimen.

for about 4 hours, after which it can be darkened again. The process is analogous to that occurring in photographic materials in which a photo-electron is captured to form metallic silver leaving an electron hole. Attempts to darken sodium beta and beta" alumina with ultraviolet light failed, showing that sodium ions in these materials do not readily trap electrons, and that therefore it is unlikely that a simple sodium ion-electron pair defect can account for the chemical darkening observed.

4.3.9 Kinetics of the Advance of the Darkened Layer in Polycrystalline Electrolytes

The results of the darkened layer growth measurements in the polycrystalline material are plotted in Figure 4.18 versus the square root of time; this was done for the "10 μm" material and for the 4, 8, and 16 day specimens of the "150 μm" material only. Penetration in the remaining specimens was not deep enough to permit accurate measurements. A parabolic time dependence of penetration applies, indicating diffusion control. For a given time of immersion, the darkened layer thickness decreased as the nominal grain size increased. Figure 4.19 presents a comparative view of the darkened cross sections of the 16 day immersion set. The grain boundaries act as rapid transport paths for the defects responsible for coloration. The effective diffusion coefficients are tabulated in Table 4.3. The normalized concentration profiles are shown in Figures 4.20 and 4.21. The "10 μm" material, after one day in molten sodium, gives almost a perfect error function dependence, but at longer times there is an increase in the slope of the normalized plot at the interface ($C = 0.5 \times C_o$). This sharpening is also seen in

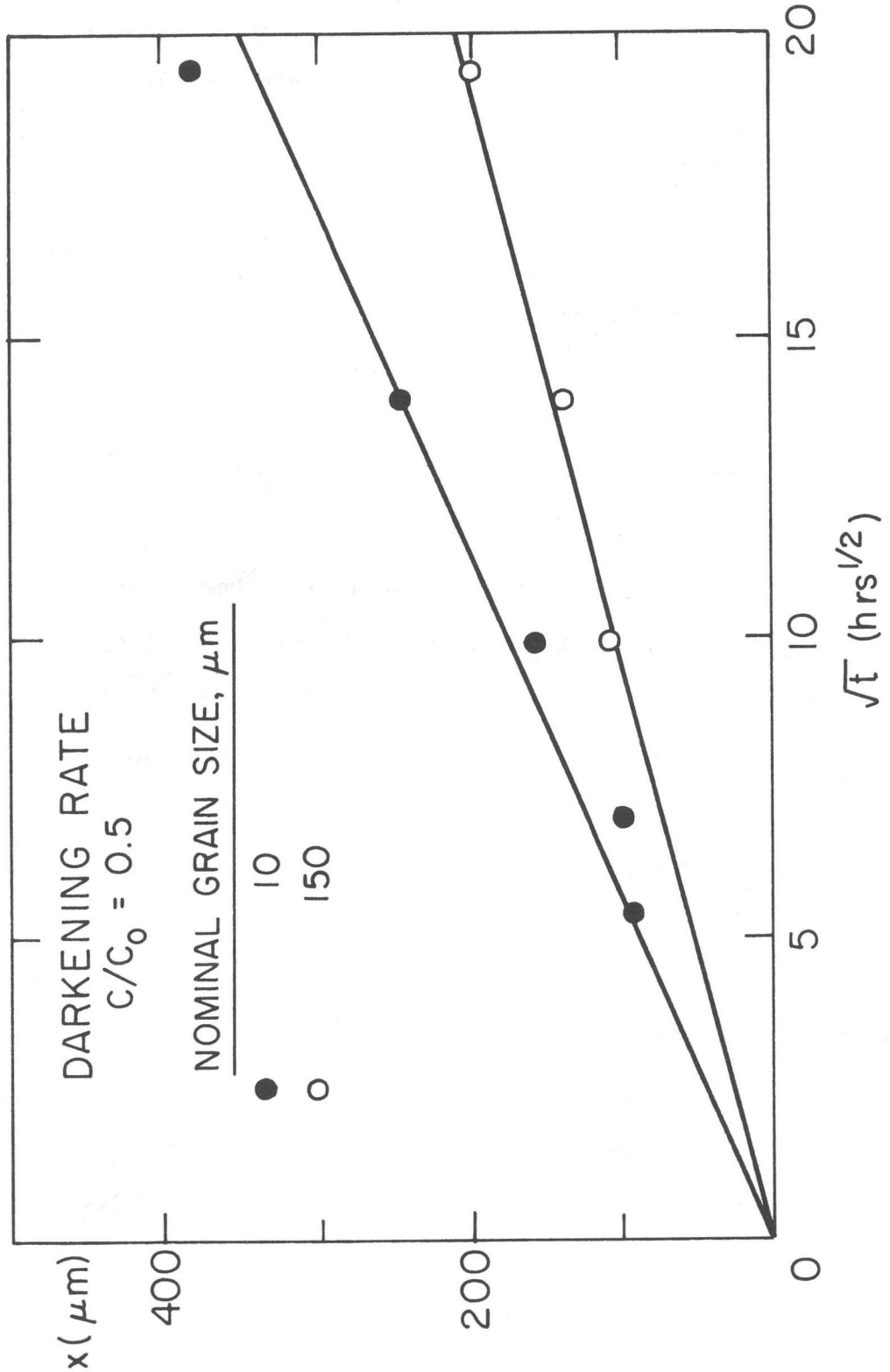

XBL 812-5137

Fig. 4.18 Darkening kinetics of polycrystalline electrolytes.

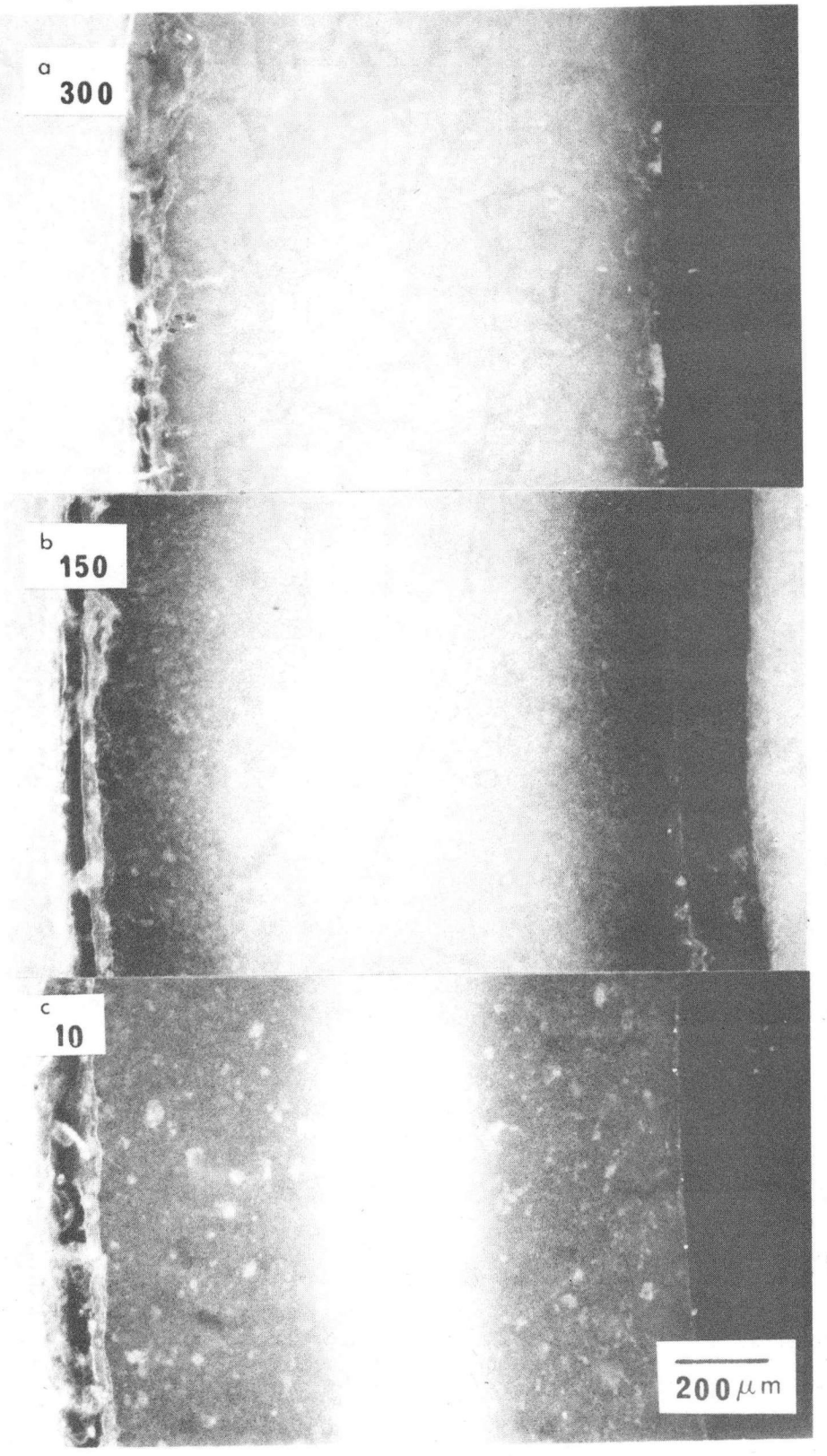

XBB 807-8889

Fig. 4.19 Polished cross sections of silver exchanged colored polycrystalline electrolytes immersed 16 days.

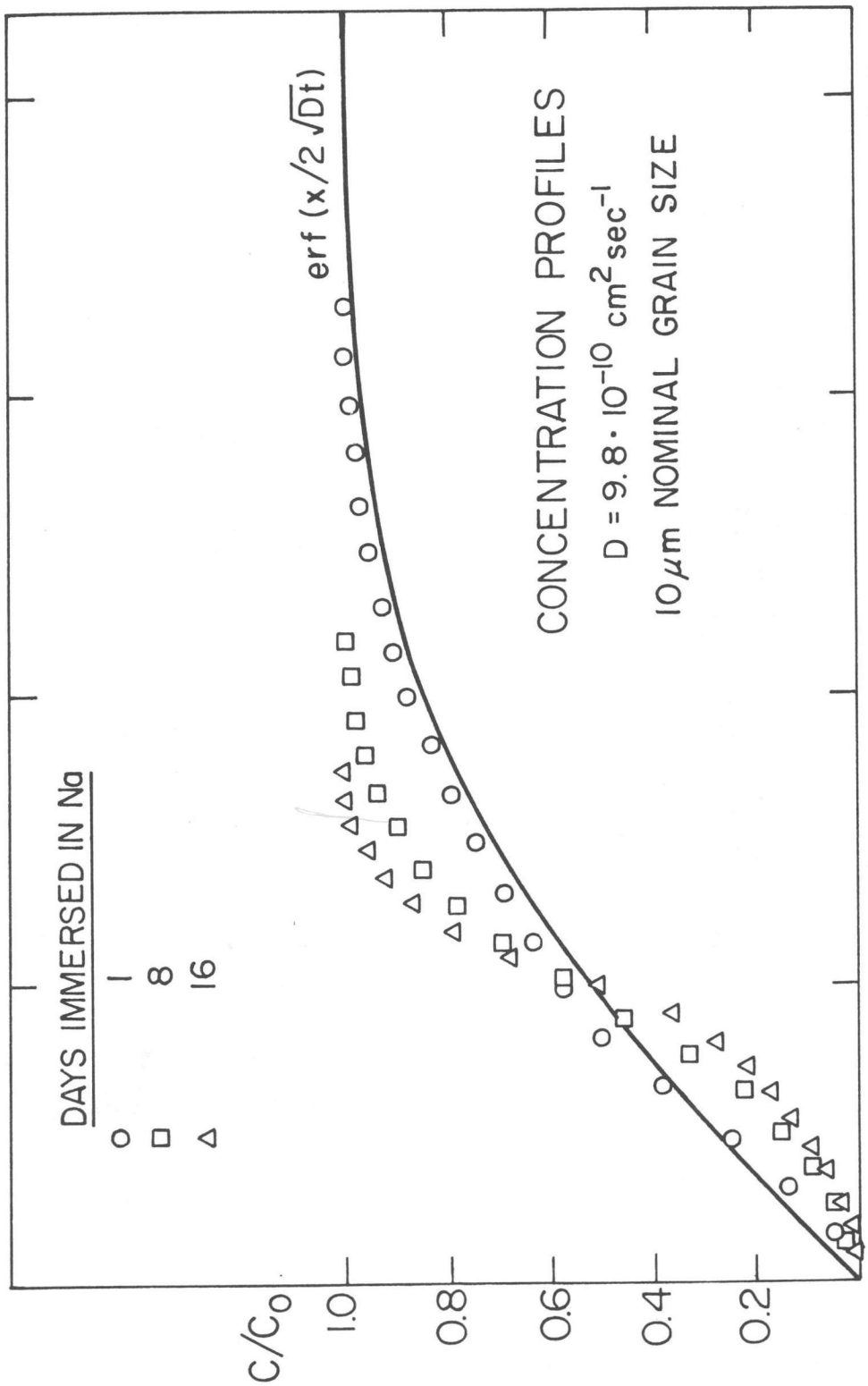

Fig. 4.20 Normalized concentration profiles in 10 μm electrolyte.

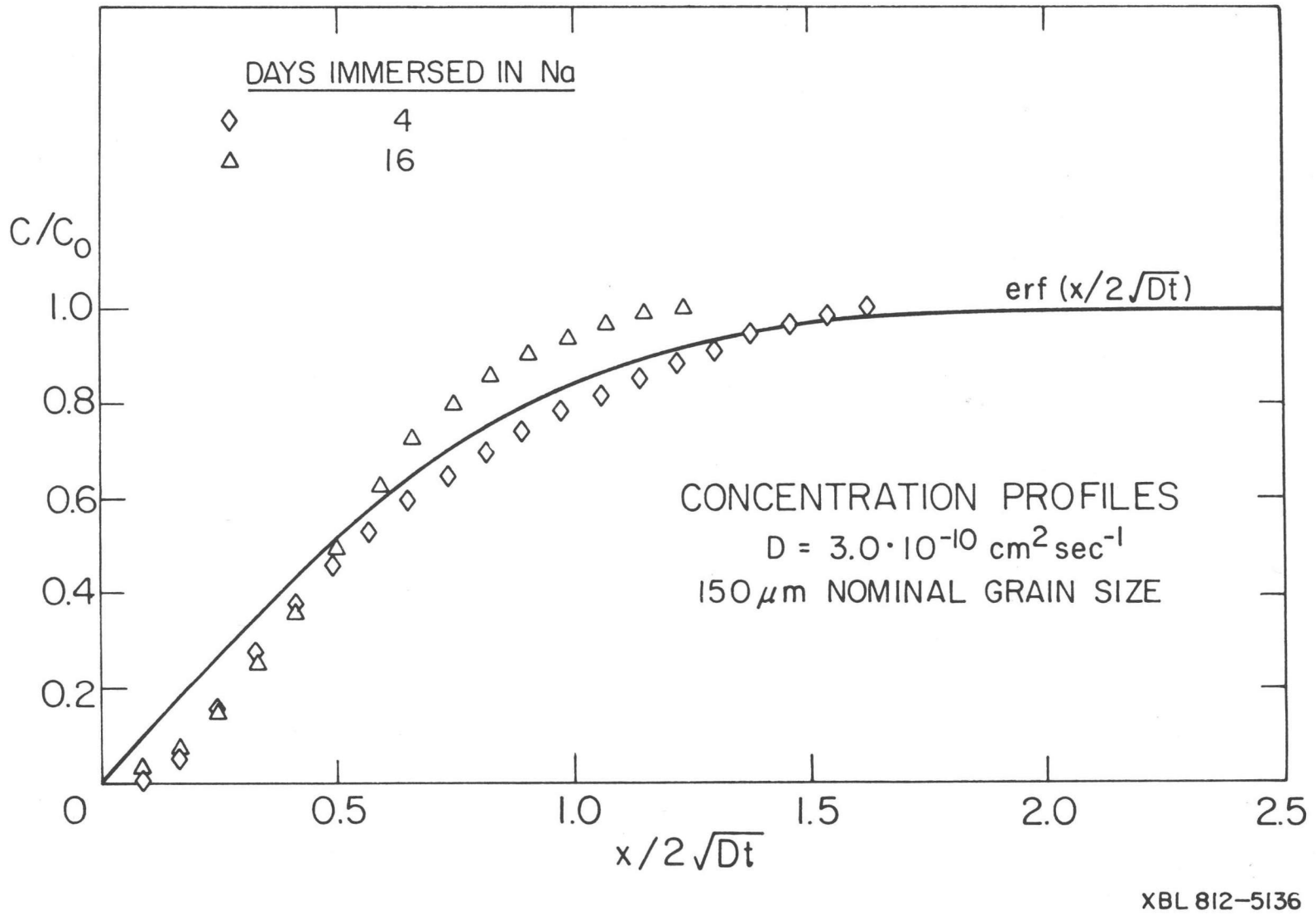

Fig. 4.21 Normalized concentration profiles in "150 μm" electrolyte.

Table 4.3: Polycrystalline Beta" Alumina Coloration Kinetics Data

Nominal grain size	D_E (cm^2 sec^{-1})	Average grain size
10 μm	9.8×10^{-10}	1.1
150 μm	3.0×10^{-10}	5.4

the "150 μm" material. Such a steep rise of the concentration profile with time is usually associated with a concentration dependence of the diffusion coefficient. This is consistent with the findings of the single crystal experiments.

An analysis first done by Hart and later expanded by others (Ha 57, Ha 61, Ca 79) can be applied to the data in Table 4.3 to evaluate the approximate bulk and grain boundary transport rates. The analysis may be applied if the penetration distance is much larger than the average grain size, a condition which is satisfied here. A lattice diffusion coefficient, D_L, which differs substantially from the grain boundary diffusion coefficient, D_B, will lead to an effective diffusion coefficient, D_E, which, according to the Hart analysis, is given by:

$$D_E = D_L + B\delta D_B/s \qquad 4.5$$

where B is a parameter of order 1 dependent on the grain geometry, δ is the grain boundary thickness, and s is the average grain size. In the present instance, D_L and D_B in equation 4.5 must be replaced by the respective scaling constants K_L and K_B. Then, taking B = 1 and δ = 10 Å gives:

$$K_L \leq 1.0 \times 10^{-10} \text{ cm}^2 \text{ sec}^{-1}$$

$$K_B = 9.8 \times 10^{-7} \text{ cm}^2 \text{ sec}^{-1}$$

In single crystal beta alumina the scaling constant was:

$$K_L = 3.41 \times 10^{-10} \text{ cm}^2 \text{ sec}^{-1}$$

K_L for the polycrystalline beta" alumina was obtained by the simultaneous solution of two equations of the form of equation 4.5, one for each set of data listed in Table 4.3 for the two different average grain sizes. Since K_L is much smaller than K_B, it is highly sensitive to slight errors in the average grain size, s. This fact and the lack of evidence for penetration of coloration into the large grains (section 4.3.10) indicates that the value of K_L determined here is only an upper bound. The ratio of grain boundary to lattice diffusion coefficients, D_B/D_L, is at least 10^4 indicating that grain boundary diffusion dominates coloration in polycrystalline electrolytes. The increase in electronic conductivity associated with the darkening will therefore develop first along grain boundaries; thus it is likely that grain boundaries and junctions will act as preferred sites for mode II breakdown. Since mode II breakdown occurs only in the presence of an electronic conductivity gradient, a rough calculation of the time required to establish a homogeneous state of darkening in an electrolyte tube was made. For "10 μm" material with a 2 mm wall thickness in contact with sodium at 350°C the value is about 0.5 year. However, in an actual cell the oxygen fugacity in the sulfur electrode is likely to be higher than that in the sodium electrode; this may lead to a permanent electronic conductivity gradient across the electrolyte tube wall.

4.3.10 Large Grain Behavior During Polycrystalline Electrolyte Coloration

In view of the similarity in average grain size (see Table 3.1) for the "150 μm" and "300 μm" material, one would expect deeper penetration of darkening than was observed in the "300 μm" material (see Figure 4.19). Recall, however, that the large grains in the "300 μm" material form a continuous network, in contrast to the situation in the "150 μm" material where they are scattered in a fine grain matrix. This continuous network probably presents a barrier to the rapid penetration of darkening.

A few thin sections of the "300 μm" and "150 μm" materials darkened for 16 days were prepared and examined in the optical microscope by transmitted polarized light. No evidence of light polarization (and hence, darkening) was found within the large grains, even in those at the surface of the tube where the surrounding fine grain material was heavily darkened. The darkening of beta" alumina crystals must therefore occur much more slowly than that of beta alumina crystals. This may possibly have some connection to the lack of conduction plane interstitial oxygen ions in beta" alumina. Such interstitials may interchange rather freely with oxygen vacancies in the spinel blocks in beta alumina facilitating the transport of the coloration defect across the conduction plane. With no conduction plane oxygen interstitials in beta" alumina, the oxygen must either jump all of the way across the conduction plane, or move across by way of the column oxygens which probably have much less mobility. There is an implication here that the coloration in beta" alumina would be more anisotropic than in beta. The darkening might be expected to propagate more rapidly perpendicular

to the [c] direction than parallel to it. No single crystals of beta" alumina were available to test this hypothesis.

4.3.11 Sodium Content and Ionic Conductivity in Colored and Bleached Polycrystalline Electrolytes

The results of the soda content and conductivity measurements are summarized in Table 4.4, and the complex admittance plots from which the D.C. conductivities at 350°C were calculated are shown in Figure 4.22. The variations in soda content overlap within the limits of uncertainty, although there is a slight hint of a trend toward lower soda content as one immerses, then bleaches. The D.C. conductivities obtained from the complex conductivity plots also overlap within the limits of uncertainty, but here too there is a suggestion in the data that immersion leads to a slightly higher resistivity. One would expect a higher resistivity for a lower soda content, so the results are at least consistent here. The most probable interpretation is, however, that there is no statistically significant change in soda content or D.C. conductivity due to immersion and/or bleaching. The possible slight loss of soda and corresponding increase in resistivity can be attributed to the effects of moisture absorbed when the sample was washed with alcohol or exposed to air between steps of the process.

4.4 Summary and Conclusions

- Chemical coloration in the beta aluminas is due to the reduction of the electrolyte by the molten sodium electrode.

- The coloration is due to the creation of oxygen vacancies, which are compensated by electrons, in the spinel blocks.

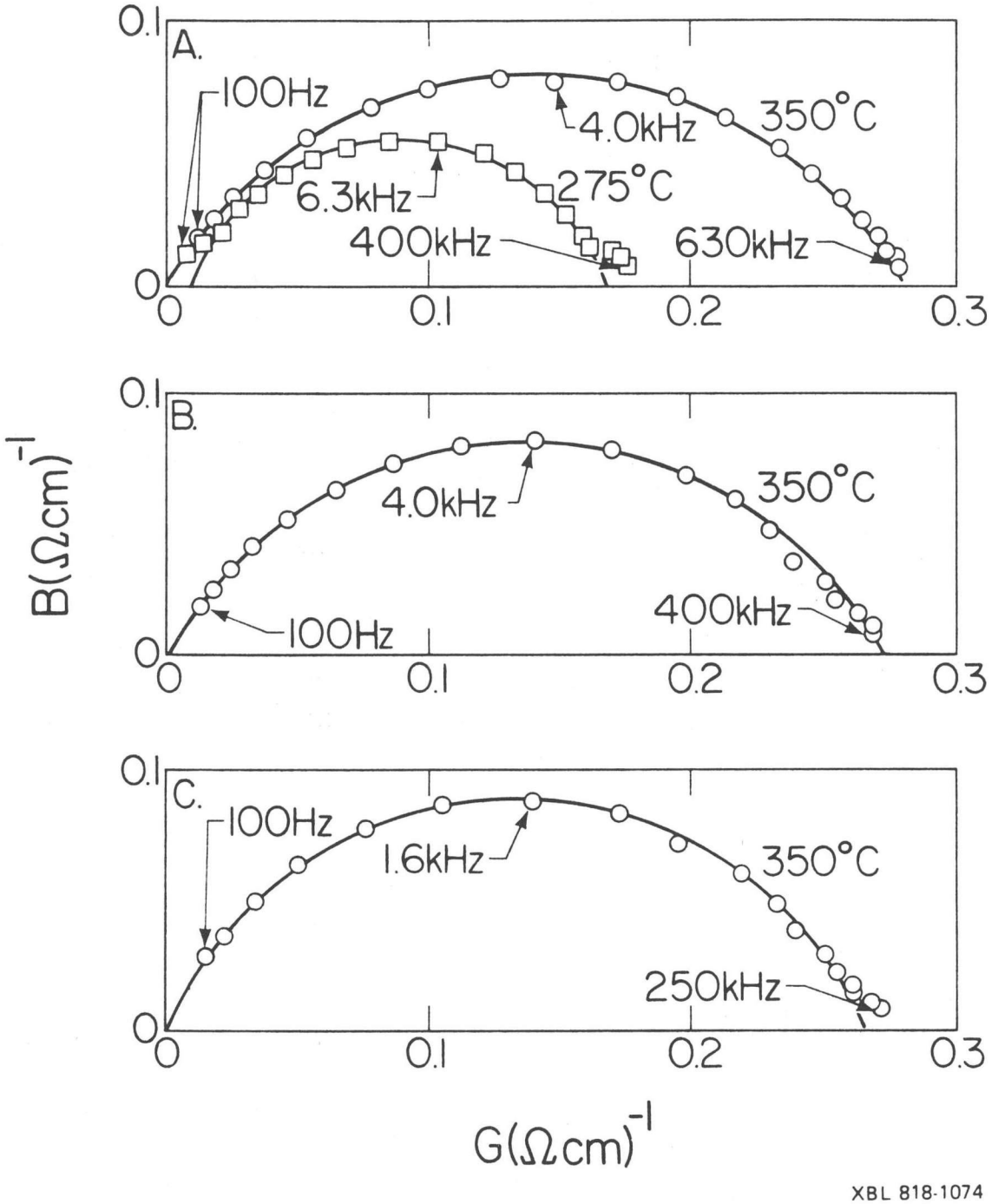

Fig. 4.22 Admittance plots for polycrystalline electrolyte: A. as received B. after 388 hours immersion in sodium at 350°C C. immersed as in B and then bleached 56 hours at 800°C.

Table 4.4: Soda Content and Conductivity Data for Polycrystalline Material

Sample	Weight% Na_2O	D.C. Conductivity	
		at 200°C	at 350°C
As received	8.74± 0.02%	12.8± 0.5Ωcm	3.5± 0.2Ωcm
Immersed in Na for 388 hrs. at 350°C	8.73± 0.02%	13.2± 0.5Ωcm	3.7± 0.2Ωcm
Immersed in Na for 388 hrs. at 350°C and bleached 56 hrs. at 800°C	8.72± 0.02%	13.1± 0.5Ωcm	3.8± 0.2Ωcm

- Coloration progresses almost isotropically in single crystals of beta alumina with a parabolic time dependence indicating diffusion control.

- Progress of coloration into single crystallites of beta" alumina was found to be much slower than into single crystals of beta alumina.

- The mobility of the coloration defects, and hence the rate of coloration, increases with temperature.

- Bleaching, or reoxidation, of the crystal proceeds mainly through the conduction planes.

- The rate of bleaching in single crystals increases with temperature, but there is a local maximum in the vicinity of 250°C. At this temperature an irreversible decrease begins in the conduction plane oxygen mobility in the bleached region of the crystal.

- The model proposed to explain the local maximum in the bleaching attributes a lower mobility to the conduction plane oxygen interstitials trapped in the "Roth defects". Some of these defects are destroyed during coloration. Restoration of these defects, during bleaching (reoxidation), does not occur until a transition temperature is reached around 300°C.

- Water plays no role in either the coloration or the bleaching reaction.

- In polycrystalline beta" alumina electrolytes coloration proceeds preferentially along grain boundaries.

- The chemical coloration introduces an electron/ion transport number gradient which can lead to mode II degradation in electrolytes used in sodium/sulfur cells.

5. SODIUM/SODIUM CELL TESTING

5.1 Introduction

In the mode I degradation process, initial flaws or cracks in the surface of the electrolyte grow by way of Poiseuille pressure generated stresses which exceed the critical stress intensity factor. The sudden release of strain energy in a material under such conditions will be accompanied by acoustic emissions. These emissions can be detected using piezoelectric transducers and processed electronically to provide information about the progress of failure.

Worrell and Redfern (Wo 78) have reported the successful use of acoustic emission monitoring to detect degradation during sodium/sodium cell cycling in two separate experiments. In the first, a magnesia-lithia composition beta alumina tube was used and cycled first at 1.0 A cm^{-2} and then at 2.0 A cm^{-2}. Acoustic emissions were detected from the outset of testing and their rate increased when the current density was increased. After 200 Ahr cm^{-2} of charge transfer, the acoustic count rate increased further and the faradaic efficiency of the cell began to decrease. The cell was removed from service at this point and its electrolyte was found to be penetrated by many dendrites. In the second experiment a lithia composition beta alumina tube was cycled at 0.5 A cm^{-2} to 44 Ahr cm^{-2} of charge transfer. No acoustic emissions were detected during this period. The current density was then raised to 2.0 A cm^{-2} and acoustic emissions were then detected, initially at a low rate and then at a gradually increasing rate as more charge was passed by the cell. These results indicate the feasibility

of using acoustic emissions techniques in determining critical current densities for the activation of mode I degradation processes.

Prior to the experiments of Worrell and Redfern, the only data reported on critical current density for electrolyte failure had been obtained by analyzing the lifetime and electrical history statistics of sodium/sulfur cells, or by fracturing specimens of electrolyte which had been cycled under specified conditions in specially prepared cells. The experiments of Tennenhouse et al. (Te 75) fall into this latter category. Sodium was electrolyzed through disks of lithia composition beta" alumina from a salt melt on the positive side of the electrolyte to a sodium-mercury amalgam on the negative side. Bars were then cut from the disks and fractured in four point bending to determine their strength with the sodium exit surface in tension. A decline in strength from the virgin material indicated that flaws had been generated or enlarged by the conditions of electrolysis the sample had been subjected to. Specimens fractured with the sodium entrance side in tension showed no decline in strength, indicating that flaws only develop or enlarge at the surface where sodium exits.

Acoustic emission testing can add a valuable dimension to electrolyte testing, because, in principle, if the detection system is adequately sensitive, it can record the first occurrence of cracking in real time, so that it can be correlated with the precise cell conditions applying at that moment. This chapter will describe how acoustic emission methods were employed to monitor crack growth during electrolysis of sodium/sodium cells, and how the technique was used to determine the effect of electrolyte microstructure on critical current density for crack growth.

5.2 Experimental

5.2.1 Cell Construction

The electrolyte tubes from Ceramatec were sectioned under kerosene on a diamond saw to produce cylindrical rings about 1 cm high. These were closed at one end by sealing them to high purity alumina (Coors AD-998) discs using Owens-Illinois IN-3 sealing glass. A slurry of the glass frit in ethyl alcohol was painted on to the region to be sealed and the cell assembly heated to 800°C and held there for at least 30 minutes to melt the frit. The temperature was then lowered to 521°C and held there for at least an hour to anneal the seal. These capped electrolyte sections were then sealed to 15 cm lengths of 19 mm O.D. high purity alumina (also Coors AD-998) tubing using the same procedure as for capping. A portion of the electrolyte surface was normally masked off with the IN-3 glass also so that the desired current densities could be attained with available equipment. Figure 5.1 shows a cutaway view of a completed cell.

5.2.2 Cell Cycling Equipment

Current for the tests was provided by a low ripple D.C. power supply. For some of the pilot tests this current source was used directly, but polarization occurring in the cell made it impossible to maintain acceptable control of either the current or voltage. Therefore, a simple circuit was designed employing monolithic integrated circuit operational amplifiers to drive the cells through a Darlington pass element. Figure 5.2 is a functional block diagram of the system used and Figure 5.3 shows a schematic diagram of the actual electronic

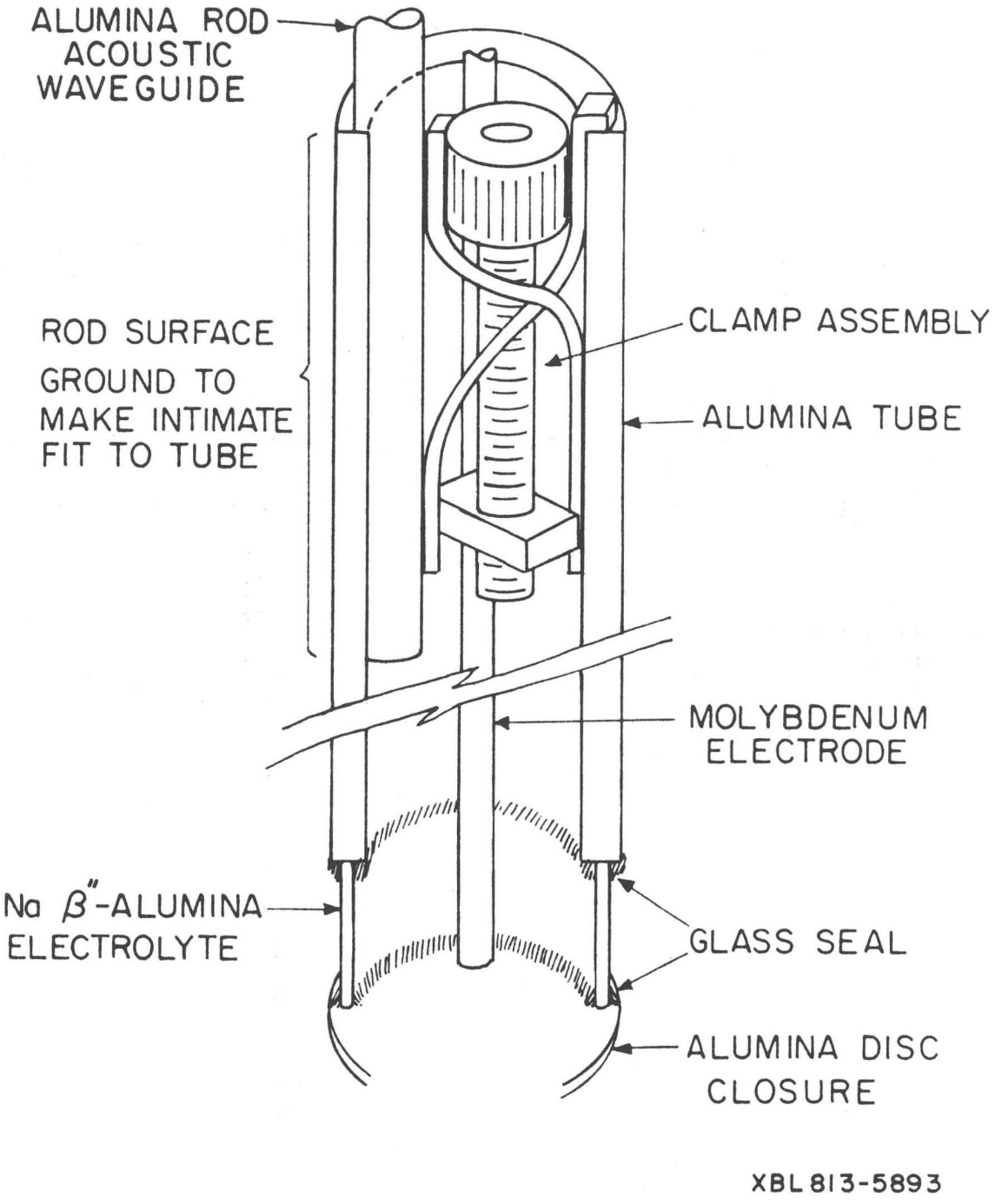

Fig. 5.1 Cut away view of sodium/sulfur cell showing mode of construction and attachment of acoustic waveguide.

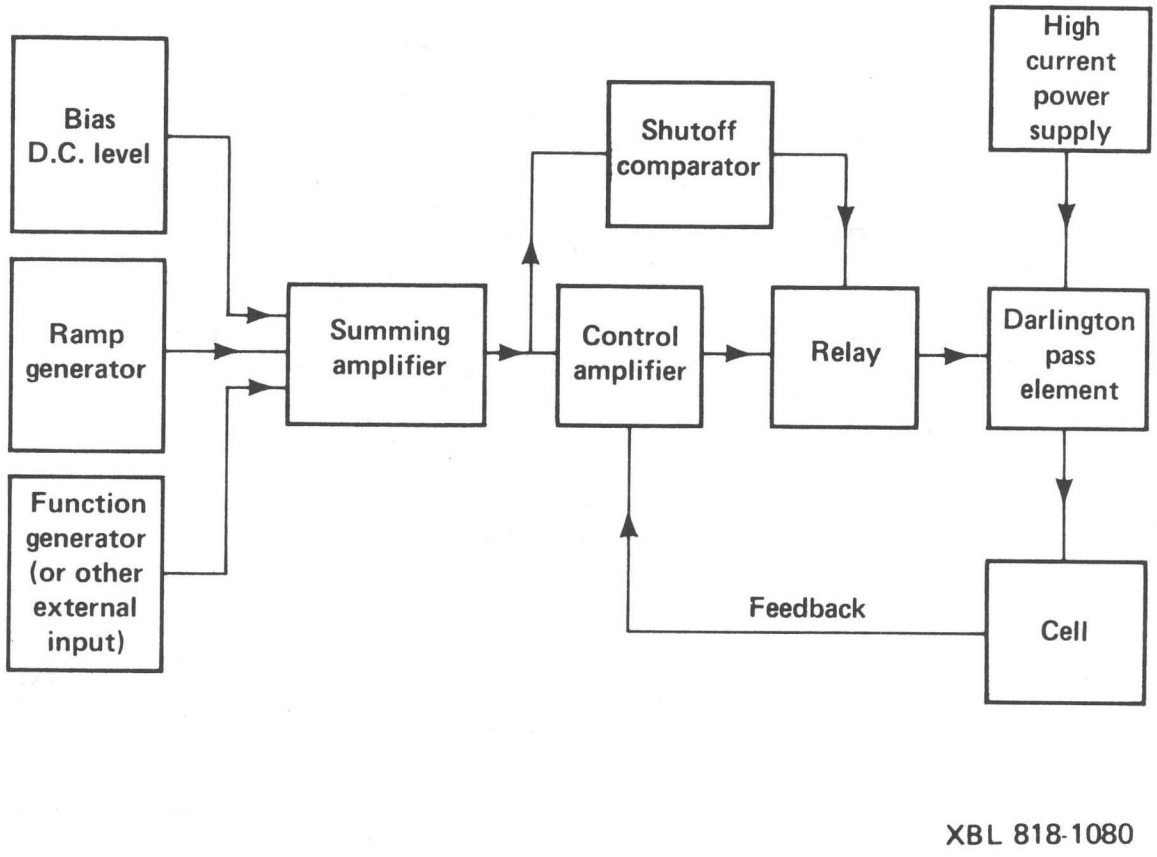

Fig. 5.2 Block diagram of control amplifier.

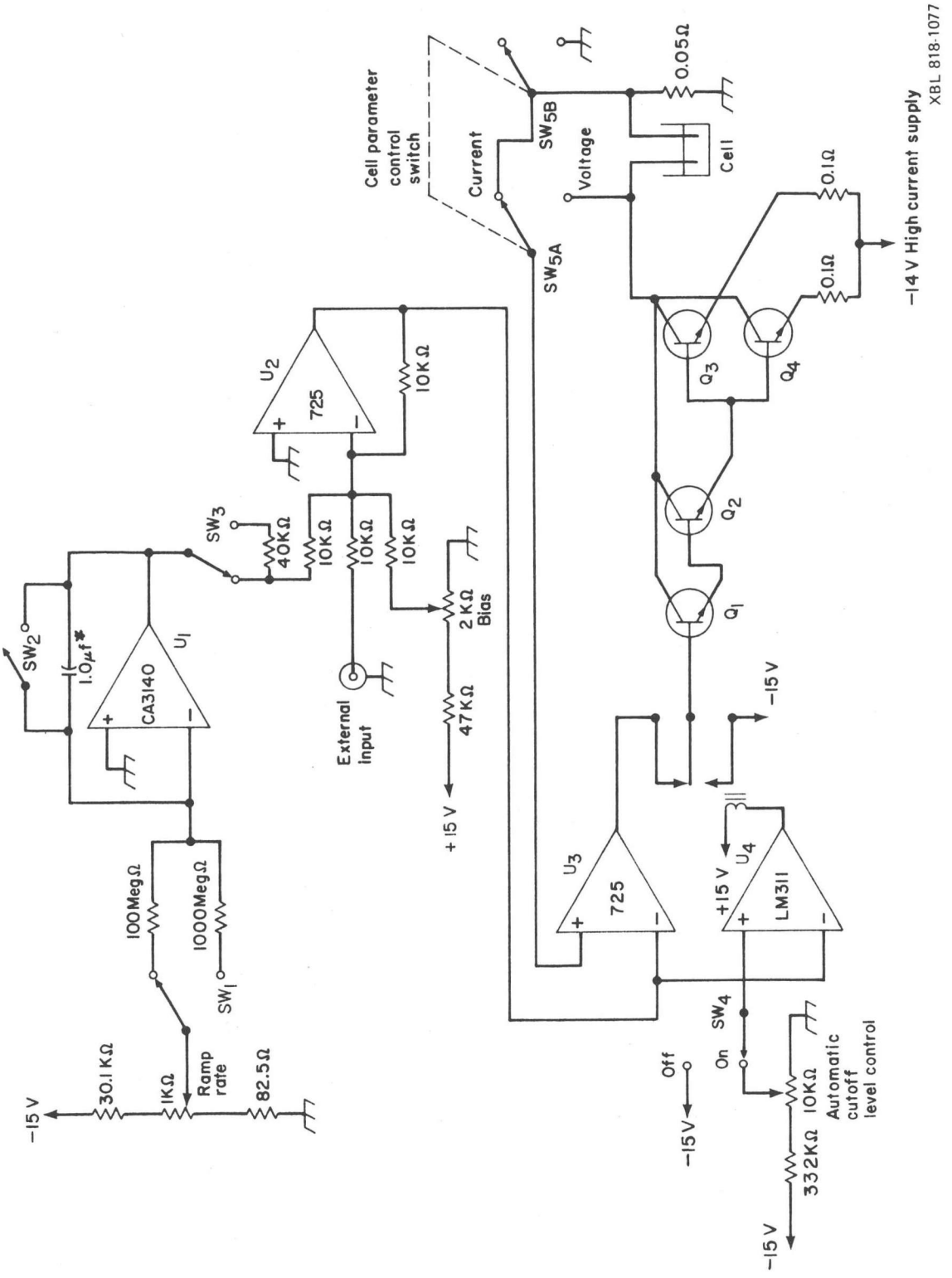

Fig. 5.3 Schematic diagram of control amplifier. Q_1 = 2N3019, Q_2 - Q_4 = 2N3716, *polystyrene.

circuitry. The system uses an input voltage to program either the output current or voltage to the cell. The current control mode was used exclusively in these experiments.

The summing amplifier made it possible to use a variety of sources simultaneously to program the output current. The bias control designed into the system employed a ten turn potentiometer to provide relatively fine manual adjustment of cell current. A panel jack to one of the summing inputs made it possible to connect any of a number of external programming devices (e.g., function generator, microcomputer + D/A converter) to the system. Ramping of cell current was the most frequently used mode of testing and very slow ramp rates were desired. Consequently, a long term integrator utilizing a high input impedance monolithic op-amp (CA-3140), polystyrene capacitor, and high value integrating resistors was built into the system. The integrator could achieve a minimum ramp rate of 50 $\mu A\ sec^{-1}$ which made possible cell current density ramp rates down to 1 $mA\ cm^{-2}sec^{-1}$ in cells constructed with active areas as small as 0.05 cm^{-2}.

Operating in the programmed current mode, the control amplifier senses the voltage fed back to its non-inverting input from the 0.05 ohm current sensing resistor in series with the cell under test and compares it with the voltage at the programmed (inverting) input. The output current from the control amplifier to the base of the darlington pass element responds to keep these voltages equal, thus maintaining the programmed current in the cell circuit.

The automatic shutoff circuit shown using a LM 311 monolithic comparator and small relay was incorporated in the system to allow for shutdown of the test at some predetermined current level.

5.2.3 Cell Cycling Procedure

For cycling, the cells were clamped into a holder which was in turn fastened to the top of the sodium pot in the glove box. The cells were preheated to about 125°C and then filled with and immersed in sodium at the same temperature. The system was then gradually heated up to 350°C. Electrodes of molybdenum wire, to provide electrical contact with the sodium in the system, were secured to ceramic insulators mounted on the cell holding assembly, as shown in Figure 5.4. The acoustic transducer and waveguide are also visible in this figure.

Most of the cells were tested at 350°C and all cells tested were first heated to this temperature to insure wetting of the surface of the electrolyte by the molten sodium. It was also found helpful to subject the cells to several minutes of current flow at 5 to 10 mA cm^{-2}. During the first few minutes of this treatment, the apparent resistance of the cell dropped and then quickly stabilized as complete wetting was achieved.

After preconditioning, the cells were subjected to the desired program of charge transfer. Modes of testing included: manual stepping of the current density (first 9 cells + 4 others), triangle wave current ramping at different amplitudes up to about 10 A cm^{-2} with a period of about 100 seconds (7 cells), A.C. on D.C. (one cell only), and long term ramping usually at about 1 mA cm^{-2} sec^{-1} (25 cells).

5.2.4 Acoustic Emission Equipment and Techniques

For most tests an acoustic transducer was attached to the cell. Good acoustic coupling to the cell was essential, and several schemes were tried before the arrangement shown in Figures 5.1 and 5.4 was

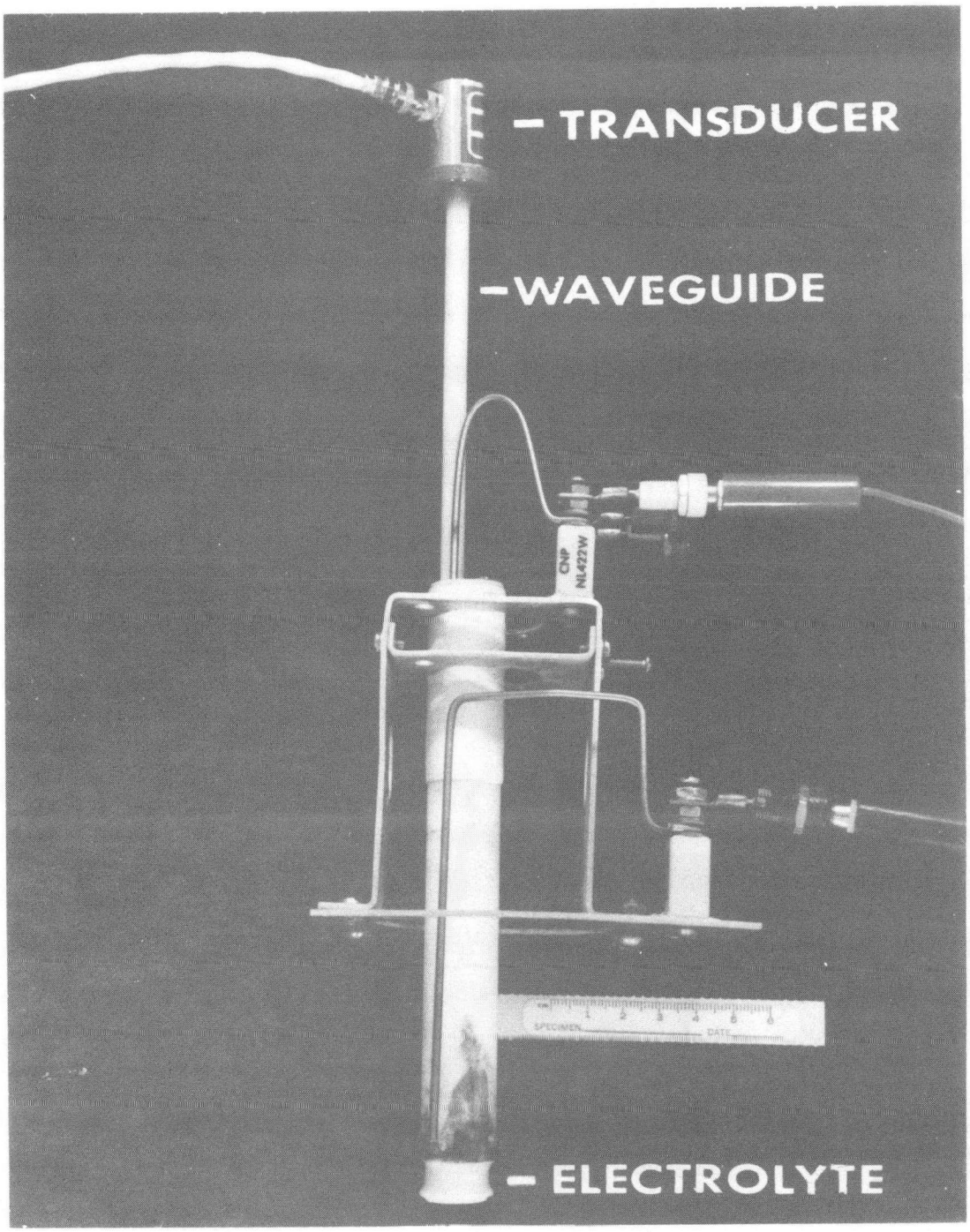

XBB 813-2152

Fig. 5.4 Cell with acoustic waveguide and transducer attached, mounted in support bracket ready to be fastened to sodium pot.

finally settled upon. The internal clamping shown was necessary to leave sufficient clearance to fit the cell into an alternate test chamber. The waveguide shown provided the thermal isolation necessary to protect the transducer from heat damage while still providing good acoustic coupling.

The burst of mechanical radiation which accompanies the sudden release of strain energy in a material through cracking is of decaying amplitude and thus has a roughly triangular envelope (Figure 5.5A). The frequency of this radiation ranges from tens of kilohertz to several megahertz. It is possible to distinguish electronically between the leading edge of each pulse and the individual oscillations within the decaying envelope or ringdown portion of the pulse. The equipment used provided for counting either only the leading edge of each pulse (events), or every oscillation in the ringdown which remained above the preset threshold level (counts) as illustrated in Figure 5.5B. The events mode could be used in situations where many events were occurring in a short time. For most tests described in this thesis, the count mode was used because it provided better identification of true acoustic events at low event occurrence rates (such as at the initiation of mode I breakdown) when random noise pulses were hard to distinguish from acoustic events. The origin of the noise pulses was electrical in nature and they contained little or no ringdown. A sharp increase in the acoustic count rate was thus a pretty reliable indication that an event had occurred.

The acoustic detection equipment used was manufactured by Acoustic Emission Technology (AET) of Sacramento, California. For most of the experiments an AET model 204A system was used in conjunction with a

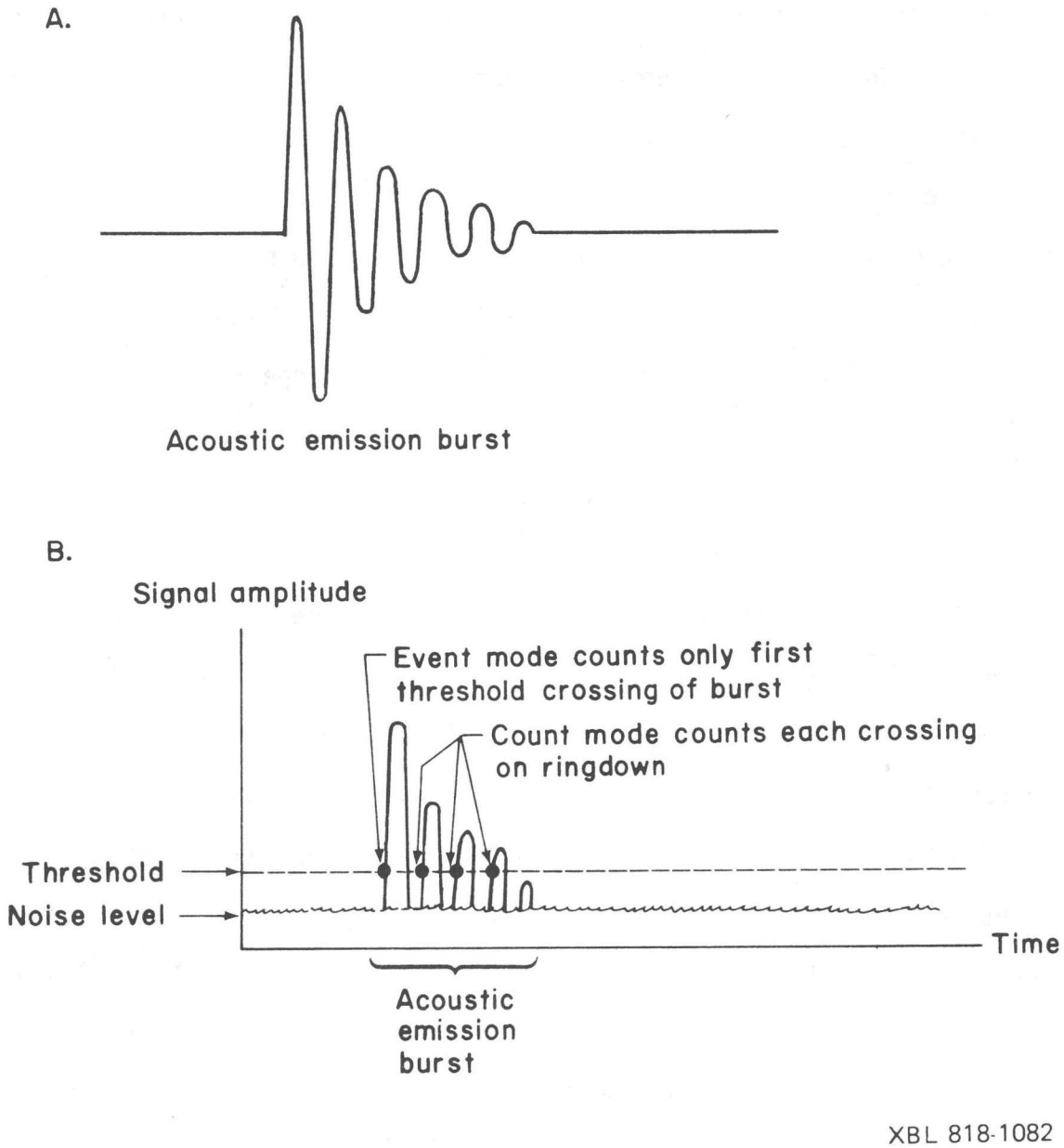

Fig. 5.5 A. Idealized acoustic signal.
B. Signal detector response.

model AC 174L transducer. In addition to choice of scaling either events or counts, the unit offered adjustable gain, adjustable signal threshold level (for scaling), and choice of two methods of scaling: cumulative mode and rate mode with adjustable sampling period. Both scaling modes were used at different times in the experiments, but the rate mode yielded the easiest identification of events of interest. A 0.5 second sampling period provided the best resolution compatible with the response of the chart recorder used. The threshold could be operated in two modes, fixed and floating. In the floating mode, the threshold is maintained at the set voltage interval above the rms background noise level which helps to minimize the effects of relatively long-term background variations. The unit was also capable of displaying the rms level of the input signal as an alternative to scaling. The rms mode would be useful in certain applications where high count rates and high persistent background noise were present simultaneously, but it did not prove useful in the experiments described here. The bandpass of the model 204A was such as to accept signals in the range from 100 to 250 khz. The resonant frequency of the transducer corresponding to its maximum output frequency was about 175 khz.

Some experiments were done using an AET model 203 detection system which was capable of recording the amplitude distribution of the pulses coming in over a 60 db range in 1.2 db increments. Other capabilities were similar to those of the model 204A described above. It had been hoped that the model 203 would prove useful in making a better discrimination between the desired signal and noise, and possibly between different types of acoustic events (e.g. between those arising from transgranular cracking, intergranular cracking, surface discharge,

etc.). The initial results were promising, but, in view of the stated objectives of this study and the added time involved in interpreting the more complex results, it was decided not to pursue amplitude distribution studies at this time.

An amplified output of the signal from the acoustic transducer was available from the detection unit and was observed on an oscilloscope. The visual representation of the signal was helpful in many ways, particularly in isolating and/or eliminating noise from electrical and mechanical sources. Emissions from such sources almost always have a different waveform from those produced by cracking in the ceramic and may occur with a low frequency regularity, for instance, at the 60 hz line frequency or at the resonant frequency of some mechanical structure coupled to the system. Noise from motors and from phase switching power controllers was particularly troublesome at times, but easy to identify because of its 60 hz frequency. The actual device producing the interference was not always easy to find. A thermocouple in the sodium melt was found to be shorted to its outer sheath and producing spurious acoustic signals through its interaction with the furnace power controller. Replacement of the thermocouple solved this problem. Pumps and valves associated with the glove box were another source of noise and either had to be sufficiently decoupled from the system or temporarily shut down for the duration of the tests.

Cell current and voltage were monitored and recorded on a separate chart recorder so that they could be correlated with the acoustic data. A block diagram of the entire cell environment and cycling/monitoring system is shown in Figure 5.6.

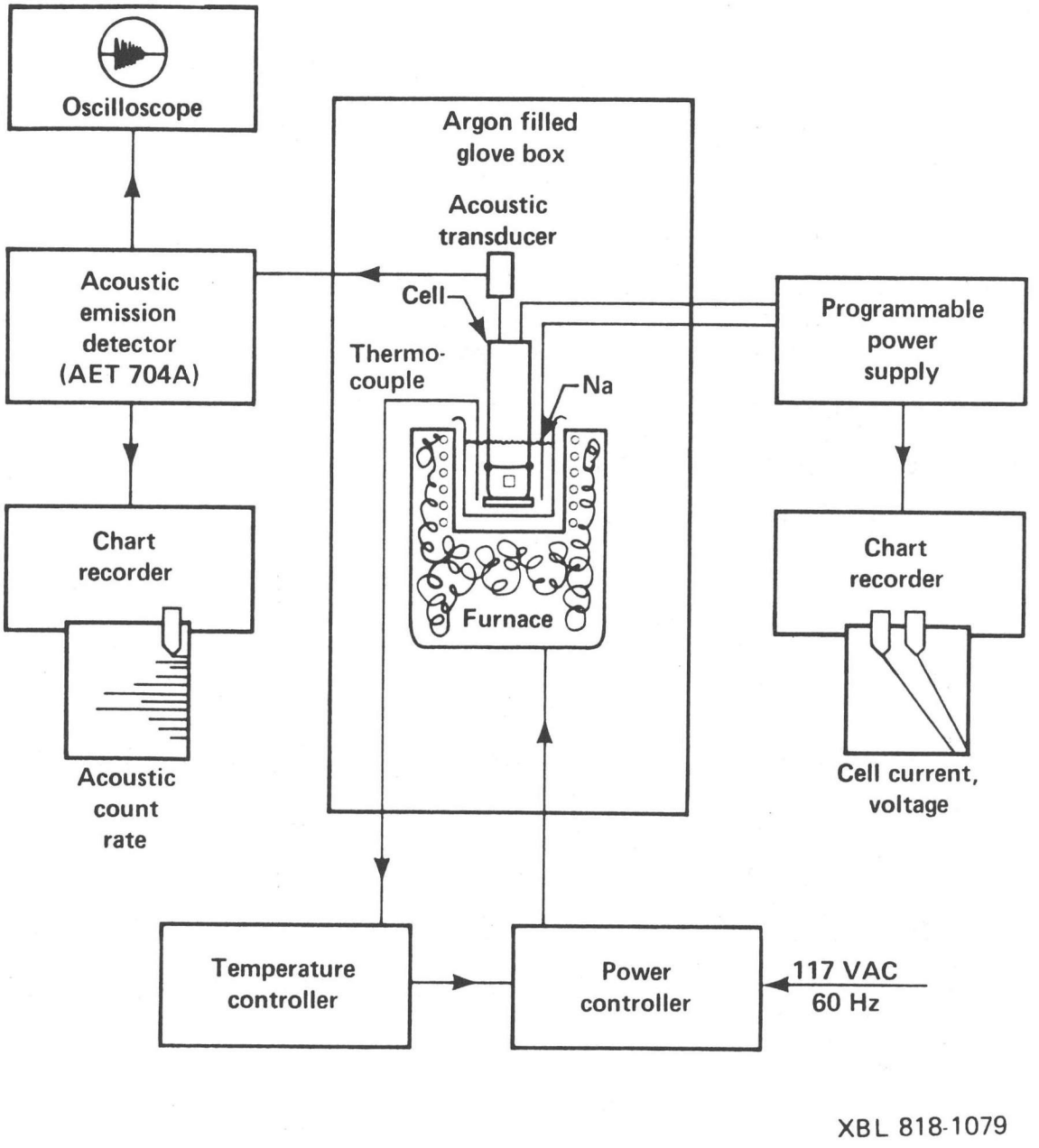

Fig. 5.6 Block diagram of cell environment and cycling system.

5.3 Results and Discussion

5.3.1 Cell Electrical Parameter Behavior During Cycling

The first few experimental cell cyclings were done with a low ripple D.C. power supply having no current regulation and only manual control of voltage by way of an autotransformer in the primary circuit. It was observed that polarization would occur in the cells when current densities in excess of 200 mA cm^{-2} were applied. The time for the onset of polarization varied but it was typical for a cell current density set initially at 1 A cm^{-2} to decay to 10-20 mA cm^{-2} in the course of about thirty minutes.

Reversing the cell polarity would restore the current to its original magnitude, although polarization would then gradually establish itself in the other direction. Even just a momentary reversal of polarity or a simple interruption of the current for a few seconds would restore the current to its original value, but polarization would reestablish itself more rapidly than at the initial onset.

The current could also be restored to its original value by raising the voltage, but the current-voltage characteristics of the cell were quite nonlinear after the onset of polarization. Polarization was observed more closely by current ramping the cells using the programmable power supply. Figure 5.7 shows the behavior of cell voltage in two typical cases. Below about 0.5 V, the response is fairly linear. Note that a kind of plateau in the voltage is reached about 13 to 14 V. (This was not due to any limitation in the power supply which had been modified to supply up to 25 V.) As these cells were being run, acoustic emissions were usually first detected at cell current densities between

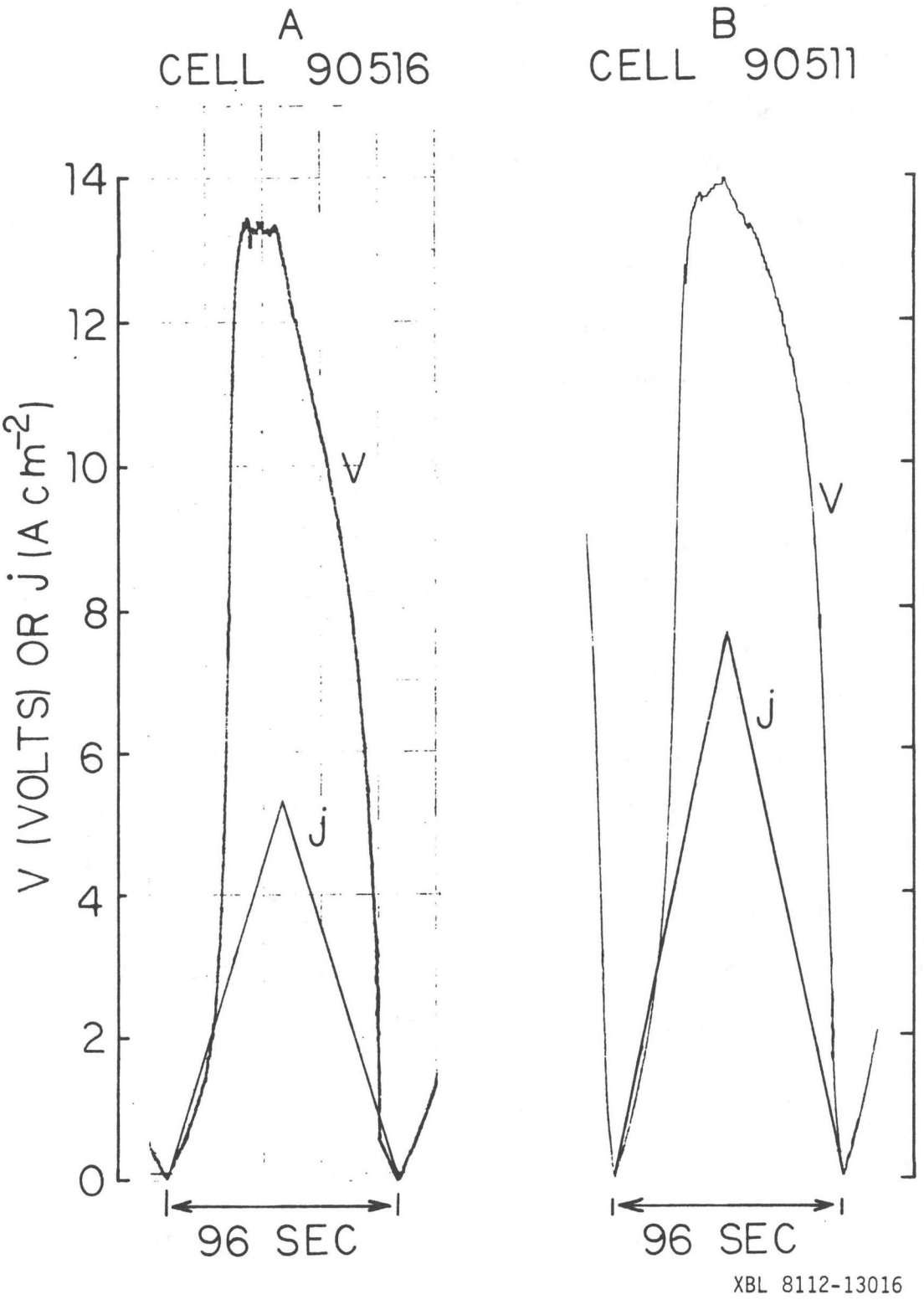

Fig. 5.7 Polarization behavior of cells during rapid triangular current wave ramping.

3 and 4 A cm^{-2}. The emissions increased sharply when the "plateau" region of the curve was reached. The ramp rates used on these cells were 113 and 163 mA cm^{-2} sec^{-1}. When ramp rates of 10 mA $cm^{-2}sec^{-1}$ or less were employed, polarization rarely occurred even at current densities in excess of 10 A cm^{-2}. Acoustic emissions were detected at lower initial current densities as methods of acoustic coupling were improved.

Polarization phenomena in cells employing beta aluminas have been reported in the literature by Breiter et al. (Br 80a), and it has been noted that they are more likely to be associated with beta" than with beta. Beta" has a higher affinity for water than beta, and, in fact, hydronium beta" alumina is reported to be a "fast" (low resistance) proton conductor, whereas hydronium beta alumina has a very high resistance and is not considered a "fast ion" conductor (Fa 78). When beta" alumina is exposed to moist air, some of the sodium exchanges for hydronium ions resulting in the formation of NaOH on the surface. This exchanged water may later react with sodium at electrolyte surface and establish a sodium oxide layer which polarizes the cell. Breiter et al. attribute cell polarization to the formation of such an oxide layer, noting that the less frequent occurrence of polarization above 320°C may be due to greater solubility of the oxide in sodium at higher temperatures. They also note that when polarization develops in batteries using beta" electrolyte, the ceramic inevitably fails after passing an additional 100 to 200 Ahr cm^{-2} and is found to have a black and crumbly appearance. Cells cycled here for extended periods of time under conditions of severe polarization also exhibited intense blackening at the sodium entrance surface. Figure 5.8 shows the sodium entrance surfaces of two such cells. The views at the left are low power optical micro-

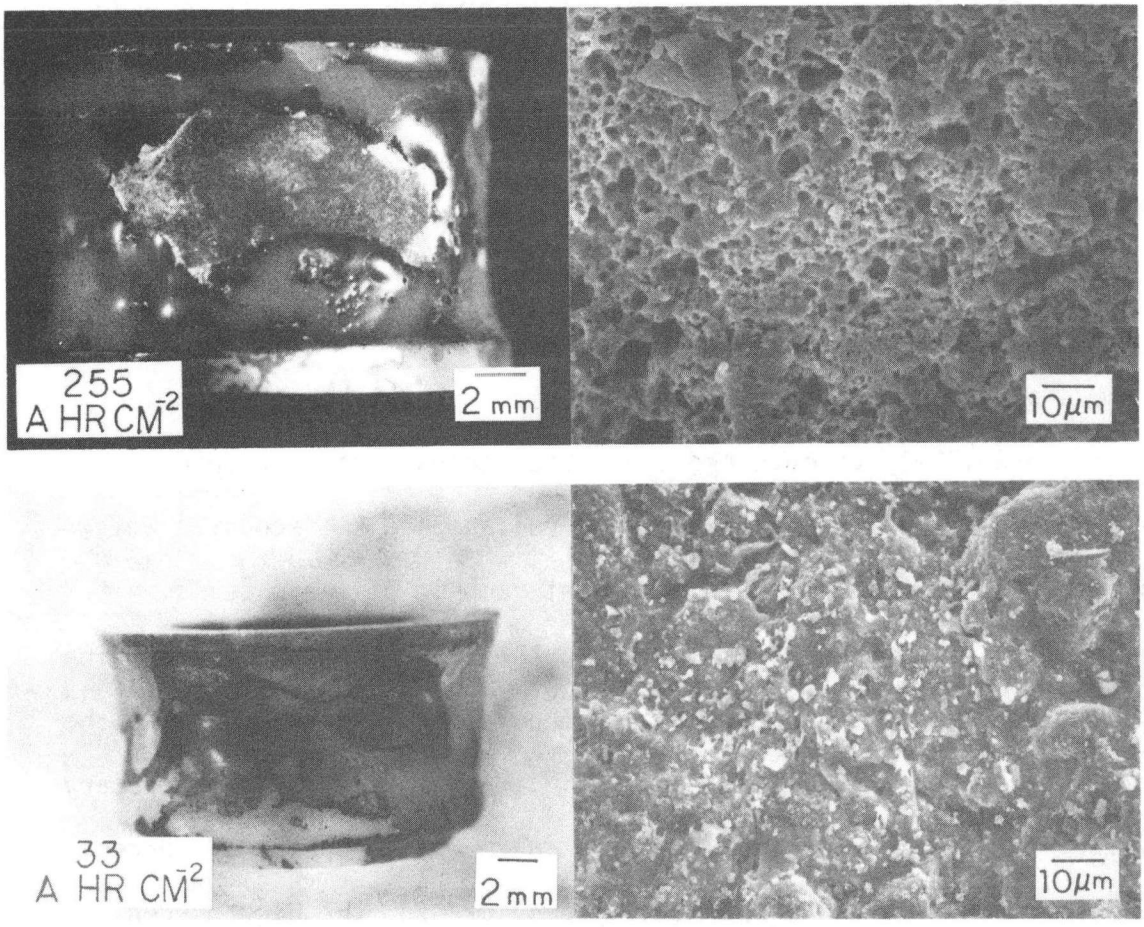

XBB 807-8885

Fig. 5.8 Sodium entrance surface of cell 90530 (top) and 91002 (bottom). Optical micrographs (left) show severe darkening of the electrolyte surface (active uncoated surface on cell 91002 has been outlined in black for clarity). Scanning electron micrographs (right) show porous surface texture produced by extended operation of the cell under conditions of severe polarization.

graphs (the unmasked active surface on the 33 Ahr cm^{-2} has been outlined in black for clarity), and the views on the right are SEM micrographs of the same active surfaces, showing the pitting which has occurred. The surface of the 255 Ahr cm^{-2} cell has developed a sponge-like appearance. The absence of evidence for stress corrosion in beta aluminas (Da 79a) makes it unlikely that the surface texture developed by such a mechanism. Stress corrosion of this nature would be highly unusual in any event at the sodium entrance surface. A repeated dielectric type breakdown and discharge through the proposed insulating polarization layer is more likely to have produced this porous surface. Such a phenomenon would produce the plateau in voltage and the acoustic emission patterns recorded during the current ramping of these cells. It was observed in Chapter 1 that, owing to the likelihood of oxygen being dissolved in the sodium, accumulation of oxide at the surface where the sodium enters the electrolyte is a distinct possibility. The temporary loss of polarization upon polality reversal or interruption of current flow occurs because of the opportunity provided for the high oxygen concentration near the surface to dissipate. Oxygen is not transported to the surface as rapidly at lower ramp rates and thus polarization is less liable to develop. Work reported recently by Demott (De 80c) also supports an oxide layer polarization theory by noting that resistance rise frequently observed in sodium sulfur cells can be counteracted by removing the sodium from the cell, washing the surface of electrolyte with alcohol, and then reassembling the cell with fresh sodium.

Eventually, after prolonged cycling at the conditions which produced severe polarization, failure occurred as indicated by a sharp drop in cell resistance and the cessation of nonlinear characteristics.

This did not always occur in a sudden fashion, and in a few cases there was a gradual decline in resistance over several hours. However, these tests always terminated in a linear, low resistance response indicating an electronic short circuit. Sodium transport also ceased at this point.

It was observed that small current pulses with rise times on the order of a millisecond could produce sudden and severe drops in cell resistance. Figure 5.9 shows current and voltage traces for cell 00626. Two small voltage drops associated with crack growth are marked (A B) as well as the substantial drop (C) produced by the marked current pulse. The pulse amplitude is about 50 mA cm^{-2} on a base current density of about 700 mA cm^{-2}. The resistance of the cell drops promptly from 7.0 ohms to 5.9 ohms. Such behavior was occasionally noted for current pulses of the same amplitude even when the base current density in test cells was below 100 mA cm^{-2}. Acoustic emissions accompanied these pulse induced resistance drops, and so they are attributed to sudden cracking in the ceramic. The phenomenon is attributed to mode I type crack growth. The amplitude of the current pulses was not large enough to establish any dangerous thermal gradients. The results imply that there is a dependence on rate of stress application at the tips of the cracks responsible for mode I breakdown. The sensitivity of the ceramic to sudden pulses indicates the need to avoid such during the charging of sodium/sulfur cells. These might most likely occur when initiating the charge cycle or because of line transients during charging.

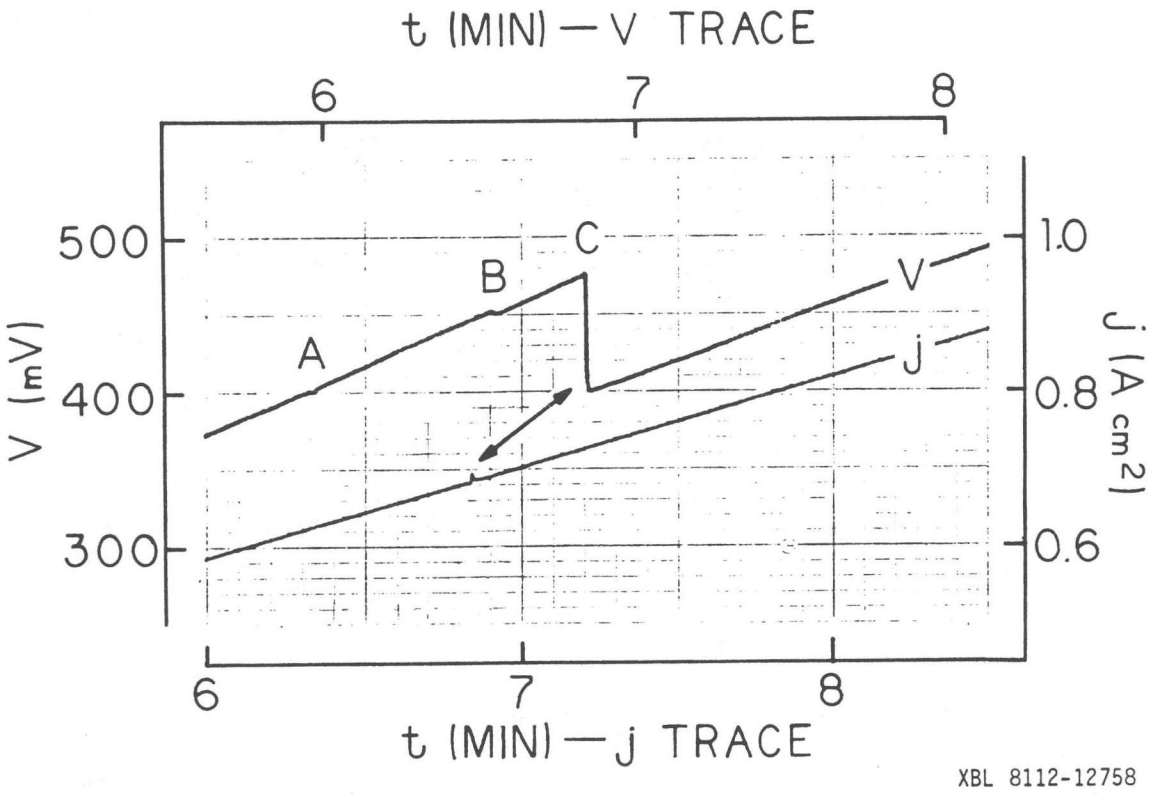

Fig. 5.9 A segment of the current/voltage versus time curve for cell 00626. The current trace lags the voltage trace by 0.375 min. A and B are small voltage drops associated with crack growth. The large drop at C corresponds to severe crack growth induced by the current pulse marked with an arrow.

5.3.2 Critical Current Density Determination

The detection of crack initiation or growth during cell operation is not easy. Sudden crack growth may affect cell resistance sufficiently to show up as voltage fluctuations which can be measured, but small incremental crack growth does not usually make enough of an impact on cell voltage to be measured above background noise.

Acoustic emission monitoring proved to be a very valuable source of information regarding the time of initiation of breakdown by the mode I process in the sodium/sodium cells. It has been noted, however, that stringent procedures are necessary to exclude external noise sources and that polarizarion phenomena as well as cracking can generate acoustic signals. When signals due to noise and polarization have been excluded from consideration either by identification or elimination procedures, one may ask whether those remaining are really due to cracking and whether the initiation of cracking can be reliably detected.

Experiments done by L. A. Feldman of this group help to answer these questions. A rectangular bar specimen coupled to an acoustic transducer was subjected to a current flow of about 40 mA cm^{-2} at a temperature several degrees above the melting point of sodium. This current density is well below that at which mode I breakdown is expected to occur. A thermocouple at the sodium exit surface of the bar monitored the temperature as the specimen was cooled through the freezing point of sodium. Mercury/sodium amalgam electrodes were used as positive supply electrodes. In the immediate vicinity of the freezing point of sodium, the acoustic emission rate increased sharply. When the experiment was repeated with no current flowing in the bar, there was no increase in

acoustic activity above background as the sample was cooled through the freezing point of sodium. Experiments were done at room temperature in which a bar with a blocking evaporated gold negative electrode and mercury/sodium amalgam positive electrode was subjected to a very slow current ramp until an increase in acoustic emissions was observed. Within a few seconds of this increase, black streaking, due to propagation of sodium filled cracks, could be observed emanating from the negative electrode. These experiments confirmed that acoustic methods had adequate sensitivity to detect the initiation of mode I degradation. Figure 5.10 shows current and voltage data superimposed on a typical acoustic emission trace for a sodium/sodium cell cycled at 350°C. The onset of mode I is clearly evident.

It is expected that the surface of the beta alumina electrolyte used in the sodium/sodium cells tested here will be populated with a number of various sized flaws of the type active in mode I breakdown. A distribution of flaw sizes in the sodium exit surface of the electrolyte will lead to a corresponding distribution in the critical current densities for initiation of mode I degradation. It is the largest active flaw in each cell that determines the critical current density for that cell. The distribution of critical currents is thus one of extreme values and hence is appropriate for description with Weibull statistics. The critical current density distribution associated with initiation of mode I degradation in a cell with active surface area A is analogous to the applied stress distribution associated with failure in a brittle solid of volume V. The Weibull analysis (Da 79b) gives the survival probability, P_s, in this latter case as:

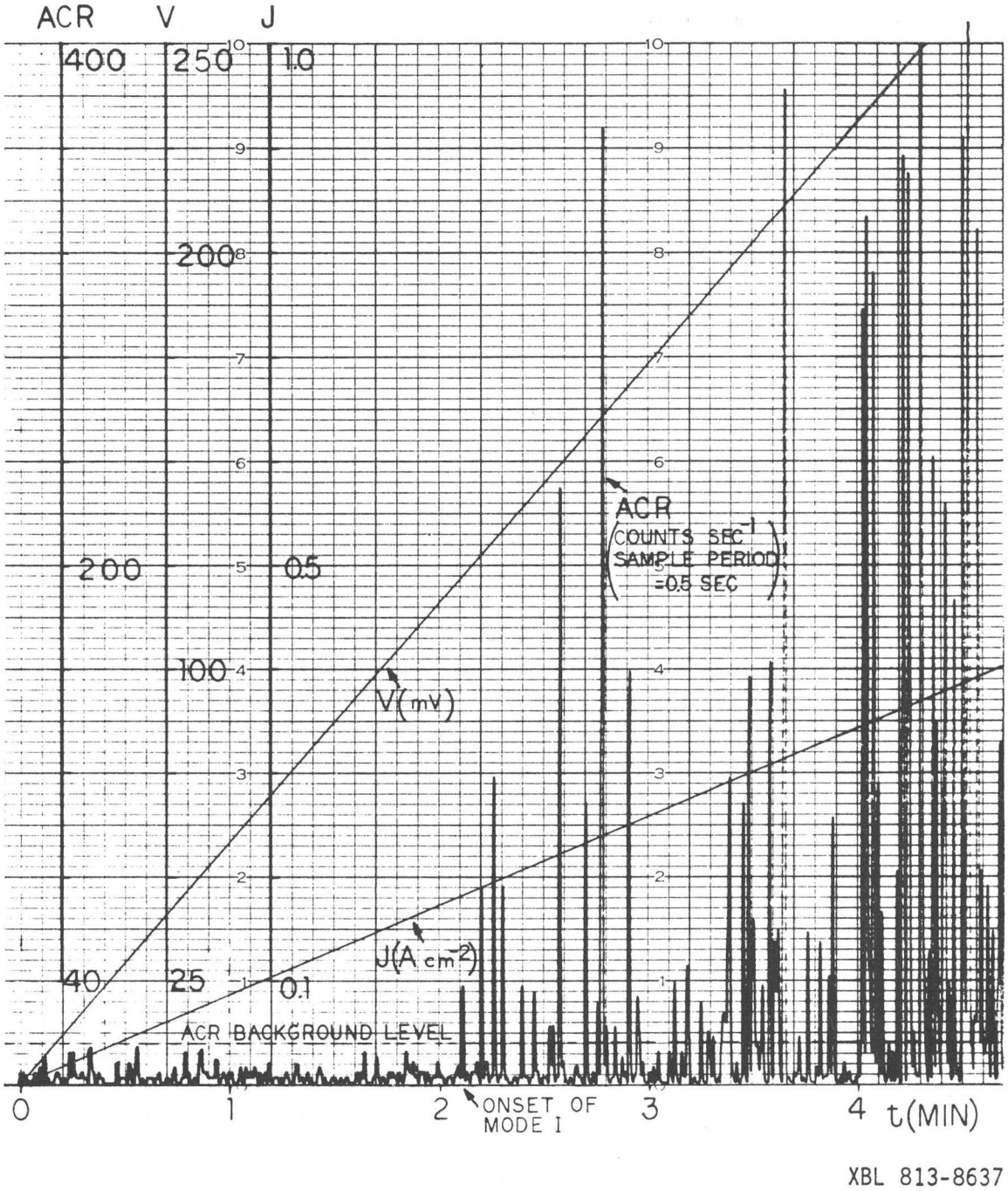

Fig. 5.10 Current density and voltage data superimposed on the acoustic count rate (ACR) for the initial stages of breakdown in cell 00626. Units of vertical axes are specified where the corresponding traces are identified.

$$P_s = (1-P_f) = \exp\left\{ \frac{-V}{V_o} \left(\frac{\sigma - \sigma_u}{\sigma_o} \right)^m \right\} \qquad 5.1$$

where P_f is the probability of failure, σ is the applied stress, σ_u is a materials constant representing the cutoff stress below which P_s is taken as equal to one, and m is a materials constant (usually between 5 and 20 for most ceramics) characterizing the width of the distribution. The larger m is, the narrower the distribution and the less the variability in the strength of the ceramic. V_o and σ_o are normalizing constants.

By analogy, the survival probability associated with critical current densities might be written:

$$P_s = \exp\left\{ \frac{-A}{A_o} \left(\frac{j - j_u}{j_o} \right)^n \right\} \qquad 5.2$$

where A is the active electrode surface area, j is the overall current density and j_u and n are materials constants of similar significance to σ_u and m, and j_o and A_o are normalizing constants. (Area is used rather than volume because mode I failure is associated exclusively with flaws in the surface and not those in the bulk.)

The assumption is frequently made that $\sigma_u = 0$ and it will be assumed here that j_u, the current density below which $P_s = 1$, is also zero. This assumption has the effect of predicting that tubes two or three orders of magnitude larger than the area (usu. 0.2 cm^2) of the cells run in this work, have almost zero probability of survival at typical sodium/sulfur cell current densities. Since large tubes are known to survive with a much higher probability, the assumption $j_u = 0$ is not correct but the actual value of j_u could not be determined from the

data reported here. The data should therefore not be used to extrapolate to much larger electrolyte tubes. The data can and will be used to compare performance of cells made from different grain size ceramics and to put an approximate upper bound on j_u.

For the purpose of plotting data so that m or n can be determined, it is customary to take the natural log of equation 5.2 twice. Hence:

$$\ln \ln 1/P_s = \ln A/A_o + n \ln (j-j_u) - n \ln j_o \qquad 5.3$$

If j_u is taken equal to zero, and A is the same for all cells tested, then a plot of $\ln\ln 1/P_s$ versus $\ln j$ will yield n as the slope of a line fit to the data points. $P_s(i)$ for the "i"th test of a series of N tests is determined as the median rank probability. It is found by arranging the values of $\ln j$ for each test in increasing order. The median rank position of the i^{th} datum is then:

$$P_s(i) = 1 - [(i - 0.3)/(N + 0.4)] \qquad 5.4$$

Sodium/sodium cells were ramped at a uniform rate of about 1 mA sec^{-1} to generate data for the Weibull analysis. Since the area A was not the same in all cells tested, an iterative procedure had to be followed to generate the Weibull curve. The procedure is outlined in Appendix 2.

The current density j, used to plot data points on the Weibull curve, was that at which mode I breakdown became evident through sharply increased acoustic activity. For most of the cells tested, there were two distinct phases in acoustic output during testing. At first, there were isolated acoustic bursts with relatively long time intervals in between. Finally, there would be a sustained period of intense acoustic

activity, usually accompanied by several downward excursions in cell resistance, indicating increasingly severe penetration of the ceramic by sodium filled cracks. Figure 5.11 shows this behavior clearly. The explanation of this two-phase behavior in acoustic activity may be found in the anisotropy of the beta alumina. At the start of the test the surface of the electrolyte is populated with flaws of various sizes and the increasing current density will start to activate some of these as the test progresses. But as the flaw grows, the crack tip encounters variations in K_{IC} because of the anisotropy of the electrolyte. These variations will be especially severe in the early stages of crack growth when the flaws are on the order of a grain size and may delay further growth for a substantial time. In their work referred to in Chapter 2, Feldman and De Jonghe (Fe 81) derive the relation:

$$j_{crit} \propto K_{IC}^4/\ell \qquad 5.5$$

which shows that even modest variations in K_{IC} can strongly affect the critical current density for flaw extension. Here, ℓ represents the length of the crack.

During the early stages of testing, the observed intermittent acoustic activity can be associated with this kind of terminated crack growth as it establishes a new flaw population in the cell surface. Two separate Weibull plots will be shown here: one for the j_{crit} at first acoustic activity, and the other for j_{crit} at sustained emissions. Relation 4.8 indicates that j_{crit} varies directly as the fourth power of K_{IC}. Since the stress required to produce failure is proportional to the value of K_{IC}, it follows that

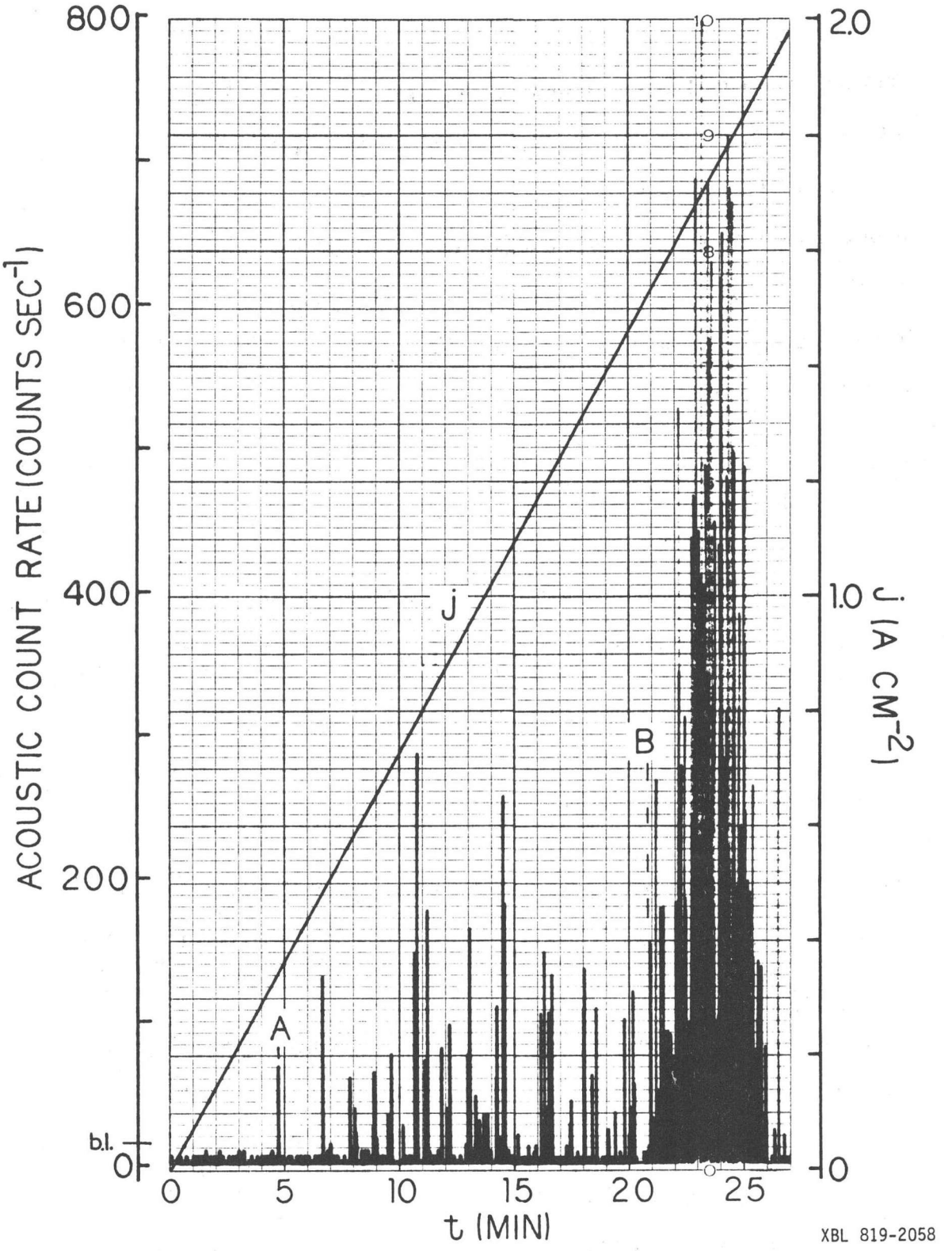

Fig. 5.11 Acoustic emission trace showing: A. first onset of Mode I typified by isolated acoustic events and B. severe onset of Mode I marked by steady acoustic activity. Cell current density (j) is also plotted. (b.l. = background level)

$$\sigma \propto j^4 \qquad 5.6$$

and so from equations 5.1 and 5.2 it can be deduced that m=4n. The value of m is a kind of indicator of the reliability or predictability of the ceramic in cell service. It is important in making projections about acceptable lifetimes and the need for proof testing. Suppose that a cell is to be operated at a current density j_{op} which is a factor B below the current density j_{50} determined from the Weibull analysis as that for a 50% probability of failure. That is:

$$B = j_{50} / j_{op} \qquad 5.7$$

Also assume that there is required a certain probability of survival P_R. Then recalling that n is the slope of the Weibull plot, we have for the required n:

$$n = (\ln \ln(1/0.5) - \ln\ln 1/P_R) / \ln B \qquad 5.8$$

Table 5.1 lists the required values of n (and m) for reasonable values of B and P_R. Values of m = 20 represent extremely high grade ceramic, and so unless relatively large values of B can be tolerated, which will be the case only if electrolytes can be fabricated with large values of j_{50}, initial failure rates of 1 to 5% may be difficult to attain. At some point it may be more attractive economically to subject the electrolyte tubes to proof testing to eliminate the weaker ones than to try to produce a uniformly high grade ceramic. Virkar has

Table 5.1: Current Density and Weibull Parameter Requirements for Selected Initial Failure Rates in Cell Operation

B	P_R = 0.95		P_R = 0.99	
	n	m	n	m
10	1.1	4.4	1.8	7.2
5	1.6	6.4	2.6	10.4
2	3.75	15.0	6.1	24.0

also proposed proof testing (Vi 79). A proof stress σ_p would be applied to the tube which would be related to the average fracture strength such that:

$$\left(\frac{\sigma}{\sigma_p}\right)^{4n} = -\frac{\ln P_R}{\ln 2} \qquad 5.9$$

This equation follows from equation 5.7 and relation 5.6. So if B, n, and P_R are determined by materials limitations and economic constraints on fabrication and operation, proof testing by mechanical or electrical means will be required when:

$$|\ln B| > |(\ln\ln(1/0.5) - \ln\ln(1/P_R)/\ n| \qquad 5.10$$

Figure 5.12 plots n versus B for various values of P_R using equation 5.8 dividing the quadrant into two subsets. Proof testing will or will not be required depending on which subset the attainable values of B and n fall into for the required P_R.

Weibull plots, for the cells cycled to determine critical current densities and values of n, are shown in Figures 5.13 and 5.14. They give information on cells constructed from both "10" and "300 μm" electrolyte material and show a definite difference in behavior. The cells made with fine grain material sustain a higher current density before failure. In Figure 5.14, showing current densities at start of sustained acoustic activity, the value of j_{50} is 640 mA cm^{-1} for the "10 μm" material and 145 mA cm^{-2} for the "300 μm" material. Referring back to Table 3.1 it can be noted that ratio of j_{50}'s for the two grain

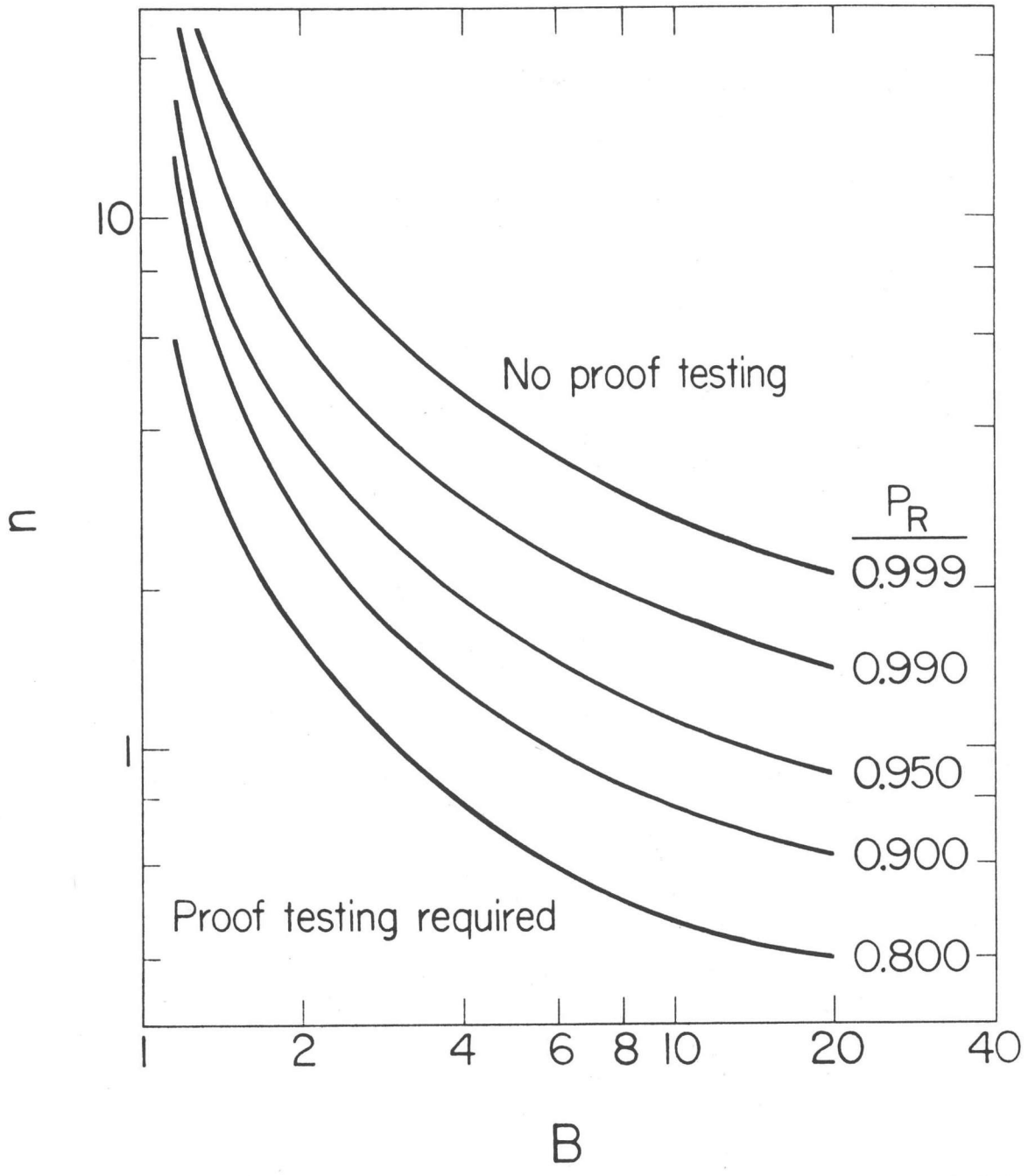

Fig. 5.12 Criteria for proof testing.

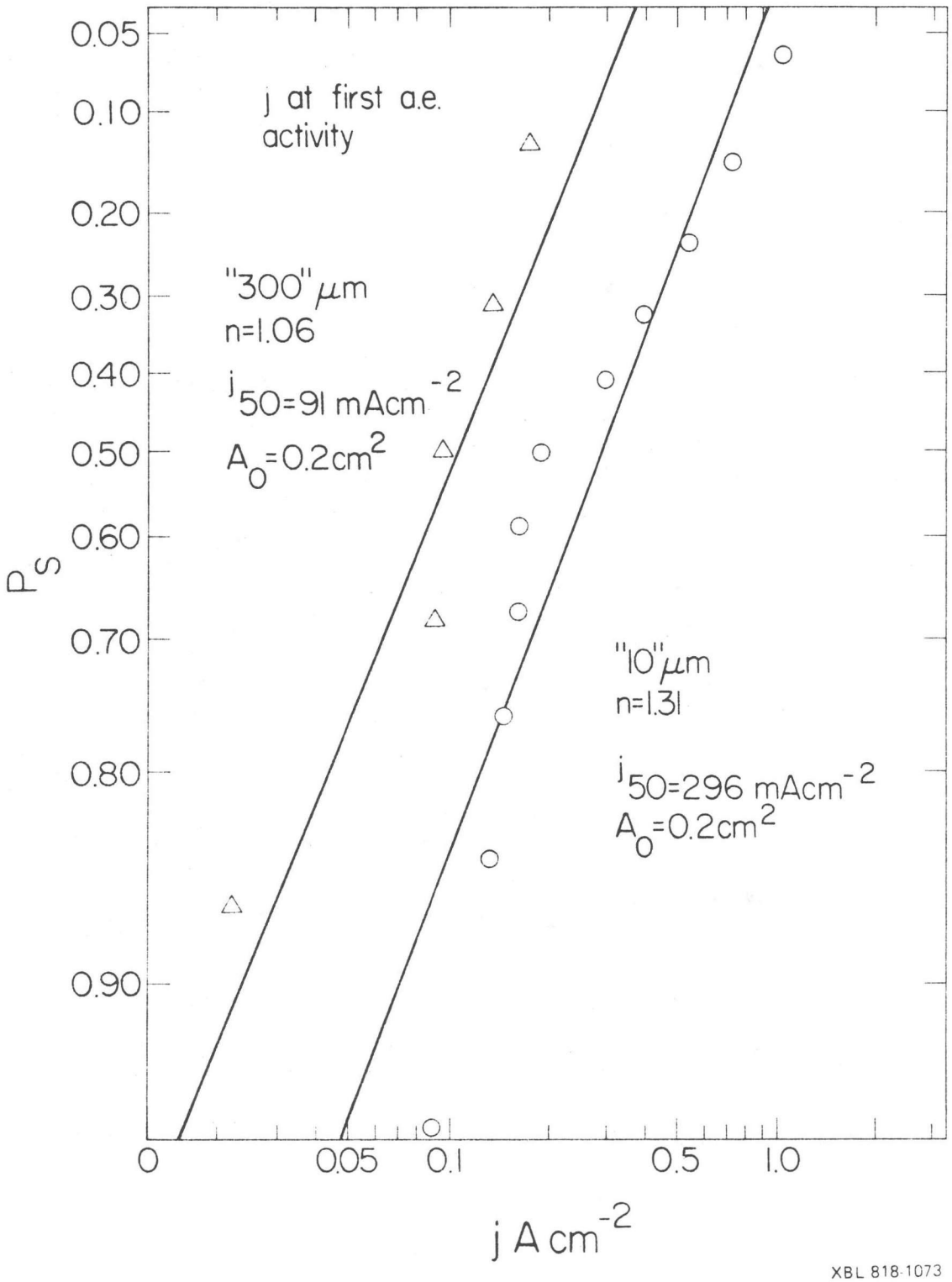

Fig. 5.13 Weibull plot for first onset of Mode I degradation as indicated by first increase in acoustic activity.

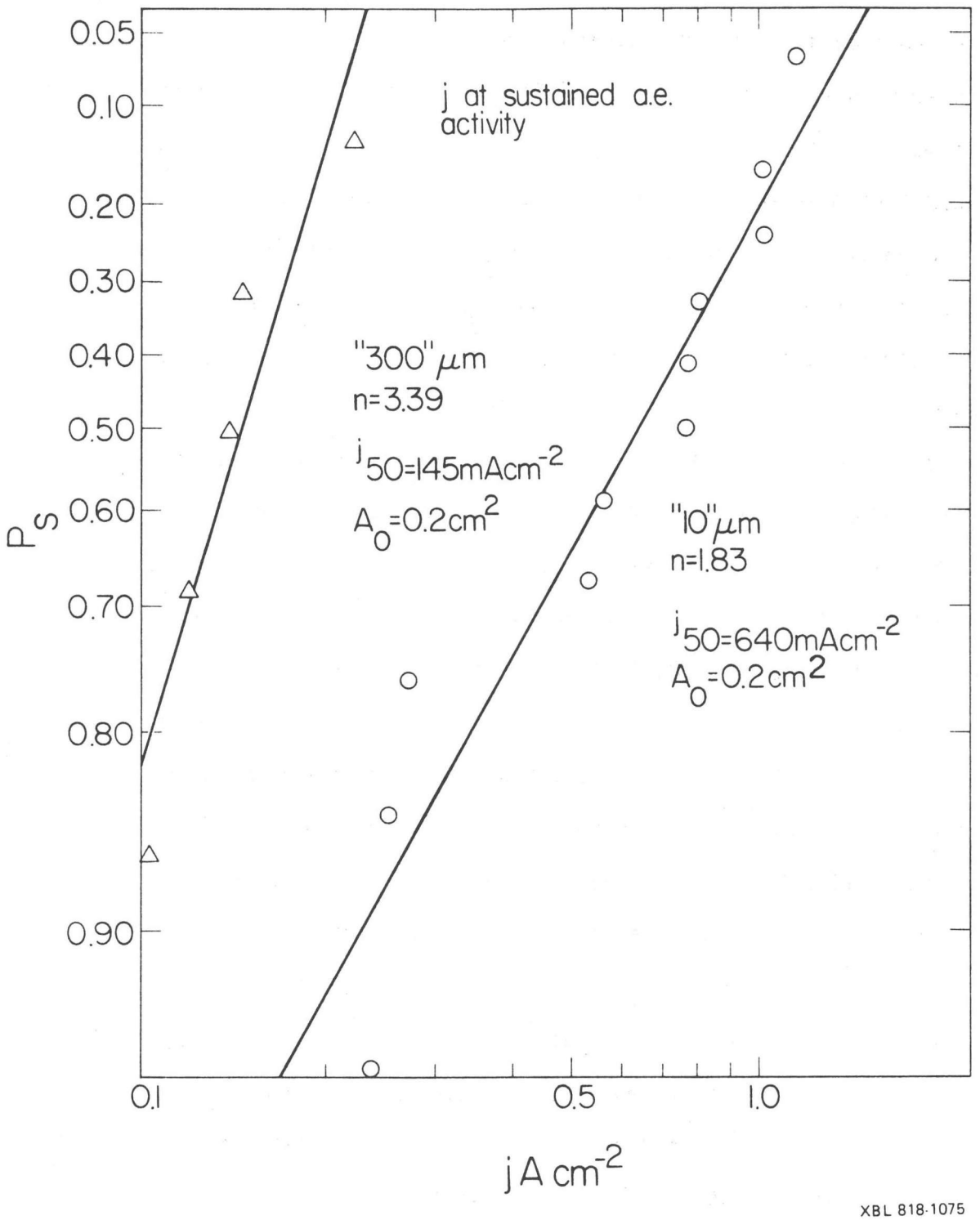

Fig. 5.14 Weibull plot for severe onset of Mode I degradation as indicated by start of sustained acoustic activity.

size materials is almost the same as the inverse ratio of the average grain size, or of the average longest grain dimensions. Assuming that cracks form easily along the boundaries of some single grains in the surface, such a correspondence of ratios is suggested by relation 5.5. The lowest current for onset of sustained acoustic activity in fine grain material is about 225 mA cm^{-2} which would set the upper bound on j_u in equation 5.2 at about 200 mA cm^{-2}. The ratio of j_{50}'s for the two grain size materials is smaller when determined by the onset of first acoustic activity (Figure 5.13), and the values of n are also smaller indicating greater spread of data and less predictability in failure properties of the ceramic. But as discussed earlier, the onset of sustained acoustic activity is considered the most important indicator of the initiation of significant mode I breakdown.

The use of Weibull analysis in the form that it is presented here is only valid if the mechanical and electrolytic criteria for failure are fully equivalent. This may not be the case, as has been noted by Virkar (Vi 81), although it is expected that the mechanical properties of the electrolyte strongly affect the electrical ones. The results presented here should be considered as a worst case possibility until the degree of correspondence between electrical and mechanical breakdown can be more fully established, and until more extensive tests can be run on full scale cells. Nonetheless, data reported here are valid for judging the effects of microstructure on breakdown and for testing the predictions made by the various models of mode I degradation processes regarding critical current density for the extension of flaws.

5.4 Summary and Conclusions

- Polarization develops during cycling at ramp rates above about 10 mA $cm^{-2}sec^{-1}$ which can lead to serious deterioration of the beta alumina solid electrolyte. This polarization is probably due an oxide layer which forms when oxygen, dissolved in the sodium used in the cell, concentrates at the electrolyte surface where sodium enters the ceramic and causes a sodium oxide precipitate to form.

- Acoustic events accompany the polarization at cell voltages of 4 to 6 volts and above. Much of this seems to be associated with a dielectric breakdown and discharge in the polarized layer and not exclusively with cracking.

- Short rise time current pulses are especially liable to induce crack growth. It is therefore very important to avoid such transients in current during the recharge cycle of sodium/sulfur cells.

- Acoustic emission monitoring can reliably be employed to detect the initiation of crack growth by electrolysis.

- Critical current density for flaw extension drops as grain size increases.

- Two phases of acoustic output are found when cycling sodium/sodium cells with linear current ramps. The first phase is one of scattered, isolated events at low current density. This phase is produced by the activation of flaws which then terminate their growth quickly because of the wide variations in K_{IC} which are a consequence of the considerable anisotropy in the microstructure. The second phase is one of sustained acoustic activity associated with extensive crack growth and crack branching in the ceramic.

6. FAILURE ANALYSIS OF CYCLED ELECTROLYTES

6.1 Introduction

Electrolytes from the cycled cells described in Chapter 5, as well as electrolytes obtained from commercially manufactured and cycled sodium/sulfur cells, were examined and compared. The expected artifacts of mode I processes and evidence of chemical darkening were found in both types of electrolyte. In the electrolytes from commercial cells, evidence of a second type of degradation was observed which is here referred to as mode II degradation. The connection between chemical coloration of the electrolyte and the mode II processes was postulated as a result of these failure analysis studies.

Features observed at the sulfur surfaces of electrolytes from sodium/sulfur cells suggest that there is a progressive degradation at this surface also which merits further investigation.

6.2 Examination of Electrolyte Material from Commercial Sodium/Sulfur Batteries.

6.2.1 Sources of Materials and Cycling History

The cooperation of two commercial manufacturers of experimental sodium/sulfur batteries made it possible to obtain electrolytes from actual cells which had been subjected to charge transfer densities ranging from 23 Ahr cm^{-2} to 703 Ahr cm^{-2} over periods of time ranging from 10 to 673 days.

One set of cycled electrolytes was obtained from the General Electric Research and Development Center in Schenectady, New York.

These were beta alumina tubes with a composition 9.6 wt% Na_2O, 0.25 wt% Li_2O, balance Al_2O_3. Starting material was a commercial beta alumina powder (Alcoa XB-2 "Superground," Aluminum Company of America, Pittsburgh, Pennsylvania) with other additions to achieve desired composition and sintering characteristics. The green tubes were produced by electrophoretic deposition on a steel mandril from a suspension of the raw powder in amyl alcohol, and were sintered by a feedthrough method in a dry oxygen atmosphere supported on saggers with appropriate bedding material to maintain soda content and compositional uniformity (Ch 76, Mi 78). The sodium/sulfur cells in which the tubes had been employed were operated at temperatures around 300°C and went through many deep charge/discharge cycles at current densities of about 100 mA cm^{-2}. Cells were of the sodium inside/sulfur outside configuration. After testing, the cells were disassembled and the electrolyte tubes washed in methanol to remove any residual sodium and sodium polysulfides. They were stored in air for a short time prior to shipment to the Lawrence Berkeley Laboratory where this work was done. Figure 6.1 is a representative cycled electrolyte tube as received from G.E.

Another batch of cycled electrolytes was obtained from British Railways Research and Development Division, Derby, U.K. These tubes had a composition 8.9 wt% Na_2O, 0.7 wt% Li_2O, balance Al_2O_3 and were a mixture of beta and beta" alumina, but predominantly (> 90%) beta". The green tubes had been prepared by isostatic pressing and were then sintered in closed crucibles of high thermal capacity in an electric kiln (Ar 80). The data provided on these electrolytes indicates that they were subjected to an average current density around 50 mA cm^{-2}, although it is known that some of the discharge cycles were run with current

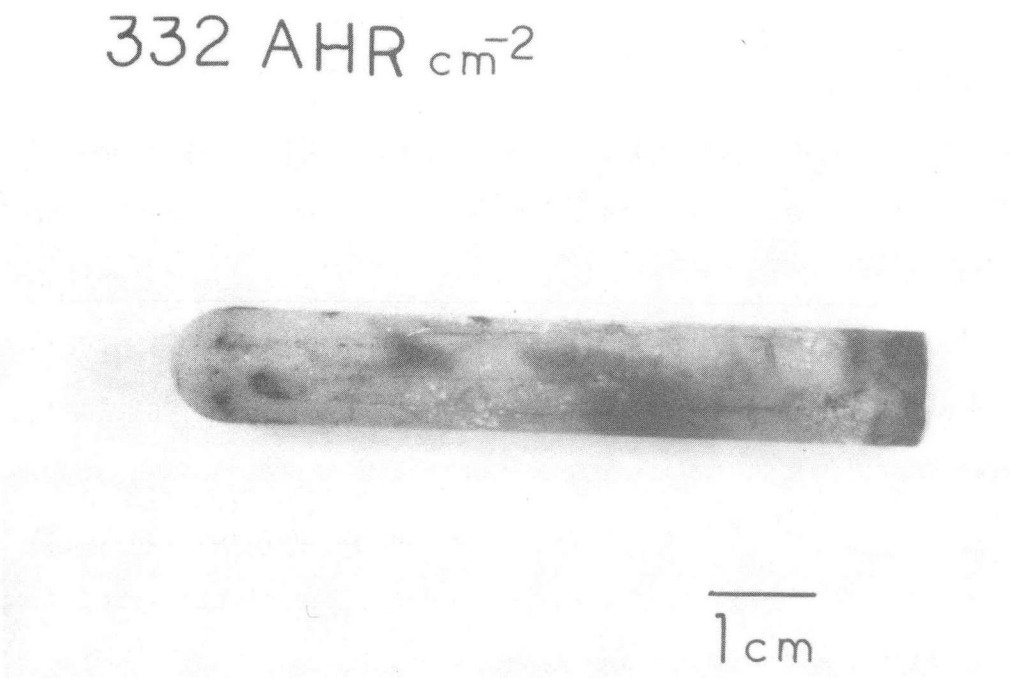

XBB 807-8869

Fig. 6.1 Beta electrolyte tube as received; removed from sodium/sulfur cell cycled to 332 Ahr cm^{-2} of charge transfer.

density as high as 100 mA cm^{-2}. For convenience in the discussion that follows, the electrolytes obtained from British Rail will be referred to as beta" electrolytes, and those received from G.E. will be called beta electrolytes.

More extensive documentation of the cycling history was available for the beta" electrolytes than for the beta electrolytes, including spotchecks of the cells' resistances at several points during their lifetimes. A gradual increase in internal resistance is frequently observed in sodium/sulfur cells during operation, and lowered efficiency results. Demott of British Rail has recently reported that it is sometimes possible to reduce the internal resistance of a cell by changing the sodium electrode (De 80c). This is particularly easy in the sodium outside configuration used by British Rail. The sodium container is removed and the bulk of the sodium is cut away with the remainder being removed by washing with alcohol. Fresh sodium is then introduced and the cell is reassembled. Usually, the cell resistance will drop after this procedure and will remain low over the rest of the cell lifetime. Some of the beta" electrolytes supplied for study has been subjected to such a sodium electrode change. The beta" tubes were treated in the same way as the beta electrolytes prior to shipment, but were not shipped intact. The original dimensions of the beta" tubes were approximately 33 mm dia X 200 mm long.

6.2.2 Preliminary Examination of Cycled Electrolytes

It was immediately evident that there was a progressive darkening present in the beta electrolytes corresponding to the amount of service that they had seen. There was also clear evidence of attack of the

sulfur surface manifesting itself in the form of darkening in some areas and white mottling in others. Sections from four of the beta electrolyte tubes are shown for comparison of the outer (sulfur) surfaces in Figure 6.2. The sodium surfaces of these same tubes along with corresponding polished tube cross sections are shown in Figure 6.3. A progressive darkening, originating from the sodium surface and proceeding into the electrolyte in a layer-like fashion, is seen in the polished cross sections. No decorating techniques were used before taking the photographs for Figures 6.1, 6.2, and 6.3. When a small segment of one of the darkened beta electrolyte tubes was raised to 1500°C to thermally etch it, it was observed that the darkening completely disappeared. Subsequently, it was discovered that most of the darkening could be removed by heating to only 400°C in air for several hours. The need to understand this darkening and bleaching more fully led to the performance of the experiments described in Chapter 4. The beta" electrolytes at equivalent or even longer cycling times were in general much less darkened than were the beta electrolytes.

6.2.3 Surface and Grain Structure

The surface texture and internal grain structure of the beta electrolyte tubes are shown in Figure 6.4. The outer and inner surfaces are of equivalent smoothness and comparable to the inner surface of the isostatically pressed tubes from Ceramatec. The internal grain structure is far more uniform and the grains more equiaxed than in the Ceramatec beta" alumina tubes. The internal grain structure of the beta" electrolytes is shown in Figure 6.5. The grain size is far less

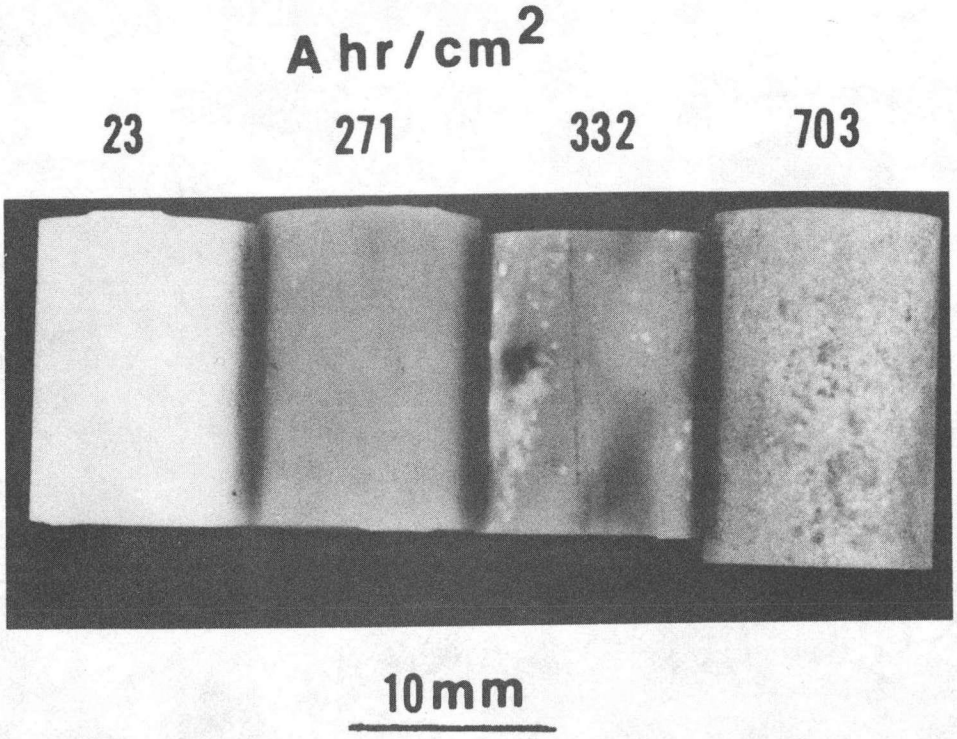

XBB 804-4114

Fig. 6.2 Comparison of beta electrolyte tube segments from four sodium/sulfur cells. Sulfur surfaces are shown.

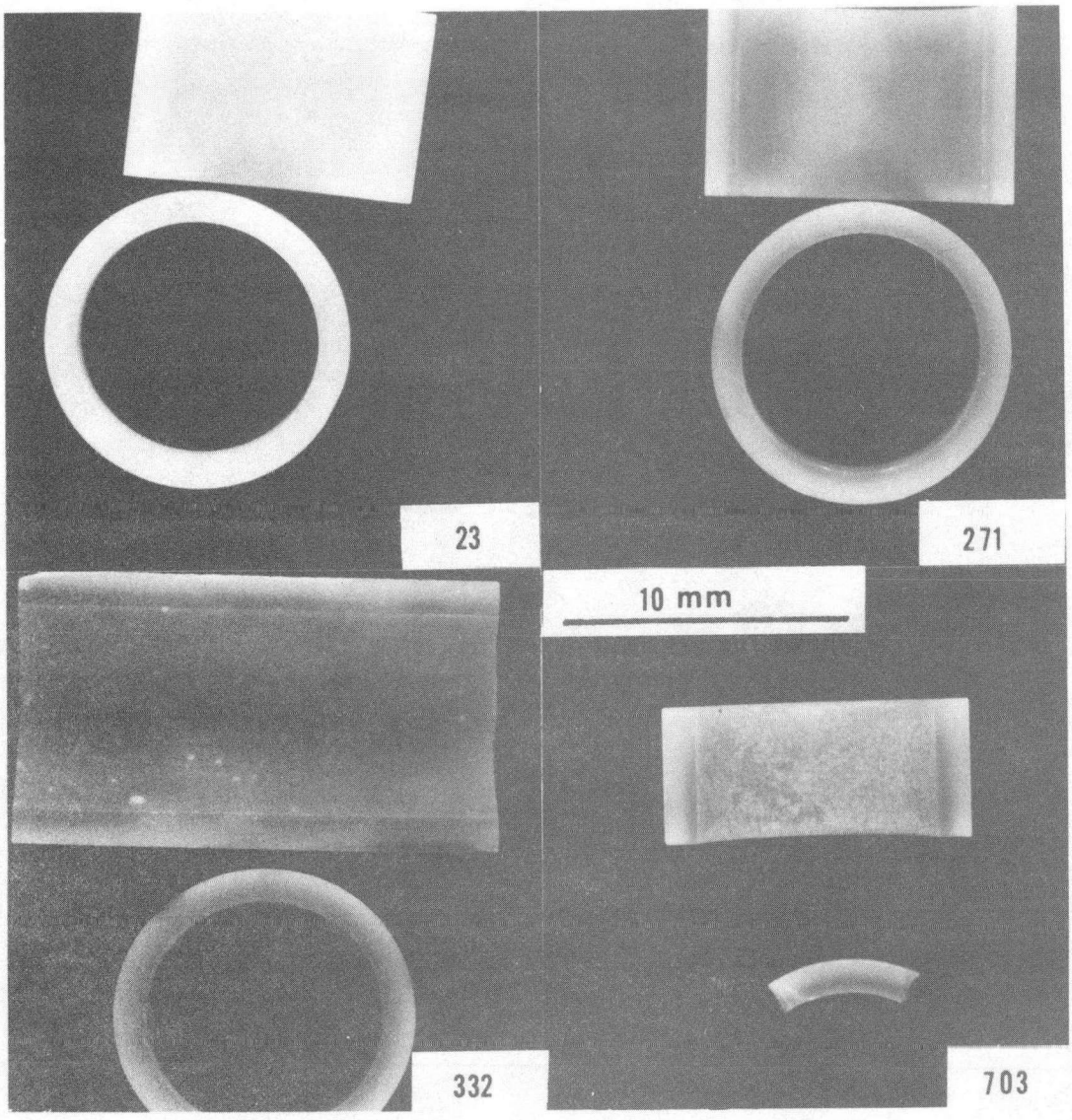

XBB 804-4133

Fig. 6.3 Sodium surfaces and polished cross sections of electrolytes shown in Figure 6.2.

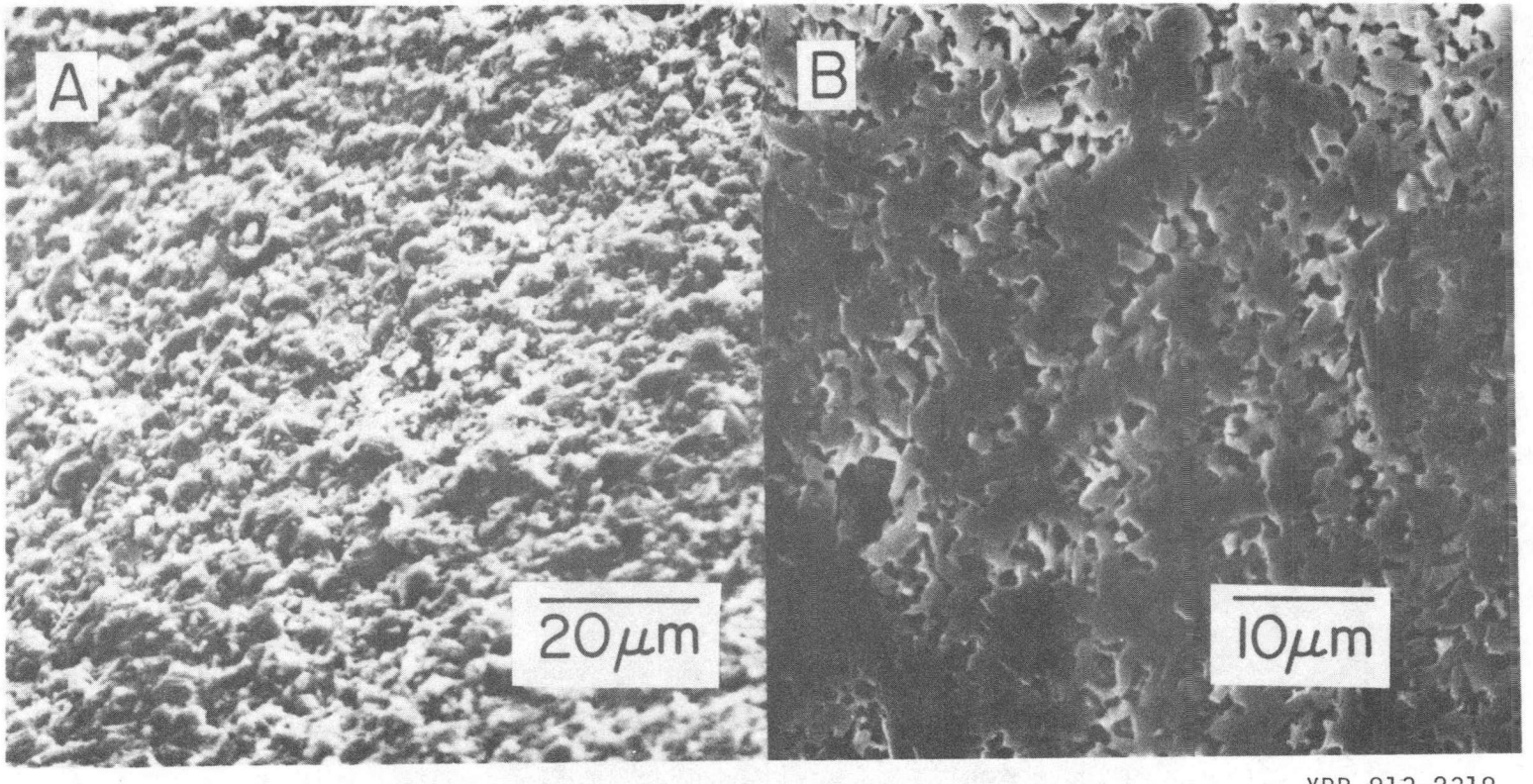

XBB 813-2318

Fig. 6.4 A. Surface texture and B. internal grain structure of beta electrolyte tubes.

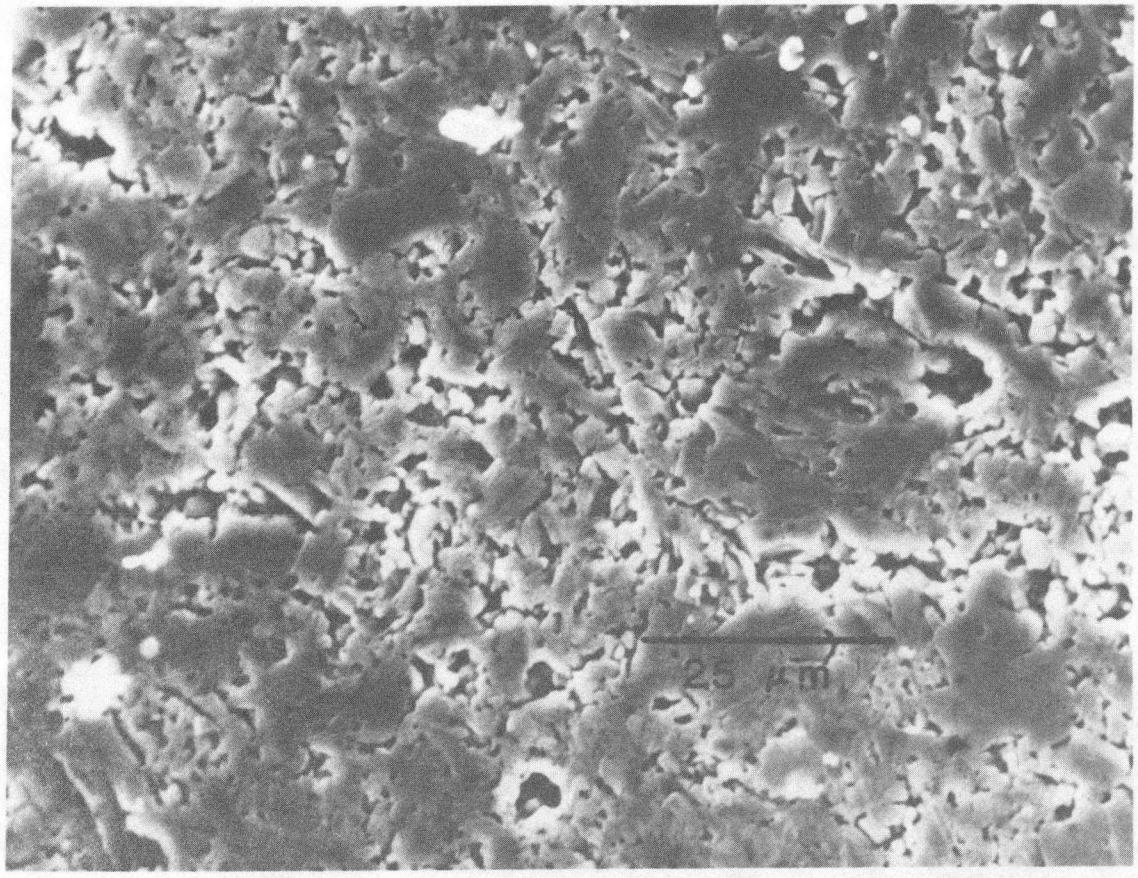

XBB 817-6527

Fig. 6.5 Internal grain structure of beta" electrolyte tubes from cycled sodium/sulfur cells.

uniform than in the beta electrolytes, but both are more uniform and the grains more equiaxed than in the Ceramatec material.

6.2.4 The Sodium Electrode/Electrolyte Interface

The surfaces of the as received, cycled electrolytes were subjected to further scrutiny by optical microscopy, but revealed no significant features of interest. In the scanning electron microscope, however, crystals rich in sodium were found on the sodium surfaces of the beta electrolytes (Figure 6.6). These crystals are sodium carbonate, and they are formed in two stages when the electrolytes are exposed to the atmosphere. Moisture in the air leaches out the sodium in the electrolyte forming NaOH at the surface and exchanging hydronium ions for the depleted sodium ions in the electrolyte. The NaOH then reacts with CO_2 in the air to form $NaCO_3$. The crystals are larger and more profuse on the surface of the 703 Ahr cm^{-2} electrolyte than they are on the surface of the 23 Ahr cm^{-2} electrolyte. Other observations which will be reported below confirm the presence of crack networks, due to mode I processes, and pockets of sodium below the electrolyte surface, due to mode II processes, which probably feed extra sodium to the surface for carbonate formation. The darkening observed in the electrolytes may also have some bearing on the amount of sodium carbonate formed upon exposure to moist air.

When specimens of the electrolytes were decorated by immersion in hot aqueous silver nitrate solution, as described in Chapter 3, several features became visible which could be correlated with the breakdown process. Micrographs of polished decorated cross sections of the beta electrolyte tubes (Figure 6.7) reveal the existence of a layer of

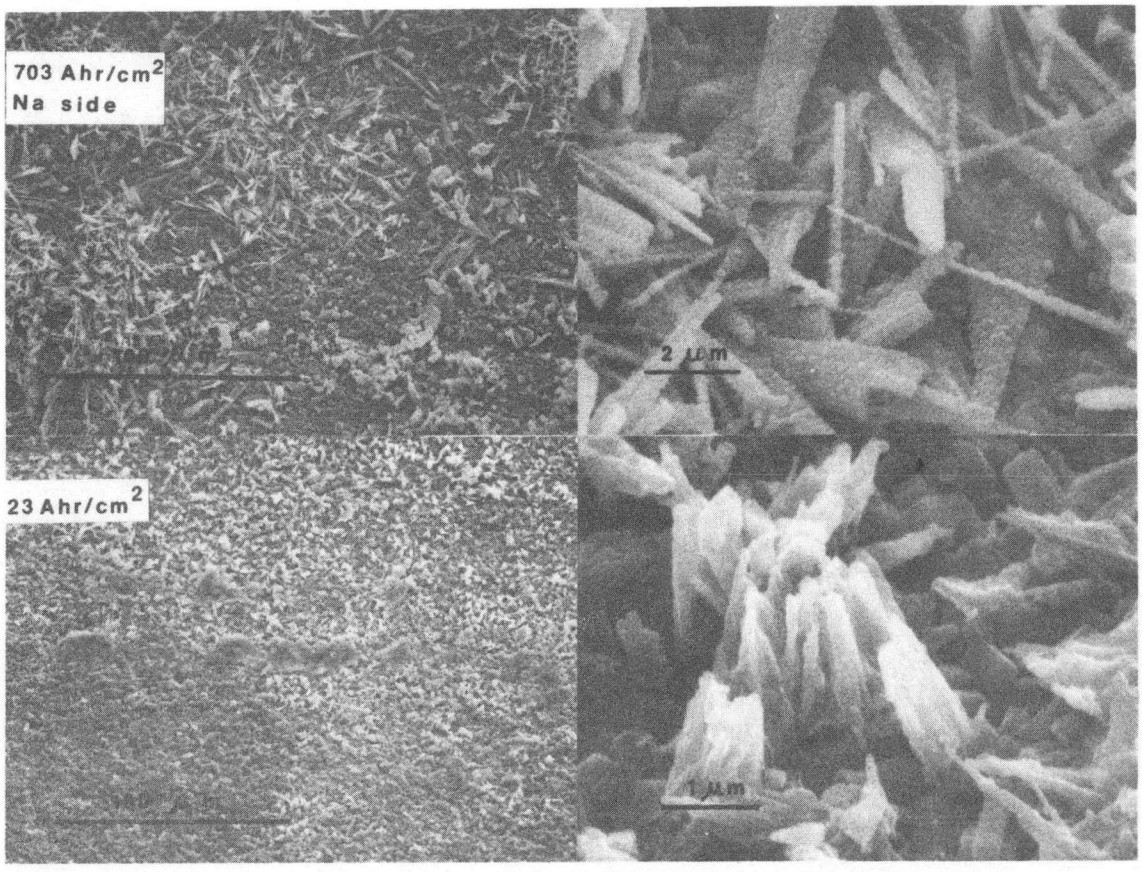

XBB 804-4134

Fig. 6.6 Sodium carbonate crystals on sodium surfaces of cycled beta electrolytes.

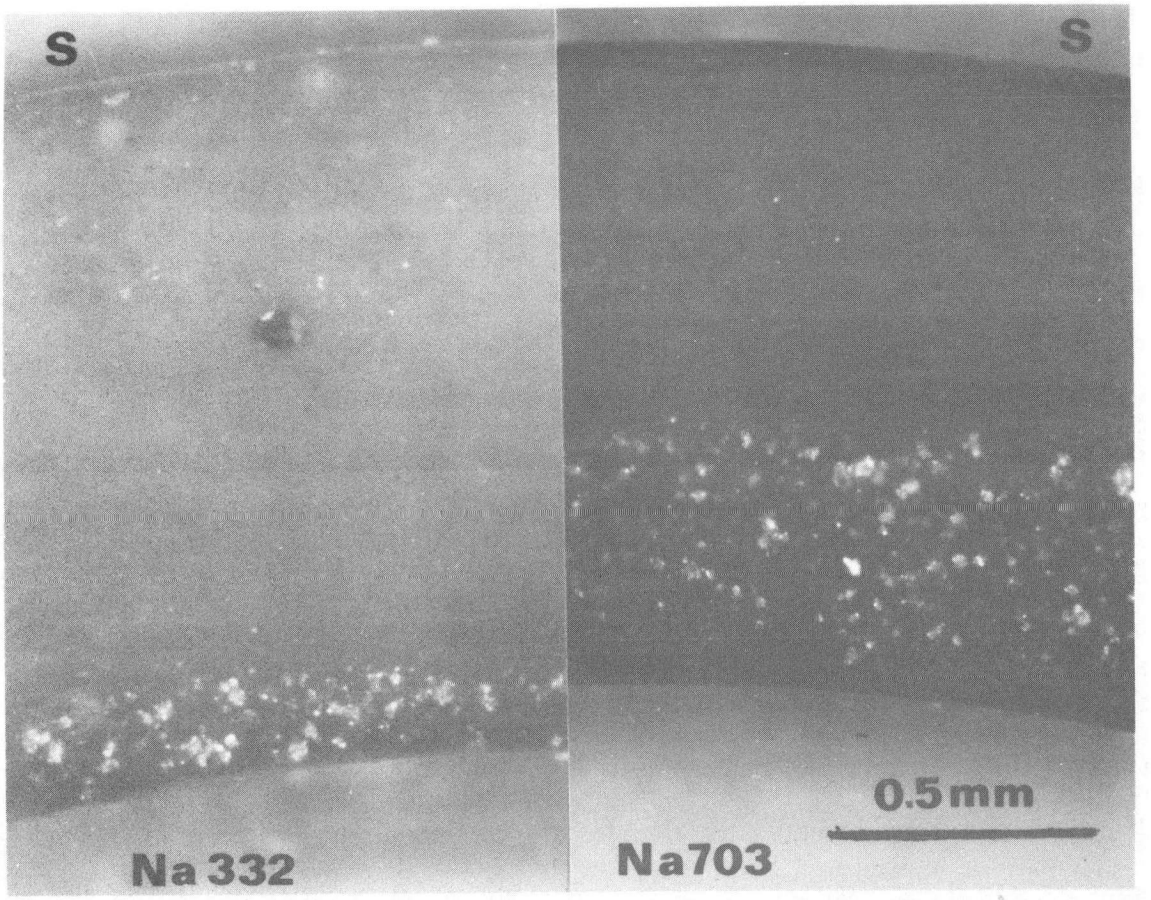

XBB 804-4119

Fig. 6.7 Polished, silver decorated cross sections of beta electrolyte tubes. Note white spotty reflections (subsurface fractures due to mode II processes) near sodium surfaces. (332 Ahr cm^{-2} left and 703 Ahr cm^{-2} right)

damaged material which appears to propagate through the wall to a depth dependent on the total charge transfer. In the 703 Ahr cm^{-2} specimen, it has progressed about 1/3 of the way through the tube wall. The white spotty reflections in the micrograph were found to be subsurface in nature by their focusing behavior in the optical microscope, and are proposed from the evidence given below to be fractures associated with the internal deposition of metallic sodium. This slow degradation cannot be accounted for by arguments based on Poiseuille pressure (mode I breakdown) since it exhibits a different morphology. The internal deposition of metallic sodium requires that there be some electronic conductivity in the electrolyte, as well as conditions of electrical potential, so that the activity of sodium metal in the electrolyte can be greater than 1. This constitutes the basis for mode II breakdown. The investigation of chemical coloration has shown that molten sodium reduces the beta aluminas creating oxygen vacancies and sodium ion-electron pairs, and increasing the electronic conductivity of the electrolyte. An electronic conductivity gradient that leads to mode II degradation is thus set up. Local fluctuations in the electric field at grain boundaries and junctions make them likely sites for the initiation of mode II breakdown. Second phase inclusions in grain boundary regions may also assist the mode II process by lowering the electrochemical potential for the nucleation of sodium metal.

Transmission electron microscopy gives strong evidence that grain boundaries and triple junctions are indeed preferred sites for sodium deposition. A 650 kV instrument was used making possible the examination of thick foils prepared by ion milling from the electrolytes. In thin foils, it is frequently difficult to distinguish true breakdown

effects from milling artifacts. Figure 6.8 is a 650 kV TEM micrograph of a thick foil of beta electrolyte cycled for 371 Ahr cm^{-2}. Arrows point to areas where degradation has occurred at a grain triple junction and along grain boundaries. Microcracking is frequently seen in such areas, and this is shown in Figure 6.9. Similar areas in thin foils were observed in the Phillips 400 STEM which made it possible to analyze their content. The result of an analysis done on such a region is shown in Figure 6.10. The dots show the x-ray peaks from the degraded and microcracked area. The vertical bars represent the peaks from an undegraded region of the sample for comparison. The detector was set to stop at the same aluminum peak height for both of the curves in Figure 6.10 to provide the basis for semi-quantitative comparison. The scan from the degraded region shows a higher concentration of sodium than in the bulk, which is to be expected in a degraded area. It is proposed that these regions are the precursors of the spotty white reflections seen in optical microscopy. The scan also shows that there is silicon present in the degraded region, consistent with the observation made earlier that the presence of a second phase may be ancillary to mode II breakdown.

Although darkening was not as pronounced in the beta" electrolytes as they were received, it was enhanced substantially by the silver decoration procedure; and it manifested a definite progression in intensity with increased cycling time, as can be seen by comparing Figure 6.11 (121 Ahr cm^{-2}) with Figure 6.12 (539 Ahr cm^{-2}). The white spotty reflections found in the beta electrolytes have not been observed in any of the beta" electrolytes examined so far.

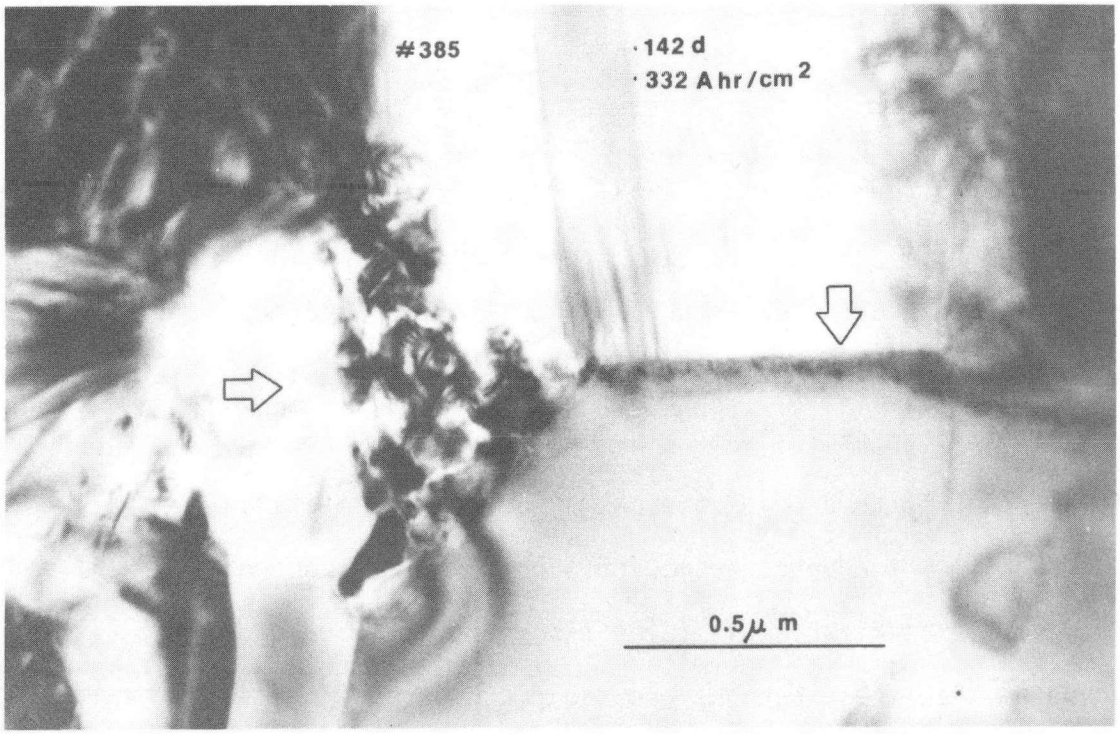

XBB 803-3889

Fig. 6.8 600 KV TEM micrograph of beta electrolyte thick foil. Arrows point to degradation at grain triple junction and along grain boundary.

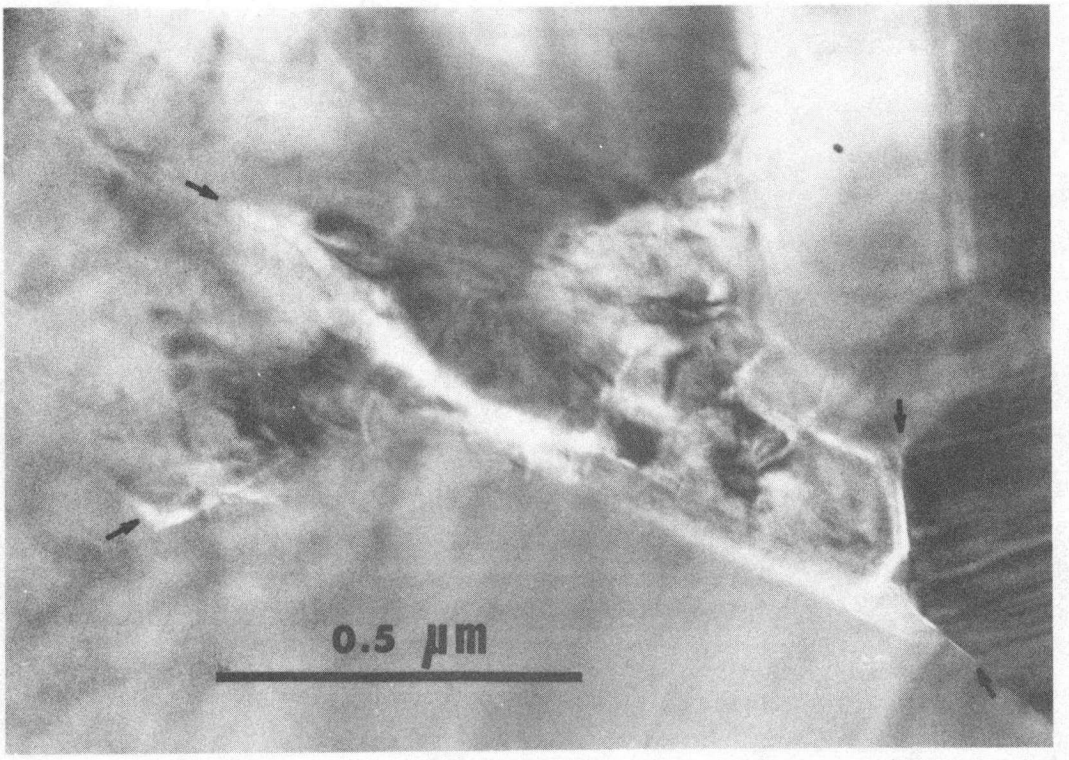

XBB 806-7055

Fig. 6.9 600 KV TEM micrograph of beta electrolyte thick foil showing microcracking associated with degradation at grain junction.

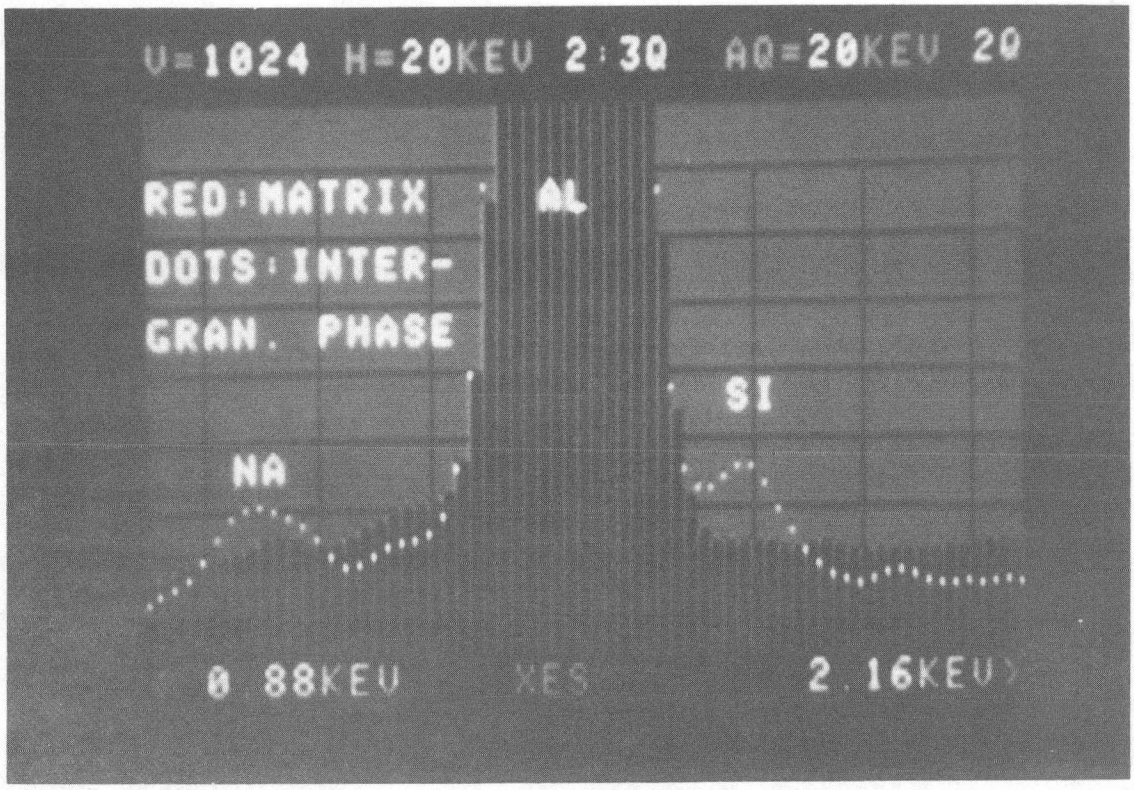

CBB 803-3568

Fig. 6.10 X-ray spectrum from degraded grain junction (dots) compared with spectrum from undegraded region (vertical bars) showing excess sodium and silicon are present in the degraded region.

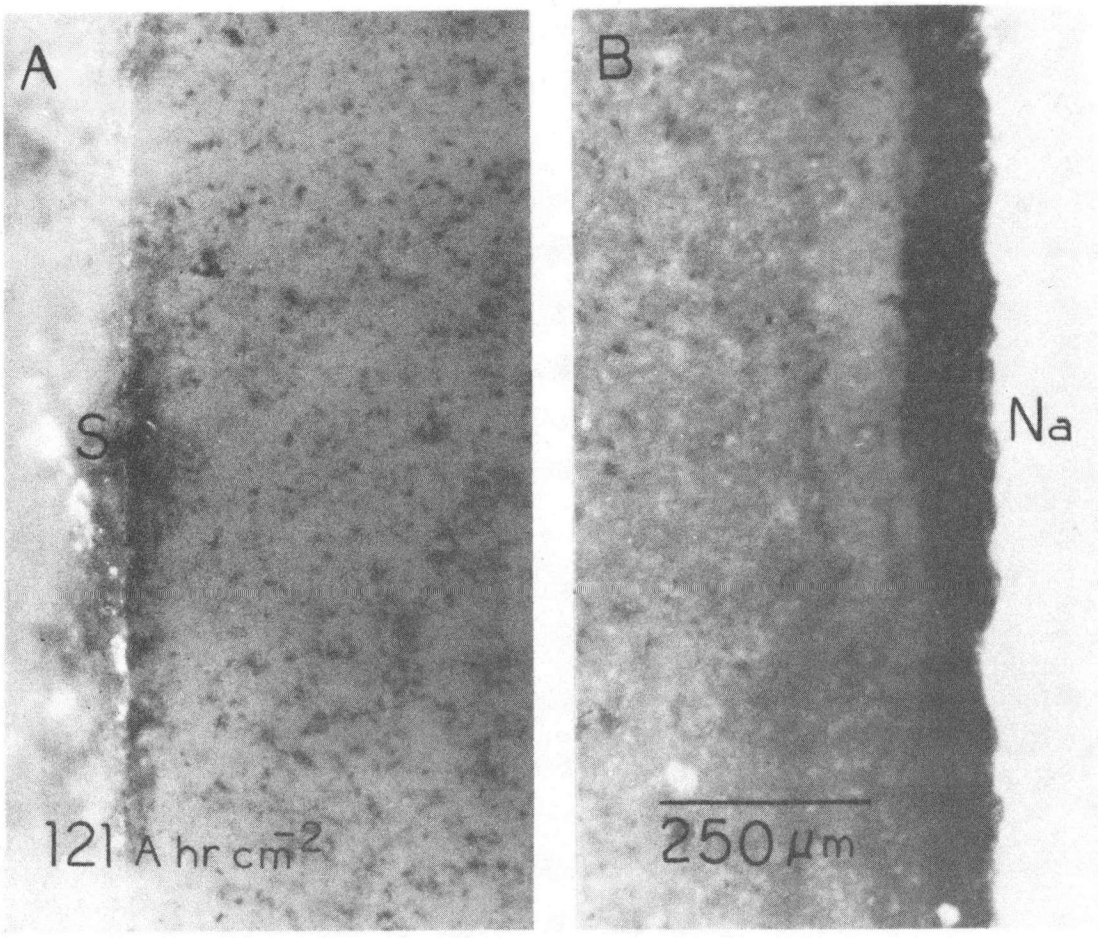

XBB 814-3170

Fig. 6.11 Silver decorated polished cross section of beta" electrolyte tube from sodium/sulfur cell cycled to 121 Ahr cm^{-2} of charge transfer over a period of 95 days. A. Sulfur side B. Sodium side

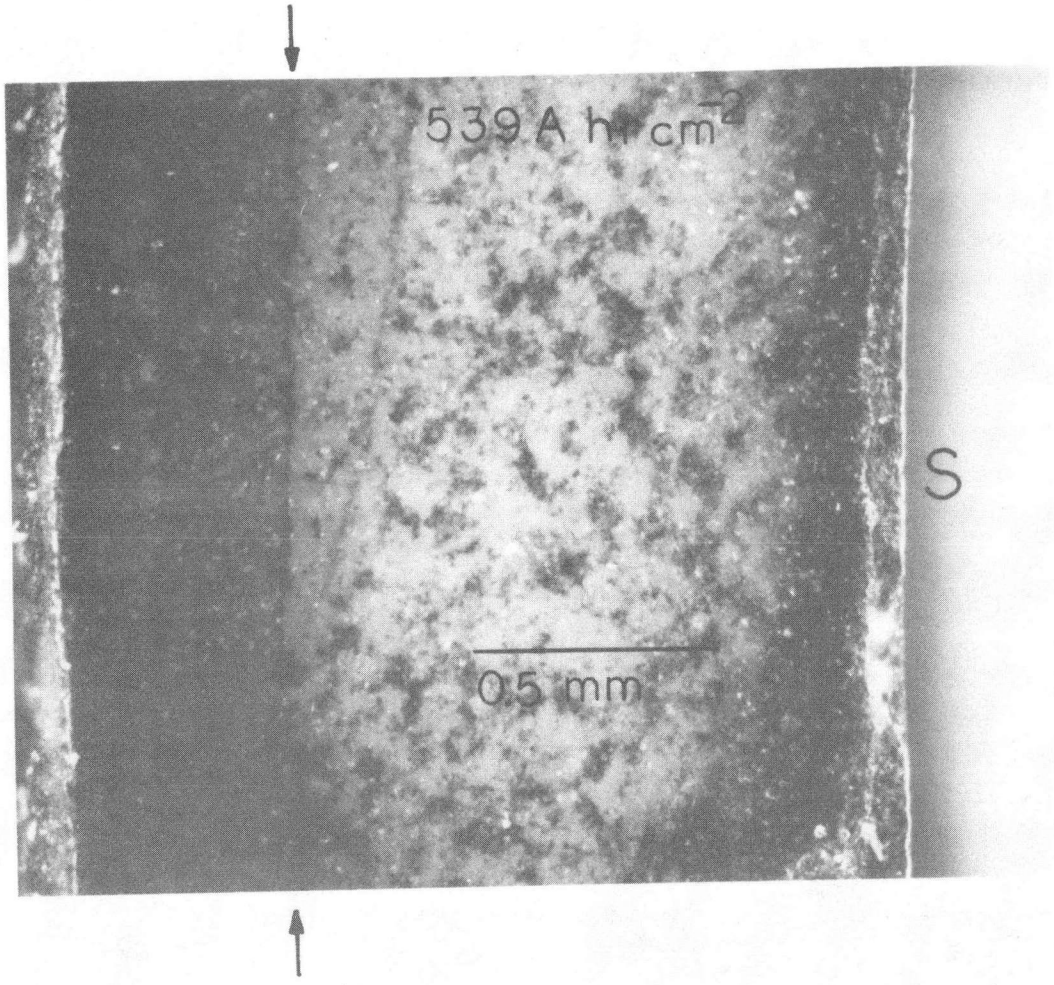

XBB 814-3174

Fig. 6.12 Silver decorated polished cross section of beta" electrolyte tube from sodium/sulfur cell cycled to 539 Ahr cm^{-2} charge transfer over a period of 673 days. Note subsurface annular crack.

Cracks running parallel, or nearly so, to the electrolyte surface are especially apparent in the beta" electrolytes. In the sections made for examination, these cracks frequently are not traceable to the sodium surface. Note particularly the annular crack in the cell wall shown in Figure 6.12 at a depth of about 1/4 the wall thickness below the sodium surface. The fact that the crack runs almost exactly parallel to the surface of the tube suggests that it may not simply be a deflected mode I crack. De Jonghe (De 81b) has considered the implications of transport number gradients in solid electrolytes and his results suggest a possible explanation. Making the simplifying assumption that the ionic conductivity remains constant over the thickness of the electrolyte while the electronic conductivity increases substantially in some manner in going from the sulfur to the sodium surface, he notes that the electrochemical potential of the sodium as a function of depth in the electrolyte, $\eta_M(x)$, can be expressed:

$$\eta_M(x) = (x/\ell)\Delta\eta_M^o + V_T F \cdot f(p^x) \qquad 6.1$$

where x is the distance from the sodium surface, ℓ is the total thickness of the electrolyte, $\Delta\eta_M^o$ is the counter EMF over the electrolyte, V_T is the total applied voltage over the electrolyte, F is Faraday's constant, and p^x is the ratio of ionic to electronic conductivity in the electrolyte as a function of x. The form of $f(p^x)$ is given explicitly in DeJonghe's paper. The first term in equation 6.1 is just the normal value of $\eta_M(x)$ under open circuit conditions and the second term modifies this as a function of the applied voltage and the electronic conductivity gradient in the ceramic. It is shown that under appropriate

recharge conditions, $\eta_M(x)$ can become positive within the ceramic making it possible, in principle, to deposit sodium metal under pressure there. The pressure associated with such deposition is given by:

$$P(x) = \eta_M(x)/v_M \qquad 6.2$$

where v_M is the molar volume of sodium. When the pressure exceeds the fracture strength of the ceramic, cracking will occur. Under appropriate conditions, a maximum will exist in the value of $\eta_M(x)$ for some x such that $0 < x < \ell$. For instance, for the assumptions of a linear change in p^x across the thickness of the electrolyte and of $p^{x=0} >> p^{x=\ell}$, the maximum exists at:

$$x/\ell = (FV_T + \Delta\eta_M^o)/2FV_T \qquad 6.3$$

If the electrochemical potential at such a maximum is high enough, cracking can be expected in the electrolyte at the depth indicated by equation 6.3. The exact conditions of applied potential which will produce this mode II situation will depend on the functional dependence of p^x on x. At present it is not possible to determine this. De Jonghe notes that his treatment implies the following conditions must be avoided if maximum cell life is to be achieved:

1. Excessive applied voltage during recharge.
2. Thick electrolyte tubes.
3. Conditions leading to polarization at the sulfur surface.

4. Increase in ionic resistance of the electrolyte due to its original composition or to contamination in the course of cell operation.

5. Local regions of low electrolyte strength.

Evidence of mode I break down was also found in the course of examining cycled cell electrolytes. Figures 6.13 to 6.15 show cracks which have originated at the sodium surface, and which probably grew by the Poiseuille mechanism. The deflection and branching evident in these cracks is typical of most of the mode I cracks, and has the effect of propagating the crack in a direction almost perpendicular to the direction of current flow. In this orientation the crack is more effectively current fed. The deflection will retard the penetration of the tube wall by cracks, but may be responsible for spalling and pitting of the electrolyte surface.

Boundaries of the large grains near the surface may act as preferential sites for the initiation of mode I breakdown. Several instances were found in the beta" electrolytes where degradation was more advanced in the vicinity of large surface grains than in other surface regions where there were no anomalously large grains. Figure 6.16 shows such a region in a beta" electrolyte which had seen 121 Ahr cm^{-2} of charge transfer. When a closer look is taken at the region of enhanced breakdown (Figure 6.17), alternation between unpolarized illumination (A) and polarized illumination (B) shows a large grain of about 80 μm in length present at the surface. Another pair of micrographs (Figure 6.18) from a different surface location in the same cell shows the morphology of this type of breakdown a little more clearly. In the non-polarized light micrograph (A) several large grains adjoining one another can be

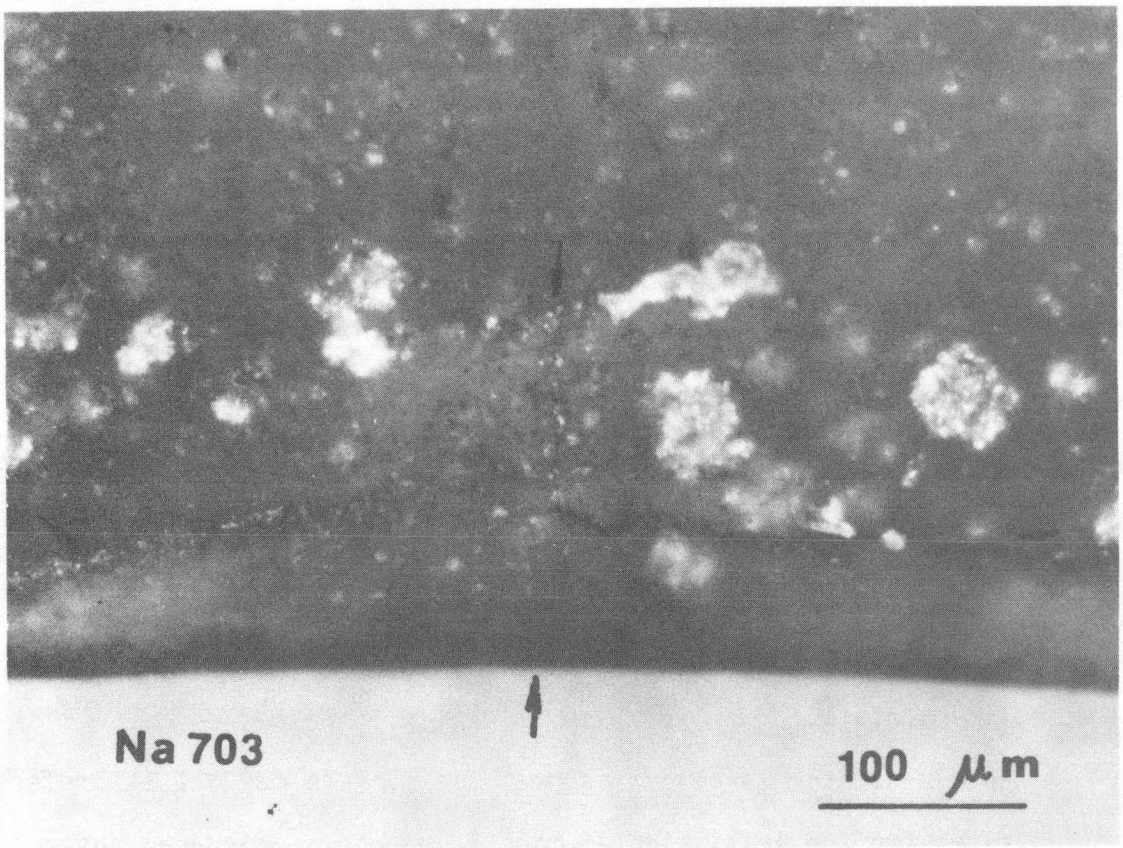

XBB 804-4121

Fig. 6.13 Macrocracking (Mode I degradation) originating sodium surface in beta electrolyte and branching to run parallel to surface. Mode II degradation is also in evidence here.

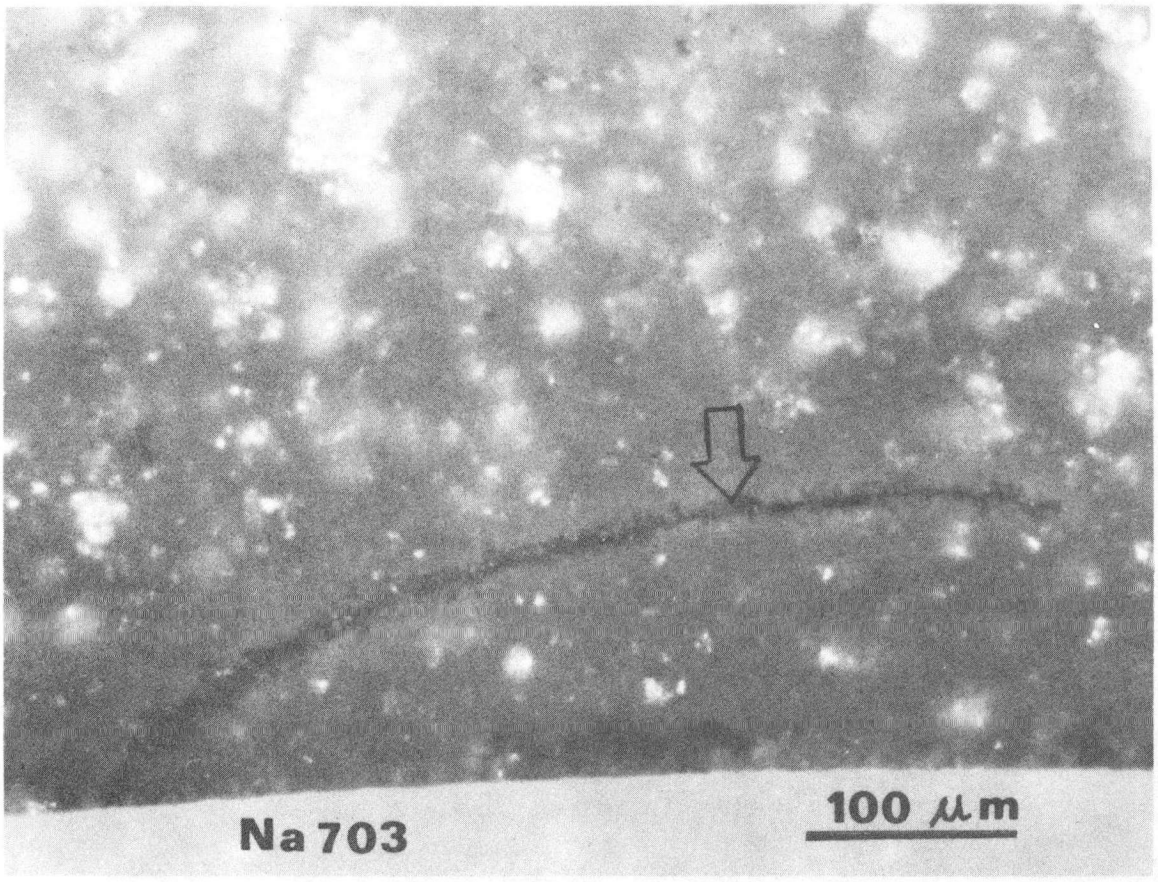

XBB 804-4120

Fig. 6.14 Mode I crack which has initiated at sodium surface in beta electrolyte and then deflected to run parallel to surface.

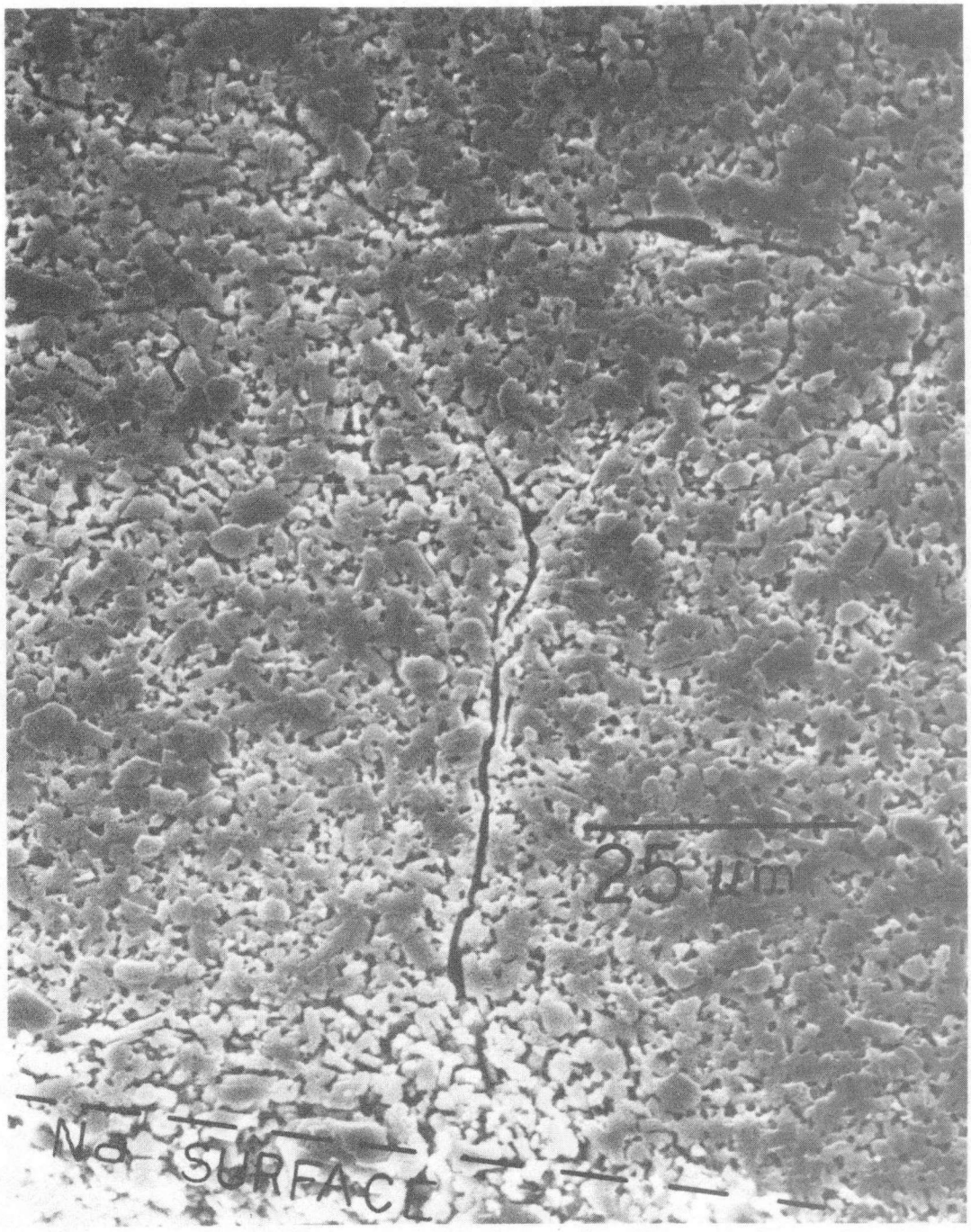

XBB 807-8875

Fig. 6.15 SEM micrograph of Mode I crack in beta electrolyte. Note how crack branched to run parallel to surface.

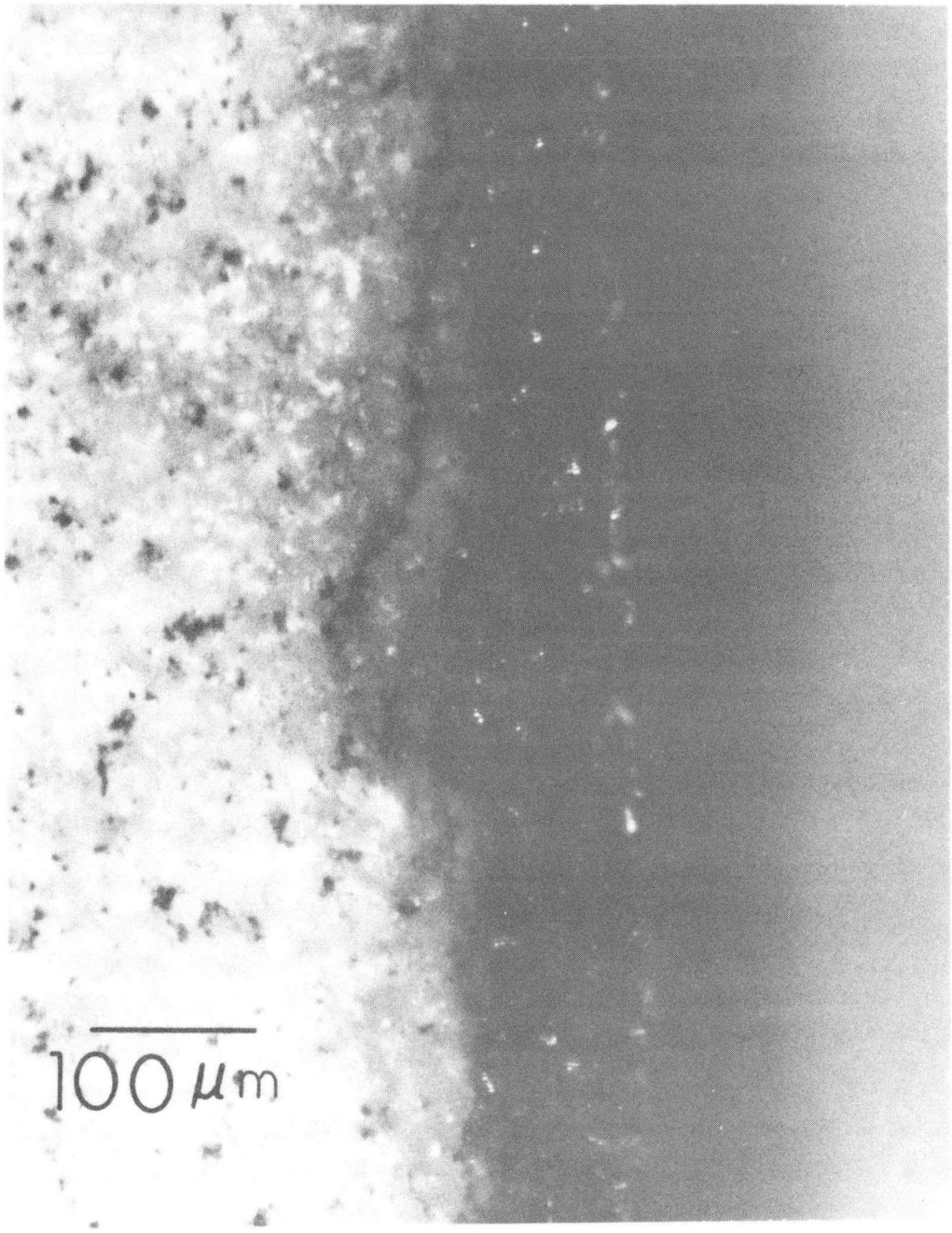

XBB 814-3176

Fig. 6.16 Region of enhanced degradation at sodium surface in beta" electrolyte from sodium/sulfur cell cycled to 121 Ahr cm^{-2} of charge transfer. (Polarized illumination)

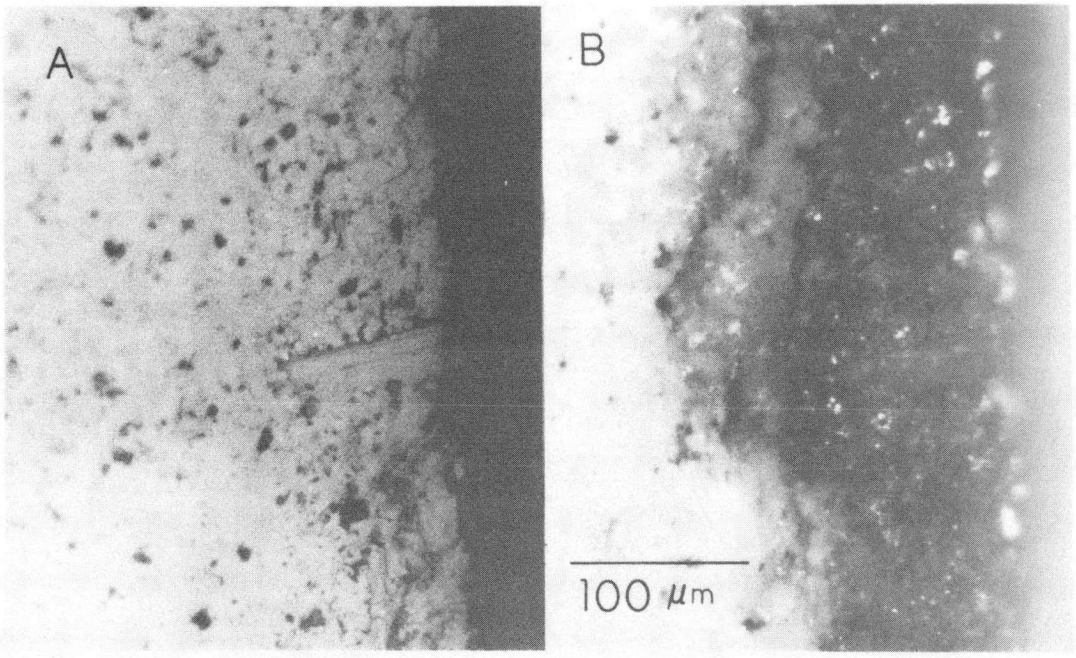

XBB 814-3175

Fig. 6.17 Detail of area shown in Figure 6.16. A. Unpolarized illumination reveals grain structure. B. Partially polarized illumination locates large grain in region of enhanced degradation.

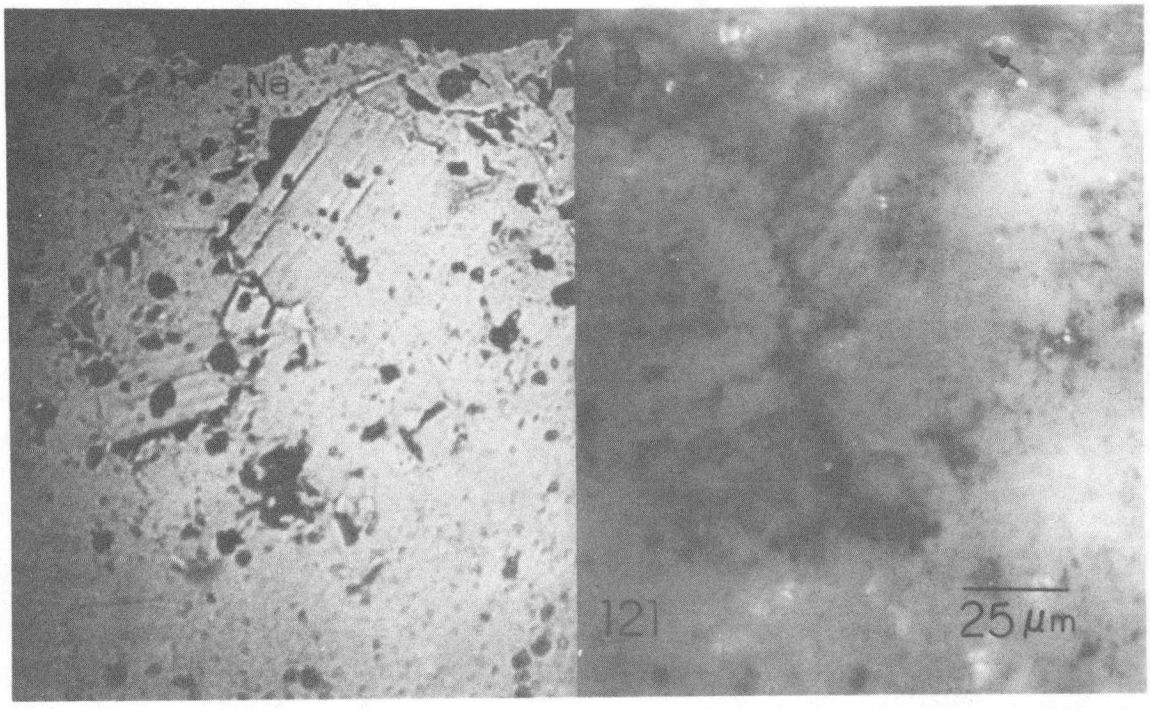

XBB 814-3576

Fig. 6.18 A. (Unpolarized illumination) Large grains near the sodium surface serve to facilitate B. (polarized illumination) breakdown along their boundaries. Arrows point to same location in both micrographs for reference. Different area from same cell used for Figure 6.16.

seen, the longest being about 50 μm across and located just below the sodium surface of the electrolyte. With polarized illumination (B) the path of degradation can be seen clearly, and it follows the boundaries of the large grains to a depth of about 125 μm beneath the surface.

6.2.5 The Sulfur Electrode/Electrolyte Interface

Deterioration of the electrolyte at the sulfur/electrolyte interface has customarily been considered to be a much less serious problem than that at the sodium/electrolyte interface, and references to it are infrequent in the literature (cf. Fa 73b, Iw 80). Consequently there is no model at hand to apply to the sulfur surface degradation which has here been observed. The sulfur surfaces of the beta electrolyte tubes shown in Figure 6.2 show signs of attack, and this is more than just a superficial effect as closer examination shows. Figure 6.19 shows the silver decorated sulfur surface of the 703 Ahr cm^{-2} beta cell and reveals a regular pattern of imprinting due to contact with the carbon felt in the polysulfide electrode. This effect has been noted by researchers at Ford Motor Company (Fo 77) and others, but it has not previously been identified as part of a progressive mode of degradation. High magnification optical micrographs of the sulfur surfaces of the 23 and the 703 Ahr cm^{-2} beta cells are compared in Figure 6.20 to show how the progress of the degradation is manifested in the severe darkening and cracking of the electrolyte surface. Decorated polished cross-sections of both the 322 and the 703 Ahr cm^{-2} beta cells are shown in Figure 6.21. A definite sursurface effect can be seen here; the degradation is spotty and scattered at first, but at later time it becomes a fully established layer.

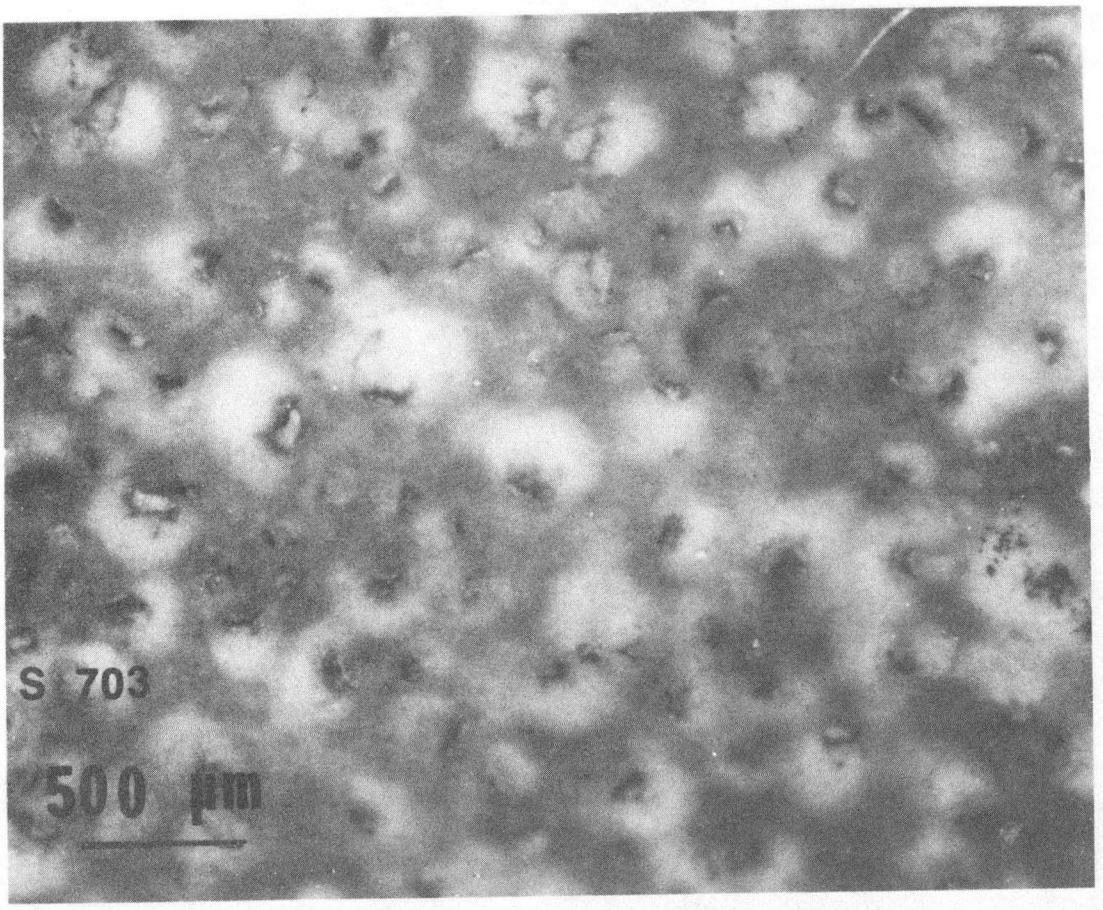

XBB 804-4125

Fig. 6.19 Silver decorated sulfur surface of beta electrolyte showing regular pattern of imprinting from carbon felt. (703 Ahr cm^{-2} charge transfer)

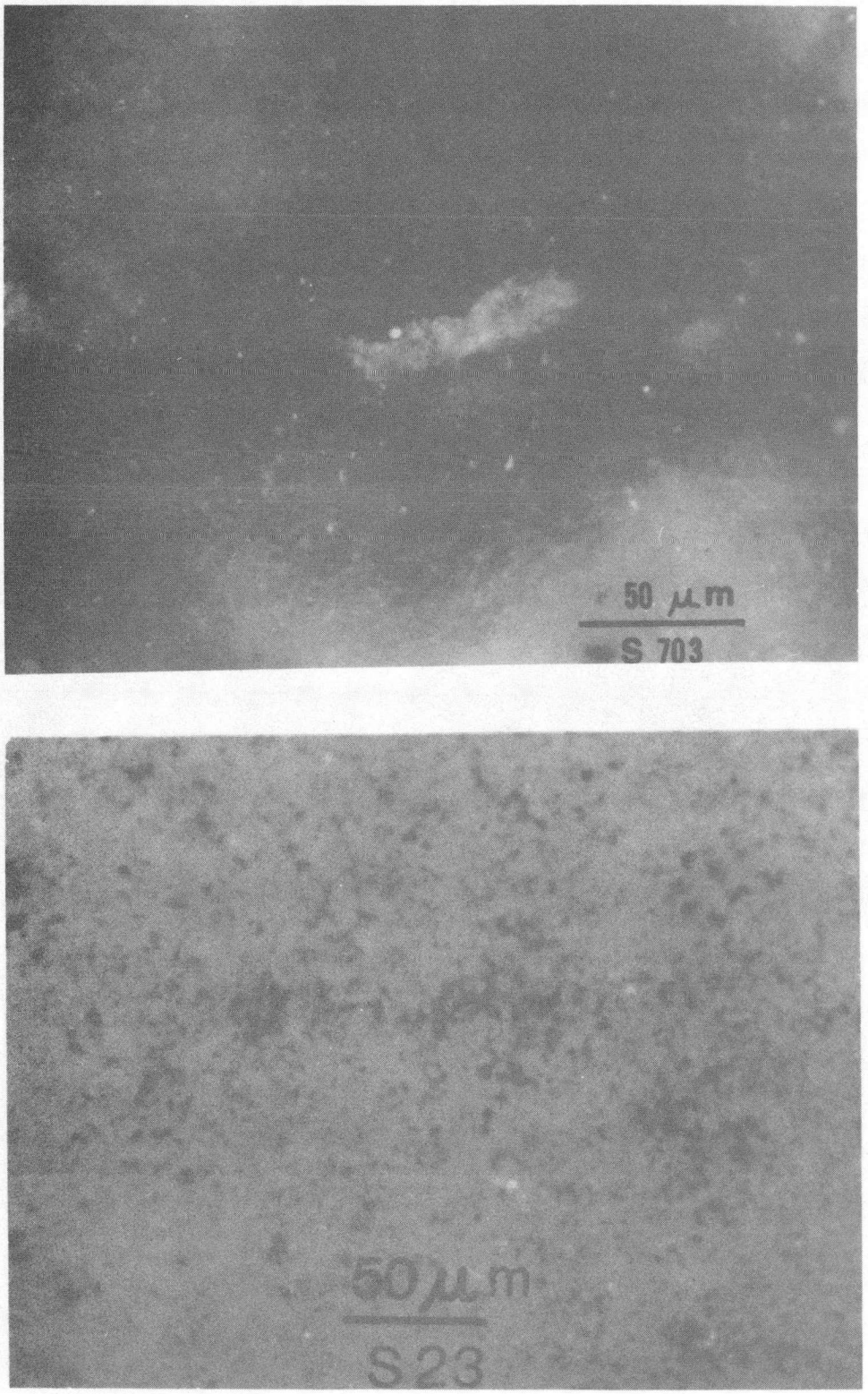

XBB 804-4116A

Fig. 6.20 Silver decorated sulfur surfaces of cycled beta electrolytes. (703 Ahr cm^{-2} top, 23 Ahr cm^{-2} bottom)

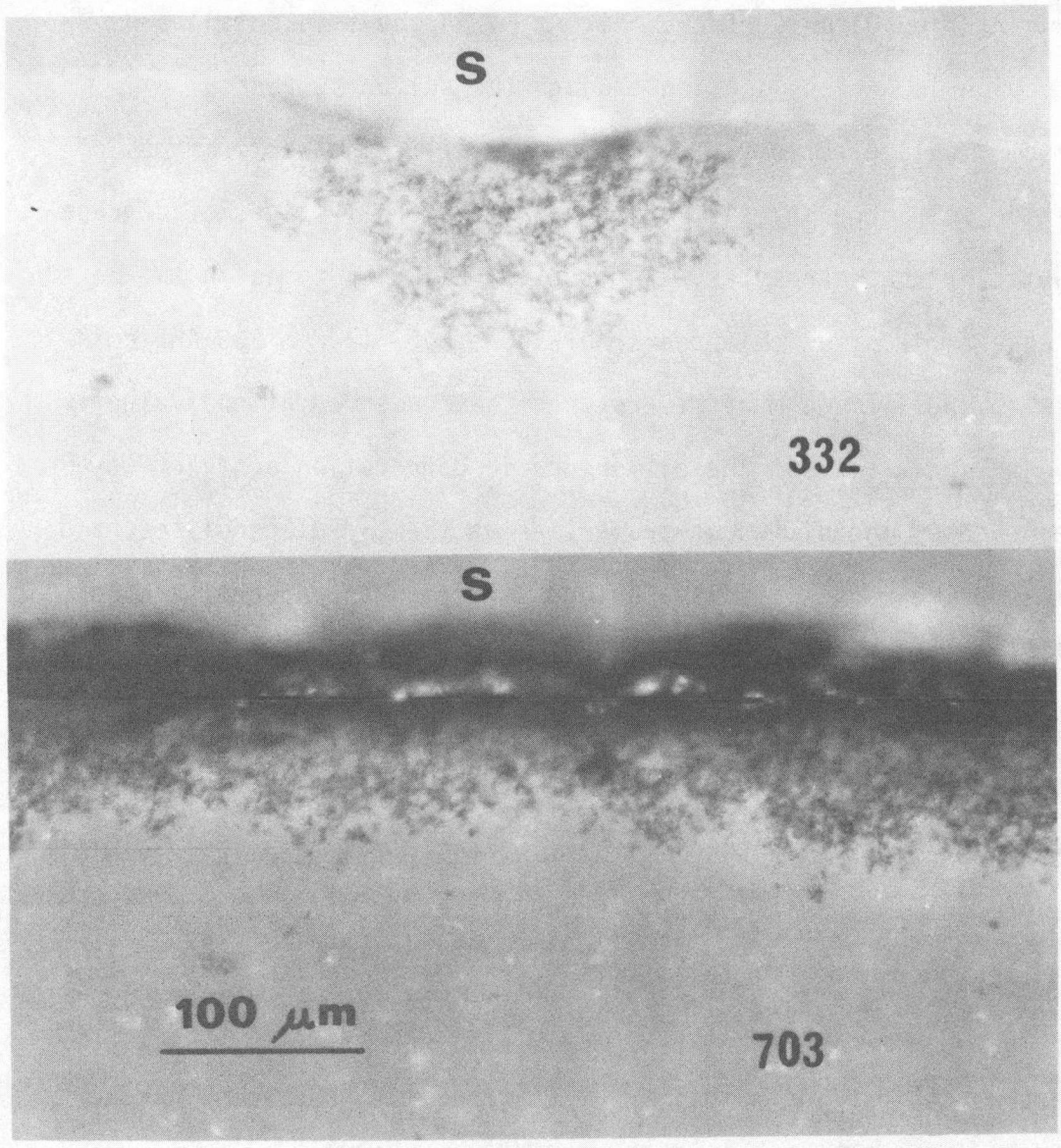

XBB 804-4128

Fig. 6.21 Silver decorated polished cross sections of cycled beta electrolytes showing progress of breakdown near sulfur surface.

The beta" electrolytes exhibit a somewhat different morphology of breakdown at the sulfur surface. Figure 6.22A shows in detail a degraded region in a cross section through the sulfur surface of a 121 Ahr cm^{-2} cell electrolyte (cf. Figure 6.11). The early stages of degradation seen here do resemble somewhat the early stages of degradation in the beta electrolytes. Degradation at later times in the beta" cells, an example of which appears in Figure 6.23 from a 539 Ahr cm^{-2} cell, is obviously much more severe than that observed at equivalent times in the beta cells. The difference in degradation behavior may be a consequence of the different properties of the two electrolytes, and/or it may be the result of different construction and operating conditions of the cells. It is not possible to determine on the basis of the data available.

The features observed indicate that a crack network develops below the sulfur surface in the electrolyte. Sulfur, sodium, or polysulfides must be present in this network to account for its decoration by the silver nitrate treatment. Fally et al. (Fa 73b) reported in early work on the Na/S cell at Compagnie Générale d'Electricité, Marcoussis, Essonne, France that conchoidal fractures frequently appeared in the sulfur surfaces of electrolytes in cells that had been operated normally. They stated further that when cells were cycled past full discharge (Na_2S_3) using an external current source, conchoidal fractures were always observed on the sulfur surface, and when the composition of the polysulfide electrode reached Na_2S_2, the electrolyte tube ruptured. Operating temperature of their cells was 330°C and the melting point of Na_2S_2 is about 450°C. The cracking and rupture was attributed to

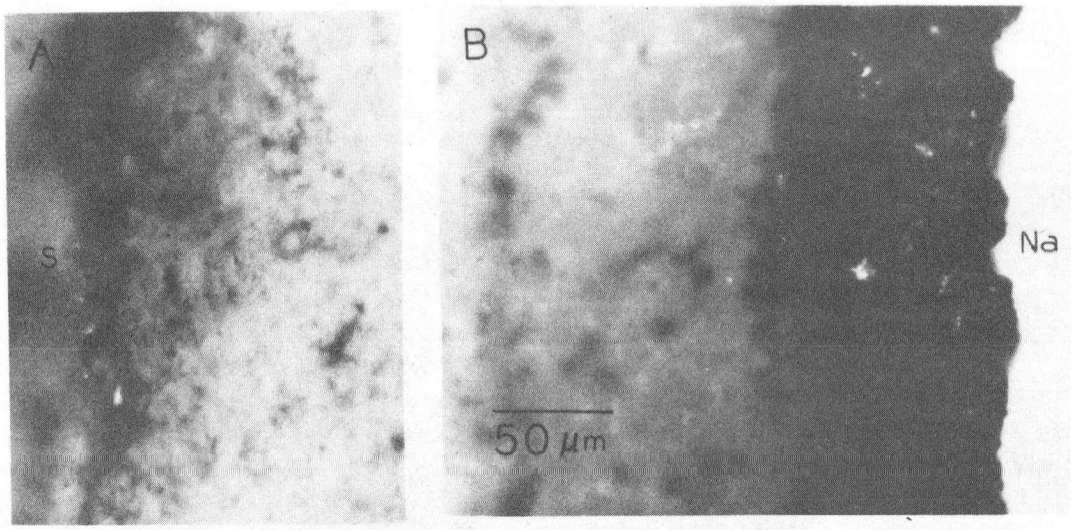

XBB 814-3172

Fig. 6.22 Silver decorated polished cross sections of beta" electrolyte first shown in Figure 6.11. Higher magnification reveals details. A. Sulfur surface B. Sodium surface

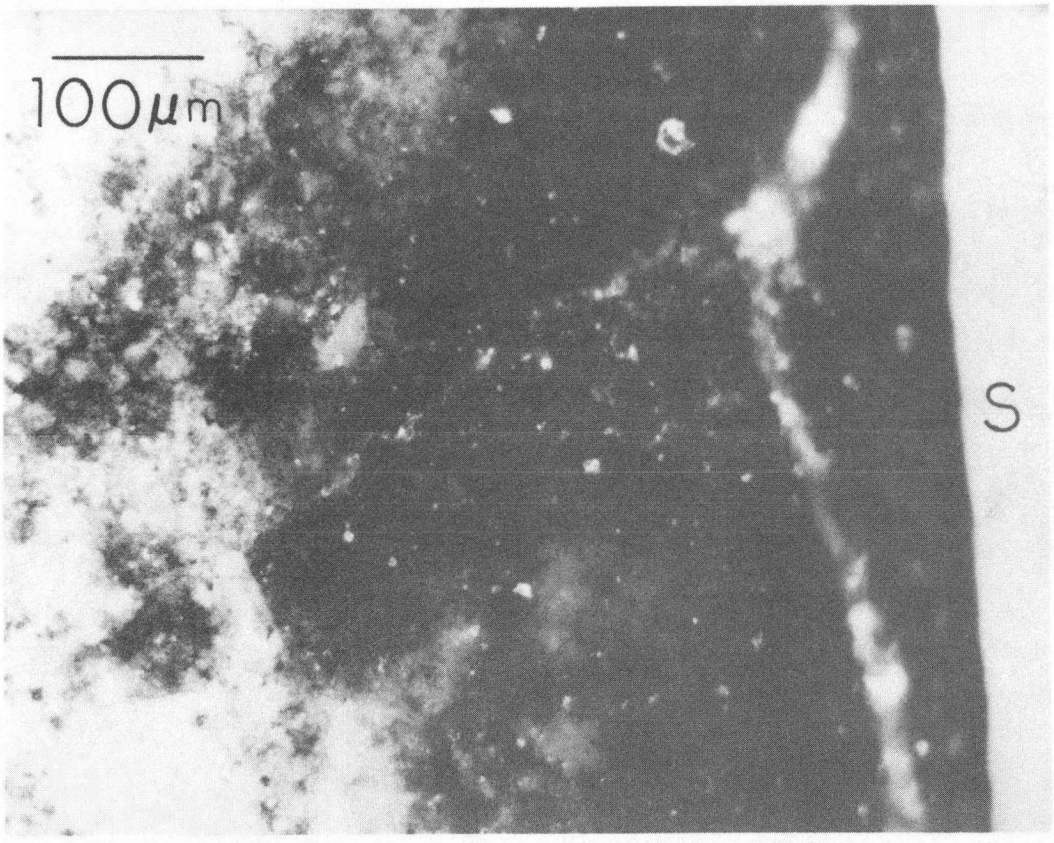

XBB 814-3173

Fig. 6.23 Silver decorated polished cross sections of beta" electrolyte first shown in Figure 6.12 revealing extensive degradation propagating from sulfur surface.

stresses arising from the deposition of solid reaction products on the electrolyte surfaces.

The appearance of degradation at the sulfur/electrolyte interface in the early stages of cell operation is that of a fine crack network. Auger spectroscopy of in situ fracture surfaces revealed the presence of sulfur beneath the electrolyte surface, which would be difficult to explain in the absence of such a network. It is proposed that the degradation initiates at points of contact of the carbon felt with the electrolyte by a process of chemical reduction assisted by the electrochemical potential conditions on recharge. During discharge, insulating accumulations of solid sulfides are likely to form around points of contact between carbon fibres and electrolyte as shown in Figure 6.24. Repeated cycling may lead to mechanical degradation as a result of the periodic strains produced by the solidification-deposition and redissolving of the sulfides. One might speculate that under charging conditions electrons may be removed from the beta alumina as well as the polysulfide electrode if the potential difference between the carbon fibre and the ceramic becomes great enough. A possible reaction in these circumstances would be:

$$O_i'' + Na_{Na} \longrightarrow V_{Na}' + O_i' + [Na^+_{(\text{negative electrode})} + e^-_{(\text{positive electrode})}] \qquad 6.4$$

Carbon would then intrude into the electrolyte reacting with the O_i' producing the observed cracking. This is only one of many possible postulates permitted by the present observations. The actual reaction taking place is the subject of another study which has been undertaken by Guhanand Raj of this research group (Ra 82).

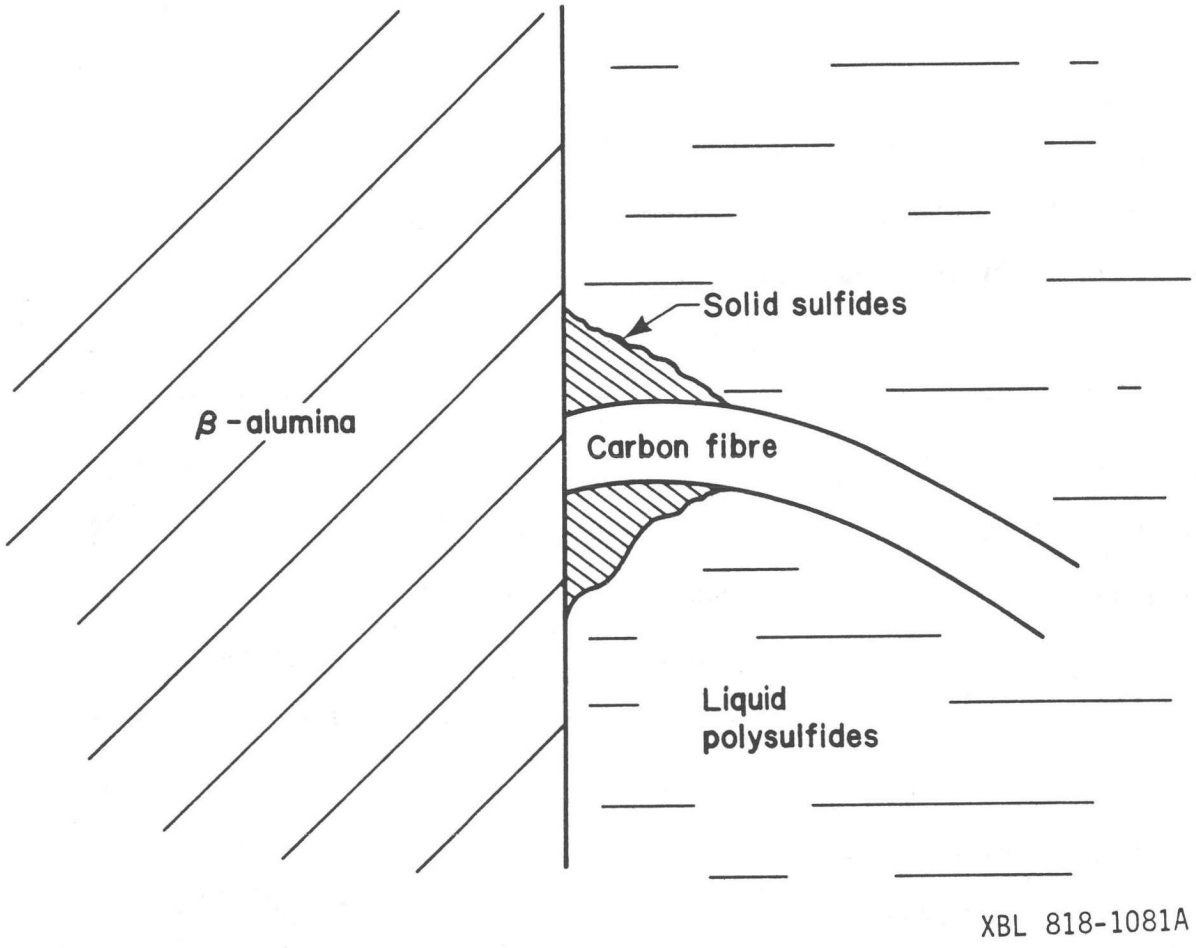

Fig. 6.24 Probable situation late in discharge cycle at positive electrode/electrolyte interface where carbon fibre contacts electrolyte.

6.2.6 Auger Analysis

A few specimens of the beta electrolytes were fractured in situ in the scanning Auger microscope to permit examination of the uncontaminated fracture surface. Figure 6.25 is an Auger spectrum from a region about 50 microns beneath the sulfur surface of a 332 Ahr cm^{-2} cell. The findings of principal interest are the carbon and sulfur peaks marked. Silicon is another element which frequently shows up via Auger analysis but its distribution is irregular. It had already been observed in TEM foils, and is a known impurity in the raw powder used to make the beta electrolytes; so its appearance here is not surprising. The carbon is hard to account for. An open crack network would permit carbon contamination from organic solvents used to clean the tube or by CO_2 from the atmosphere reacting with sodium residue. However, such an explanation is at least as likely to apply at the sodium surface where the carbon peak was always absent or much weaker. It seems likely, therefore, that the carbon felt is the source of the carbon found in the electrolyte. One possible mechanism for the transport of carbon into the electrolyte has already been offered in the previous section of this chapter. It is also possible that colloidal carbon may be formed and carried into cracks under the influence of cell cycling, or that electrical discharge occurring at the contact between felt and ceramic, or felt and positive terminal, might cause some carbon disulfide to be formed which could easily penetrate any cracks.

Polysulfides would eventually enter any crack network formed as long as it was open to the surface, so its presence in the spectrum shown just adds to the evidence for such a crack network. The sulfur peak disappeared as expected when a very small (0.1 μm) beam was used

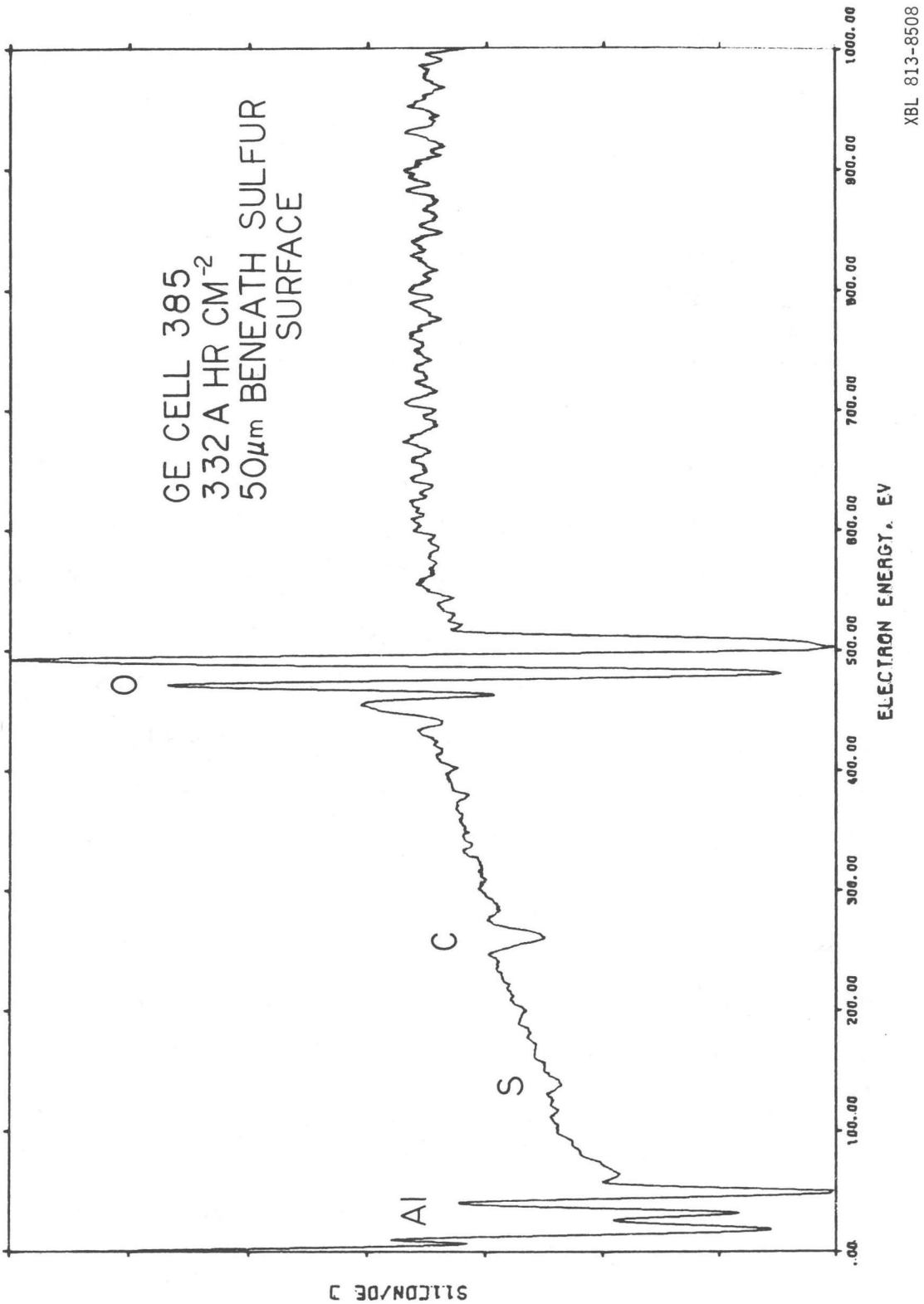

Fig. 6.25 Auger spectrum from beta electrolyte.

and positioned on raised portions of the fracture surface corresponding to transgranular fracture. The sodium peak was generally absent or too weak to provide any information about the relative distribution of sodium in the ceramic. This is due to the high mobility of the sodium ion in the electrolyte. The observation has been made by several researchers (see e.g., Pa 76) that the detection of ions of high mobility in materials by Auger spectroscopy is frequently difficult or impossible without involved procedures, because the fields produced by irradiation of the sample surface with the electron beam tend to cause the ions to migrate away from the beam.

6.2.7 Complex Conductivity Measurements on the 23 Ahr cm^{-2} Beta Cell

When a piece of 23 Ahr cm^{-2} beta electrolyte from G.E. was silver exchanged in molten silver nitrate, a dark bluish-black layer formed extending from the sodium surface to a depth of about half the tube thickness. Specimens from other beta tubes which had been subjected to charge transfers of over 200 Ahr cm^{-2} were darkened all the way through. Figure 6.26 compares silver exchanged specimens from 23 and 703 Ahr cm^{-2} beta electrolyte tubes which had been on test for 10 and 301 days respectively. Electrolyte samples of two other beta electrolyte tubes, from cells which had merely been maintained over a long period of time at operating temperature with little or no cycling, also darkened completely on silver exchange. Mere contact with sodium at elevated temperature seemed sufficient to produce the darkening observed, and this hypothesis was confirmed by the experiments described in Chapter 4 in which beta alumina single crystals and virgin beta" alumina

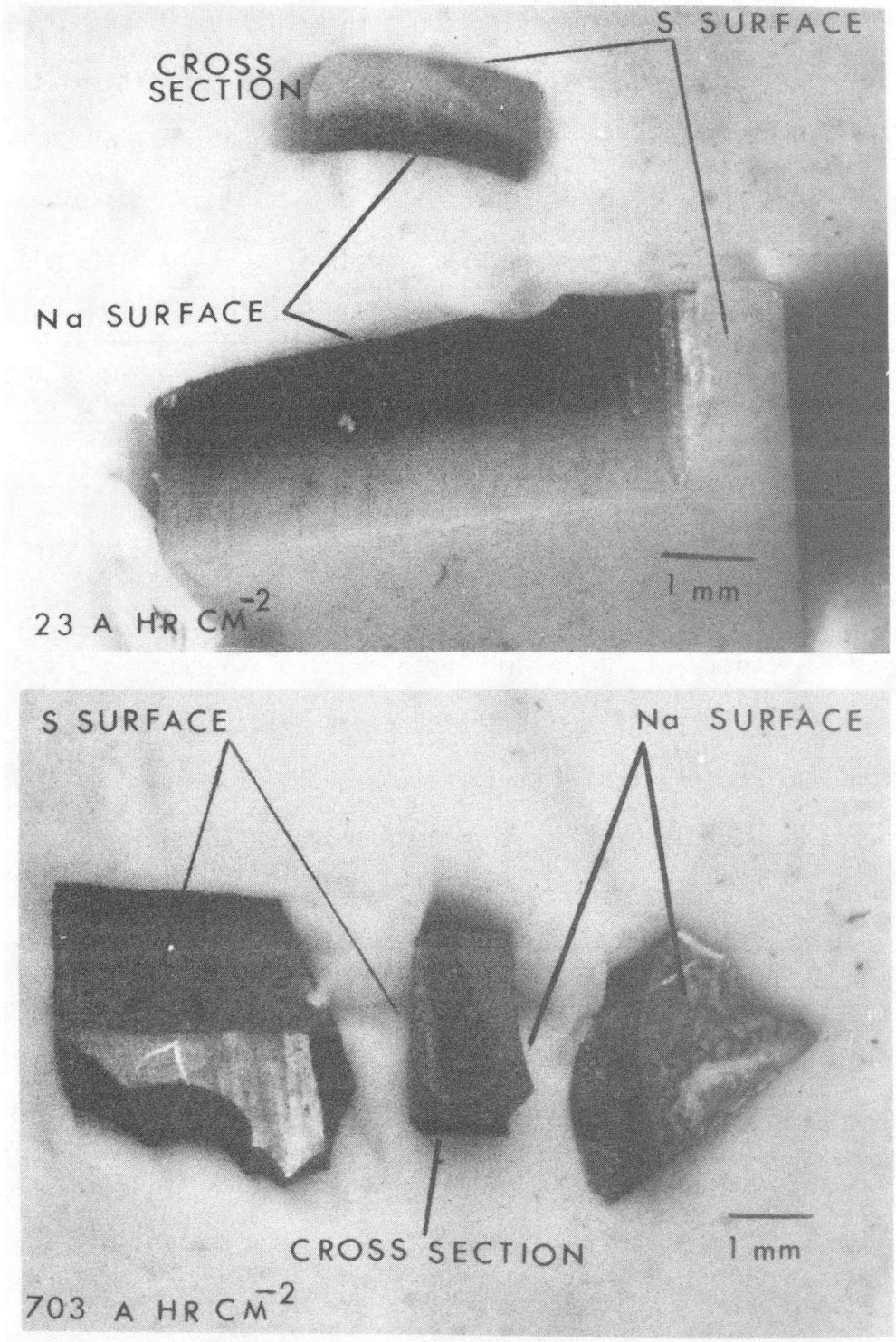

XBB 807-8883

Fig. 6.26 Silver exchanged beta electrolyte material from 23 Ahr cm^{-2} cell (top) and 703 Ahr cm^{-2} cell (bottom) showing how darkening progresses from partial to full depth.

polycrystalline electrolytes were immersed in molten sodium. The blackening requires that exchanged silver ions acquire an electron from some source, so that they can be reduced to metallic silver.

Specimens from the beta" electrolyte tubes also exhibited darkening on exchange, but the progression of the darkening through the electrolyte was obviously much slower than in the beta electrolytes. The coloration was also more dark brown than black. Figure 6.27 shows the polished cross section of a beta" electrolyte tube from a 539 Ahr cm^{-2} cell which had been on test for 673 days.

It was thought that a comparison of the complex conductivity of the discolored and not discolored part of the 23 Ahr cm^{-2} beta electrolytes might provide some clues as to what was taking place, so a small longitudinal section was cut out of the tube and carefully sliced down the middle to create two rectangular bar specimens for such measurements. The admittance plots obtained at 200°C are shown in Figure 6.28. The intercept at the left of the dispersion curve with the conductivity axis gives the transgranular conductivity of the sample. The conductivity of the sample from the heavily darkened sodium side of the electrolyte is about 12% lower than that of the sample from the sulfur side indicating a change has taken place within the electrolyte grains on the sodium side. The specimen from the sulfur side shows only one semicircle which is normal behavior for this kind of sample. The specimen from the sodium side shows two overlapping semicircles which is indicative of lower conductivity in the grain boundary regions (Bu 78, pp. 64-69), perhaps due to the presence of microcracks. It is probable that much of the difference observed in these measurements developed after the cycled electrolytes were exposed to the atmosphere.

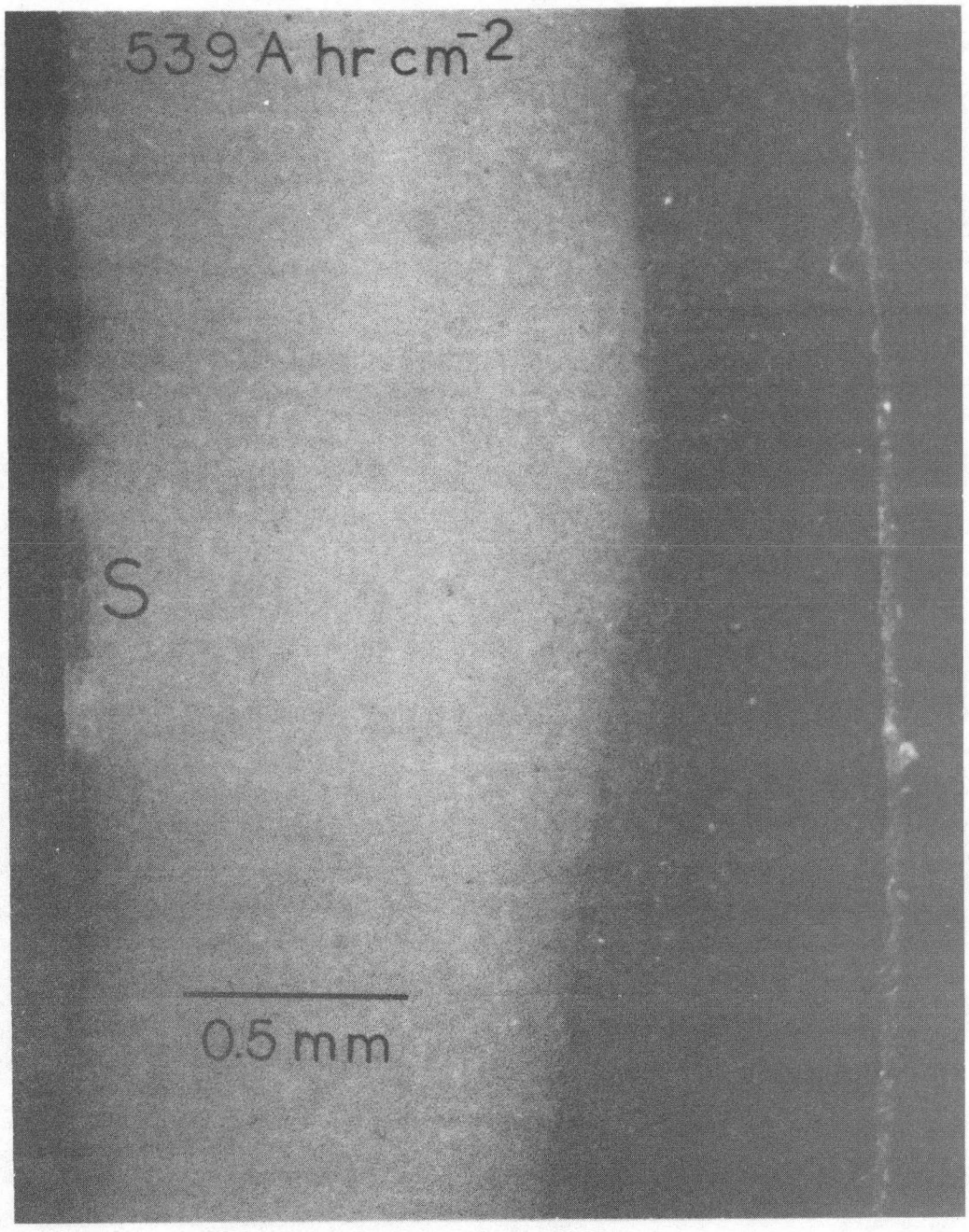

XBB 814-3177

Fig. 6.27 Cross section of silver exchanged beta" electrolyte material from 539 Ahr cm^{-2} cell.

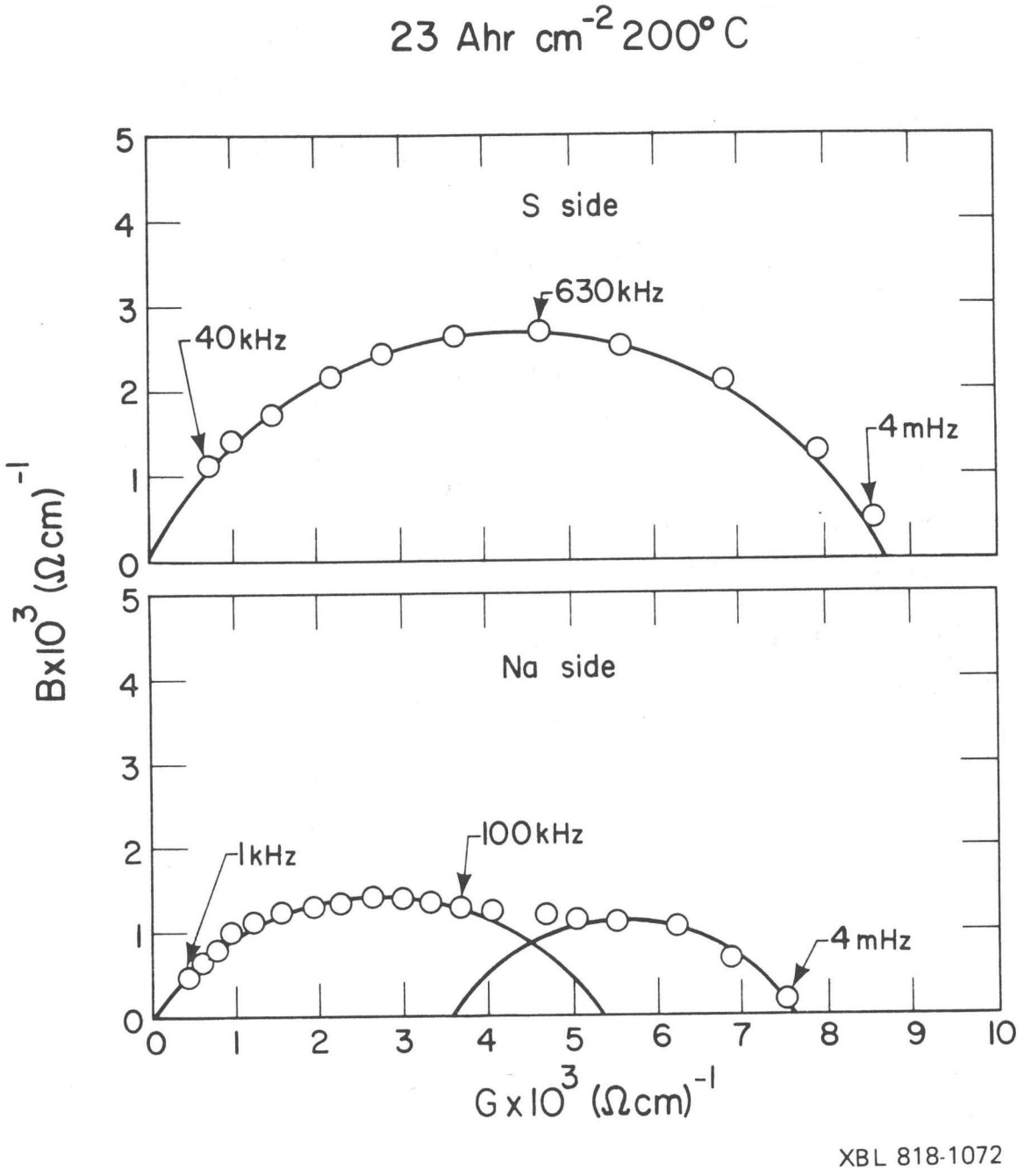

Fig. 6.28 Admittance plots at 200°C for beta electrolyte specimens from 23 Ahr cm^{-2} cell.

Reported changes in cell internal resistance during operation, have been associated more with interfacial polarization effects than with changes in the electrolyte itself (De 80c). Still, it is the modification of the ceramic exposed to sodium which is responsible for its greater sensitivity to atmospheric exposure. The complex conductivity measurements show this modification affects both the bulk and the grain boundaries. The existence of electron-oxygen vacancy pairs in darkened electrolyte is consistent with greater sensitivity to atmospheric attack.

6.2.8 X-ray Analysis of Surface Impurities in the SEM

The sodium carbonate crystals observed on the surface of the beta electrolytes have already been mentioned. Impurities found on the surfaces of the electrolytes by energy dispersive analysis of x-rays generated in the SEM are listed in Table 6.1.

Table 6.1 Surface Impurities Found on Cycled Beta Electrolytes by X-ray Analysis in the SEM

Cell #	Ahr cm^{-2}	Impurities Identified	
		Sodium Surface	Sulfur Surface
DM 4-5	0	Ca, Cl, S, Si	Cl, Cr, Fe, (S)
414	23	Ca, Cl, K	Cl, Fe (weak), K, Si (weak)
392	271	Ca, Cl, Mg, Rb, S, Si (weak)	Ca, Cl (weak), Fe, K, Mg, P, Si, Ti
385	332	Ca	K
358	703	Ca, Cl, K (weak), Mg (weak)	Ca, Cl, K, Mg (weak), Pb, Si (weak)

Small crystals rich in calcium, such as those shown in Figure 6.29, were found on the sodium surfaces of all the beta electrolytes examined. Figure 6.30 shows an enlarged view of such a crystal and the x-ray spectrum obtained from it. Fracture surfaces of the beta electrolytes were examined by x-ray analysis in the SEM, but they yielded no evidence of calcium in the bulk. Calcium oxide on the electrolyte surface is still cause for concern, because it has been shown that it can enter the conduction planes in beta alumina increasing its resistivity, and that it produces drastic increases in resistivity in the grain boundary regions. (Bu 78, Bu 79).

Calcium and potassium are the most common contaminants in commercial sodium. Table 6.1 indicates that potassium is also commonly found in the cells although it is a bit surprising that it is more frequently found on the sulfur surface. Potassium beta alumina has a substantially higher resistivity that its sodium counterpart and a larger [c] lattice parameter also. The assimilation of potassium at the electrolyte surface will definitely contribute to polarization and degradation in Na/S cell operation. Sufficient incorporation of it into surface grains could produce stresses which may initiate or facillitate cracking. The potassium found at the sulfur surface could well be instrumental in the degradation observed there.

Iron is another impurity which shows up frequently in Table 6.1, usually on the sulfur side. It is probably introduced by corrosion of the polysulfide container, or it may have been introduced intentionally to serve, as mentioned earlier, as a wetting agent for the carbon felt.

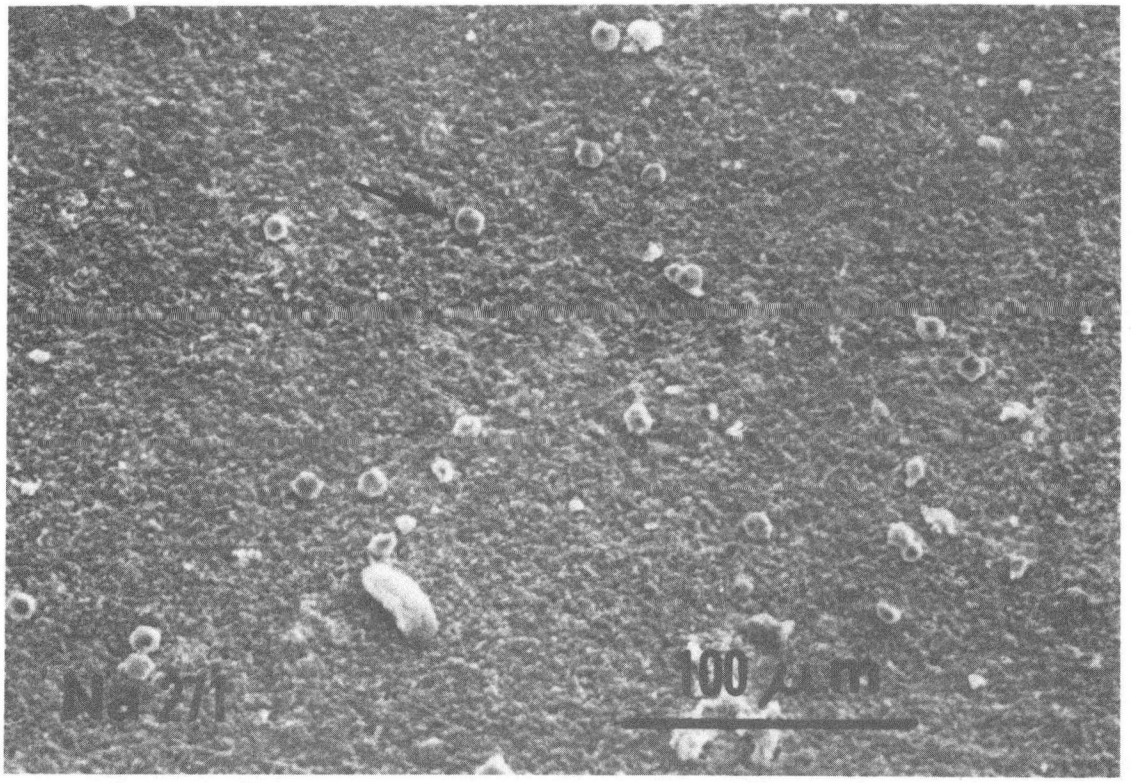

XBB 804-4118

Fig. 6.29 Sodium surface of beta electrolyte from 271 Ahr cm^{-2} cell showing deposited small crystals.

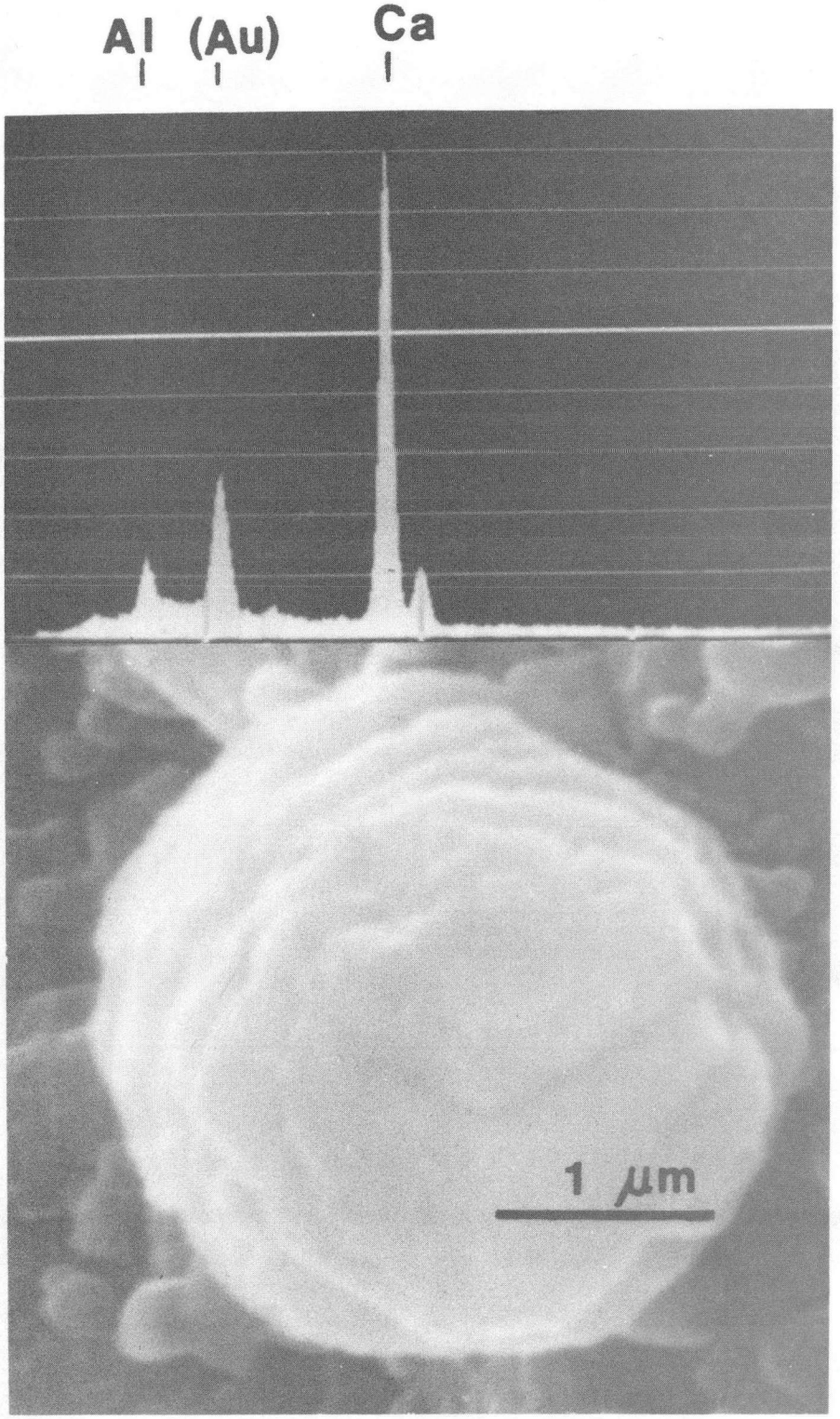

XBB 804-4115

Fig. 6.30 Close up of a crystal in Figure 6.29 and its x-ray spectrum.

6.3 Examination of Electrolyte Material from Sodium/Sodium Cells

6.3.1 Evidence for Grain Size Effects

Results of the critical current density determinations (Chapter 5) show a connection between the presence of large grains in the electrolyte and failure at lower relative current density. Commercial electrolytes examined after silver staining show evidence of enhanced degradation around boundaries of anomalously large grains. To explore this grain size effect further, a cell was constructed from "300 μm" material in which the sodium exit surface was polished before cycling. The cell was ramped at the standard 1 mA cm^{-2}, and removed from testing after the onset of sustained acoustic emissions. Total charge transfer density was about 22 Ahr cm^{-2}. After cycling, the cell was silver stained and examined. Figure 6.31 shows the appearance of the exit surface of the cell after this treatment. It is clear that there is greater degradation evident along the boundaries of the large grains. The cell was sectioned and polished, and Figure 6.32 is typical of the observed subsurface nature of the crack networks found in the bulk. Two additional polished surface cells were made from the 300 μm material and cycled, one using the polished area as a sodium exit surface, and the other using it as an entrance surface. Figure 6.33 shows micrographs of the surfaces for comparison after cycling and decoration. There is greater decoration on the exit surface than on the entrance surface; and, in particular, there is heavy decoration preferentially present along the boundaries of the large grains. The cell with the polished exit surface actually saw less charge transfer (30 Ahr cm^{-2}) than the cell with the polished entrance surface (44 Ahr cm^{-2}). The enhanced

Fig. 6.31 Silver decorated sodium exit surface of cell 00324, 22 Ahr cm^{-2}, "300 μm" material. Surface of cell had been prepolished and cell was removed from service after the onset of sustained acoustic activity. Note the heavy decoration along the boundaries of the large grains indicating severe degradation in these regions.

XBB 815-4089

Fig. 6.31

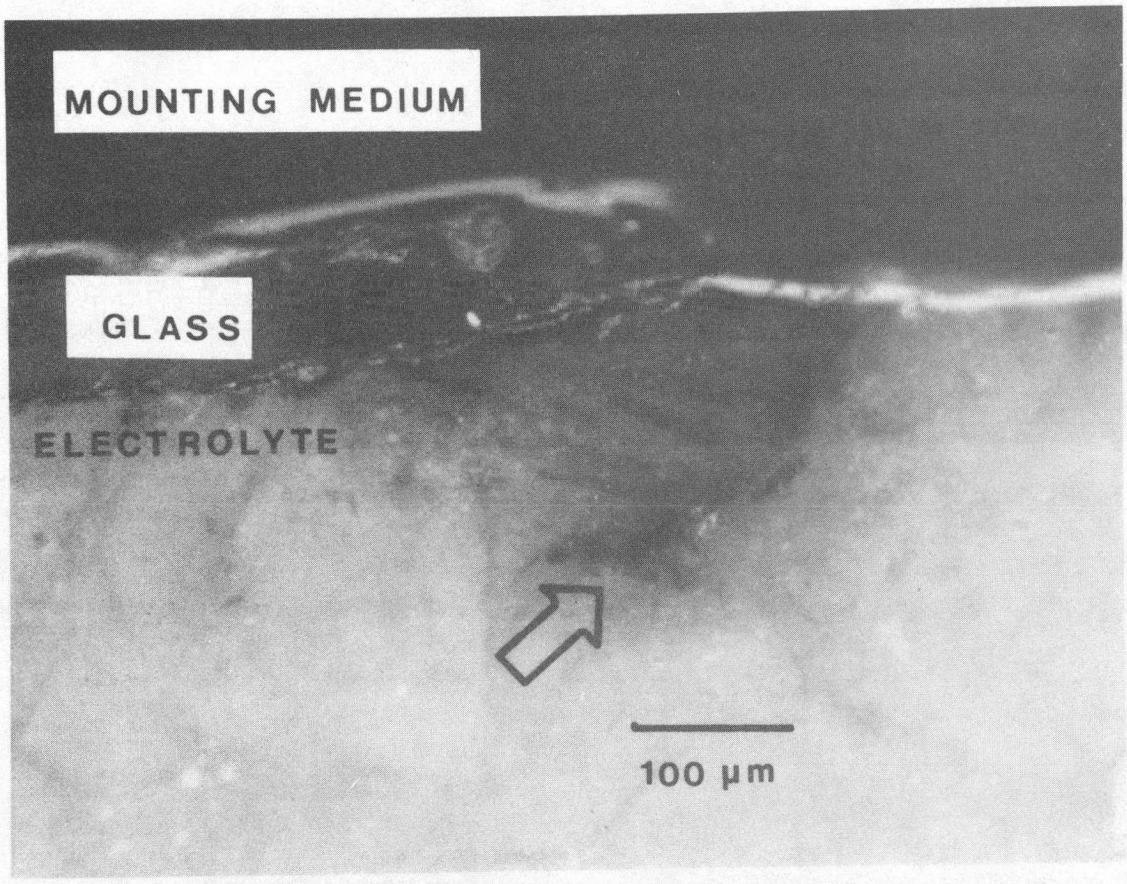

XBB 817-6529

Fig. 6.32 Polished cross section of cell shown in Figure 6.31. Arrow points to mode I crack.

Fig. 6.33 Silver decorated prepolished surfaces of cell 00624 (exit) surface, 30 Ahr cm^{-2}) and of cell 00527 (entrance surface, 44 Ahr cm^{-2}) shown for comparison. Black droplet-like areas on surface are patches of sealing glass which got there accidentally during cell fabrication.

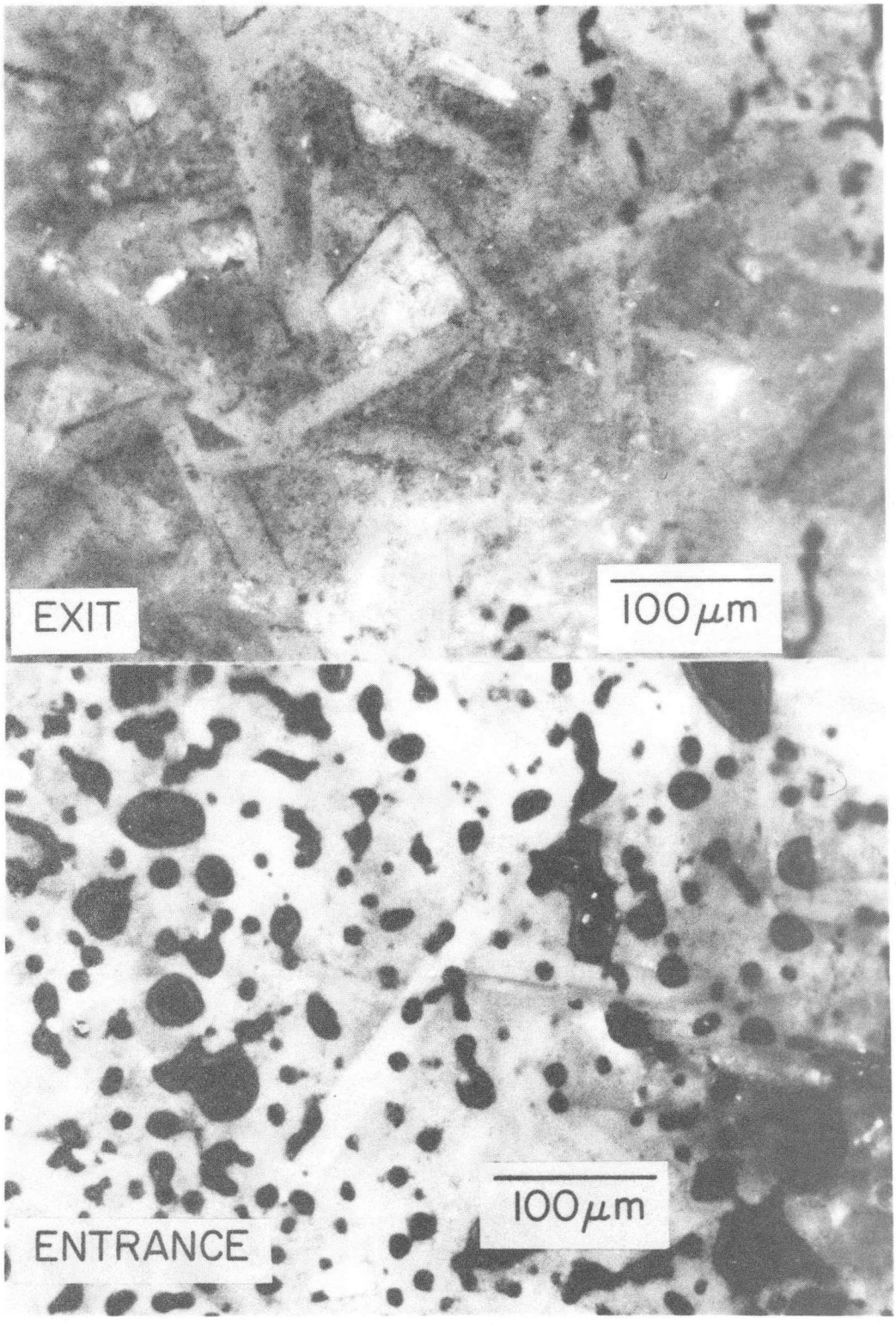

XBB 807-8894

Fig. 6.33

degradation at the large grain boundaries is probably the result of a current concentrating effect, which would be expected where the large grains are inclined to the surface as schematically illustrated in Figure 6.34, combined with the likelihood of larger initial cracks being present here.

Polished, virgin electrolytes decorate slightly in the fine grain regions after sodium immersion, but not on the faces of the large grains; and no strong preferential decoration is found along the boundaries of the large grains (Figure 6.35A). What is apparent here is only the effect of the grain boundary chemical coloration. Polished, virgin electrolytes, not previously immersed in sodium, are affected not at all or only to a minor degree by the decoration process (Figure 6.35B). The strong, preferential decoration of large grain boundaries on the exit surface of cycled cell electrolytes is therefore clearly a result of electrolysis, and not an artifact of polishing. The results of polished electrolyte cycling, the independent evidence from electrical cycling of as-prepared electrolytes, and the degradation found around large surface grains in the commercially cycled beta" electrolytes from sodium/sulfur cells all point to the conclusion that anomalously large grains in the electrolyte, particularly near the surface, will contribute to premature electrolyte failure.

6.3.2 Evidence for Mode I Processes

Cracks of the type shown in Figure 6.36 were found in the first sodium/sodium cell cycled for this work, and continued to be seen in most of the cells. They were roughly parallel to the surface and perpendicular to the direction of current flow. As remarked before, it is

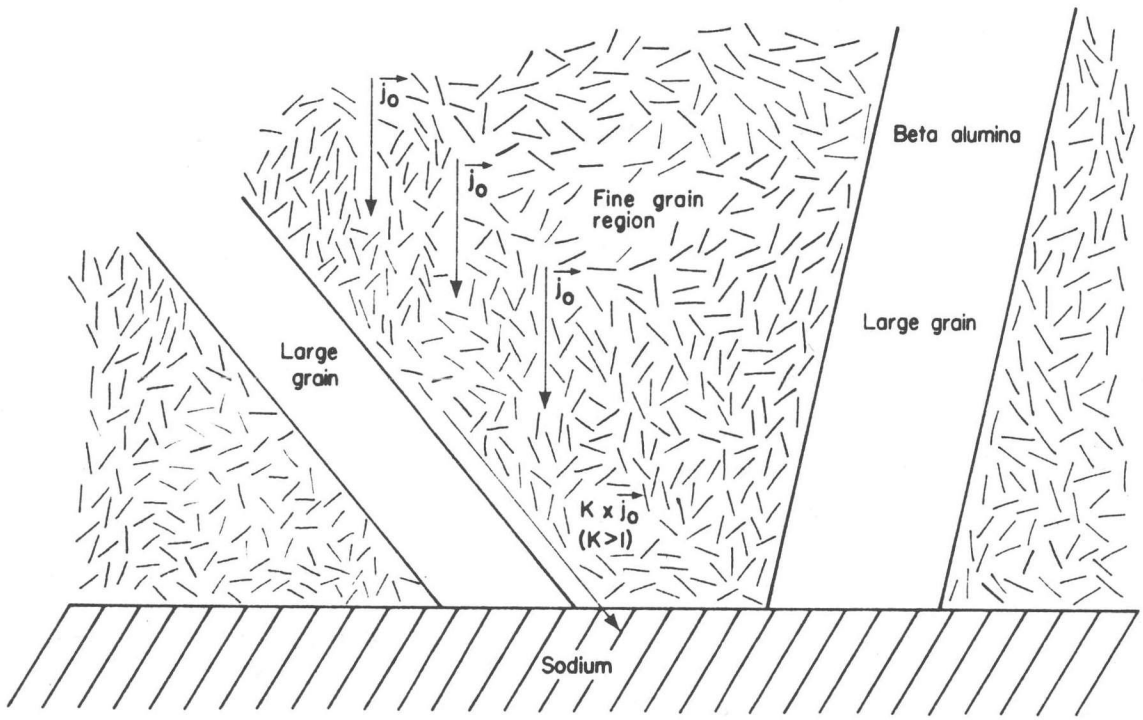

Fig. 6.34 Schematic representation of mode of current concentration at edge of large grain inclined to electrolyte surface.

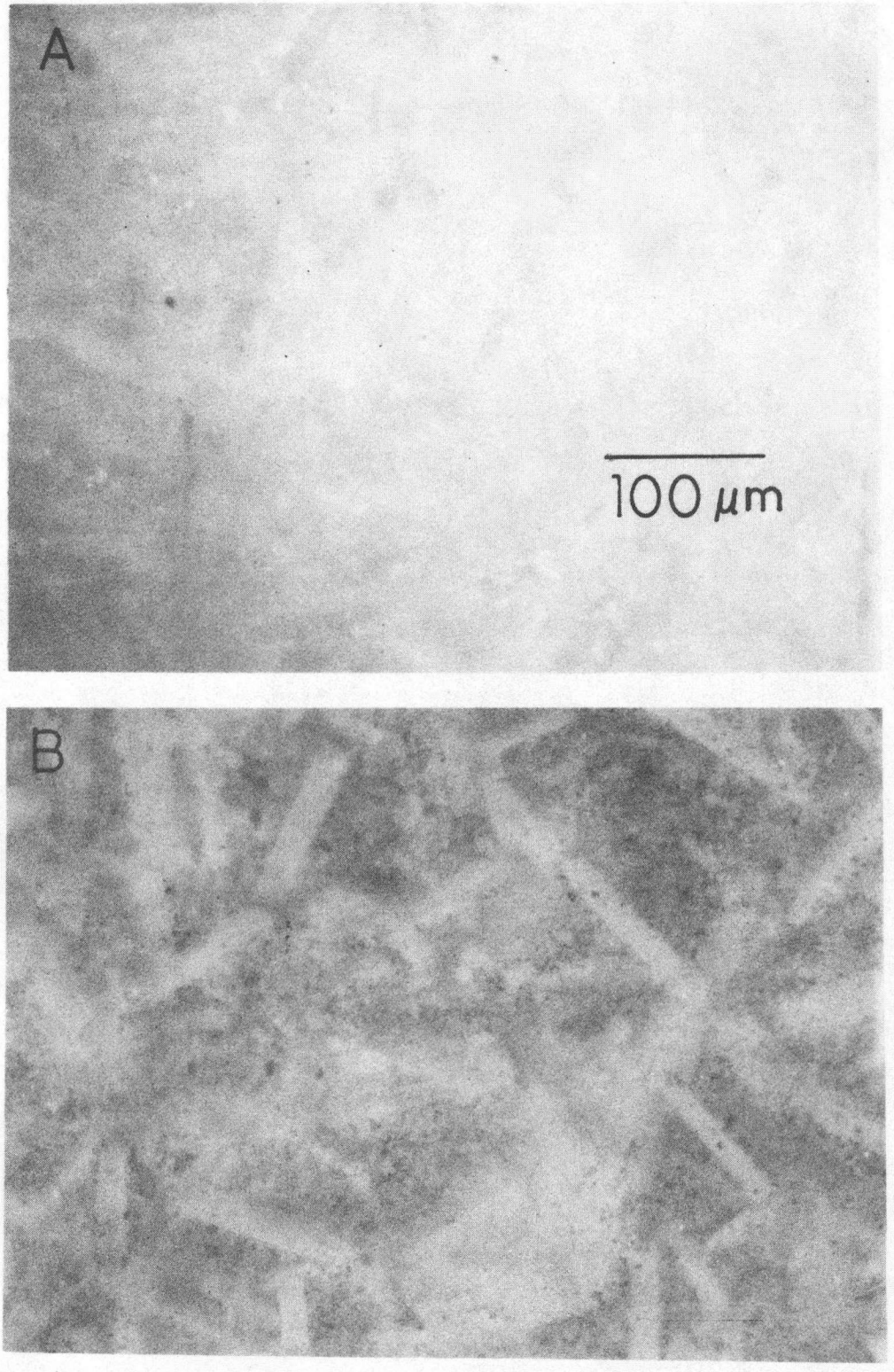

XBB 8112-11641

Fig. 6.35 Decorated polished specimens of "300 μm" material: A. immersed in sodium 24 hours at 350°C and baked 1 hour at 800°C B. baked 1 hour at 800°C only.

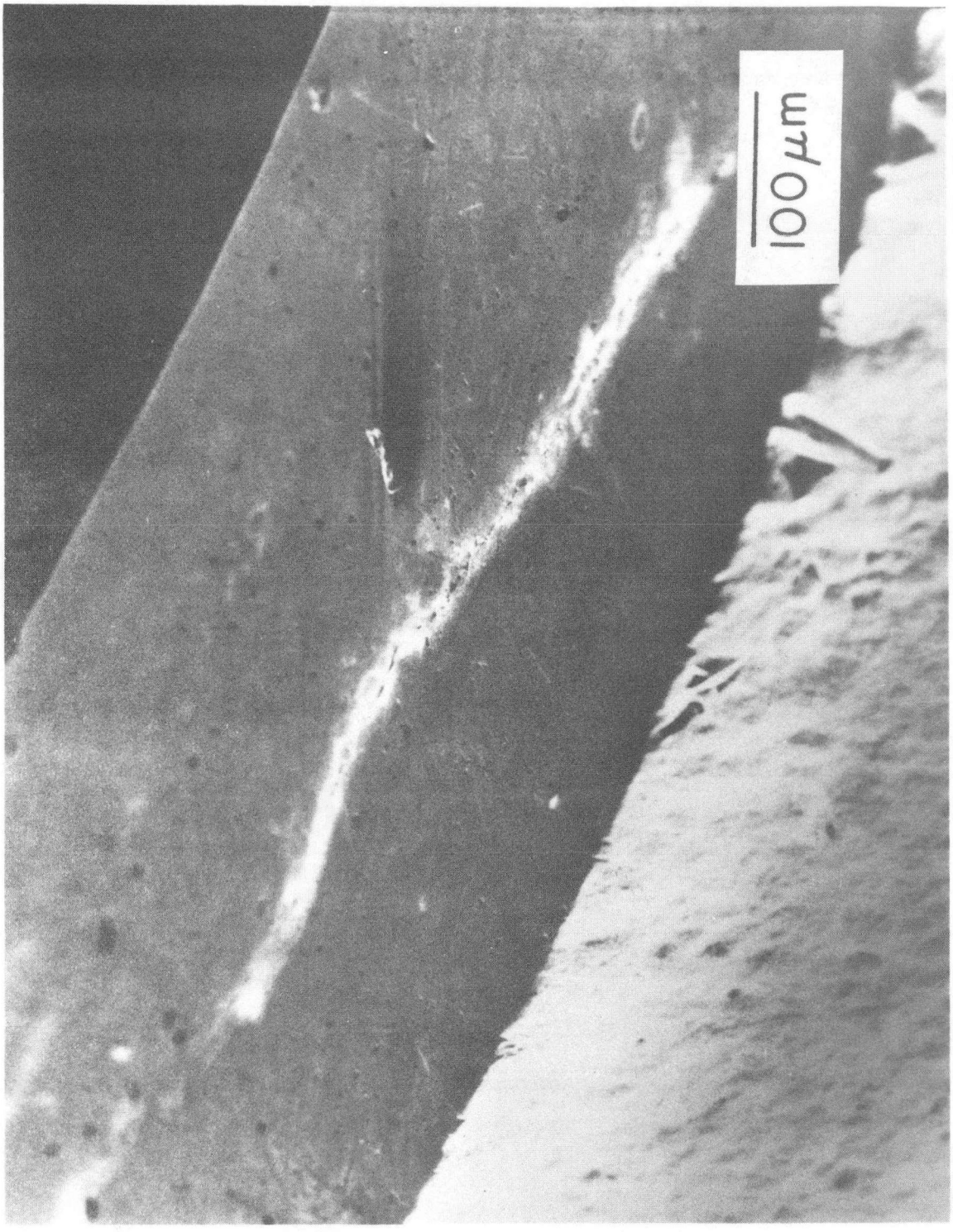

XBB 807 8874

Fig. 6.36 Cross section of cell 90425 showing crack approximately parallel to electrolyte tube walls.

believed that this prevailing orientation of the crack is due to a basic instability of crack growth in the direction of current flow. Clearly, a crack can be more effectively fed when it is transverse to the direction of current flow. This factor is not presently considered in treatments of breakdown but has some obvious importance in modeling the progress of degradation propagation. Figure 6.37 shows cell 90521 constructed of "300 μm" material. It was subjected to 10.2 Ahr cm^{-2} of charge transfer and a maximum current density of 11.0 A cm^{-2} before catastrophic failure occurred. A region of subsurface sodium about 4 mm across is visible through the translucent surface grains of the cell, indicating the extent of crack branching which occurred before the terminal failure. Figure 6.38 is an unstained cross section of cell 90530 showing extensive diffuse darkening and many cracks which are, for the most part, perpendicular to the direction of current flow. This cell was made with the "10 μm" material and was subjected to 255 Ahr cm^{-2} of charge transfer.

Silver decoration of the sodium/sodium cells made for this work showed the same layer-like darkening seen in the used commercial cells, but, of course, here it proceeded inward from both surfaces since both were in contact with sodium. Cell 90901 is shown in Figure 6.39. This cell had seen 65 Ahr cm^{-2} when it was removed from testing and sectioned, but it had not yet failed catastrophically. It is clear that significant cracking may be tolerated before a complete short circuit is established. The predominant orientation of the cracks is again transverse to the direction of current flow. Silver decoration has highlighted the darkened layers at the surfaces. A large crack is seen originating at the exit surface and then deflecting. The enlarged

Fig. 6.37 Cell 90521 (10 Ahr cm^{-2}, "300 μm" material) showing crack network visible through transparent large grains of the sodium entrance surface.

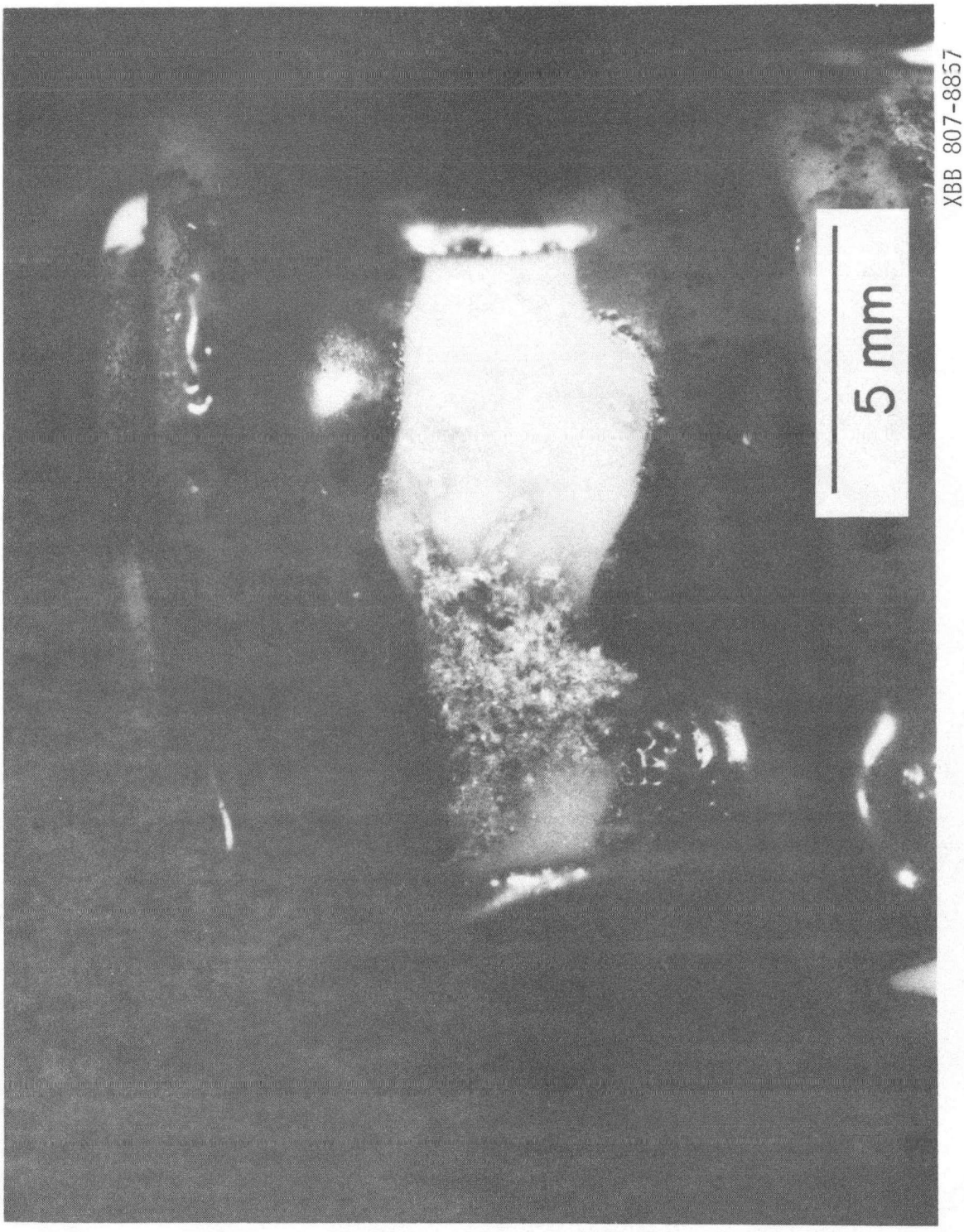

XBB 807-8857

Fig. 6.37

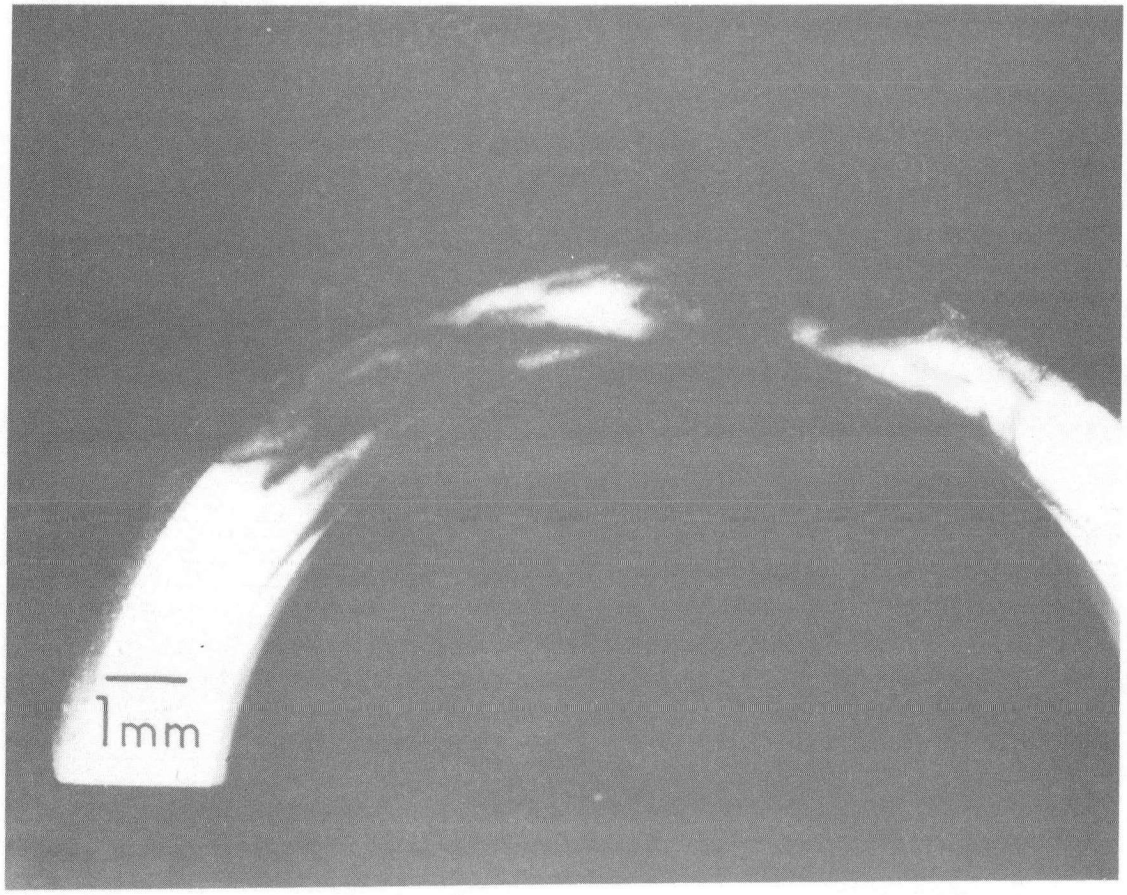

XBB 807-8873

Fig. 6.38 Cross section of cell 90530 (255 Ahr cm^{-2}, "10 μm" material) showing extensive cracking and darkening.

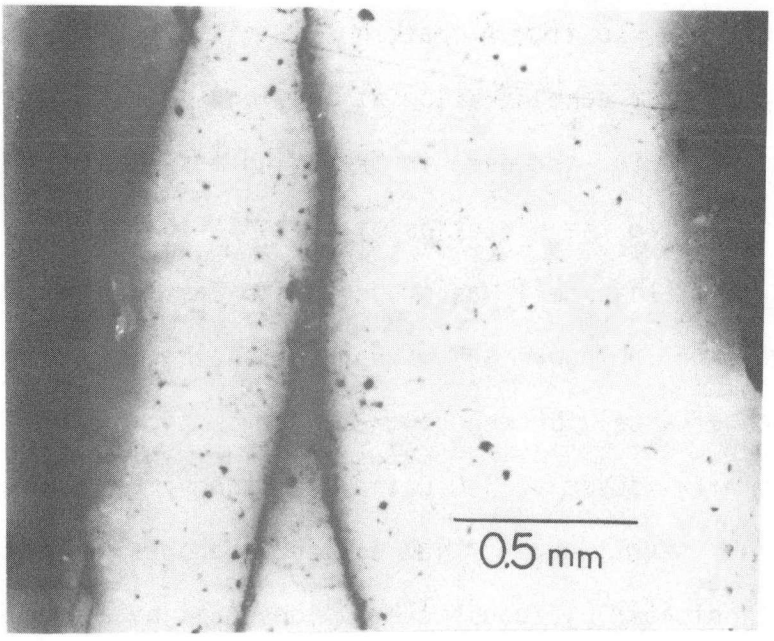

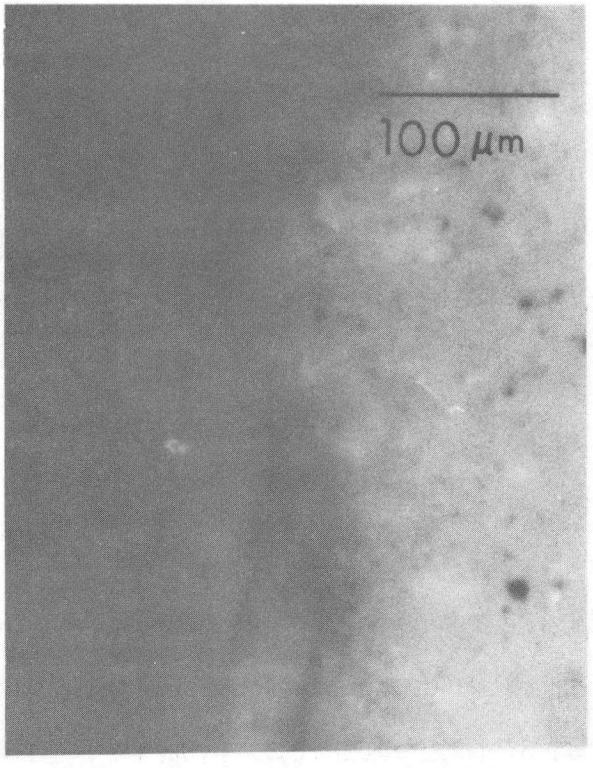

XBB 807-8882

Fig. 6.39 Silver decorated cross section of cell 90901 and detail of section near adherent patch of sealing glass.

detail is a region on the sodium exit surface which has a small drop of sealing glass adhering to it. A crack has initiated at the edge, perhaps because of current concentration at the edge of this blocking area, but it also has deflected and even in branching has remained substantially perpendicular to the direction of current flow. The maximum current density that this cell was subjected to was 6.0 A cm^{-2}.

Figure 6.40 is a low power SEM micrograph showing the cross section and exit surface of a cell broken down at room temperature. The surface was wetted with sodium at 350°C and then the system was cooled to room temperature. A voltage was then applied and breakdown occurred immediately as indicated by acoustic emissions, and by a prompt drop in cell resistance obviously caused by the penetration of the cell wall by many sodium filaments. L. A. Feldman of this group has studied the problem of breakdown in the temperature range from 20° to 120°C far more extensively using different electrode system and a different sample geometry. Many of the morphological features of breakdown he observes are in evidence here: extensive internal cracking and crack branching, considerable spalling from the surface, and again, cracks which run predominantly at a low angle to the surface instead of going straight through parallel to the direction of current flow.

6.3.3 Impurities

The only impurity which showed up consistently in the cells was potassium. The sodium entrance surfaces of the cells showed the greatest concentration of this impurity. Figure 6.41 shows an SEM micrograph of the entrance surface of cell 90613 (20 Ahr cm^{-2}) and the x-ray energy spectrum from it with the potassium peak identified. The

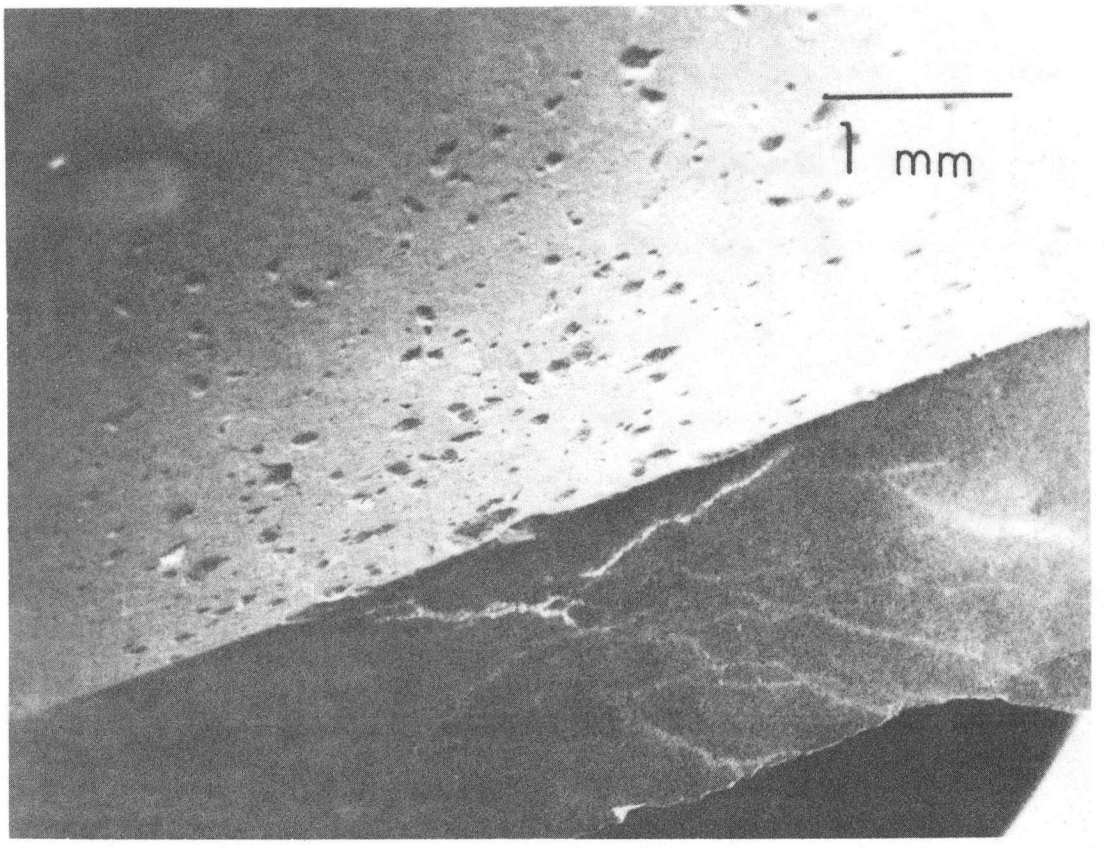

XBB 807-8871

Fig. 6.40 Selection of electrolyte from cell 90427-B broken down at room temperature. Sodium exited through inside surface of tube where extensive spalling is evident.

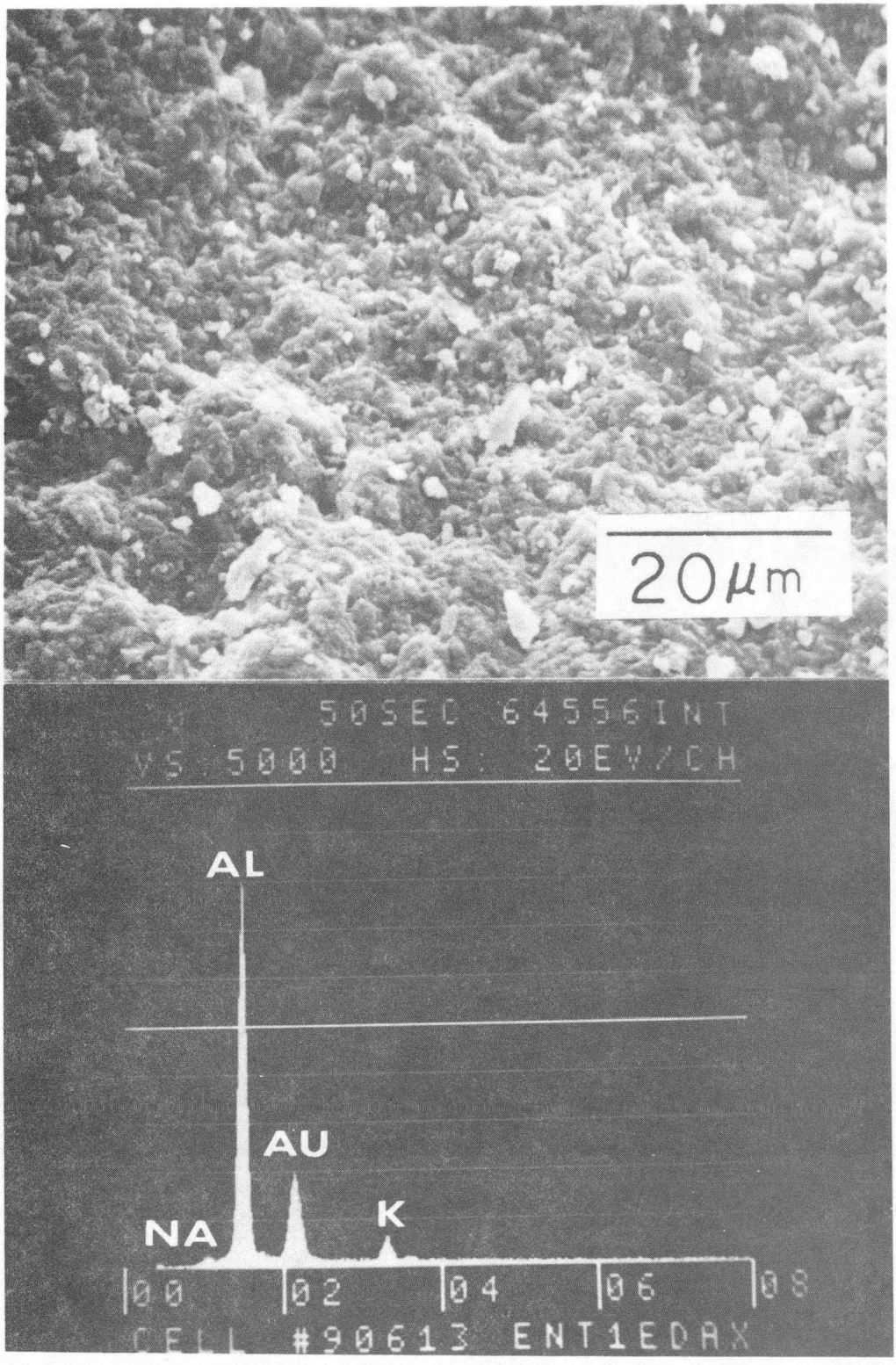

XBB 807-8890

Fig. 6.41 Entrance surface of cell 90613 (20 Ahr cm^{-2}, "10 μm" material) and x-ray spectrum from it showing presence of potassium.

detrimental effects of this element have already been noted. It was undoubtedly a contributing factor to the polarization observed in operation of these cells. By decreasing the ionic conductivity in the vicinity of the surface, it would also contribute to the ionic transport number gradient in the electrolyte, which can lead to mode II failure as previously noted.

6.4 Summary and Conclusions

- Cycled electrolytes from sodium/sulfur cells and from sodium/sodium cells show the presence of mode I cracks even when the cells have not failed catastrophically. The morphology of these cracks indicates that their growth is unstable in the direction of current flow, so that they branch and deflect to an orientation in which they are more effectively current fed. The branching and deflection retards the com- plete penetration of the electrolyte by mode I cracks, partially explaining why catastrophic failure does not follow immediately on mode I initiation.

- Cycled electrolytes from some sodium/sulfur cells show evidence of a second mode of degradation resulting from the internal deposition of sodium under pressure in the electrolyte. Grain boundaries and, possibly, intergranular phases appear to act as preferred sites of initiation for this mode II breakdown.

- A gradient in the chemical coloration of the electrolyte is found even in cells which have been in service for extended periods of time. It therefore appears that a uniform saturation effect, which might terminate or supress mode II degradation, cannot be attained in normal cell service.

- Patterns of coloration in electrolytes taken from sodium/sulfur cells indicate that there are substantial differences between the coloration process in sodium beta alumina and in sodium beta" alumina.

- A progressive mode of degration is observed to propagate from the sulfur surface of the electrolyte. This initiates at points of contact between the carbon felt current collector and the electrolyte, and involves chemical, electrolytic and probably mechanical effects.

- Many impurities are observed in electrolytes taken from cycled sodium/sulfur cells. Of these, calcium and potassium are of special concern because of their known detrimental effects on the electrolyte. Polarization may be caused or enhanced by these impurities. The ionic conductivity gradient, induced by their incorporation into the ceramic surface layers, may facilitate mode II degradation.

- A.C. dispersive conductivity behavior of darkened and clear sections of electrolyte from sodium/sulfur cells supports the findings of the chemical coloration experiments that darkening preferentially affects grain boundaries, but that bulk modification is also present.

- Cycled electrolytes reveal clearly that boundaries of anomalously large grains at the surface of the electrolyte are preferred sites for initiation of degradation.

7. OVERALL SUMMARY AND DISCUSSION

Rather than simply collecting and repeating the various conclusions stated at the ends of the foregoing chapters of this thesis, this concluding chapter will discuss in broad terms the impact of this thesis work on practical batteries.

Perhaps the most significant conclusion that can be drawn from this work is that there are no fundamental limitations on the service life of beta alumina solid electrolytes. It is apparent, however, that the operating parameters of existing batteries are very close to the threshold at which rapid degradation mechanisms begin to operate. These mechanisms include the mode I degradation and the newly discovered mode II degradation. Of substantial importance is the new finding that the electronic conductivity of the electrolyte plays a major role in the degradation mechanisms which have been reported here. The heterogeneity of electronic conductivity, introduced by contact with the sodium electrode, appears to be responsible for the operation of certain degradation mechanisms. This might well suggest that a uniform doping of the solid electrolyte to achieve an overall electronic conductivity of, say, on the order of 0.1' of the total conductivity of the electrolyte would have the effect of very significantly decreasing the gradients in electronic conductivity that can possibly develop as a result of reduction. This level of electronic conductivity could easily be tolerated without a major sacrifice in cell efficiency. Such an idea might be explored in future work.

This thesis may be seen as the first unraveling of the complexity of the breakdown processes in beta alumina. A significant observation,

that will have to await future studies for clarification, is that slow crack growth can occur during charge transport in the solid electrolyte. So far, the only mechanisms that have been proposed of the mode I and even of the mode II type involve catastrophic failure at some particular current density or at some particular applied voltage. But the data clearly indicate that slow crack growth is occurring, and for this no explanation has yet been put forth. In future studies this point might be further explored by, for example, studying the change in critical current density for mode I initiation as a function of rate at which the current density is increased. Such a study has in fact been initiated in this research group by David Hitchcock (Hi 82).

In summary, this thesis has made the following important contributions to the understanding of the breakdown process in beta alumina solid electrolytes:

1. Clarification of the nature of chemical coloration and the role that it plays in degradation.
2. Measurement of critical current densities for mode I degradation initiation which are substantially lower than those reported by other investigators.
3. The experimental observation that grain boundary facets of large, anomalously grown grains have a deleterious effect on the current density for mode I initiation.
4. Experimental observation of a new type of degradation, the mode II degradation.

APPENDIX 1. THE LIKELIHOOD OF FAILURE FROM CURRENT INDUCED THERMAL EFFECTS

Consider a crack, in the surface of the solid electrolyte, which is a flat sided rectangular crevice 100 μm deep and 20 Å wide with a semi-circular tip. The cross section of such a crack and a representation of the current flow pattern into it is shown in Figure A1.1A. Using a more realistic elliptical cylindrical shaped crack, Feldman, et al. (Fe 81) have shown that the current density at the crack tip, j_t, is $j_o \ell/a$ where j_o is the average current density in the electrolyte far from the crack tip, ℓ is the length of the crack, and a is half the crack opening displacement. By making the approximation of the focusing situation shown in Figure A1.1B where all the current impinging on a semi-circle of radius ℓ centered on the crack tip is considered to flow into the tip in a symmetric radial fashion, one obtains for the current density j at any point r in the semicircle:

$$j = j_o \ell / r \qquad \text{A1.1}$$

This gives a realistic estimate of the current density of $j_o \ell/a$ at the crack tip where a is the tip radius. The geometry is equivalent to the case of current flow between the outer and inner surfaces of a hollow cylinder of outer radius $b(= \ell)$ and inner radius a. Heat is generated in the cylinder at the rate $j^2\rho$ per unit volume where j is given by equation A1.1 and ρ is the electrical resistivity of the electrolyte.

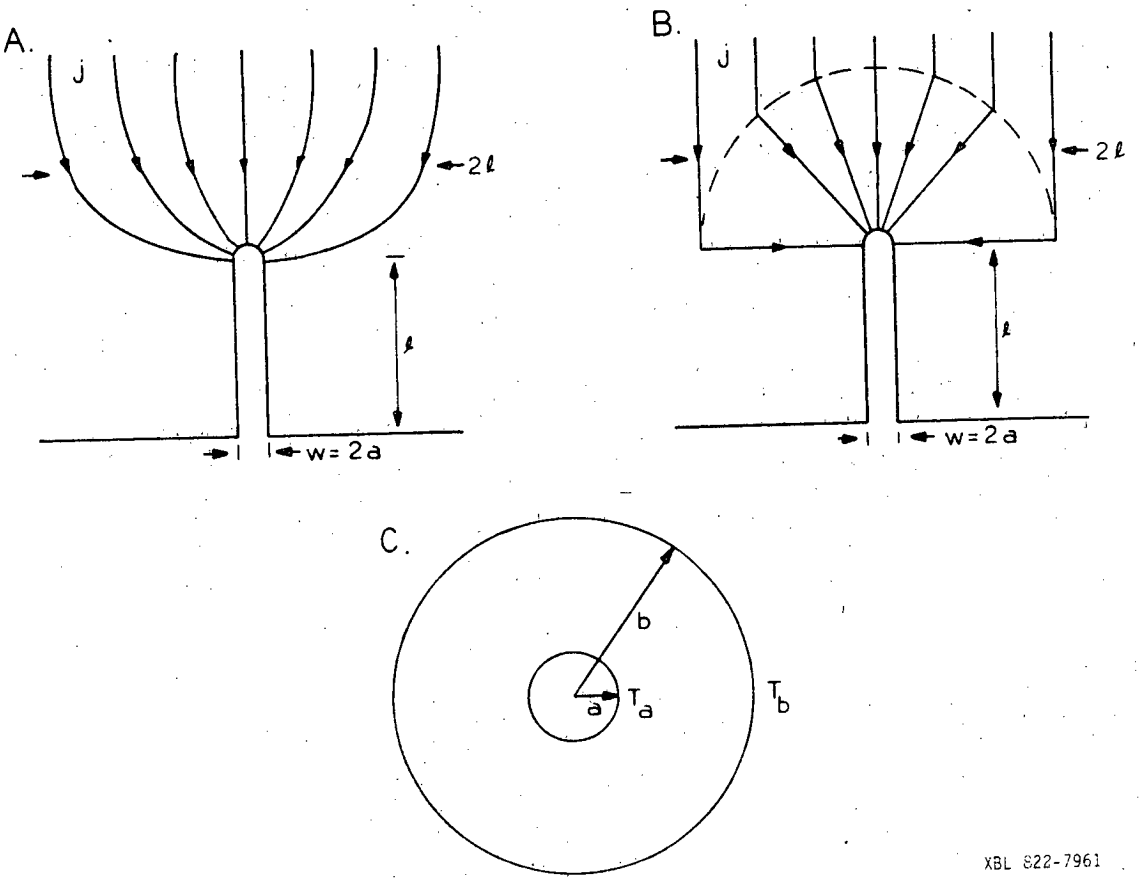

Fig. A1.1 A. Normal current flow into crack. B. Approximation of current flow into crack. C. Basic geometry for solution of Poisson's equation.

Poisson's equation must be solved to give the temperature at any point r in the cylinder. For the steady state (Ca 59):

$$\nabla^2 T = -A(x,y,z)/K \qquad \text{A1.2}$$

where A is the rate of heat generation per unit volume, T is the temperature at any given point, and K is the thermal conductivity. In cylindrical coordinates for the present case this becomes:

$$\frac{1}{r}\frac{d}{dr}\left(r\frac{dT}{dr}\right) + j_o^2 b^2 \rho / K r^2 = 0$$

or:

$$\frac{d}{dr}\left(r\frac{dT}{dr}\right) + j_o^2 b^2 \rho / K r = 0 \qquad \text{A1.3}$$

When no heat source exists in the volume, this becomes Laplace's equation:

$$\frac{d}{dr}\left(r\frac{dT}{dr}\right) = 0 \qquad \text{A1.4}$$

to which the general solution is:

$$T = A' + B' \ln r \qquad \text{A1.5}$$

If we assume ρ to be constant, a particular solution to equation A1.3 is:

$$T_p = -(j_o b)^2 \rho (\ln r)^2 / 2K \qquad \text{A1.6}$$

and so adding A1.5 and A1.6 gives the general solution to A1.3:

$$T = A' + B' \ln r - C(\ln r)^2 \qquad \text{A1.7}$$

where $C = (j_o b)^2 \rho / K$.

Matching boundary conditions determines the constants A' and B':

$$B' = (T_b - T_a)/\ln b/a + C \ln ab \qquad \text{A1.8}$$

$$A' = (T_b \ln a - T_a \ln b)/\ln a/b + C \ln a \ln b \qquad \text{A1.9}$$

where T_b and T_a are the temperatures at the outer and inner surfaces of the cylinder respectively. Differentiating A1.7 and setting the derivative equal to zero gives for the location of the maximum in temperature:

$$r_{max} = e^{(B'/2C)} \qquad \text{A1.10}$$

at which the temperature will be:

$$T_{max} = A' + B'^2/4C \qquad \text{A1.11}$$

Now assume that the average current density j_o in the electrolyte is 0.1 A cm^{-2}. Since it has been pointed out in the body of the text that the temperature rise in the center of a slab of electrolyte 2 mm thick would only be about 0.003°C under such circumstances, it will further be assumed that $T_b = T_a$. It will also be assumed that $T_a = T_s$, where T_s is the temperature at the crack opening in the electrolyte

surface, which is reasonable on the basis of the amount of sodium which would be flowing through the crack (8.6×10^{-7}cm^3 sec^{-1} through a crack with a volume of 2×10^{-9} cm^3), and on the basis of the higher thermal conductivity and lower electrical resistivity of sodium compared to beta" alumina (see Table A1.1). The above assumptions would have to be modified if the value of T_{max} calculated using them were much greater than T_s, but it will be seen that this is not the case. Equations A1.8 and A1.9 give, for the assumptions made above:

$$B' = C \ln ab \qquad \text{A1.12}$$

$$A' = T_x + C \ln a \ln b \qquad \text{A1.13}$$

For the specified crack dimensions and values listed in Table A1.1, equations A1.10 and A1.11 yield:

$$r_{max} = 3.16\times10^{-5} \text{ cm}$$

$$T_{max} = T_s + 0.005^{\circ}C$$

The results suggest that thermally induced stresses are unlikely to produce failure.

Table A1.1

Comparative Properties of Sodium and

Sodium Beta" Alumina at 350°C

	Sodium	Sodium Beta" Alumina
Thermal Conductivity (cal sec^{-1} cm^{-1} $°C^{-1}$)	0.18	0.035 (value for Al_2O_3 assumed)
Electrical Resistivity (ohm cm)	1.8×10^{-5}	4.0

APPENDIX 2. CALCULATION OF THE WEIBULL CURVE FOR CELLS OF DIFFERING AREAS

The Weibull curve is determined for a cell of reference surface area, say A_o. When the parameter n is known from a fixed area curve, the current density j_1 required to produce a probability of failure P_f in an electrolyte of surface area A_1 is determined from the relation:

$$j_1 = j_r(A_o/A_1)^{1/n} \qquad \text{A2.1}$$

where j_r is the current density associated with the probability of failure P_f in a cell of the reference area A_o. Then to construct a Weibull curve for a set of failure data from cells of differing surface areas:

1. Plot the data as if all of the cells had the same area (A_o) to determine a trial parameter n_t. This is done by plotting ln j versus ln ln $(1/P_s)$ using the median rank probability of survival for P_s.

$$P_s \ (= 1 - P_f) = 1-(i-0.3)/(N+0.4) \qquad \text{A2.2}$$

where N is the total number of cells represented in the plot and i is the number of the cell determined by arranging the values of ln j_i in increasing order. Since:

$$\ln \ln (1/P_s) = \ln(A_i/A_o)+n \ln (j_i-j_u)-n \ln j_o \qquad \text{A2.3}$$

n ($= n_t$) is the slope of the plot if the $\ln A_i/A_o$ term is ignored. This value of n_t is then used in equation A1.1 to determine a new effective value, j_i' of the current density for each cell:

$$j_i' = j_i(A_o/A_i)^{1/n_t} \qquad \text{A2.4}$$

2. These new values of j_i' are then used to plot a new Weibull curve and to determine a new value of n_t'. The values of $\ln j_i'$ may have to be reordered in increasing value and the indices, i, reassigned. This process is repeated using n_t' as the new n_t each time until the two converge to within acceptable limits.

A program was written (Figure A2.1) for the TI 59 calculator which facilitates this procedure. The program makes use of a trivariate data entry program from the Applied Statistics Solid State Software module (Te 77). As written, the program can accommodate up to 17 data triplets which are entered in the form:

$$x_i = \ln j_i \qquad \text{A2.5}$$

$$y_i = \ln \ln 1/P_s \qquad \text{A2.6}$$

$$Z_i = \ln A_i/A_o \qquad \text{A2.7}$$

To run the program, 9 E+99 is stored in memory location 89 as a reciprocal trial slope (0 is actually the trial slope but 1/0 is undefined and would cause a calculator error condition), and 87 is stored in memory location 85 as a pointer to the location of the x count. The program

```
000  76 LBL
001  13  C
002  69 OP
003  12  12
004  32 X≷T
005  98 ADV
006  99 PRT
007  35 1/X
008  75  -
009  48 EXC
010  89  89
011  95  =
012  42 STO
013  88  88
014  76 LBL
015  23 LNX
016  43 RCL
017  29  29
018  42 STO
019  87  87
020  76 LBL
021  33 X²
022  53  (
023  43 RCL
024  87  87
025  65  X
026  03  3
027  85  +
028  03  3
029  02  2
030  54  )
031  42 STO
032  86  86
033  75  -
034  02  2
035  95  =
036  42 STO
037  84  84
038  53  (
039  73 RC*
040  86  86
041  65  X
042  43 RCL
043  88  88
044  54  )
045  74 SM*
046  84  84
047  97 DSZ
048  40 IND
049  85  85
050  33 X²
051  36 PGM
052  05  05
053  10 E'
054  09  9
055  69 OP
056  17  17
057  36 PGM
058  05  05
059  19 D'
060  98 ADV
061  69 OP
062  12  12
063  99 PRT
064  93  .
065  00  0
066  00  0
067  01  1
068  32 X≷T
069  99 PRT
070  91 R/S
071  98 ADV
072  35 1/X
073  75  -
074  48 EXC
075  89  89
076  95  =
077  42 STO
078  88  88
079  50 |X|
080  77  GE
081  23 LNX
082  69 OP
083  13  13
084  99 PRT
085  02  2
086  23 LNX
087  23 LNX
088  69 OP
089  15  15
090  22 INV
091  23 LNX
092  99 PRT
093  98 ADV
094  92 RTN
```

Fig. A2.1 Listing of TI 59 program.

computes the new values of $\ln j_i'$, prints these and halts allowing inspection and reordering if they are not still in increasing order. If reordering is required, the corresponding values of $\ln A_i/A_o$ must also be reordered. The memory locations between which values must be exchanged are easily determined from instructions in the Applied Statistics module user's manual. After reordering, which is usually only required on the first or second iteration, the calculator must be given the command GTO 051 RUN which reinitializes the intermediate data base in the calculator and recompiles a new intermediate data base. Running the calculator beyond the halt at step 070 then initiates a check of the difference between the value of n and n'. If this difference is more than or equal to 0.001, the program initiates another iteration. Otherwise, the final value of n is printed together with the correlation coefficient for a linear least squares fit to the data, and j_{50}, the current density for $p_f = 0.50$. A halt then occurs at step 094.

The process used in calculating each new j_i' is based on the following sequence:

$$j_i' = j_i(A_i/A_o)^{1/n} \qquad \text{A2.8}$$

$$\ln j_i' = (1/n)\ln(A_i/A_o) + \ln j_i \qquad \text{A2.9}$$

$$\ln j_i'' = (1/n')\ln(A_i/A_o) + \ln j_i \qquad \text{etc.} \qquad \text{A2.10}$$

Let

$$1/n' = 1/n + \delta \qquad \text{A2.11}$$

$$\delta = 1/n' - 1/n \qquad \text{A2.12}$$

then from A2.10:

$$\begin{aligned} \ln j_i'' &= (1/n + \delta)\ln(A_i/A_o) + \ln j_i \\ &= (1/n)\ln(A_i/A_o) + \ln j_i + \delta \ln(A_i/A_o) \end{aligned} \qquad \text{A2.13}$$

and from A2.9:

$$\ln j_i'' = \ln j_i' + \delta \ln(A_i/A_o) \qquad \text{A2.14}$$

so that in calculation algorithm only $\delta \ln(A_i/A_o)$ need be added to the previous $\ln j_i$ to get the new $\ln j_i'$.

BIBLIOGRAPHY

Ar 74 Armstrong, R. D., T. Dickenson, and J. Turner. Electrochim. Acta 19, 187 (1974).

Ar 75 Armstrong, R. D., T. Dickenson, and M. Reid. Electrochim. Acta 20, 709 (1975).

Ar 80 Archer, W. I., R. D. Armstrong, D. P. Sillick, W. G. Budgen, and J. H. Duncan. J. Mat. Sci. 15, 2066 (1980).

Be 36 Beevers, C. A. and S. Brohult. Z. Kristallogr. 95, 472 (1936).

Bo 77 Boilot, J. P., A. Kahn, J. Thery, R. Collongues, J. Antoine, D. Vivien, C. Chevrette, and D. Gourier. Electrochim. Acta 22, 741 (1977).

Bo 78 Bones, R. J. and T. L. Markin. J. Electrochem. Soc. 125, 1587 (1978).

Br 78 Bradt, R. C., et al. (eds.). Fracture Mechanics of Ceramics, v. 4. (New York: Plenum Press, 1978).

Br 79a Brennan, M. P. J. Electrochim. Acta 24, 473 (1979).

Br 79b Brennan, M. P. J. Electrochim. Acta 24, 529 (1979).

Br 79c Breiter, M. W. and B. Dunn. J. Appl. Electrochem. 9, 291 (1979).

Br 79d Breiter, M. W. and B. Dunn. J. Appl. Electrochem. 9, 671 (1979).

Br 80a Breiter, M. W., B. Dunn, and R. W. Powers. Electrochim. Acta 25, 613 (1980).

Br 80b Brennan, M. P. J. Electrochim. Acta 25, 621 (1980).

Br 80c Brennan, M. P. J. Electrochim. Acta 25, 629 (1980).

Bu 78 Buechele, A. C. Effects Produced by the Introduction of Calcium into Sodium Beta-Alumina Solid Electrolyte. Masters Thesis. (Ithaca, NY: Cornell University, 1978).

Bu 79 Buechele, A. C. and L. C. De Jonghe. Am. Ceram. Soc. Bull. 58, 861 (1979).

Ca 59 Carslaw, H. S. and J. C. Jaeger. Conduction of Heat in Solids. (London: Oxford University Press, 1959).

Ca 79 Cahn, J. W. and R. W. Balluffi. Scripta Met. 13, 499 (1979).

Ch 76 Chatterji, D. (principal investigator). Development of Sodium-Sulfur Batteries for Utility Application. EPRI EM-266. Research Project 128-3, Annual Report, December 1976. (Palo Alto, CA: EPRI, 1976).

Ch 80 Chiku, T. "Application of β-Alumina to Na-S Storage Batteries," in Ta 80, p. 149 (1980).

Cl 73a Cleaver, B., A. J. Davies, and M. D. Hames. Electrochim. Acta 18, 719 (1973).

Cl 73b Cleaver, B. and A. J. Davies. Electrochim. Acta 18, 727 (1973).

Cl 73c Cleaver, B. and A. J. Davies. Electrochim. Acta 18, 733 (1973).

Cl 73d Cleaver, B. and A. J. Davies. Electrochim. Acta 18, 741 (1973).

Cl 73e Cleaver, B. and A. J. Davies. Electrochim. Acta 18, 747 (1973).

Cr 56 Crank, J. The Mathematics of Diffusion. (London: Oxford University Press, 1956).

Da 79a Davidge, R. W., G. Tappin, J. R. McLaren, and G. May. Am. Ceram. Soc. Bull. 58, 771 (1979).

Da 79b Davidge, R. W. Mechanical Behavior of Ceramics. (Cambridge: Cambridge University Press, 1979).

De 77 De Jonghe, L. C. (principal investigator). Substructure and Properties of Sodium Beta Alumina Solid Electrolyte. EPRI EM-494. Research Project 252-2, Interim Report, July 1977. (Palo Alto, CA: EPRI, 1977).

De 79a De Jonghe, L. C., L. A. Feldman, and P. Millett. Mat. Res. Bull. 14, 589 (1979).

De 79b De Jonghe, L. C. J. Am. Ceram. Soc. 62, 289 (1979).

De 80a De Jonghe, L. C. and L. A. Feldman. Mat. Res. Bull. 15, 777 (1980).

De 80b De Jonghe, L. C. and L. A. Feldman, and A. C. Buechele. "Initiation of Degradation in Polycrystalline Sodium-Beta Alumina Electrolytes," in So 80, p. 108 (1980).

De 80c Demott, D. S. J. Electrochem. Soc. 127, 2312 (1980).

De 80d De Jonghe, L. C. Improved Beta-Alumina Electrolytes for Advanced Storage Batteries. Progress Report - September 1980. LBL-12357. (Berkeley, CA: Lawrence Berkeley Laboratory, 1980).

De 81a De Jonghe, L. C., L. A. Feldman, and A. C. Buechele. J. Mat. Sci. 16, 780 (1981).

De 81b De Jonghe, L. C. Transport Number Gradients and Solid Electrolyte Degradation. LBL-12070R. (Berkeley, CA: Lawrence Berkeley Laboratory, 1981). J. Electrochem. Soc. 129, 753 (1982).

El 65 Elliott, R. P. Constitution of Binary Alloys, First Supplement. (New York: McGraw-Hill, 1965).

Fa 73a Fally, J., C. Lasne, Y. Lazennec, Y. Le Cars, and P. Margotin. J. Electrochem. Soc. 120, 1296 (1973).

Fa 73b Fally, J., C. Lasne, Y. Lazennec, and P. Margotin. J. Electrchem. Soc. 120, 1292 (1973).

Fa 78 Farrington, G. C., and J. L. Briant. Mat. Res. Bull. 13, 763 (1978).

Fe 81 Feldman, L. A. and L. C. De Jonghe. Initiation of Mode I Degradation in Sodium-Beta Alumina Electrolytes. LBL-12194. (Berkeley, CA: Lawrence Berkeley Laboratory, 1981). J. Mat. Sci. 17, 517 (1982).

Fo 77 Ford Motor Company - Research Staff. Research on Electrodes and Electrolytes for the Ford Sodium-Sulfur Battery, Semiannual Report for the Period June 30, 1976 to December 30, 1976. (Dearborn, MI: Ford Motor Company, 1977).

Fo 80 Foster, L. M., G. V. Chandrashekhar, J. E. Scardefield, and R. B. Bradford. J. Am. Ceram. Soc. 63, 509 (1980).

Gi 74 Gibson, J. G. J. Appl. Electrochem. 4, 125 (1973).

Gu 72 Gupta, N. K. and R. P. Tischer. J. Electrochem. Soc. 119, 1033 (1972).

Ha 57 Hart, E. W. Acta Met. 5, 597 (1957).

Ha 61 Harrison, L. G. Trans. Faraday Soc. 57, 1191 (1961).

Hi 82 Hitchcock, D. Work in Progress. Lawrence Berkeley Laboratory, Berkeley, CA (1982).

Im 80 Imai, Atsuo. "Studies of Beta-Alumina Ceramics at Toshiba," in Ta 80, p. 75 (1980).

Iw 80 Iwabuchi, S. and S. Hattori. "Material Properties of the Solid Electrolyte in Sodium-Sulfur Cells," in Ta 80, p. 82 (1980).

Jo 77 Jones, I. W. Electrochim. Acta. 22, 681 (1977).

Ka 76 Kao, Y. K. and P. C. Wagner. J. Electrochem. Soc. 123, 632 (1976).

Kr 74 Kroger, F. A. The Chemistry of Imperfect Crystals, v. 3. (Amsterdam: North Holland Publishing Co., 1974).

Ku 68 Kummer, J. T. and N. Weber. SAE Trans. 76, 1003 (1968).

Ku 72 Kummer, J. T. Prog. in Solid State Chem. 7, 141 (1972).

Li 79 Lingscheit, J. N., G. J. Tennenhouse, and T. J. Whalen. Am. Ceram. Soc. Bull. 58, 536 (1979).

Ma 76 Mahan, G. D. and W. L. Roth (eds.). Superionic Conductors. (New York: Plenum Press, 1976).

Mi 78 Mitoff, S. P. (principal investigator). Development of Sodium-Sulfur Batteries for Utility Application. EPRI EM-683. Research Project 128-4, Interim Report, May 1978. (Palo Alto, CA: EPRI, 1978).

Mi 79 Miller, M. L., B. J. McEntire, G. R. Miller, and R. S. Gordon. Am. Ceram. Soc. Bull. 58, 522 (1979).

Mo 78 Moffat, W. G. The Handbook of Binary Phase Diagrams. (Schenectady, NY: General Electric Co., 1978).

No 58 Noden, J. D. and K. Q. Bagley. U. K. At. Energy Authority, Ind. Group R. and DB(C) TN-80, 1958.

Pa 76 Patano, C. G. Jr., D. B. Dove, and G. Y. Onoda Jr. J. Vac. Sci. Technol. 13, 414 (1976).

Ra 16 Rankin, G. A. and H. E. Merwin. J. Am. Chem. Soc. 38, 568 (1916).

Ra 82 Raj, G. Work in Progress. Lawrence Berkeley Laboratory, Berkeley, CA (1982).

Ri 75 Richman, R. H. and G. J. Tennenhouse. J. Am. Ceram. Soc. 58, 63 (1975).

Ro 76 Roth, W. L., F. Reidinger, and S. La Placa. "Studies of Stabilization and Transport Mechanisms in Beta and Beta" Alumina by Neutron Diffraction," in Ma 76, p. 223 (1976).

Sh 77 Shen, L. Y. L., G. A. Pasteur, and D. E. Aspnes. Phys. Rev. B 16, 3742 (1977).

Sh 78 Shetty, D. K., A. V. Virkar, and R. S. Gordon. "Electrolytic Degradation of Lithia Stabilized Polycrystalline β"-Alumina," in Br 78, p. 651 (1978).

Si 56 Sittig, M. Sodium: Its Manufacture Properties and Uses. (New York: Reinhold Publishing Corp., 1956).

So 72 South, K. D., J. L. Sudworth, and J. G. Gibson. J. Electrochem. Soc. 119, 554 (1972).

So 80 The Society of Solid State Ionics and Galvanic Cells. Third International Meeting on Solid Electrolytes-Solid State Ionics and Galvanic Cells. Sept. 15-19, 1980, Extended Abstracts. (Tokyo, Japan: 1980).

Ta 80 Takahashi, T. and A. Kozawa (eds.). Applications of Solid Electrolytes. (Cleveland, OH: JEC Press, 1980).

Te 75 Tennenhouse, G. J., R. C. Ku, Richman, and T. J. Whelan. Am. Ceram. Soc. Bull. 54, 523 (1975).

Te 77 Texas Instruments, Inc. Applied Statistics. Solid State Software Module Users Manual. (Dallas, TX: Texas Instruments, Inc., 1977).

Te 80 Tennenhouse, G. J. Private Communication (1980).

Tr 55 Trocki, T., W. H. Breggeman, and F. E. Crever. Proc. U.N. Conf. Peaceful Uses Atomic Energy, Geneva, 1955. v. 9, pp. 241-251 (1955).

Va 79 Vashishta, P., J. N. Mundy, and G. K. Shenoy (eds.). Fast Ion Transport in Solids, Electrodes and Electrolytes. (Amsterdam: North Holland Publishing Co., 1979).

Vi 79 Virkar, A. V., and G. R. Miller. "Degradation of Rapid Ion Conductors Under Electrolytic Conditions," in Va 79, p. 87, (1979).

Vi 80 Virkar, A. V., L. Viswanathan, and D. R. Biswas. J. Mat. Sci. 15, 302 (1980).

Vi 81 Virkar, A. V. J. Mat. Sci. 16, 1142 (1981).

Wa 80 Walsh, W. J. Phys. Today 33, 34 (1980).

We 74 Weber, N. Energy Conversion 14, 1 (1974).

Wh 71a Whittingham, M. S. and R. A. Huggins. J. Electrochem. Soc. 118, 1 (1971).

Wh 71b Whittingham, M. S. and R. A. Huggins. J. Chem. Phys. 54, 414 (1971).

Wo 78 Worrell, C. A. and B. A. W. Redfern. J. Mat. Sci. 13, 1515 (1978).

Ya 67 Yao, Y. Y. and J. T. Kummer. J. Inorg. Nucl. Chem. 29, 2453 (1967).

This report was done with support from the Department of Energy. Any conclusions or opinions expressed in this report represent solely those of the author(s) and not necessarily those of The Regents of the University of California, the Lawrence Berkeley Laboratory or the Department of Energy.

Reference to a company or product name does not imply approval or recommendation of the product by the University of California or the U.S. Department of Energy to the exclusion of others that may be suitable.

TECHNICAL INFORMATION DEPARTMENT
LAWRENCE BERKELEY LABORATORY
UNIVERSITY OF CALIFORNIA
BERKELEY, CALIFORNIA 94720